1-1-2007

Using electrical resistance tomography (ERT) and computational fluid dynamics (CFD) to study the mixing of pseudoplastic fluids with a SCABA 6SRGT impeller

Leila Pakzad
Ryerson University

USING ELECTRICAL RESISTANCE TOMOGRAPHY (ERT) AND COMPUTATIONAL FLUID DYNAMICS (CFD) TO STUDY THE MIXING OF PSEUDOPLASTIC FLUIDS WITH A SCABA 6SRGT IMPLELLER

by
LEILA PAKZAD

M.Sc., Science and Research University, Tehran, Iran, 2003
B.Sc., Science and Research University, Tehran, Iran, 2000

A Thesis
Presented to Ryerson University
in Partial Fulfillment of the Requirements for the Degree of
Master of Applied Science
in the Program of Chemical Engineering

Toronto, Ontario, Canada, 2007

ABSTRACT

Leila Pakzad

Using Electrical Resistance Tomography (ERT) and Computational Fluid Dynamics (CFD) to Study the Mixing of Pseudoplastic Fluids with a Scaba 6SRGT Impeller

MASc, Chemical Engineering, Ryerson University, Toronto, 2007

The objective of this work is to use electrical resistance tomography (ERT) and computational fluid dynamic (CFD) modeling to investigate the flow field generated by a Scaba 6SRGT impeller in the agitation of the xanthan solution, as a pseudoplastic fluid with yield stress. ERT provides a non-destructive technique to measure, in three dimensions, the concentration fields inside the mixing tanks. Using ERT, the impeller flow pattern, the dimensions of the cavern formed and the mixing time in the agitation of xanthan solutions were evaluated. The sizes of cavern measured using ERT were in good agreement with that calculated using Elson's model (cylindrical model). ERT provides both overall mixing time using 1264 probes (316 probes for each plane) and local mixing time using 4 selected probes or pixels. The dimensionless mixing times (Nt_m), obtained from ERT were correlated well with the Moo-Young correlation, confirming that increasing impeller speeds decreases the mixing times. The 3D flow field generated by a Scaba 6SRGT impeller and tracer homogenization in the agitation of xanthan gum were also simulated using the commercial CFD package (FLUENT). The experimental torque measurements were used to validate the numerical simulations. The validated CFD model provided useful information regarding the impeller pumping capacity and flow pattern, the velocity profiles, the formation of cavern around the impeller, and the mixing time. CFD results show good qualitative as well as quantitative agreement with the experimental results and theory. The sizes of cavern measured using CFD were in good agreement with that calculated using Elson's model. The local mixing times predicted from CFD simulations agreed well with literature in a way that mixing times varied inversely with the cube root of the power consumed per unit volume of the solution. CFD under predicted the local mixing times measured using ERT by 11-47%.

Table of Contents

List of Tables

List of Figures

Acknowledgement

I would first like to express my sincere gratitude and appreciation on my supervisors Dr. Farhad Ein-Mozaffari and Dr. Philip Chan for their guidance and encouraging enthusiasm during all times of this work.

I acknowledge the assistance of all the staff and technologists in the Chemical Engineering Department at Ryerson University.

I also would like to acknowledge the advice and helpful suggestion of my friends in the Fluid Mixing Technology Laboratory at Ryerson University.

Financial support from Natural Sciences and Engineering Research Council of Canada (NSERC) is gratefully acknowledged.

To Mehrdad,

For his love and support.

1. INTRODUCTION

Mixing is among the most common processes in chemical, biochemical, pharmaceutical, polymer, mineral, food and wastewater treatment industries. Understanding mixing mechanisms, crucial to industrial scale-up, still remains difficult especially in the case of complex fluids. Some complex fluids in industrial mixing are yield-pseudoplastic fluids. The yield-pseudoplastic fluid is a fluid with a yield stress and shear–thinning behaviour (Skelland, 1967), which have low apparent viscosities at high shear rates and high apparent viscosities in low shear rates. Examples of this type of behaviour can be found in a number of polymer solutions and in solid-liquid suspensions, e.g. paints, pigment slurries, and paper pulp (Elson, 1988).

Mixing of yield-pseudoplastic fluids such as xanthan results in the formation of well-mixed zone around the impeller, which is called cavern with stagnant regions in the rest of the tank. Understanding the cavern is an important component of mixing design of non-Newtonian fluids so one can be sure that the whole fluid in the tank is in motion and there is no stagnant region. The stagnant region around the impeller gives rise to poor mass and heat transfer (Amanullah *et al.*, 1997). It is desirable to eliminate these stagnant regions by properly designing the agitation systems. Several techniques have been used and reported in the literature for assessment of cavern size and shape such as coloring with dye and taking pictures (Wichterle and Wein 1975 & 1981), traversing hot film anemometer (Solomon *et al.*, 1981), taking X-ray photographs (Elson *et al.*, 1986 and Elson, 1988), and using laser Doppler anemometer (Hirata and Aoshima, 1994).

Among the mixing parameters, mixing time as a key variable provides a powerful means for the evaluation of mixing effectiveness. It is defined as the time required to a specific homogeneity level and it is usually measured after a small amount of a tracer had been injected into the stirred vessel. Over the years, several experimental techniques (Fox and Gex, 1956; Raghav Rao *et al.*, 1988; Distelhoff *et al.*, 1997; Lee and Yianneskis, 1997; Pant *et al.*, 2001; and Masiuk and Lacki, 1993) have been used for the mixing time measurements. Most of these techniques suffer from two important disadvantages: the

difficult applicability in the case of non-transparent fluids and the confinement of the mixing time to a small number of the locations inside the tank.

The general practice for the evaluation of stirred vessels has been done over the years through experimental investigation for a number of different impellers and vessel geometries and fluid rheology. Such an approach is usually costly and sometimes is not an easy task. Attempts are being made to use the science and fundamentals of mixing by using advanced computational fluid dynamics (CFD). With CFD, the various parameters contributing in the process can be examined in shorter time and with less expense, a task otherwise difficult in experimental techniques. However, this approach is limited by a relative lack of sufficiently detailed measurements for validation and corroboration. One advantage of CFD is that, once a validated solution is obtained, it can provide valuable information that would be not easy to obtain experimentally.

Proper validation of the computer predictions relies upon alternative measurement techniques such as photographic techniques, laser based techniques (LDA and PIV) suited to optically transparent systems, and tomographic techniques based on such properties as resistance, capacitance, and impedance (Williams and Beck, 1995).

A tomographic technique is a tool to identify the dynamics characteristics of industrial processes based on real-time measurements such as electromagnetic (X-ray, γ-ray and etc.), electrical (ERT, ECT, and EIT) and acoustic (ultrasonic). The selection of tomographic tool is defined by the purpose of the measurement information and the measurement that needs to be obtained (Williams and Beck, 1995).

Among mentioned techniques, the electrical resistance tomography presents some interesting new opportunities for both validating CFD and understanding of mixing processes (Bolton *et al.*, 2004). The recent and rapid development of non-intrusive ERT seems to provide a valuable set of tools for the analysis and control of mixing processes especially in the case of non-Newtonian fluids (either opaque or transparent). The

technology is particularly suited for monitoring different processes and has the potential to provide enough information for the chemical development process.

The objective of this work is to investigate the effect of viscoplastic behaviour (shear thinning viscosity and yield stress) and impeller speed on mixing of xanthan solutions agitated by a Scaba 6SRGT impeller using ERT and CFD. Mixing performance is investigated experimentally in terms of flow pattern, cavern size, and mixing time measurements. The experimental torque measurements are used to validate the CFD flow model. The CFD model is then used to determine the effects of fluid rheology and impeller speed on impeller flow pattern, pumping capacity, velocity profile, cavern size, and mixing times.

Chapter two gives a brief review of literature to present the fundamentals in non-Newtonian mixing such as fluid behaviour, power consumption, pumping capacity, impellers type and flow pattern, cavern formation, and mixing time. At the end, some ERT and CFD applications especially in the mixing process are presented.

Chapter three is concerned with the design, specification, structure, and operation of a typical ERT. In chapter four, the fluid rheology, the experimental setup (including ERT system), and experimental procedures are described.

Chapter five is organized in two sections: first section reviews the general information about CFD such as governing equations, numerical methods, and methods of discretizing the equations as well as grid generation and other relevant information and the second section of the chapter is devoted to the current CFD model development.

Chapter six provides the experimental and CFD results as well as discussions and finally chapter seven summaries the overall conclusions of this study and gives recommendations for future work.

2. LITERATURE REVIEW

2.1 Introduction

Mixing operation is an integral part of the chemical industries. The efficiency of mixing performance has a significant effect on the product quality. Therefore, it is essential to achieve a detailed knowledge of mixing in stirred vessels. Among other important process parameters, the power consumption and mixing time are some of the parameters that should be determined. These parameters are dependent on the impeller flow patterns which themselves are influenced by the fluid rheology.

Fluid exhibits a wide variety of rheological behaviour ranging from Newtonian to viscoelastic (Rao, 1999). While Newtonian agitation is well understood, understanding non-Newtonian mixing still remains difficult. The viscoplastic fluids, which can be found frequently in food, paint, cosmetic, and pharmaceutical industry are common class of non-Newtonian fluids. These fluids have high apparent viscosity at low shear rate, which has effect on the mixing performance. Agitation of viscoplastic fluids such as xanthan results in the formation of a well-mixed zone around the impeller (the so-called cavern). Therefore, another important parameter in viscoplastic fluids is the cavern size.

Although several works have been done on the fundamental understanding of non-Newtonian mixing experimentally (Norwood and Metzner, 1960; Hoogendoorn and Den; Wichterle and Wein, 1975 and 1981; Solomon *et al.*, 1981; Elson *et al.*, 1986; Elson, 1988; Hirata *et al.*, 1991 and 1994; Galindo and Neinow, 1992 and 1993; Hirata and Aoshima, 1994 and 1996; Serrano-Carreon and Galindo, 1997; Amanullah *et al.*, 1997 and 1998; Nienow and Elson, 1988; Jaworski and Nienow, 1994; Wang *et al.*, 2000; Ascanio *et al.*, 2003; and Foucault *et al.*, 2006) and using CFD (Armenante *et al.*, 1997; Sahu *et al.*, 1998; Kelly and Humphrey, 1998; Wilkstrom *et al.*, 1998; Torrez and Andre, 1999; Kelly and Gigas, 2003; Murthy and Jayanti, 2003*a*; Murthy and Jayanti, 2003*b*; Montante *et al.*, 2005; Wu *et al.*, 2006; Adams and Barigou, 2006; Arratia *et al.*, 2006;

and Saeed *et al.*, 2007), there are still uncertainties especially in terms of cavern size and mixing time.

The aim of this chapter is to give a brief review of literature to present the fundamentals in non-Newtonian mixing such as fluid behaviour, power consumption, pumping capacity, impellers type, and flow pattern, cavern formation and mixing time. Finally, some CFD and ERT applications in mixing are presented.

2.2 Xanthan Gum Rheology

2.2.1 Rheology

By definition, rheology is the study of the flow behaviour and deformation, which results from fluid being subjected to shear stress by the application of a force (Rao, 1999). The rate at which the fluid deforms (shear rate) depends not only on the magnitudes of the applied force (shear stress) but also on a property of the fluid called viscosity (Wilkes, 2006). Viscosity is the property of a liquid to resist flow or a change in shape through internal forces and molecular attraction (Holland and Chapman, 1966). According to the effects produced because of a shear stress, fluids can be classified as shown in Fig. 2.1

With Newtonian fluids, the shear stress is directly proportional to the shear rate and the proportional constant is equal to fluid viscosity, i.e. the plot of the shear stress versus shear rate, the so-called 'flow curve' or 'rheogram' yields a straight line with a slope of fluid viscosity passing through the origin refer to Fig. 2.2. Newton's law of viscosity is written in the general form as:

$$\tau = \mu\dot{\gamma} \tag{2.1}$$

where τ is the shear stress, μ is Newtonian viscosity, and $\dot{\gamma}$ is the shear rate.

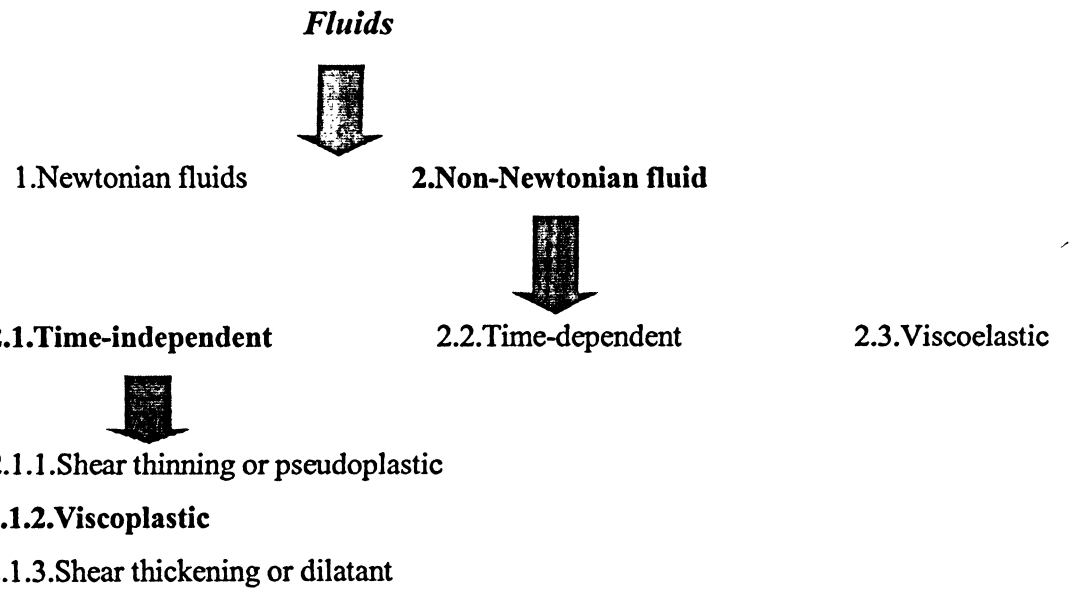

Fig. 2.1. Fluid behaviour classification (Source: Chhabra and Richardson, 1999).

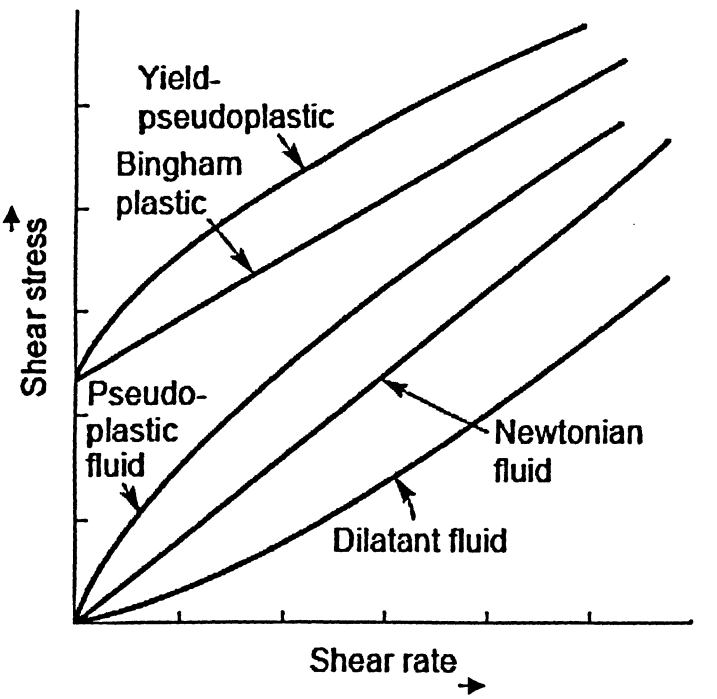

Fig. 2.2. Flow curves of Newtonian and non-Newtonian fluids (time-independent) on linear co-ordinates.

2.2.2 Non-Newtonian Fluids

A non-Newtonian fluid is one whose shear stress versus shear rate plot (flow curve) is non-linear such as pseudoplastic (shear thinning) or dilatant (shear thickening) fluid and/or does not start at the origin such as viscoplastic fluid, or that the material exhibits time-dependent rheological behaviour as a result of structural changes (Rao, 1999 and Chhabra and Richardson, 1999). Such material can usually be grouped into three main general classes (Skelland, 1967):

1. Time-independent fluids; The rate of shear at any point is determined only by the shear stress at that point and depends on nothing else.

2. Time-dependent fluids; The relation between shear stress and shear rate depends upon the duration of shearing, i.e. the shear stress and hence the viscosity changes (decreasing or increasing) with the duration of the shearing.

3. Viscoelastic fluids; These fluids exhibit both elastic solids and ideal viscous fluid characteristics after deformation.

2.2.2.1 Time-independent Fluid Behaviour

The flow behaviour of this class of the non-Newtonian fluid can be described by the following equation:

$$\dot{\gamma} = f(\tau) \tag{2.2}$$

Eq. (2.2) shows that the value of $\dot{\gamma}$ at any point within the sheared fluid is determined by the shear stress at that point or vice versa. This class may be further subdivided into three types based on the form of the function in eq.(2.2):

1. Shear-thinning or pseudoplastic; The flow curve starts at the origin of the shear stress-shear rate plot but is concave upward (Rao, 1999). With this type of the fluid, viscosity decreases with increasing shear rate; therefore, an increasing shear stress gives a less than proportional increase in shear rate. In this case, good mixing may occur in the impeller region with near-stagnant regions in the rest of the vessel (Harnby *et al.*, 1992).

2. Viscoplastic; The flow curve may be linear or non-linear but will not pass through the origin because the flow of such materials cannot begin until a threshold value of stress i.e. the yield stress is exceeded (Chhabra and Richardson, 1999).

3. Shear-thickening or dilatant; The flow curve starts at the origin of the shear stress-shear rate plot but is concave downward. With this type of fluid, viscosity increases with increasing shear rate; therefore, an increasing shear rate gives a less than proportional increase in shear stress.

2.2.2.1.1 Viscoplastic Fluid

This type of fluid is characterized by the existence of a yield stress, which must be exceeded before the flow commences (Chhabra and Richardson, 1999). It is found that a minimum stress is required to break down the structure sufficiently before the fluid will flow. In this case, the well-mixed region close to the impeller, which has been called a cavern and a relatively stagnant fluid elsewhere, can be formed (Solomon *et al.*, 1981). Two general groups can be found in this type:

1. Bingham plastic fluid is a fluid with linear flow curve characterized by a constant plastic viscosity (the slope of the shear stress versus shear rate curve) and a yield stress.

2. Yield-pseudoplastic fluid is a fluid with a yield stress and a non-linear flow curve. It is possible to consider these materials as the particular class of shear–thinning behaviour.

A model may be considered a mathematical equation that can describe rheological properties. Several mathematical models have been developed in the literature some of which are listed in Table 2.1. Models that account for yield stress are known as viscoplastic models (Bird *et al.,* 1982). Three commonly used models for viscoplastic fluids are the Bingham plastic, Casson and Herschel-Bulkley fluid models (Wilkinson, 1959).

As shown in Fig. 2.2, the Newtonian model and the Bingham plastic model can be described by straight lines in shear stress-shear rate plot where the former has one parameter as viscosity and the latter has two parameters as viscosity and yield stress. As can be seen in Table 2.1, the Bingham plastic model is the simplest one describing the rheology of a fluid with a yield stress. The Herschel–Bulkley fluid model (Herschel and Bulkley, 1926) can be assumed as a simple generalization of the Bingham plastic model with the non-linear flow curve (Chhabra and Richardson, 1999). This model combines the effect of Bingham and power-law behaviour in a fluid.

To find the relation between shear stress and shear rate, the fluid sample is subjected to a uniform rate of shear in a suitably designed instrument (rheometer) and the corresponding shear stress is measured. This can be done using rotational instruments such as a coaxial cylinder, cone and plate, or parallel plate (Skelland, 1967).

2.2.3 Xanthan Gum[1]

Xanthan gum is a natural polysaccharide and one of the important industrial biopolymer (García-Ochoa, 2000). Xanthan gum is a high-molecular-weight extracellular heteropolysaccharide produced by the bacterium Xanthomonas campestris (Hassler and Doherty, 1990).

[1]Xanthan gum was found in the 1950s at the Northern Regional Research Laboratories (NRRL) of the United States Department of Agriculture (Margaritis and Zajic, 1978).

Table 2.1. Some flow models for describing shear rate versus shear stress data.

$\tau = \mu\dot{\gamma}$	Newtonian model
$\tau = \dfrac{\dot{\gamma}}{\left[\dfrac{1}{\mu_0} + K(\tau)^{(1/n)-1}\right]}$	Ellis model for low shear rate data containing μ_0 (Brodkey, 1967)
$\tau = \left[\mu_\infty \dot{\gamma} + K\dot{\gamma}^n\right]$	Sisko model for high shear rate data containing μ_∞ (Brodkey, 1967)
$\mu_{app} = \mu_\infty + \dfrac{\mu_0 - \mu_\infty}{1 + (\alpha_c\dot{\gamma})^m}$	Cross model for data over a wide range of shear rates
$\mu_{app} = \mu_\infty + \dfrac{\mu_0 - \mu_\infty}{\left[1 + (\lambda_c\dot{\gamma})^2\right]^N}$	Carreau model for data over a wide range of shear rates
$\tau = K\dot{\gamma}^n$	Power law model
$\tau = \tau_y + \mu\dot{\gamma}$	Bingham model
$\tau = \tau_y + K(\dot{\gamma})^n$	Herschel-Bulkley model (Herschel-Bulkley, 1926)
$\tau^{0.5} = \tau_y + K(\dot{\gamma})^{0.5}$	Casson model (Casson, 1959 and Mill, 1959)
$\tau^{n_1} = \tau_y{}^{n_1} + \eta_\infty(\dot{\gamma})^{n_2}$	Generalized model (Ofoli *et al.*, 1987)

Source: Rao (1999)

Xanthan gum has been used in food industry because of it's emulsion stabilization, temperature stability, compatibility with food ingredients, and pseudoplastic rheological properties (García-Ochoa, 2000). Because of such properties as thickening the aqueous solutions and stabilizer of the emulsions and suspensions, xanthan gum is used in pharmaceutical formulations, cosmetics, and agricultural products (Rao, 1999). It is also used in textile printing pastes, ceramic glazes, slurry explosive formulations, and rust removers (García-Ochoa, 1994).

2.2.3.1 Xanthan Properties

Xanthan gum is highly soluble in water (either cold or hot) because of the polyelectrolyte nature of the xanthan molecule (García-Ochoa, 1994). A small amount (<1%) of xanthan will increase water's viscosity by a factor of 100,000 at low shear rates and by a factor of 10 at high shear rates (Whitcomb, 1978). Few other polymers can match this behaviour (pseudoplasticity). Therefore, it is useful in many industrial applications, especially in the food industry where xanthan is used as a thickener, and to stabilize suspensions and emulsions.

2.2.3.1.1 The Temperature Effect

Xanthan solution viscosity depends on the temperature in such way that the viscosity decreases with increasing temperature. Morris (1977) studied the change in solution viscosity with temperature for xanthan solution and found that the viscosity declines as the dissolution temperature is increased up to 40°C. Between 40°C and 60°C, the viscosity increases with increasing temperature. For temperatures >60°C, the viscosity declines as the temperature is raised. Whitcomb (1997) measured viscosity as a function of temperature (5-95°C) for solutions of xanthan in distilled water. They found that there is a drop in viscosity with temperature beginning at 50°C. This behaviour is related to conformational changes[1] of the xanthan molecule. The conformation shifts from an ordered (low-dissolution temperature) to a disordered (high dissolution temperature) state (Ferguson and Kemblowski, 1991).

2.2.3.1.2 The Salt Effect

The presence of salts in xanthan solution influences its viscosity. At low xanthan concentration, the viscosity decreases slightly when a small amount of salt is added to the solution (Ferguson and Kemblowski, 1991). This effect has been associated to the reduction in molecular dimensions resulting from weakened intermolecular electrostatic

[1] The xanthan molecule seems to have two conformations, helix (ordered), and random coil (disordered), depending on the dissolution temperature and salinity (Rochefort and Middleman, 1987 and Garcia-Ochao and Casas, 1993).

forces (Smith and Pace, 1982). Viscosity increases at higher xanthan concentration when a large amount of salt is added (Rochefort and Middleman, 1987). This behaviour can be because of increased contacts between the polymer molecules (Milas *et al.*, 1985). It was shown that the viscosity of a xanthan solution is independent of the salt concentration when the salt content exceeds 0.1% w/v (Kang and Pettit, 1993).

2.2.3.1.3 The pH Effect

García-Ochoa (2000) showed that the viscosity of xanthan solutions is unaffected by pH changes between 1 and 13 while it was shown that at pH 9 or higher, xanthan is gradually deacetylated (Tako and Nakamura, 1984), and at pH lower than 3, xanthan loses the pyruvic acid acetyl groups (Bradshaw *et al.*, 1983). Either deacetylation or depyruvylation has hardly any effect on xanthan solution viscosity (García-Ochoa, 1994), and the deacetylated or depyruvylated xanthan shows similar rheological properties as native xanthan (Bradshaw *et al.*, 1983 and Kang and Pettit, 1993).

2.2.3.1.4 The Pseudoplastic Behaviour

At sufficient dilution and low shear rates, xanthan solutions show a region of Newtonian viscosity behaviour (Skelland *et al.*, 1967). However, more concentrated xanthan solutions exhibit a yield stress that must be overcome for the solution to flow (Whitcomb *et al.*, 1997 and Torres *et al.*, 1995). Yield stress gives stability to emulsions in low stress situations (Ma and Barbosa-Canovas, 1995). Generally, the main rheological features, which give xanthan solutions their utility, are a significant yield stress and a very high degree of pseudoplasticity (Galindo *et al.*, 1989; Hannote *et al.*, 1991; and Solomon *et al.*, 1981).

Several authors (Marcotte *et al.*, 2001; Whitcomb *et al.*, 1997; and Elliot, 1977) have employed the power-law equation, assuming the absence of a yield stress to model the viscosity of xanthan solutions. One rough approximation of the rheological behaviour of xanthan solution may be obtained using the Bingham model that is the simplest model for

a fluid with yield stress (Rao, 1999). However, in xanthan solutions, viscosity decreases as the shear rate increases and this means that xanthan solutions exhibit non-linear viscoplastic properties such as shear thinning. Therefore, a model which can explain both mentioned properties (yield stress and shear thinning) is needed; this model can be the Casson model (Hannote *et al.*, 1991) or the Hershel and Bulkley model (Ahmad *et al.*, 2005 and Sikora *et al.*, 2007).

The Herschel-Bulkley rheological model, eq.(2.3) encompasses the Bingham, power-law, and Newtonian relations. Since the Herschel-Bulkley model can successfully capture the rheological behaviour of xanthan solution, it is widely used (Ahmad *et al.*, 2005).

$$\eta = \frac{\tau_y}{\dot{\gamma}} + K|\dot{\gamma}|^{n-1} \tag{2.3}$$

where $\dot{\gamma}$ is the shear rate, τ_y is the yield stress, and K and n are shear rate independent constants often used to represent power-law fluids.

2.3 Power Consumption

To operate the impeller, knowledge regarding the required power consumption is very necessary (Chhabra and Richardson, 1999). Because of the very different flow pattern and mixing mechanisms involved, it is important to consider power consumption in Newtonian and non- Newtonian fluids separately.

2.3.1 Power Requirements for Mixing of Newtonian Fluids

The impeller power in a homogeneous liquid depends upon the geometry of the impeller and the tank, the liquid properties such as density and viscosity, the impeller rotational speed and the gravitational force (Tatterson, 1991):

$$P = f(\mu, \rho, N, D, T, g) \tag{2.4}$$

where P, μ, ρ, N, D, T, and g are power, fluid viscosity, fluid density, impeller rotational speed, impeller diameter, tank diameter and gravitational acceleration, respectively.

Applying dimensional analysis, we should get (Skelland, 1967):

$$\frac{P}{\rho N^3 D^5} = f\left(\frac{\rho N D^2}{\mu}, \frac{N^2 D}{g}\right) = f(\mathrm{Re}, Fr) \tag{2.5}$$

This relation shows that the dimensionless power coefficient $P/\rho N^3 D^5$ depends on both Reynolds number and Froude number for a fluid. The dimensionless groups can be presented as follow:

1. Power Number, P_o is a non-dimensional measure of the power drawn by the impeller.

$$P_o = \frac{P}{\rho N^3 D^5} \tag{2.6}$$

2. Froude Number, Fr represents the ratio of applied forces to gravitational forces. Thus, Fr is only considered when there are significant gravitational effects.

$$Fr = \frac{DN^2}{g} \tag{2.7}$$

3. Reynolds Number, Re indicates the relative importance of the inertial forces to the viscous forces.

$$\mathrm{Re} = \frac{\rho N D^2}{\mu} \tag{2.8}$$

If two immiscible liquids are being mixed the interfacial tension should be considered as:

$$\frac{P}{\rho N^3 D^5} = f\left(\frac{\rho N D^2}{\mu}, \frac{N^2 D}{g}, \frac{N^2 D^3 \rho}{\sigma}\right) \tag{2.9}$$

where $N^2D^3\rho/\sigma$ is the Weber group, and σ is the surface tension. For a single-phase fluid, it has been found that the functional relation becomes as:

$$\frac{P}{\rho N^3 D^5} = C\left(\frac{\rho N D^2}{\mu}\right)^a \left(\frac{N^2 D}{g}\right)^b \tag{2.10}$$

C, a and b are the constants and depend on the geometry of the system and on the state of flow. In a baffled tank, or in a vessel with an offset impeller to eliminate swirl, the gravitation effect will be negligible and we can neglect the Froude number in the above relations; and the power number is only a function of the Reynolds number.

The relation between power number and Reynolds number can be divided to three parts (Skelland, 1967): at small values of Reynolds number (<~10), laminar flow occurs and the slope of the power curve on log-log coordinates is -1. At very high values of the Reynolds number (>10^4), the flow is fully turbulent. In this region, Power number is about constant and independent of Reynolds number. In between the laminar and turbulent zones, there exists a transition zone. No simple mathematical relationship exists between P_o and Re in this flow region (Chhabra and Richardson, 1999). It is generally accepted that laminar flow occurs for Re<~10, but for transitional region is strongly dependent on the impeller and vessel geometry.

2.3.2 Power Requirements for Mixing of non-Newtonian Fluids

The Reynolds number (*Re*) for a non-Newtonian fluid is commonly determined in the laminar flow regime by the method introduced by Metzner and Otto (1975). The basis of their method is the determination of the range of shear rate in the mixing system. In order to do this, they defined an apparent viscosity as the viscosity of a Newtonian fluid, which requires the same power input under the same conditions of size and speed (in the laminar region). The next stage is to relate this to the other variables of the system. They assumed that the fluid motion in the region of the impeller could be characterized by an average shear rate, which was proportional to the rotational speed of the impeller, i.e.

$$\dot{\gamma}_{ave} \propto N = k_S N \tag{2.11}$$

where N (rotation per second, rps, s^{-1}) is the impeller rotational speed and k_S is a function of the impeller type and the vessel configuration.

The value of k_S obtained by Metzner and Otto (1957) was 13 for the disk flat-blade turbine. Calderbank and Moo-Young (1959) have repeated and extended this work for a wide variety of sizes and types of impellers. They found the value of k_S as 10 rather than 13 for Bingham and pseudoplastic fluids, suggested by Metzner and Otto (1957). For dilatant fluids the relative size of the impeller and mixing vessel has an effect on the shear rate and therefore on the effective value of k_S. Skelland (1967) has reported the experimental values for k_S for a variety of the impeller, turbines, propeller, paddle, and anchor. For pseudoplastic fluids, k_S, lies approximately in the range 10-13 for most impeller types, while slightly larger values 25-30 have been reported for anchors and helical ribbons (Bakker and Gates, 1995).

It is believed that Metzner and Otto correlation provides an engineering basis for design of mixing processes (Doraiswamy *et al.*, 1994). This correlation has been widely accepted and used in non-Newtonian fluid mixing studies such as Nienow and Elson (1988).

2.4 Impeller Type

Mixing is widely used in the process industries to carry out many different physical processing such as blending miscible liquids in reactors, dispersing of gases or immiscible liquids into a liquid phase, and suspension of solids. Based on the operation purpose, the best choice for the geometry of the tank and impeller type can be selected. The efficiency of the mixing system is influenced by its impeller flow pattern dependent upon the geometry of the impeller (Chhabra and Richardson, 1999). It is convenient to classify the agitators into two types; axial flow and radial flow refer to Fig. 2.3.

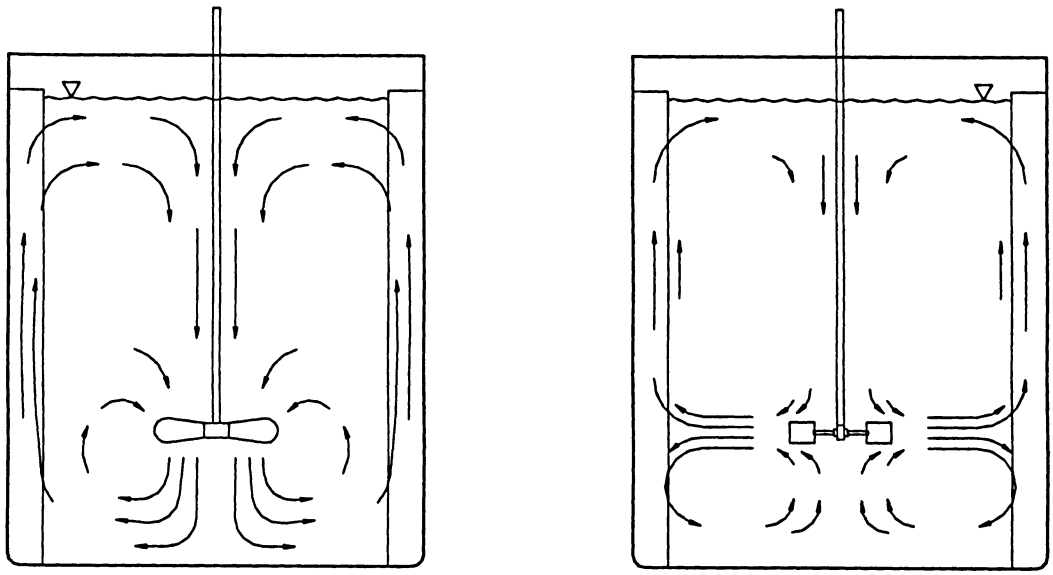

(a) (b)

Fig. 2.3. Flow patterns in a baffled tank, generated by: (a) axial-flow impeller, and (b) radial-flow impeller.

The axial-flow impellers such as propellers, marine-type and pitch-blade impellers discharge fluid parallel to the impeller shaft, i.e. in a vertical direction which may be upwards or downwards (Oldshue, 1983). These types are used for blending, solid suspension, heat transfer, etc. (Paul *et al.*, 2004). The axial flow turbine is significantly more efficient than the radial flow turbine in terms of flow per horsepower.

The radial-flow impellers such as disc turbine (Rushton), hollow-blade turbine (Scaba) and flat-blade impeller discharge fluid to the tank wall in radial direction, i.e. horizontal one (Oldshue, 1983) and then the flow splits into two equal flows (up and down) after leaving the blade tips and consequently produce strong top-to-bottom flows both above and below the impeller with the equal suction. They are more efficient for gas-liquid and liquid-liquid dispersion. They provide higher shear and turbulence level with lower pumping. A radial-flow impeller may either have a disc (Rushton and Scaba) or be open (flat blade turbine) and may have either flat blades as Rushton or curved ones as Scaba. The Impellers with the disc provide more uniform radial flow pattern than open ones.

The hollow-blade impellers (e.g., Scaba SRGT, Chemineer CD-6 or BT-6, and smith) provide great dispersion, high rates of interphase mass transfer and minimal power draw sensitivity to changes in liquid viscosity and gas flow rate (Paul *et al.*, 2004)

A group led by J. M. Smith developed the original concave blade concept (Van't Riet and Smith, 1973). ICI in England and Scaba in Sweden have further developed the concave-blade disc impeller (Saito *et al.*, 1992). Finally, Chemineer (Chemineer, Inc; 1998) developed the Concave Disc (CD-6) and (BT-6) impellers.

It was shown that the concave-blade disc impeller have dramatic improvements over the standard flat-blade disc turbine i.e. Rushton (Paul *et al.*, 2004). Galindo and Nienow (1993) showed that at the same Reynolds number, the decline in power consumption of the Scaba agitator due to aeration is 20 to 50% smaller than that observed with Rushton (flat-blade disc) turbine.

A concave disc impeller, called Scaba, Smith, (CD-6) or (BT-6), commonly used for gas-liquid mixing is shown in Fig. 2.4.

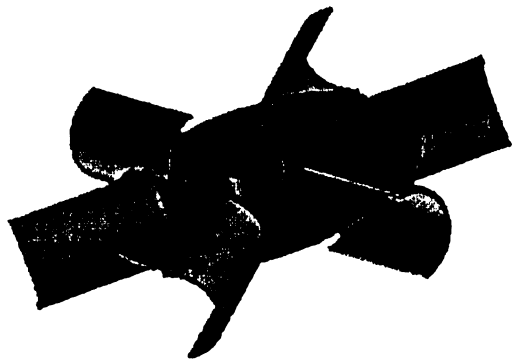

Fig. 2.4. Concave disc impeller.

2.5 Pumping and Circulation Flow Rates

All the power applied to the mixing system produces circulating capacity (Paul *et al.*, 2004). Pumping capacity, depending on the impeller type, impeller rotational speed, and tank and impeller geometry is the amount of liquid discharged by the rotating impeller.

Mean flow rates in either the axial (Q_z) or radial (Q_r) directions were estimated by integration as follow (Jaworski *et al.*, 1996):

$$Q_z(z) = 2\pi \int_{r_1}^{r_2} r(\bar{v}_z)_z dr \tag{2.12}$$

$$Q_r(r) = 2\pi r \int_{z_1}^{z_2} (\bar{v}_r)_r dz \tag{2.13}$$

where z and r are axial and radial coordinates respectively and $\bar{v}$ is mean velocity.

As mentioned, depending upon the impeller type, the liquid near the stirrer is pumped axially, either tangentially or radially. Pumping capacity (Q_p) of the impeller is meant the liquid flow, which is passed through the surface swept by the impeller (Zlokarnik, 2001).

The rates of the volumetric flow entering (Q_{in}) and leaving (Q_{out}) the zone swept by an impeller can be obtained from:

$$Q_{in} = \int_{A_s} \bar{v}_{n,in} dA_s \tag{2,14}$$

$$Q_{out} = \int_{A_s} \bar{v}_{n,out} dA_s \tag{2.15}$$

where A_s is swept surface area and $\bar{v}_n$ is the mean velocity component (radial or axial) normal to the surface. In general, the swept surface (A_s) is given by $\pi D^2/4$ for axial-flow impellers and by πdb for radial-flow impellers, D is the impeller diameter and b is the blade height. By definition, at steady state, their absolute values should be equal to the pumping capacity (Q_p):

$$|Q_{in}| = |Q_{out}| = Q_p \tag{2.16}$$

The dimensionless flow rate number known as flow number can be defined by normalized Q_p by ND^3:

$$N_Q = \frac{Q_p}{ND^3} \tag{2.17}$$

Fig. 2.5 shows the typical control volume for a radial-flow impeller, it shows that fluid enters the impeller axially and exits radially. Therefore, the pumping capacity and circulation flow for radial impeller are calculated as follows:

$$pumping\ \ capacity = Q_p = \pi(2r + 2d)\int_{blade\ width} v_r dz \tag{2.18}$$

where d is an arbitrary radial distance from the tip of the blade to the point where Q_P is determined. It can be assumed as zero, i.e. the flow rate can be determined at the blade tip. The circulation flow Q_C defined as the flow rate of fluid returning to the impeller in the axial direction (z). As shown in Fig. 2.5, in the region above the impeller (upper loop), Q_{C1} is the flow rate of all the fluid moving downward along the shaft. Below the impeller (lower loop), Q_{C2} is the flow rate of the fluid moving upwards:

$$Q_{C1} = \int_{blade\ diameter} 2\pi r (v_z)_{z=z_1} dr \tag{2.19}$$

$$Q_{C2} = \int_{blade\ diameter} 2\pi r (v_z)_{z=z_2} dr \tag{2.20}$$

Finally, the circulation and pumping number (flow number) for a radial impeller are defined as follow:

$$N_C = \frac{Q_C}{ND^3} = \frac{Q_{C1} + Q_{C2}}{ND^3} \quad and \quad N_Q = \frac{Q_P}{ND^3} \tag{2.21}$$

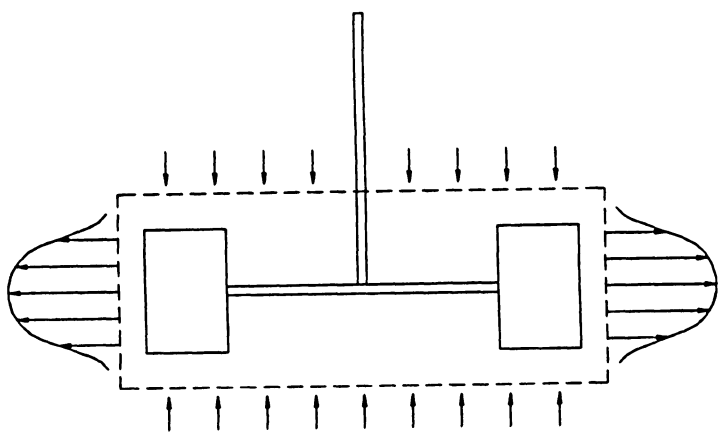

Fig. 2.5. Typical control volume for a radial-flow impeller.

2.6 Cavern

Mixing of non-Newtonian fluids is one of the most challenging tasks, especially for highly shear thinning fluids exhibiting yield stresses. Yield stress fluids play significant roles in the chemical, polymer, food, biochemical, biopolymer, and pharmaceutical industries (Arratia *et al.,* 2006). Agitation of yield stress fluids such as xanthan results in the formation of a zone of intense motion around the impeller (the so-called cavern) with essentially stagnant regions elsewhere. The term cavern was first used by Wichterle and Wein (1975) to describe the mobile zone around the impeller in extremely shear thinning suspensions of finely divided particulate solids. The stagnant regions as the poorly mixed give rise to poor mass and heat transfer (Amanullah *et al.*, 1997). It is desirable to eliminate these stagnant regions by properly designing and operating agitation systems. Measuring cavern size, one can be sure that the whole fluid in the tank is in motion (good mixing) or there is no undesirable stagnant or poor mixing region.

2.6.1 Experimental Methods to Evaluate the Cavern

Several experimental methods have been applied to investigate the cavern shape and size such as coloring with dye and taking pictures (Wichterle and Wein, 1975 and 1981; Galindo and Neinow, 1992 and 1993; Serrano-Carreon and Galindo, 1997; and Amanullah *et al.,* 1997 and 1998), traversing hot film anemometer (Solomon *et al.,* 1981), taking X-ray photographs (Elson *et al.,* 1986; Elson, 1988; and Nienow and Elson, 1988), using laser Doppler anemometer (Hirata *et al.,* 1991 and 1994 and Hirata and Oshima, 1994 and 1996; and Jaworski and Nienow, 1994), and using planner laser induced (Adams and Barigou, 2006; and Arratia *et al.,* 2006) and ultraviolet fluorescence (Arratia *et al.,* 2006). It can be observed that several techniques have been used and reported in the literature for assessment of cavern size and shape. With visual technique involving addition of a dye as a tracer and taking picture and laser based techniques, the medium must be transparent (Drain, 1980) while most of the non-Newtonian fluids are opaque. However, hot film anemometer (HAW) has considerable advantages specially compared with laser Doppler anemometers (LAD) in the case of cost, frequency response, size of sensor, and signal to noise ratio (Bruun, 1995), it has the disadvantage of delicate

probes presence which modifies the local flow field. The X-ray technique provides a non-intrusive measurement in opaque fluids (Elson, 1988), a task otherwise impossible for LDA and HAW. The penetration depth of X-rays is restricted by the X-ray opacity of the fluids used and the vessel walls (Nienow and Elson, 1999).

To summarize, a good technique to evaluate the cavern formation, shape and size should not offer obstruction /disturbance to flow; it should be applicable in the case of nontransparent medium and vessel; it should have high temporal and spatial resolution; it should be used easily; and finally it should be cheap in cost.

The most important techniques for cavern evaluation reported in literature are LDA, HWA, and X-ray technique.

2.6.1.1 Laser Doppler Anemometry (LDA)

LDA is a single point optical technique for measuring the velocity in a non-intrusive manner by using seeded particles conveyed by a fluid flow (Drain, 1980). This is based on the measurement of laser light scattered by particles that pass through a pattern of light and dark surface. This technique was first developed by Yeh and Cummins (1964). It is useful in studies of fluid dynamics since there is no obstruction to the flow. The spatial and temporal resolution for this technique is very high and it can cover a wide range of flow velocities (magnitude and direction). Reed *et al.* (1977) used LDA in a stirred tank for the first time and then considerable progress in this application has been made, especially in the turbulent flow regime (Jaworski *et al.*, 1996; Nouri and Whitelaw, 1990; and Ranade and Joshi, 1989) which has some essential advantages as compared with hot-wire anemometry (Costes and Couderc, 1988). The main limitations of this technique are that it depends on the presence of sufficient particles in the flow (Ruck, 1991), fluid studied by LDA must be transparent; and optical access is required. Most often in industrial situations, the vessels are made of non-transparent materials and the operating liquids are opaque.

2.6.1.2 Hot-Wire Anemometry (HWA)

This technique is based on the convective heat transfer from a heated wire or film element placed in the fluid flow (Bruun, 1995). Therefore, any changes in the fluid flow condition affecting the heat transfer from the heated element can be studied with HWA system. HWA can then provide information related to the velocity and temperature of the flow, concentration changes in gas mixtures, and phase changes in multiphase flows. However, HWA has some advantages compared with LDA in the case of cost, fast response, and signal to noise ratio (Bruun, 1995), it has the disadvantages of delicate probes presence in the flow, which modifies the local flow field, and probes must be cleaned and recalibrated after each time use.

2.6.1.3 X-ray Technique

X-ray photons are a form of electromagnetic radiation produced following the discharge of an inner orbital electron and subsequent shift of atomic orbital electrons from statuses of high to low energy (Chung and Smith, 2000). When a monochromic beam of X-ray photons falls onto a given case, three basic phenomena may result: absorption, scatter, or fluorescence. These three phenomena form the bases of three important X-ray methods: the absorption technique, which is the basis of radiographic analysis; the scattering effect, which is the basis of X-ray diffraction; and the fluorescence effect, which is the basis of XRF spectrometry. Elson *et al.* (1986) have used the absorption X-ray technique to study the flow patterns and cavern sizes during the mixing of opaque fluids exhibiting yield stress.

Absorption occurs where only a certain fraction of the radiation may pass through the absorber. Therefore, a number of photons have been lost in the absorption process. In order to use X-ray, the heavy metal tracer, which is performed as an opaque solution (absorber), should be added to the mixing tank. The main disadvantages of this method are relatively long data analyses, which make it as a slow method and also radiation control (Willimas and beck, 1995).

2.6.2 Cavern Mathematical Models

Several works attempted to correlate cavern size to the power drawn by yield stress fluids using theoretical and empirical models. The models improved over the years by assuming different cavern shapes such as spherical (Solomon *et al.*, 1981), cylindrical (Elson *et al.*, 1986 and 1988 and Hirata and Aoshima 1994 and 1996), and toroidal (Amanullah *et al.*, 1998 and Wilkens *et al.*, 2005), considering different forces (tangential and axial), assuming different flow regimes inside the cavern, and using different rheological models such as Power-law, Herschel-Bulkley, Bingham plastic and etc.

2.6.2.1 The Spherical Model

Solomon *et al.* (1981) developed a mathematical model (eq. (2.22)) for a spherical cavern centered upon an impeller mixing a fluid with a yield stress based on a momentum balance, assuming that the power dissipated by the impeller is transmitted through the fluid to the cavern wall, the shear stress at the cavern boundary equals the fluid yield stress (the stress at all points beyond the cavern boundary must be less than the yield stress), and the predominant motion of the fluid within the cavern is tangential:

$$\left(\frac{Dc}{D}\right)^3 = \left(\frac{4P_o}{\pi^3}\right)\left(\frac{N^2D^2\rho}{\tau_y}\right) \tag{2.22}$$

when $D \leq D_C \leq T$ (Tank diameter).

D_C, D, N, ρ, τ_y and $P_o=P/\rho N^3D^5$ are cavern diameter, impeller diameter, impeller speed, fluid density, fluid yield stress and power number, respectively. The term $N^2D^2\rho/\tau_y$ on the right hand side of eq. (2.22) is called the yield stress Reynolds number, Re_y (Etchells *et al.*, 1987). This equation shows cavern size governed by the properties of the fluid (density and yield stress), power input, and agitator design (diameter and speed).

2.6.2.2 The Cylindrical Model (Elson's Model)

Using X-ray flow visualization technique, the spherical model was modified by Elson *et al.* (1986 and 1988) to the cylindrical model (eq. (2.23)) which successfully predicts the behaviour of the cavern until it hits the vessel walls, or some other boundary. This model indicates that the dimensionless cavern diameter D_C/D is proportional to the product of the power number and the "yield Reynolds number".

$$\left(\frac{Dc}{D}\right)^3 = \left(\frac{1}{\left(Hc/Dc + 1/3\right)\pi^2}\right)\left(\frac{N^2D^2\rho}{\tau_y}\right)P_0 \qquad (2.23)$$

where Hc is the cavern height.

Although both models (eqs. (2.22) and (2.23)) predict the cavern diameter equally well, the cylindrical model (eq. (2.23)) is a better representation of the cavern shape (Amanullah *et al.*, 1998). Once the cavern reached the wall, the impeller type has little influence on the vertical expansion of the fluid (Amanullah *et al.*, 1997). The cavern studies using different impellers in fluid possessing yield stress have been continued by several works including those by Elson (1990) for marine propeller, Galindo and Nienow (1992 and 1993) for THE Lightnin A315 and Scaba 6SRGT impeller respectively, Underwood (1994) for the axial flow Prochem Maxflo T impeller, Amanullah *et al.* (1997) for axial flow SCABA 3SHPI impeller, and Serrano-Carreon and Galindo (1997) for four different impellers (Rushton turbine, Chemineer He-3, CD-6 and Scaba 6SRGT) in individual and dual arrangements.

2.6.2.3 The Dissipation Model

Using LDA measurements, a mathematical model (eq. (2.27)) for a right circular cylinder cavern was proposed by Hirata and Aoshima (1994 and 1996). This model also assumes that fluid motion ceases if the shear stress in the dissipating zones near the cavern boundary is less than the fluid yield stress. The difference between this model (dissipation

model) and the cylindrical one is the representative shear stress τ_d in the dissipating zones, which is assumed proportional to the average shear stress τ_{av} responsible for the dissipation rate in a cavern:

$$\tau_d = \alpha \tau_{av} \tag{2.24}$$

where α is a proportional constant. τ_{av} in (eq. (2.24)) may be expressed in terms of the average dissipation rate per volume (ε_v) and the apparent viscosity (μ_{app}) as:

$$\tau_{av} = \left(\varepsilon_v \mu_{app}\right)^{1/2} \tag{2.25}$$

and

$$\varepsilon_v = P/V_C = P_o \rho N^3 D^5 / V_C \tag{2.26}$$

where P is the impeller power and V_C is the volume of a cavern. Assuming the right circular cylinder and $\tau_d = \tau_y$ on the cavern boundary and rearranging the above equation, one obtains the following relation:

$$\left(\frac{Hc}{Dc}\right)\left(\frac{Dc}{D}\right)^3 = \left(\frac{4\alpha^2}{\pi}\right)\left(\frac{N^2 D^2 \rho}{\tau_y}\right)^2 P_0 \,\mathrm{Re}^{-1} \tag{2.27}$$

Under the condition where the cavern does not meet the sidewall of the vessel and $Hc/Dc = 0.5$, they obtained $\alpha = 0.43$. This model is also applicable to the estimation of the cavern height for a baffled and unbaffled vessel with $\alpha = 1/6$.

2.6.2.4 The Torus-shaped Model

A torus-shaped cavern is another approximation as seen by eye using dye tracers in transparent fluids (Galindo and Nienow, 1992). Based on this shape, a mathematical model (eq. (2.28)), axial force model, was developed by Amanullah *et al.* (1998). This

model considers the total momentum imparted by the impeller as the sum of both tangential and axial shear components, transported to the cavern boundary by the pumping action of the impeller.

$$\left(\frac{Dc}{D}\right)^2 = \frac{1}{\pi}\sqrt{N_f{}^2 + \left(\frac{4P_0}{3\pi}\right)^2}\left(\frac{N^2D^2\rho}{\tau_y}\right) \tag{2.28}$$

where $N_f = F_a / PN^2D^4$ is the dimensionless axial force number and F_a is the axial force imparted by the impeller. This model can also be applied to the caverns generated by the radial flow impellers if N_f=0 as follows:

$$\left(\frac{Dc}{D}\right)^2 = \left(\frac{1}{3}\right)\left(\frac{4P_0}{\pi^2}\right)\left(\frac{N^2D^2\rho}{\tau_y}\right) \tag{2.29}$$

They also used a method, which does not require an estimation of the fluid yield stress for the prediction of cavern diameters since the power-law rheological model is used and relies on an estimation of the fluid velocity at the cavern boundary.

2.6.2.5 The Elliptical Torus Model

Wilkens *et al.* (2005) proposed an experimental approach to determine the cavern dimensions (diameter and height) for an opaque Bingham plastic fluid (ketchup) by injecting glitter, freezing the fluid, and dissecting the frozen solid. They also developed an elliptical torus model (eqs. (2.30) and (2.31)) without accounting axial force to predict the cavern diameter and height with the cavern boundary defined by the yield stress of the fluid.

$$Dc = \left(\frac{32M}{\pi^2\alpha\tau_y}\right)^{1/3} \tag{2.30}$$

where α is the ellipse parameter, found as 2.3 for a radial flow impeller and 3.4 for an axial flow impeller and M is torque imparted to the fluid, and cavern height can be determined from:

$$Hc = \frac{\beta Dc}{2} \tag{2.31}$$

where β is a ratio of ellipse major axis to minor axis. The β average values were found to be 1.6 and 2.3 for a radial and axial impeller respectively. This shows that the cavern for an axial impeller is taller than that of a radial impeller at equal cavern diameters, which is in good agreement with the flow pattern of two types of impellers.

Besides all works done to determine the cavern size, some studies were focused on the nature of the flow in the cavern region such as Moore *et al.* (1995), Mavros *et al.* (1996), Amanullah *et al.* (1998), and Jaworski and Nienow (1993 *a,b* and 1994).

2.7 Mixing Time

One important process parameter for the mixing processes is the blending time, which is usually termed the mixing time. Experimental determination of the mixing time involves giving a tracer input with different properties at some locations in the bulk and measuring the tracer concentration as a function of time by means of a suitable sensor. The tracer is then distributed through the vessel and mixes with the contents of the mixing tank, and finally a uniform concentration is achieved. The mixing time is defined, as the time required achieving a certain degree of uniformity. Mixing time is typically considered, as the time required the tracer concentration to reach within 95% of the completely mixed value. The tracer used can be a chemical species, an electrolyte, or a thermal species. There are physical and chemical methods to determine the mixing time, for which the attainment of a particular degree of mixing is required.

2.7.1 Experimental Methods to Measure the Mixing Time

Over the past several years, several techniques based on the measurements of concentration, electrical conductivity, temperature colorimetry and other optical methods have been developed to provide quantitative understanding of the mixing behaviour as a mixing time (Nere *et al.*, 2003). As the obtained mixing times depend on the technique used for their determination, the most important experimental techniques used in the other studies to measure the mixing time will be discussed as follow:

2.7.1.1 Visual Techniques

The simplest technique for measuring mixing time is to add a dye and see how the dye moves throughout the mixing tank (Shervin *et al.*, 1991). The technique most commonly used is known as dye decolorization (Menisher *et al.*, 1999). In this method, the contents of the mixing tank are coloured using one chemical, and then a second chemical is added to remove the color (Fox and Gex, 1956; Lee *et al.*, 1957; Norwood and Metzener, 1960; Pandit and Joshi, 1983; Kawase *et al.*, 1997; Ascanio *et al.*, 2002; Delaplace *et al.*, 2004; Foucault *et al.*, 2006; and Delaplace *et al.*, 2007). However, this technique is simple but can rarely be used in industry because the industrial vessels are nontransparent and a sight glass cannot cover the whole vessel (Nere *et al.*, 2003). On the other hand, this method is in the lack of an objective definition of mixing time and consequently, depends on visual observations used to determine the mixing time. It is believed that the visual technique as a qualitative technique just can provide an approximation for mixing time in mixing tanks (Paul *et al.*, 2004).

2.7.1.2 Conductivity Probe Technique

This technique (Kramers *et al.*, 1953; Biggs, 1963; Holmes *et al.*, 1964; Khang and Levenspiel, 1976; Komori *et al.*, 1988; and Raghav Rao *et al.*, 1988) uses a probe as a single-point sensor, which measures the conductivity of the solution that can be converted to concentration using a proper calibration. In this technique, the tracer has to be an electrolytic solution. However, this technique is cheap, fast (suitable for mixing systems

with short mixing times) and easy to use, but it provides an inaccurate mixing time (local mixing time) because the probe can only measure the local conductivity; thus the mixing time obtained by this method is a function of the probe position especially when the multiple impellers and dead zones exist. In complex processes such as mixing in non-Newtonian fluids, this method may be inadequate. On the other hand, it has the disadvantage of affecting the local flow pattern as well. In this method, the number, locations, and size of the probes have effect on the estimated mixing times (Paul *et al.*, 2004). Further, this technique is not suitable for using in nonconducting systems, in the systems where the rheological properties of the bulk are sensitive to changes in salt (as a tracer) concentration and in the systems with high temperature.

2.7.1.3 Light Intersection Imaging Technique (Laser-induced Fluorescence)

This technique (Hackl and Wurian, 1979 and Distelhoff *et al.*, 1997) consists of a laser sheet generator, which is directed toward the mixing tank. If a tracer with a fluorescent indicator is added, it glows only in the plane of the laser sheet. The mixing time is measured as the time required for achieving an image with homogeneous color throughout. This technique like visual technique requires a transparent vessel, and then it cannot generally be used in industry.

2.7.1.4 Liquid-Crystal Thermography (LCT)

This technique (Lee and Yianneskis, 1997) is based on the coloring of thermochromatic liquid crystals (LCs) viewing a different color when subject to different temperatures. The crystals are suspended in the mixing tank. A thermal pulse is given, and the mixing of this thermal pulse conveys different colors to the liquid crystals in different parts of the vessel. This can then be analyzed either visually or by a camera. However this technique is fast, it is difficult to be used because of the imperfect color response of the crystals and also needs transparent vessels and hence is not useful in industry. The accuracy of this technique depends on the calibration of the crystals, which consecutively depends on the lighting settings.

2.7.1.5 Radioactive Liquid Tracer Technique

In this technique (Pant *et al.*, 2001), a pulse of a radioactive liquid tracer is injected and the profile of the tracer concentration is monitored. This technique can be applied to nontransparent vessels, also in high temperature such as 300 °C, and does not disturb the flow pattern (Nere *et al.*, 2003). As a very small amount of the tracer is required, the time of injection is very small. The use of this technique is limited by its unavailability, transportation difficulty, and health hazards.

2.7.1.6 Computer Tomography with Coherent Light

This technique (Zlokarnik, 2001) needs radiations from four lines in mixing tank to be able to calculate the concentration field. First, an object marked by a dye is irradiated with a monochromic light, and then a 2D image is obtained: with irradiation in different directions, the image of the object can be reconstructed in horizontal planes using mathematical techniques. The negatives of the black and white film are scanned and processed by image analysis. Then the obtained images are used for the tomographic reconstruction. The results are concentration profiles of mixing performance, from which the mixing time is calculated. This technique needs transparent vessels; therefore, it cannot be used in industry.

2.7.1.7 Thermocouple-based Technique

A thermocouple-based mixing test can be performed by adding a liquid that has a different temperature from the bulk (Masiuk and Lacki, 1993). The temperature at different points in the bulk is monitored by time, and the probe is used to measure the mixing time. This technique can be used with nontransparent and/or nonconducting liquid. The problem with this technique is that it may not be suitable if the fluid properties such as viscosity are very sensitive to temperature changes.

2.7.1.8 Electrical Resistance/Impedance Tomography

In electrical tomography techniques (Williams *et al.*, 1993; Mann *et al.*, 1997; Holden *et al.*, 1998; Li and Wie, 1999; Wang *et al.*, 2000; Stanley *et al.*, 2001; Ricard *et al.*, 2005; Bolton *et al.*, 2004; Stanley *et al.*, 2005; Kim *et al.*, 2006; and Stanley, 2006), the electrical conductivity distribution in the mixing tank is reconstructed. A number of the electrodes with equal space between are positioned around the wall of the mixing vessel in horizontal planes. For recording the measurements, current is injected into two adjacent electrodes and then voltage is measured between the other adjacent electrode pairs (based on adjacent algorithm)[1]. The voltage difference measured represents necessary information over the conductivity distributions inside a tank. The local distribution of the electrical conductivity from voltage measurements is then reconstructed tomographically with a linearized back-projection process. Therefore, the behaviour of two liquids with different electrical conductivities can be investigated. The feasibility of this method to measure the mixing time was first established at a laboratory scale (Williams *et al.*, 1993) and then at full plant scales (Mann *et al.*, 1997).

As can be seen, in the case of the mixing time, several techniques have been proposed to measure the mixing time in an agitated vessel. Because of the simplicity, the visual and conductivity techniques have been commonly used in the past. Among the mentioned techniques, the measurement method based on the 3-D measurement of electrical resistance/impedance seems to be capable to measure mixing time (Nere *et al.*, 2003), since this technique can be used in the case of nontransparent vessels, task otherwise impossible by most of the techniques, does not disturb or obstruct the flow inside the tank, and can be used to identify the dead zones in mixing tank which is so critical in industry.

Using different experimental techniques, several studies (Kramers *et al.*, 1953; Fox and Gex, 1956; Norwood and Metzner, 1960; Biggs, 1963; Holmes *et al.*, 1964; Moo-Young *et al.*, 1972; Brennan and Lehrer, 1976; khang and Levenspiel, 1976; Sasakura *et al.*,

[1] More information will be found in chapter 3.

1980; Shiue and Wong, 1984; Raghav Rao *et al.*, 1988; Rewatkar and Joshi, 1991; Masiuk and Lacki, 1993; Rzyski, 1993; Shaw, 1994; Rutherford *et al.*, 1996; Distelhoff *et al.*, 1997; Nienow, 1997; Fentiman *et al.*, 1998; Zlokarnik, 2001; Bujalski *et al.*, 2002; Ascanio *et al.*, 2003; Bolton, 2006; and Foucault *et al.*, 2006) have been done to evaluate the effect of the various parameters such as impeller type and diameter, vessel diameter and geometry, impeller off-bottom clearance, impeller eccentricity, and baffles on the mixing time.

The mixing time is often combined with data power consumption in order to find the efficiency of the mixing system (Ascanio *et al.*, 2003). In fact, it is desirable to get a level fluid homogenization with minimum power impute per unit volume, *P/V*. A unique relationship exists between mixing time and power consumption per unit volume and is given by following equation (Moo-Young *et al.*, 1972 and Nienow, 1997).

$$t_m = c\left(\frac{P}{V}\right)^d \tag{2.32}$$

where t_m is the mixing time, P is a power, V is the volume, and c and d are exponent and proportionally constant respectively. The value of d have been found as -1/3 (Rewatkar and Joshi, 1991; Rzyski, 1993; and Foucault *et al.*, 2006) in most turbulent cases. The only difference is in c dependent on the impeller type and vessel geometry.

2.7.2 Mathematical Models for the Mixing Processes

An estimation of the mixing time may help one to evaluate the performance of the mixing tank. In such cases, correlations are expected to be useful. In the correlations, the dependent variable is the mixing time and independent variables are the impeller design, impeller diameter, number of the impellers and their relative spacing, mixing tank geometry, and impeller locations and speed.

The mixing process is a result of the transport at three levels (Patwardhan and Joshi, 1999) Molecular, eddy, and the bulk (convection). Usually, the bulk motion is more effective than either molecular or eddy diffusion or both (Nere *et al.,* 2003). Several approaches have been developed to model the mixing process. These approaches can be classified into five categories as empirical models, circulation models, eddy diffusion models, network of zones models, and CFD models.

1. Empirical Correlations; These models correlate the experimental data with the various operating parameters. The range of their applicability limits them. Results of several experimental studies have been combined into empirical correlations relevant to industrial applications (Hoogendoorn and Den Hartog, 1967 and Nienow, 1997). Table 2.2 shows some of the mixing time empirical models.

2. Circulation Models; These models assume that mixing process is controlled by the bulk flow, both eddy and molecular diffusion are unimportant and also circulation can be characterized by an average velocity (Norwood and Metzner, 1960; Joshi *et al.,* 1982; Raghava Rao *et al.*, 1988; and Rzyski, 1993). It is clear that the mean velocities change with the location in the stirred tank therefore, this assumption is just an estimate of the flow generated by the impeller.

3. Eddy Diffusion Models; These models assume that the mixing processes controlled by diffusion during motion (Brennan and Lehrer, 1976 and Nienow, 1997). This assumption leads to a very simplified image of the blending processes.

4. Network of Zones (NoZ) Models; These models divide the entire stirred vessel into a network of interconnected zones, each of which is considered to be well mixed (Mann and Mavros, 1982; Mann and Ying, 1994; Holden and Mann, 1996; Mann *et al.,* 1997; Rahimi and Mann, 2001; and Hoyle and Jia, 2004). They were the basis and a starting point for the CFD models. This model is more reliable as compared to the eddy and circulation models, because it assumes local flow filed.

Table 2.2. Several empirical correlations

Correlation	Measurement technique	Reference
$t_m = \frac{fH^{1/2}T}{(ND^2)^{4/6} g^{1/6}}$	Visual	Fox and Gex, 1956
$t_m = b_0 N^{b_1} D^{b_2} v^{b_3}$	Conductivity	Biggs, 1963
$Nt_m = a\,\mathrm{Re}^b$	Conductivity	Moo-Young *et al.*, 1972
$Nt_m = 6.7(T/D)^{5/3} N_P^{-1/3}$	-	Mersmann *et al.*, 1976
$\frac{Pt_m^{\,2}}{\mu T^3} = H_T \frac{T^2 \rho}{\mu t_m}$ Where $H_T = N_P (Nt_m)^3 (D/T)^5$	Thermal	Shiue and Wong, 1984
$\frac{1}{Nt_m} = C(D/T)^{2.5} N_P^{\,0.75} (n_b W/T)^{-0.1}$	Conductivity	Sano and Usui, 1985
$Nt_m = 5.37 \beta_A^{-0.87} (W/D)^{-0.314} n_b^{-0.482} (T/D)^{1.83} \times (C/T)^{-0.27} (H/T)^{0.413}$	Conductivity	Rewatkar and Joshi, 1991
$t_m = 5.91 T^{2/3} \left(\frac{\rho V}{P}\right)^{1/3} \left(\frac{T}{D}\right)^{1/3}$	Conductivity	Ruszkowski, 1994

5. CFD Models; CFD models enable computation of the flow field and homogenization of the tracer by a direct solution of their governing equations (Ranade *et al.*, 1991; Mann *et al.*, 1997; Sahu *et al.*, 1999; Patwardhan and Joshi, 1999; Jaworski *et al.*, 2000; Bujalski *et al.*, 2002; and Iranshahi *et al.*, 2006). In fact, CFD models can be considered as a further advancement of the "network of zones model". This model considers both bulk and eddy diffusion on a local level.

Using experimental LDV data as the boundary conditions for the impellers and using the Eulerian procedure, Ranade *et al.* (1991) was one of the first to simulating mixing time for a vessel agitated with pitched blade turbine. They investigated the effect of different axial positions for injection point.

Sahu *et al.* (1999) calculated flow fields and mixing time for five different designs of axial flow impellers. They tried to improve CFD predictions by means of network of zones modeling. The calculated mixing times were in excellent agreement with experimental values.

Various authors (Jaworski *et al.*, 2000 and Bujalski *et al.*, 2002) used sliding mesh or multiple reference frame techniques for flow driven by Rushton turbines combined with species transport equations to predict mixing time, but got values 2-3 times higher than the experimental values.

A simulation of flow field and tracer homogenization in stirred tank was performed using computational CFD package software (Kukukova *et al.*, 2005). Their results, i.e. dimensionless velocity profiles, power and pumping numbers, dimensionless concentration curves, and mixing times were compared with experiments, and they all showed good agreements except in the case of the mixing time.

Using CFD and LDA, Buwa *et al.* (2006) studied the flow characteristic of a new grid disc impeller under a wide range of operating conditions in terms of mixing time, power consumption velocity profile and turbulent kinetic energy. They found promising results for the new impeller as far as the mixing time and power consumption.

2.7.3 Non-Newtonian Mixing Time

Non-Newtonian mixtures are homogenized more slowly than Newtonian fluids in laminar and transition ranges due to the shear rate field existing in the mixing vessel (Ascanio *et al.*, 2003). In processes involving non-Newtonian fluids, mixing can become difficult because of the existence of dead zones. The dead zones also persist when baffles are added to the tank wall. The objective of the pervious studies was to minimize mixing time and eliminate the appearance of dead zones.

Some investigation results (Hoogendoorn and Den Hartog, 1967; Wang *et al.*, 2000; and Ihejirika and Ein-Mozaffari, 2007) show that helical impellers provide shorter mixing times and more uniform mixing than turbines, propellers and anchors.

Norwood and Metzner (1960) used a visual technique (acid/base indicator reaction) for measuring the mixing times with turbine impellers in baffled vessels in the turbulent regimes for Newtonian and non-Newtonian fluids.

Using color-discoloration technique, Ascanio *et al.* (2003) evaluated the new hybrid axial/radial flow impeller with Newtonian and non-Newtonian fluids in terms of power consumption and mixing times.

Foucault *et al.* (2006) studied the mixing time of a dual impeller mixer composed of an anchor impeller and three types of impellers (Rushton turbine, Rayneri-sevin impeller or new hybrid dispersing impeller) for Newtonian and shear thinning fluids. They found that the Rushton turbine is more effective in terms of mixing time in both Newtonian and non-Newtonian fluids.

2.8 Computational Fluid Dynamic[1] (CFD)

In CFD, we analyze the flow field, heat transfer, mass transfer, chemical reactions, and related phenomena by solving the mathematical equations using numerical methods. More and more CFD is becoming a necessary tool in the design of industrial processes. While mixing is an obvious application of CFD, there are hundreds of others, ranging from blood flow to supersonic flow (Paul *et al.*, 2004).

The main part of CFD is the fundamental governing equations of fluid dynamics (the continuity, momentum, and energy equations). The basic procedural steps of CFD modeling are explained below (Fluent, 2006).

[1] CFD will be discussed in detail in chapter 5.

1. Create the model geometry and grid; An important part of CFD modelling is the construction of the mesh since it has a strong effect on accuracy of the simulation. The geometry is first discretized into a number of computational cells. Discretization is the technique of approximating the differential equations appearing in the governing equations by a system of algebraic equations for the flow field variables at the discrete grid points in the flow domain.

2. Specify the material properties; Some properties such as density, viscosity, heat capacity, thermal conductivity, mass diffusion coefficients, and kinetic theory parameters should be specified as constant, selected from a database, or they can be functions of temperature, pressure or any other variable of state. Fluids can be modeled as being either incompressible or compressible. The viscosity of the fluid can be Newtonian or non-Newtonian.

3. Specify the boundary conditions; Once the grid is ready, the boundary conditions should be applied such as flow inlet and exit boundaries (pressure, velocity, and mass flow inlet and outlet), or wall boundary (temperature, shear rates, and heat fluxes on the walls).

4. Set up the solver and physical models; CFD provides complete modeling capabilities for a wide range of incompressible and compressible fluids, laminar and turbulent flow models, and steady state, transient or turbulent analyses.

5. Compute and monitor the solution; Once the grid is created and the physical properties and the boundary conditions are specified, the calculations can be started. The CFD codes solve the related governing equations for the divided domain using an iterative procedure.

2.8.1 CFD Applications in the Stirred Tanks

The general practice for the evaluation of stirred vessels has been done over the years through experimental investigation for a number of different impellers, vessel geometries, and fluid rheology. The experimental studies have limitations regarding the range of parameters that can be studied because it is very costly and time-consuming to investigate the effect of every possible combination of parameters on the vessel performance, a task otherwise easy for CFD such as the evaluation of the flow behaviour index (n) for power law fluid done by Kelly and Gigas (2003), shape factors (K_S and K_P) evaluation for yield stress fluids done by Torres and Andre (1999) and the evaluation of shear rates for a non-Newtonian power-law fluid done by Wu *et al.* (2006).

During the last two decades, CFD has become a powerful tool for understanding the flow phenomena (Armenante *et al.,* 1997), developing of new processes, and optimizing the existing processes (Sahu *et al.,* 1998). The design of an agitator for a mixing system is usually based on empirical correlations for mixing, heat transfer, and power consumption. Using CFD techniques, it is also possible to investigate the detail of the complicated flow field generated by the impellers (Tanguy *et al.,* 1992).

Although, in a case of non-Newtonian fluids, the CFD modelling approaches developed so far to characterize mixing in agitated vessels are limited, but the improvements in numerical grid refinement techniques and the development of sliding mesh and multiple reference frame methods now make it possible to use CFD modeling to forecast the mixing behaviour in terms of mixing time, power consumption, flow pattern, velocity profiles and so on.

Using a computational fluid dynamics software package (Fluent), extensive calculations were performed to study the flow of non-Newtonian fluids in a large fermentor with hydrofoil flow impellers (Kelly and Humphrey, 1998). They investigated how key parameters such as impeller speed and non-Newtonian rheology effect flow near the perimeter of a fermentor.

Using CFD-calculations, Wilkstrom *et al.* (1998) investigated the effect of fibre suspension rheology on the flow behaviour at low velocity such as cavern formation.

Murthy and Jayanti (2003*a*) investigated mixing of power-law fluids with the help of CFD. They have focused on the flow field created by an anchor impeller. A latter study by Murthy and Jayanti (2003*b*) showed that accurate calculations of the flow field and power consumption can be carried out for the helical ribbon impeller for power-law fluids.

Montante *et al.* (2005) evaluated the mixing processes by means of mixing time in stirred tanks for non-Newtonian fluid using CFD. They investigated the influence of the tracer injection position, turbulence modelling and numerical parameters such as time step on the predicted mixing times.

The laminar flow patterns and several mixing performance criteria in non-Newtonian fluids agitated by an anchor and double ribbon impellers were investigated using CFD by Iranshahi *et al.* (2006).

Arratia *et al.* (2006) presented an experimental and numerical investigation of mixing in shear-thinning fluids with yield stress in stirred tanks. It was shown that the numerical simulations of shear-thinning yield stress fluids seem to capture the essential features of the flow, such as cavern formation.

By means of CFD, Rivera *et al.* (2006) analyzed the performance of a coaxial mixer in terms of mixing time, power consumption and pumping rate in Newtonian and Non-Newtonian shear thinning fluids. They found that a co-rotating mode is more efficient than counter-rotating mode.

Using commercial CFD software, Ford *et al.* (2006) simulated pulp mixing in a rectangular chest agitated by a Maxflo impeller. Their simulations showed that in high bypass flow situation the CFD model could not quite capture the mixing dynamics of the

mixing chest, which was attributed to the chosen rheological model. Saeed *et al.* (2007) developed a CFD model of a cylindrical pulp-mixing chest equipped with a side entering axial-flow A-310 impeller. They studied the mixing performance of the chest in terms of the impeller flow pattern, velocity profile, cavern formation, and mixing time.

By means of CFD simulations, Shekhar and Jayanti (2003) investigated the flow field generated by anchor impellers in Newtonian and non-Newtonian fluids and also developed a correlation based on Metzner-Otto concept for predicting the power number.

Using numerical simulation (finite element method), Tanguy *et al.* (1992) studied the flow field generated by a helical ribbon impeller in mixing of Newtonian and power-law fluids in terms of circulation time and torque.

Using CFD and ultrasonic Doppler velocimetry, Ihejirika and Ein-Mozaffari (2007) studied the effect of the impeller speed, power, yield stress, and impeller-pumping direction on the mixing performance of a helical ribbon impeller agitated in non-Newtonian fluids. They found encouraging CFD results compared with experimental ones.

Despite all works done using CFD, still it has been used to investigate non-Newtonian flows only in a few studies (Moilanen *et al.*, 2006). A basic cause for the lack of using CFD in such cases is the shortage of experimental data that can adequately verify the CFD models. Proper validation of CFD predictions relies upon techniques that provide the commensurable measurements.

Alternative measurement techniques such as Laser Doppler Anemometry (LDA) (Wu and Patterson, 1989; Aubin *et al.*, 2001; Mavros *et al.*, 2001; Li *et al.*, 2005; Buwa *et al.*, 2006; and Rice *et al.*, 2006), Particle Image Velocimetry (PIV) (Armenante and Chou, 1996; Lamberto *et al.*, 1999; Zalc *et al.*, 2001; and Arratia *et al.*, 2006), and planner Laser Induced Fluorescence (pLIF) and UltraViolet (UV) fluorescence (Arratia *et al.*, 2006) have been successfully deployed for validating CFD predictions. However, inherent

opacity of most non-Newtonian fluids however has made it difficult for researchers to use LDV and PIV.

Electrical resistance tomography is found to be ideal for validation of CFD simulations in mixing tanks (Holden *et al.*, 1998), which will be discussed in the next section (2.9).

2.9 ERT[1] Applications in the Stirred Tanks

Tomography is an imaging technique that defines the contents of a closed system, for example pipelines and mixing vessels without physically looking inside (Williams and Beck, 1995). This involves sending a signal across the system and making an image based on the signal received through sensors. Sensors are placed around a cross-sectional plane of the system. A computer is used to reconstruct a tomographic image observed by the sensors. The image data can be analysed quantitatively for use in process control or qualitatively to develop models to describe individual processes (Williams and Beck, 1995). Process tomography can provide, for instance, measurements of two-phase pipe flow (Huang *et al.*, 1989), temperature profiles (Ostendorf *et al.*, 1986) and identification of the distribution of mixing zones in fluidized beds (Dyakowski *et al.*, 1999).

Electrical resistance tomography (ERT) is one of the most common techniques in the tomographic process (Dickin and Wang, 1996). The aim of electrical resistance tomography is to reconstruct the conductivity properties of an object from measurements of electrical signals taken from all possible views of the sensing electrodes (Mann *et al.*, 1997).

ERT is a measurement technique with a wide range of research and development applications including investigating of mixing processes (Kim *et al.*, 2006), monitoring stability of reaction in the polymerization reactor (Kaminoyama *et al.*, 2005), investigating solid-liquid filtration processes (Vlaev *et al.*, 2000), monitoring the performance of a hydrocyclone (Williams *et al.*, 1999), measuring and controlling of

[1] ERT will be discussed in detail in chapter 3.

bubble columns (Wang *et al.*, 2001 and Fransolet *et al.*, 2005), and monitoring multiphase processes such as solid-liquid (Lucas *et al.*, 1999 and Ricard *et al.*, 2005) gas-liquid (Wang *et al.*, 2001) and liquid-liquid (Dickin and Wang, 1996).

The feasibility of ERT to evaluate mixing was first established by UMIST group (Manchester, UK) at a laboratory scale (Williams *et al.*, 1993) and then at full plant scales (Mann *et al.*, 1997). Several ERT studies at UMIST (Manchester, UK) have been performed on a 2.7 m^3 capacity tank with eight rings of 16 stainless steel electrodes. For instance, Dickin and Wang (1996) applied the ERT to evaluate the mixing performance of miscible water/saline agitated by a Lightnin-A15 impeller at the low speeds.

The ability of ERT to distinguish different flow patterns from two types of impeller (Lightnin-A310 and Rushton disk turbine) has been shown by monitoring the dispersion of a brine pulse tracer at the plant scale (Holden *et al.*, 1998).

Using the UMIST pilot plant, ERT results were presented for gas-liquid mixing which can distinguish differences in liquid mixing behaviour between low viscosity (water) and high viscosity (0.25% Carbopol solution) liquids (Wang *et al.*, 1999).

Electrical resistance tomography has also been shown to be useful in detecting pathological mixing behaviour related to apparatus failures such as a misplaced gas sparger, undesirable solids accumulation, and a displaced feed point behind a baffle (Holden *et al.*, 1999).

ERT is proved useful for the validation of CFD predictions of mixing behaviour. ERT is chosen to validate CFD results because it allowed tests to be carried out on a meaningful scale (>1 m diameter) and with enough temporal resolution (Bolton *et al.*, 2004).

Some augmented-reality visualizations were presented for three practical mixing cases (dynamic unsteady mixing of a homogeneous fluid, pseudo-stationary two phase solid-liquid mixing, and dynamic two phase solid-liquid mixing) as carried out on a

polypropylene baffled tank stirred with six-blade Rushton turbine (Mann *et al.*, 2001). The obtained data conveys an understanding of the mixing behaviour, which in turn can be invaluable for the validating of CFD calculations.

The pixel distribution plots and 3D ERT images provided a powerful measure of the homogeneity within the vessel, which has been used to investigate the nature of the feed plume induced by the semi-batch feed (Stanley *et al.*, 2002). It was shown that ERT is a feasible technique for observing a semi batch process with reasonable temporal and spatial resolutions. The results presented are extremely useful for the validation of CFD predictions of mixing behaviour.

Kagoshima and Mann (2005) extended the ERT technique for the investigation of a semi batch barium sulphate precipitation process.

The performance of Lightning A310 in a gas-sparged tank was investigated by using Electrical Impedance Tomography (EIT) and the results were compared well with those obtained from CFD (White and Doblin, 2003).

Ricard *et al.* (2005) evaluated the applicability of ERT to the chemical development of active pharmaceutical ingredients (APIs) in stirred tank. The results were used to assess the validity of associated CFD models and correlations.

Applications of ERT technology to processes in pharmaceutical and related application areas include the on-line measurement of solids distribution in stirred tanks and crystallizers, monitoring the performance of an industrial pressure filter, and flow profile and velocity measurements in a physical model of a catalytic reactor (Bolton *et al.*, 2005).

2.10 Research Objectives

It is obvious from the literature review abovementioned that the information regarding mixing of non-Newtonian fluids is still inadequate. This study will try to employ ERT and CFD to study the mixing of pseudoplastic fluids with a Scaba 6SRGT impeller. The main contributions of this work are:

- To understand the flow field generated by Scaba.

- To study the effects of the xanthan rheology and impeller rotational speed on the power consumption, impeller flow pattern, dimensions of the cavern formed around impeller and the mixing time in the agitation of xanthan solutions.

- To develop a CFD model using FLUENT to enable prediction of power consumption, pumping capacity, velocity profile, cavern size, and mixing times.

3. PROCESS TOMOGRAPHY

3.1 Introduction

Tomographic technology is the attainment of measurement signals from sensors located around a cross-sectional plane of an object, such as a process vessel or pipeline (Williams and Beck, 1995). This makes known the distribution of components within the sensing zone. The basic aspect is to install a number of non-intrusive sensors around the vessel or pipe to interrogate process space. The sensor output signals depend on the position of the component boundaries within their sensing zones (Huang *et al.*, 1992). A computer is used to reconstruct a tomographic image of the cross-section observed by the sensors.

There are various sensing methods for process tomography based on transmission, diffraction, and electrical measurements with different features in relation to specific applications such as acoustic (Norton and linzer, 1979), electrical, and electromagnetic (Yu *et al.*, 1993) tomography systems, Table 3.1.

Tomography based on radiation sources such as X-rays can be easily found in nuclear engineering, where it finds its use in laboratories as a popular experimental device (Lahey and Ohkawa, 1989). On the other hand, in such industries as chemical and food, the routine use of X-rays should be limited in order to ensure the sensitivity of experiment and safety of the experimenter (Mann *et al.*, 1997). Such techniques for routine use based on electrical, optical and ultrasound principles are being developed (Dyakowski, 1996). In semi-transparent or opaque liquors, the use of instruments those based on optics is not possible.

The electrical tomography systems based on measurement of electrical properties such as resistance, capacitance, eddy current, permeability, etc. (Williams and Beck, 1995), are the best choice for the real-time imaging of industrial processes because of their simplicity, rugged construction and high-speed capability (Mann *et al.*, 1997). The most common techniques in electrical tomography (Table 3.2) are Electrical Impedance

Tomography (EIT), and Electrical Capacitance Tomography (ECT). Electrical Resistance Tomography (ERT) is a particular case of electrical impedance tomography.

This chapter is concerned with the design, specification, structure, and operation of a typical ERT.

3.2 Electrical Resistance Tomography System Structure

In the case of electrical resistance tomography (ERT), multiple electrodes are arranged around the periphery of the process vessel or pipeline in such a way that they are in contact with the process fluid but do not disturb the process flow pattern (Bolton and Primrose, 2005).

The block diagram of a typical ERT system is shown in Fig. 3.1 consisting of three main parts as a sensors system / process vessel, a data acquisition system (DAS) and a host computer/ image reconstruction system.

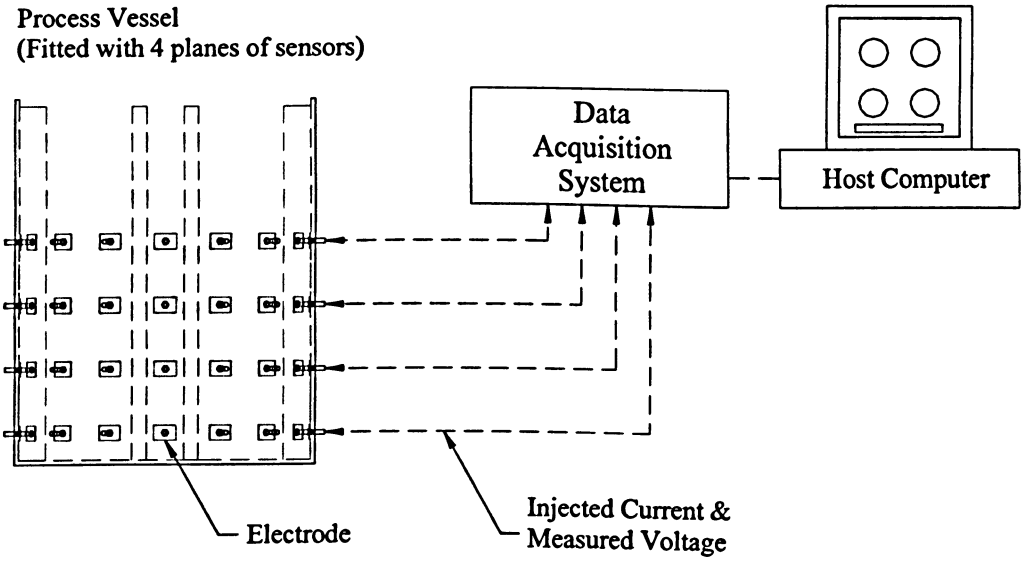

Fig. 3.1. The structure of a typical electrical resistance tomography system.

Table 3.1. Process tomography

Principle	Practical realization	Comments	References
Electromagnetic radiation	Optical	Fast. Optical access required.	Burns, 1994 Wright *et al.*, 2005
	X-ray and γ-ray	Slow. Radiation containment.	Toye *et al.*, 1994
	Positron emission	Labelled particle. Not on-line.	Parker *et al.*, 1994
	Magnetic resonance	Fast. Expensive for large vessels.	Sederman and Gladden, 2005
Acoustic	Ultrasonic	Sonic speed limitation. Complex to use.	Norton and linzer, 1979 Schelaberg *et al.*, 2000
Measurement of electrical properties	Capacitive, conductivity, and inductive	Fast. Low cost. Suitable for small or large vessels.	Dickin and Wang, 1996

Source: Williams and Beck (1995)

Table 3.2. Electrical tomography technique

Electrical methods	Principle realization	General remarks	Typical industrial applications
Capacitance (Dyakowski, 1999)	Capacitance sensing electrodes which are non-invasive if separated from the process fluid by a 10 mm thick plastic liner	Electrode may need to be of 10 cm^2 area to give sufficient capacitance change	Electrically insulating systems gas/oil, gas/solids two phase flow imaging fluidizing bed imaging
Resistance (Mann *et al.*, 1997)	Resistivity sensing, which are invasive but non-intrusive.	Very small electrodes can be used, Similar to system used for medical imaging.	Electrically conducting systems hydrocyclone imaging mixing study geophysical prospecting
Impedance	Similar to above but without current injecting electrodes. Current is induced by coils surrounding the vessel.	Similar to above.	Ground water monitoring and soil remediation

Source: Williams and Beck (1995)

3.2.1 Sensors

The goal of ERT is to obtain the resistance distribution in the domain of interest. The resistance distribution in a cross-section can be obtained by injecting currents (or applying voltages) on the domain and measuring voltages (or current) via a number of spaced electrodes mounted non-invasively on its boundary.

Sensors are the heart part of ERT system. It is very important to design the electrodes, which maximize the electrode's ability to sense conductivity changes in the domain of interest such as a mixing tank (Seagar *et al.*, 1987). They must be in continuous contact with the electrolyte inside the vessel. The electrodes attached on the periphery of the process vessel must have low cost, ease of installation, good conductivity (more conductive than the electrolyte), and resistance to corrosion/abrasion effects, or the process operation environment such as temperature, pressure, electrical fire hazards, vessel wall thickness and material (Williams and Beck, 1995). They can be fabricated from gold coated, platinum, stainless steel, brass, silver (Tapp and Williams, 2000), or silver palladium alloy which are commercially available in bolt or screw form and can often be threaded into the vessel wall and any suitable material depending largely on the process application (Dickin and Wang, 1996).

The position of electrodes is also important since the reconstruction algorithm is based on that the electrodes are located at exactly defined intervals in order to outline the maximum amount of information from inside of the vessel (Dickin and Wang, 1996). However, position is less critical if the measurements are fed into a qualitative reconstruction algorithm because they are normalized with respect to the reference data, the quantitative algorithm is highly sensitive to the electrode placement problems (Mann *et al.*, 1997). For a certain application, the electrodes may be installed inside the vessel on the impeller.

The size of electrodes is another important factor in measuring the electric field distribution (Mann *et al.*, 1996). A large surface area is required for the current injecting

electrodes to ensure that enough current is generated within the vessel (Dickin and Wang, 1996) while the voltage measuring electrodes are required to be as small as possible (Paulson *et al.*, 1992). Using the group-node finite element method (FEM), Wang *et al.* (1995) indicated that the smaller the size of electrode, the higher the sensitivity of the voltage measurement at the measurement electrodes and consequently the higher the common voltage at the current driven electrodes (when voltage measurement and current injection use the same electrode system). It is clear that the higher common voltage will produce a poor signal-to-noise (SNR) ratio because of the restrictions of the common voltage rejection ratio of the circuits used in the DAS (Mann *et al.*, 1997). Pinheiro *et al.* (1998) performed a theoretical analysis of the proportion of the boundary which the electrodes should cover to provide high SNR measurements and they recommended electrodes covering 80 and 60 % of the surface of the region of interest for the adjacent and opposite data collection schemes, respectively.

Fig. 3.2 shows two electrode structures for ERT system described by Hua *et al.* (1993) and Paulson *et al.* (1992). In these structures, more complex sensor designs, separate electrodes are employed for each task, i.e. injecting current and applying voltage. In Hua's electrode, a structure called a compound electrode (Fig. 3.2 (a)), the current source is injected to the relatively large surface area outer section, and the voltage is measured via an insulated point-sized central electrode. Fig. 3.2 (b) shows differently sized electrodes for generating current and measuring voltage. The smaller point sized measuring electrodes are located between the larger current-injecting ones. Therefore, both approaches require twice the amount of connectors, cabling and associated circuitry and the amount of time required to fabricate and install these types of electrode are significant. Despite these alternative configurations, the same sized electrodes both for current injection and voltage measurement are generally employed (Vlaev and Bennington, 2004 and Fransolet *et al.*, 2005) because of its simplicity. In this approach, the electrode size is selected in an optimum way for both current injection and voltage measurement.

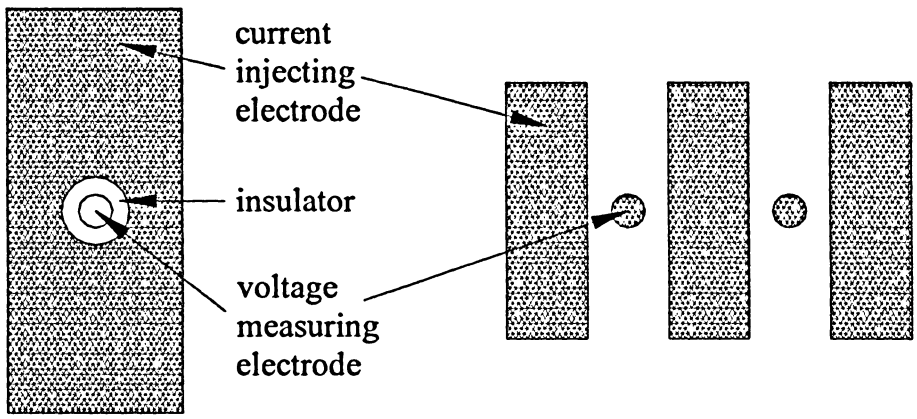

Fig. 3.2. Two electrode structures: (a) a compound electrode and (b) an interleaved electrode structure.

Number of the electrodes for taking the measurements is another important factor as the time taken to collect data and reconstruct the image is a function of number of electrodes (N) which affects the number of independent measurements (M) whereas the spatial resolution is proportional to $M^{1/2}$ (Williams and Beck, 1995).

Attaching electrodes to the wall of process vessels can be achieved by drilling holes into the vessel in order to mount the electrodes. In some cases, this kind of access in not possible. In another method, the electrodes can be retrofitted in vertical tubes or in a circular conduit, which are attached to the vessel wall. By retrofitting method, the process vessel is unaffected and the plastic tubes or conduit can be easily used in the other process vessels but the measurement procedure is an intrusive one.

Generally, the electrodes, positioned around the boundary of the vessel at fixed locations, make electrical contact with the fluid inside the vessels and are connected to the data-acquisition system by short length of signal-carrying co-axial cables to reduce the electromagnetic nosiness, which are common in process environments (Dickin and Wang, 1996).

3.2.2 The Data Acquisition System (DAS)

The data acquisition system (DAS) is located in a portable unit, which is connected to electrode module (attached to each electrode) and communicates with the host image reconstruction computer. DAS is responsible for obtaining the quantitative data describing the state of the conductivity distribution inside the vessel or pipeline. It performs the following functions: signal measurement, de-modulation, filtering, and control; waveform generation and synchronization; multiplexer control (share the current source and voltage measurement stages between any numbers of electrodes); and power supply (Mann *et al.*, 1997). Fig. 3.3 shows a schematic diagram of the ERT data acquisition system (DAS), made of six functional parts (Holden *et al.*, 1998).

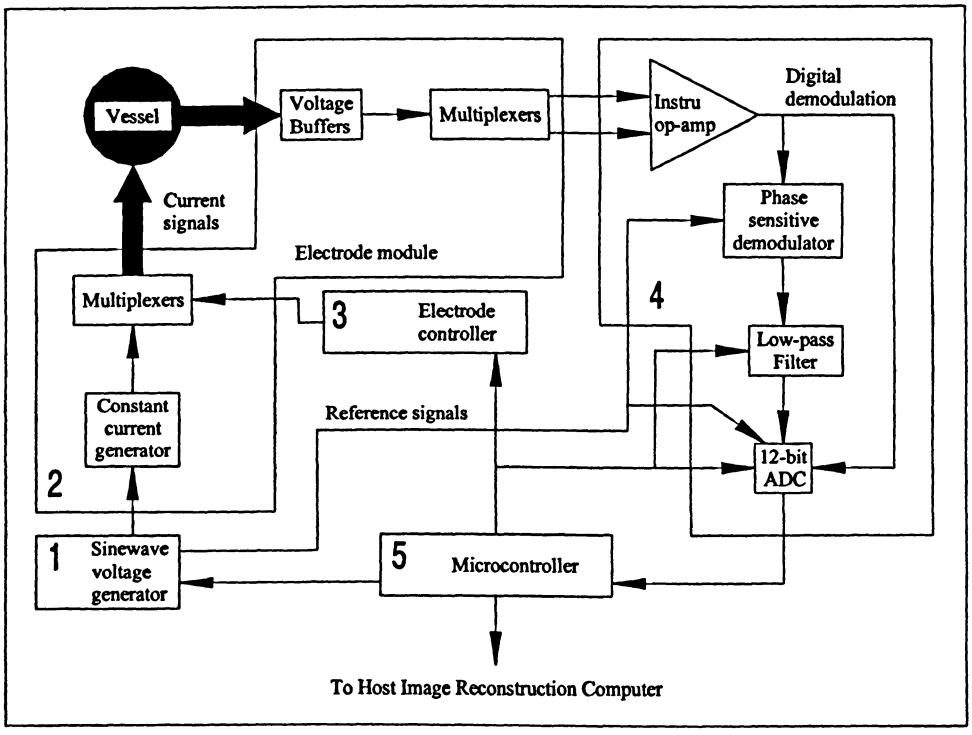

Fig. 3.3. Components of a typical data-acquisition system.

The voltage generator, shown in the bottom left-hand corner of Fig. 3.3, is an important part of DAS. The digital "stir-case" function generators are used to generate staircase wave. The digital pattern is converted to analogue by a high-speed digital to analogue

converter (DAC) and subsequently filtered to remove unwanted harmonics. Then the output of this part (a sine wave voltage) is fed into a voltage to current converter (referred to a voltage controlled current source-VCCS). Generally, current is used more (in comparable with voltage) to probe the material under investigation, because a good current source has a high output impedance whereas a voltage source has a low one (Dickin and Wang, 1996). Consequently, the effects of electrode/electrolyte contact impedance will be serious for a voltage source but negligible for a current one. As shown in Fig. 3.3, multiplexers (MUX) are necessary in order to share the current source and voltage measurement stages between any numbers of electrodes.

The output voltage because of injecting current into the vessel must be exactly measured for further use in the reconstruction algorithm. In general, this section includes the voltage measurement, demodulation, and filtering components. The high common-mode voltage may be larger than the desired differential voltage. Therefore, DAS needs a high common-mode rejection ratio (CMRR) over the range of injection. To solve this problem, an extra-grounded floating measurement (GFM) lead is attached to one of the unused electrodes as a ground electrode on the vessel (Beck *et al.*, 1993). The other end of the lead is attached to the output of the common-mode voltage. The effect of this simple arrangement is to produce a zero potential in the conducting region inside the vessel and therefore the high common-mode voltage is removed from the current-driven electrodes. This process is performed in instrumentation amplifier. A filter is placed after amplifier to remove unwanted components from the sine wave generator. After removing all undesirable components, a suitable analogue-to-digital converter (ADC) is needed. Finally using a digital demodulation, a desirable signal-to-noise (SNR) can be attained.

3.2.2.1 Data Collection Strategies

Good data collection strategies are very important because generally misleading images can be rebuilt if a full set of independent measurements is not collected (Dickin and Wang, 1996). It is necessary to select the scheme that has a good distinguishability and high sensitivity to conductivity changes in the process.

3.2.2.1.1 Distinguishability

Distinguishability (δ) is a parameter to check if the strategy chosen has the ability to distinguish between two conductivities (Gisser *et al.*, 1987):

$$\delta = \delta(i) = \frac{\|R(\sigma_1) - R(\sigma_2)\|}{\|i\|} \geq \varepsilon \tag{3.1}$$

where i, ε, σ_1 and σ_2 are current, precision of measurements, and two conductivities respectively and R donates a nonlinear functional associated with the resultant boundary voltage. There are four main strategies (refer to Fig. 3.4) as follows:

1. The adjacent strategy; The current is applied through two neighbouring electrodes and the voltages measured from successive pairs of neighbouring electrodes and then repeated again. In this case, the total number of independent measurements M is given by:

$$M = \frac{N(N-3)}{2} \tag{3.2}$$

where N is the number of electrodes. This strategy is employed minimum hardware and image reconstruction can be achieved fast with minimal resources (Dickin and Wang, 1996).The main disadvantage of this scheme is that it has a non-uniform current distribution because most of the current travels close the vessel walls and the current density in center of the vessel is low (Hua *et al.*, 1993). Another disadvantage is the considerable common-mode voltage when taking measurements is close to the injection electrodes (Loh *et al.*, 1998).

2. The opposite strategy; The current is applied through diametrically opposed electrodes and the voltage reference is the electrode adjacent to the current-injecting electrode and then the procedure is repeated in the clockwise direction. In this case, the

total number of independent measurements M is given by (Viergever and Todd-Pokropek, 1988):

$$M = \frac{N}{4}\left(\frac{3N}{2} - 1\right) \tag{3.3}$$

In this scheme, most of the current passes through the central part of the vessel, then it is less sensitive to the conductivity changes close to the vessel wall (Hua *et al.*, 1993). The main disadvantage of this strategy is associated to the number of the measurements, which is less than adjacent protocol. The image resolution is almost 23% lower than adjacent strategy for the same number of electrodes (Abdullah, 1993).

3. The diagonal strategy or cross method; The current is applied between electrodes separated by large dimensions. For 16 electrodes, electrode 1 is fixed as a current reference and electrode 2 as the voltage reference; current is applied to electrode 3, 5, ..., 15, and voltage measured from electrodes left with respect to electrode number 2. Then, a 16-electrode system yields 104 independent measurements. This strategy has a good sensitivity over the entire vessel and produces a reasonable quality image (Hua *et al.*, 1993).

4. The conducting boundary strategy; Both current and voltage are applied between two electrodes and effects of electromagnetic interference are reduced by the earth-conducting boundary. The main advantage of this strategy is its low common-mode voltage component. Dickin and Wang (1996) reported that the common-mode voltage for this strategy is 800 times smaller than adjacent strategy but the amplitude of the measured voltages is also low. Then its sensitivity is similar to adjacent one.

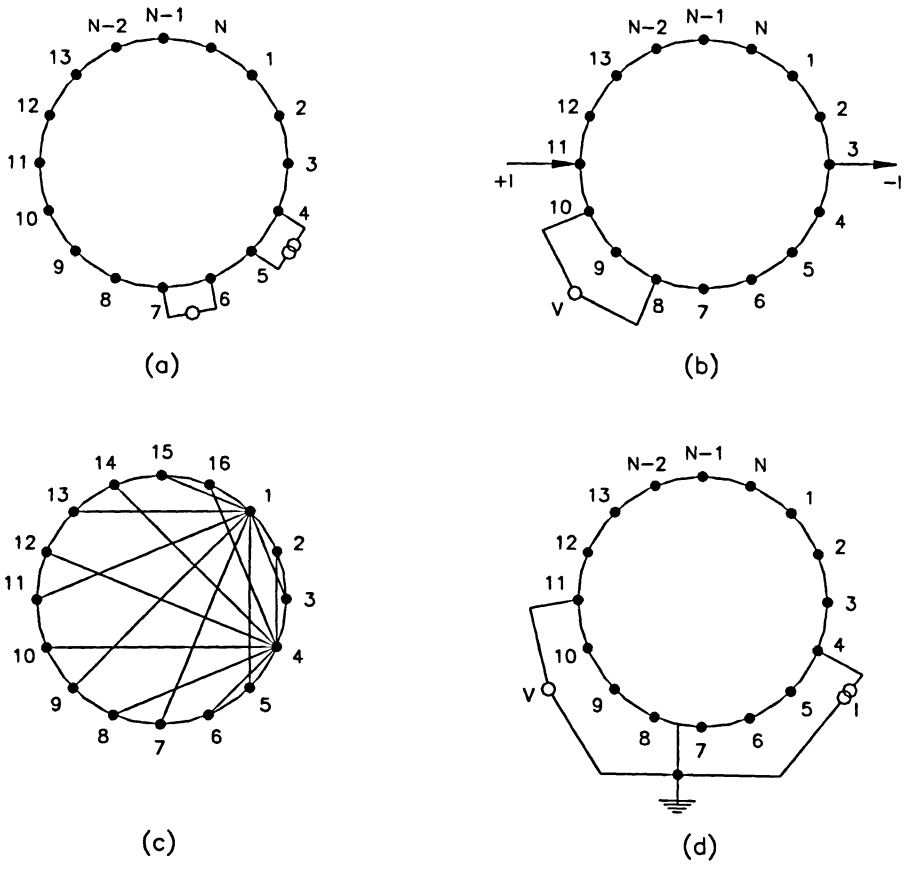

Fig. 3.4. Data collection strategies: (a) The adjacent measurement strategy, (b) The opposite measurement strategy, (c) The diagonal measurement strategy, (d) The conducting boundary measurement strategy.

3.2.3 Image Reconstruction

Following the acquisition of data from the boundary of the system, it is required to process this data using a suitable image reconstruction algorithm. The reconstructed image may contain information on the cross-sectional distribution of a parameter, which depends on the physical principle of the sensing system such as electrical resistance tomography. The algorithm can be used on-line or off-line, depending on the reconstruction time. In general, there are two types of algorithm: non-iterative and iterative. The choice of image reconstruction algorithm is a selection between accuracy of image and time required for reconstruction.

3.2.3.1 Non-iterative Image Reconstruction

The image reconstruction process involves determining the electrical conductivity of each pixel within the image from the set of electrical measurements. This is known as the inverse problem. However, the electrical measurements taken at the boundary of the process vessel are not enough to allow the inverse problem to be solved directly. First the forward problem should be solved (ITS, 2006), i.e. the changes in electrical measurements when the electrical conductivity of one pixel only in the cross section is changed by a known amount, should be found.

3.2.3.1.1 The Forward Problem

The governing model for a source free conducting inhomogeneous domain Γ, with a conductivity distribution $\sigma(x,y)$, the steady-sate current injected and the corresponding voltage $V(x,y)$ measured is derived by Poisson's equation as follows (Williams and Beck, 1995):

$$\nabla.\{\sigma(x,y)\nabla V(x,y)\}=0 \quad in\ \Gamma \tag{3.4}$$

and for boundary conditions:

$V=0$ *at reference point (ground electrode)*

$\int\sigma\left(\frac{\delta V}{\delta n}\right)=+I$ *on Source (input) electrode*

$\int\sigma\left(\frac{\delta V}{\delta n}\right)=-I$ *on sink (output) electrode*

where I is the current applied on the electrode and n is the outward unit normal to the sensor.

The finite element method (FEM) is used to solve Poisson's equation for electrical resistance tomography. The FEM models developed here is completely 2-dimensional. It

is clear that this assumption is not valid because the injected current flows in entire tank. However, 2D current injection and measurement protocol (in horizontal cross-sectional plane) can support this assumption (Dickin and Wang, 1996). First, an automatic mesh generator program generates the circular-shaped mesh (combination of triangular- or quadrilateral-shaped elements). Therefore, FEM converts the Poisson's equation to a series of simultaneous equations describing the behaviour of each of the element. For 16-electrode system, there are 14 pairs of electrodes, which are used for current injection in adjacent protocol, therefore:

$$AV_{(i)} = b_{(i)} \quad (i = 1,...,14) \tag{3.5}$$

where A is the system's stiffness matrix of $N \times N$ entries and N is the number of nodes within finite-element mesh, $V_{(i)}$ is a vector representing the N unknown nodal potentials and $b_{(i)}$ is $N \times 1$ vector indicating the boundary conditions as described above.

3.2.3.1.2 The Inverse Problem

The inverse problem is to determine the conductivity distribution $\sigma(x,y)$ from a finite number of boundary voltage measurements. There are three important reconstruction techniques (Tapp and Williams, 2000): linear back projection (LBP), modified Newton-Raphson Method (MNR), and parametric model based technique (PM). The P2000 system (Industrial Tomography Systems-ITS, Manchester, UK) comes with a qualitative, non-iterative algorithm on linear back-projection.

3.2.3.1.2.1 Linear Back Projection

The linear back projection algorithm (Barber and Brown, 1984) is used to convert the voltage measurements to conductivity values within the elements for all possible injection and measurements combinations using sensitivity matrix (Dickin *et al.*, 1993):

$$S_{(e,M)} = \frac{1}{\beta^{(e)}} \frac{V_{(e,M)} - V_{(M)low}}{-V_{(M)high} - V_{(M)low}} \tag{3.6}$$

The variables e and M are the number of the element in the horizontal cross section and the number of measurements respectively. The sensitivity matrix, $S_{(e,M)}$, is composed of the voltages, $V_{(M)low}$ as the voltage in the case where all the elements were occupied by the lower resistance phase, $V_{(M)high}$ as the voltage in the case where all the elements are occupied by the higher resistance phase , and $V_{(e,M)}$ as the voltage in the case where only the e^{th} element is occupied by the higher resistance phase. All mentioned voltages are calculated using FEM based on the Poisson equation (forward problem).

The electrical resistance distribution is graphically reconstructed in the section $P_{(e)}$, using the sensitivity matrix, $S_{(e,M)}$, and the boundary conditions based on the measured voltages, $V_{(M)meas}$. It should be noted that $P_{(e)}$ is the change in electrical resistance from the initial state for each element, therefore the effect of the initial resistance distribution due to the impeller, baffles and etc. ($P_{(e)ref}$) should be eliminated:

$$P_{(e)} = \frac{\sum_{M=1}^{104} S_{(e,M)} V_{(M)meas}}{\sum_{M=1}^{104} S_{(e,M)}} - P_{(e)ref} \tag{3.7}$$

The general flowchart of image reconstruction is shown in Fig. 3.5.

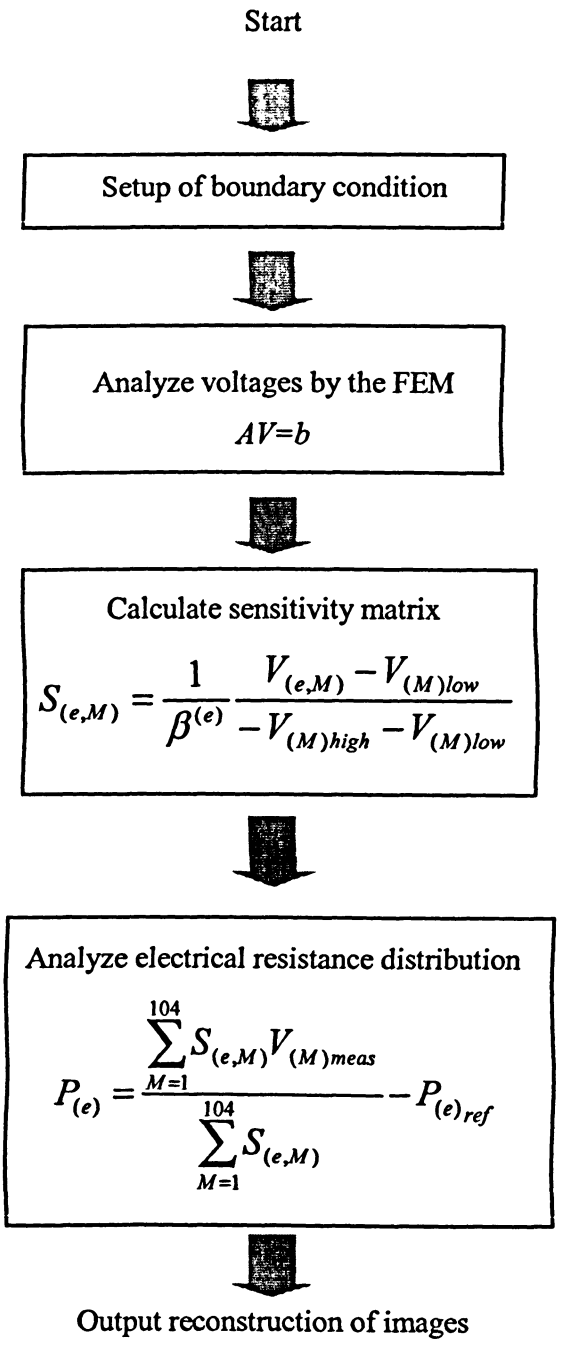

Fig. 3.5. Flow chart for the image reconstruction (source: Kaminoyama *et al.*, 2005)

4. EXPERIMENTAL

4.1 Experimental Setup

4.1.1 Vessel/ Impeller

The mixing vessel designed, built and used in this study was a flat-bottomed cylindrical tank of diameter 0.4m (T) fitted with four equally spaced axial baffles ($T/10$). The liquid height, H, was equal to the tank diameter, providing a total volume around $0.05m^3$. A Scaba 6SRGT impeller with diameter 0.18m (D) was centrally positioned at an off-bottomed clearance of 0.21, and 0.17m (C) for mixing time measurements. The impeller was driven using a variable speed motor. Further details about the geometrical characteristics of the stirred tank with all internal dimensions are shown schematically in Fig. 4.1.

4.1.1.1 Impeller Specifications

As mentioned, the impeller built and used in this work was a six-blade Scaba 6SRGT shown in Fig. 4.2. The power number of a fully turbulent flow ($P_{o,tu}$) of a hollow-blade impeller is (Paul *et al.*, 2004):

$$P_{o,tu} = \frac{P}{\rho N^3 D^5} = 4.4 \qquad (4.1)$$

where P, ρ, N and D are power, fluid density, impeller rotational speed, and impeller diameter, respectively.

The dimensionless flow number (N_Q) for a hollow-blade impeller is (Paul *et al.*, 2004):

$$N_Q = \frac{Q_r}{ND^3} = 0.76 \qquad (4.2)$$

where Q_r is volumetric flow rate (Q_r).

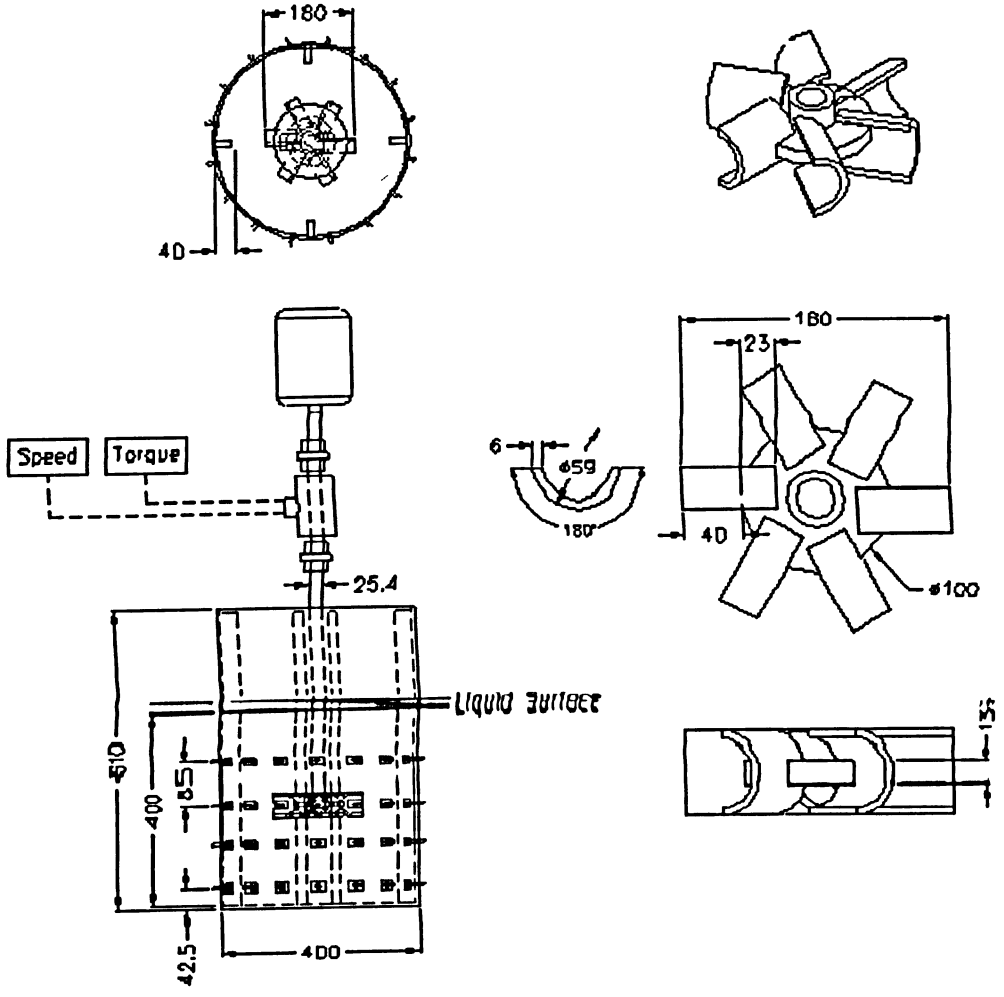

Fig. 4.1. Schematic diagram of experimental setup.

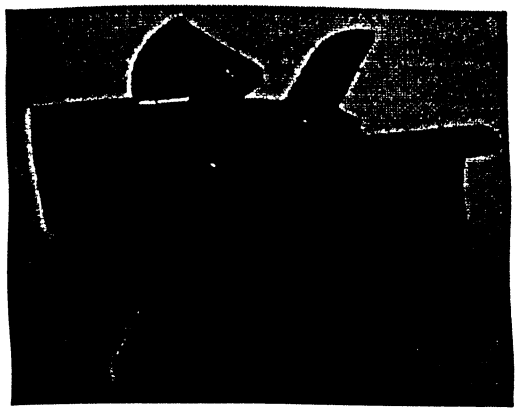

Fig. 4.2. Scaba 6SRGT impeller.

4.1.1.2 Power Measurements

The power input to the impeller (P) was obtained from torque (M) and impeller rotational speed (N) measurements using:

$$P = 2\pi NM \tag{4.3}$$

Impeller torque and speed were measured using a torque sensor (type 0170/01MS20RAU, Staiger Mohilo, Germany) mounted on the shaft with two flexible couplings at each end to accommodate radial, angular, and axial misalignment. The bearing friction was measured by operating the system with the vessel, which was empty. This friction torque was subtracted from all the measured torques.

4.2 ERT System

The ERT system comprises of three components; the sensor electrodes, the data acquisition system (DAS), and the host computer/ image reconstruction system, refer to Fig. 4.3.

4.2.1 Sensor Electrodes

The tank was fitted with an ERT system consisting of four sensor planes at intervals of 85 mm between planes and 42.5 mm from the base of the tank to the center of bottom plane, i.e. plane 4 (Fig. 4.3). Each sensor plane contains 16 equispaced stainless steel sensors, and each sensor was 20 mm high, 30 mm wide and 1mm thick (Fig. 4.3). The planes are numbered from top downward. The electrodes are connected to the DAS (Industrial Tomography . Systems-ITS, Manchester, UK) using a network of co-axial cables terminating with four 36-pin centronix connectors.

4.2.2 Data Acquisition System

The DAS is responsible for co-ordinating the desired measurement protocol. The system makes use of an adjacent measurement protocol (Barber *et al.*, 1983) at 9.6 kHz, applying an AC current between two adjacent electrodes and measuring the resultant potential difference (voltage) between all other adjacent electrode pairs (Fig. 4.4). The AC drive current then rotates to the next electrode pair and the voltage for all other electrode pairs is measured. This process is then repeated until all possible combinations have been tried, and provides 104 individual voltage measurements according to the equation $N(N\text{-}3)/2$, where N is the number of electrodes per plane, i.e., 16 in this study. The four axial planes provide 416 interrogative measurements of the liquid volume (0.05 m^3).

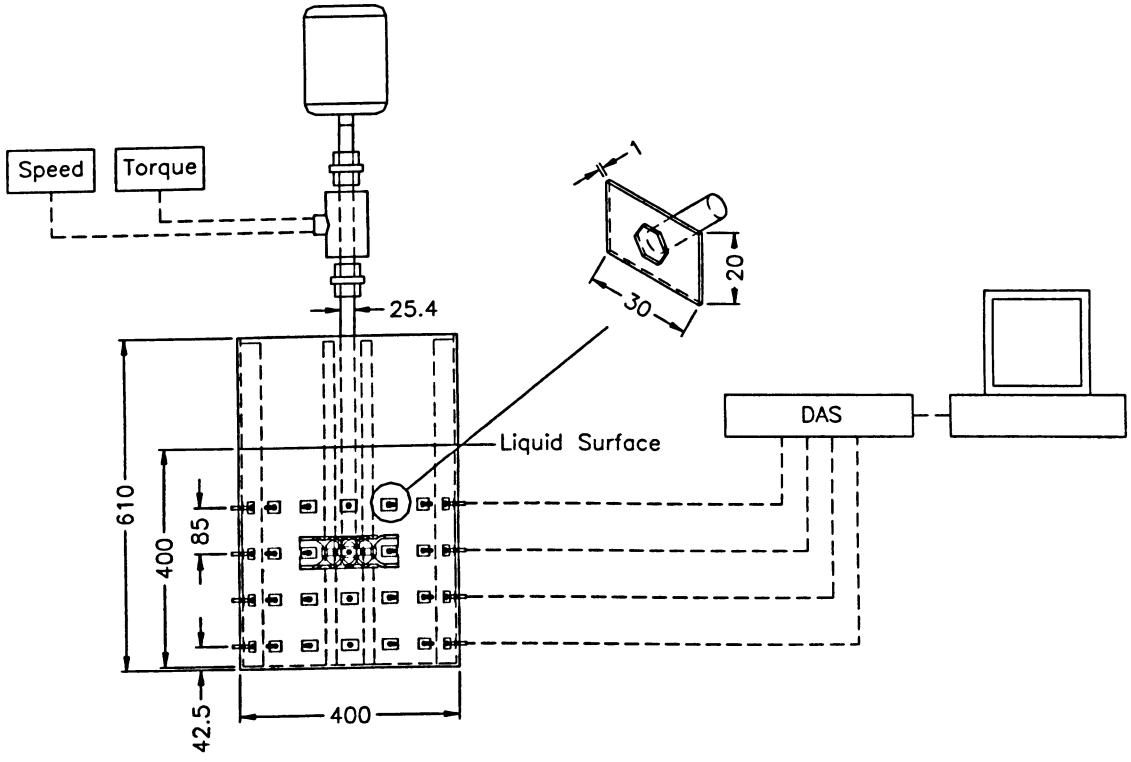

Fig. 4.3. Schematic diagram of ERT System.

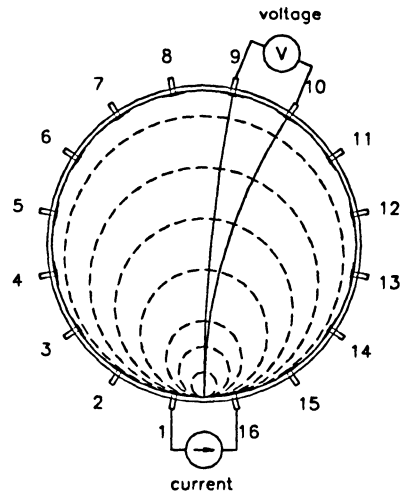

Fig. 4.4. Data collection strategy; adjacent measurement strategy.

A P2000 ERT system (Industrial Tomography Systems-ITS, Manchester, UK) was used for all experiments. The main specifications of the DAS used in this study were: frequency, 75-153.6kHz; injecting current range, 0-75mA (peak–peak); frame speed, <20ms; output voltage range, -10V to +10V; and voltmeter sensitivity, 0.0488mV. The ERT system operates to a spatial resolution around 5% of the vessel diameter, using 16 equispaced electrodes (Holden *et al.*, 1998). The DAS measurements, connected to a computer (Pentium 4, CPU 2 GHz, and 512 MB of Ram) via a nine-pin communication port, can be recorded through ITS 'ERTWIN' software (Industrial Tomography Systems-ITS, Manchester, UK) for control, image reconstruction, and data storage.

4.2.3 Host Computer/ Image Reconstruction System

A non-iterative image reconstruction algorithm (Linear Back Projection-LBP) was applied to convert raw voltage measurements into a 2-D conductivity map of each plane. The linear back projection algorithm (Barber and Brown, 1984) has a low computational requirement, which makes it online in real time. Although, not applied here, there is also an iterative image reconstruction algorithm (Sensitivity Conjugate Gradient Method-SCG) from ITS (Wang, 2002). These algorithms are qualitative ones, as the images depict relative change in conductivity against an initial set of reference data. Each individual tomogram consists of a 20×20 pixel array giving 400 spatial elements. However, some of

these pixels lie outside the vessel circumference and the image is therefore formed from pixels inside the vessel. The circular image is constructed using 316 pixels from a 400 pixels square grid (refer to Fig. 4.5). Since the vessel has 4 sensing planes, this results in 1,264 non-intrusive conductivity probes. The 3-D solid body realisations were smoothed by interpolation between the 4 planes using Slicerdicer software (Pixotec, LLC, USA).

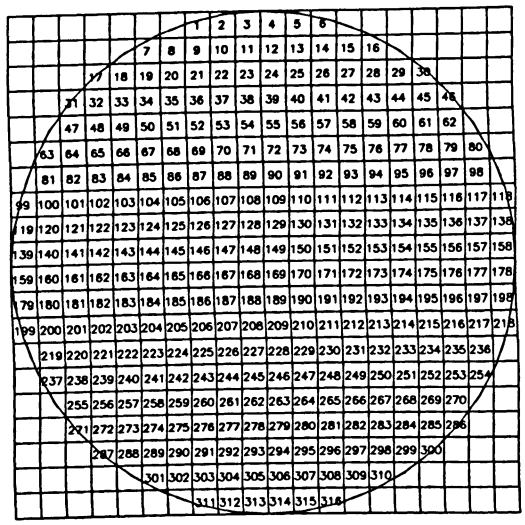

Fig. 4.5. Image reconstruction grid

4.3 Fluid Rheology

The working fluids were food grade xanthan[1] (NovaXan, ADM, USA) solutions with concentration of 0.5%, 1.0%, and 1.5%. Rheological properties of the solutions were measured at 22°C in a Bohlin CVOR Rheometer 150 (Malvern instruments, USA) using a 40mm 1° cone and 60mm plate measuring system. The range of the shear rate applied in the controlled shear rate rheometer varied from 0.14 to 130s^{-1}, which was supposed to be the range of that encountered in the mixing system. The temperature, at which these measurements were made, was the same as the bulk fluid temperature (22 ± 0.5°C) in the tank. This latter temperature varied slightly depending on the daily room temperature and the work done by the impeller on the solution.

[1] Xanthan gum is supplied in powder form.

The rheology of the solutions was modelled best (with high regression coefficients) by a Hercshel-Bulkley model (Herschel and Bulkley, 1926), as shown in Fig. 4.6. Then the viscosity is given by:

$$\eta = \frac{\tau_y}{\dot{\gamma}} + K|\dot{\gamma}|^{n-1} \tag{4.4}$$

where $\dot{\gamma}$ is the shear rate, τ_y is the yield stress, and K and n are shear rate independent constants often used to represent power-law fluids. The rheological characteristics of the solutions are listed in Table 4.1.

Table 4.1. Rheological properties of xanthan solutions

Xanthan Concentration (%)	Consistency index, K (Pa s^n)	Power-law index, n -	Yield stress, τ_y (Pa)	Regression Coefficient, R^2	Chi-square Parameter, χ^2
0.5%	3	0.11	1.789	0.9905	0.0885
1.0%	8	0.12	5.254	0.9985	0.1111
1.5%	14	0.14	7.455	0.9992	0.0460

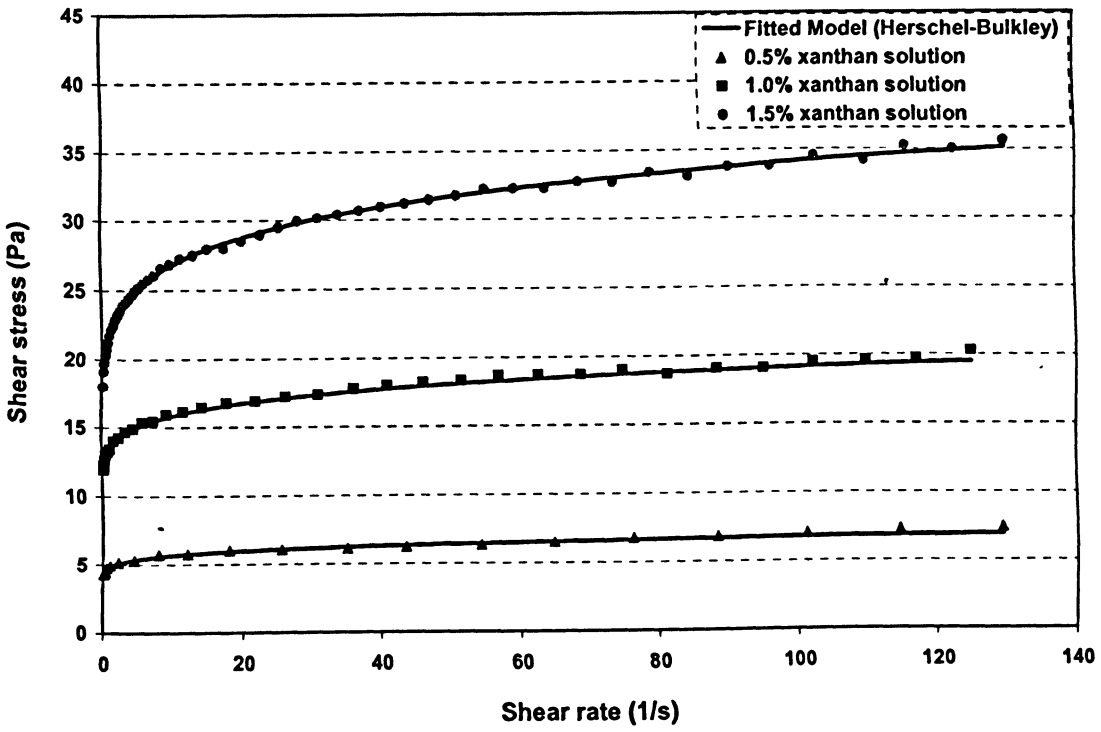

Fig. 4.6. Shear stress versus shear rate for xanthan solutions used in this study

4.3.1 The Effect of Salt on the Rheological Properties of the Solutions

The effect of salt on the rheological properties (especially yield stress) of xanthan was evaluated for 0.5 and 1.5% xanthan concentrations. The maximum amount of salt solution added to the xanthan solutions during the experiments was 50ml of 10% saline solution (referred to Section 4.4) which is 0.01% wt salt in the entire working liquid. Fig. 4.7 and Fig. 4.8 show the effect of salt at three different concentration levels on the shear stress-shear rate curves. The obtained rheological data were fitted with the Herschel-Bulkley model. The model parameters are presented in Table 4.2.

It can be easily observed in both xanthan solutions that these three levels of salt had no significant (<6%) effect on the yield stress (the most effective rheological parameter in mixing performance).

Table 4.2. Effect of addition of salt on xanthan solutions

Solution		K (Pa s^n)	n -	τ_y (Pa)
Xanthan (0.5%)	no salt	3	0.11	1.789
	With 0.01% salt	3.1	0.115	1.839
	With 0.05% salt	3.3	0.115	1.867
	With 0.10% salt	3.4	0.116	1.89
Xanthan (1.5%)	no salt	14	0.14	7.455
	With 0.01% salt	14.31	0.145	7.463
	With 0.05% salt	14.6	0.147	7.501
	With 0.10% salt	15	0.148	7.514

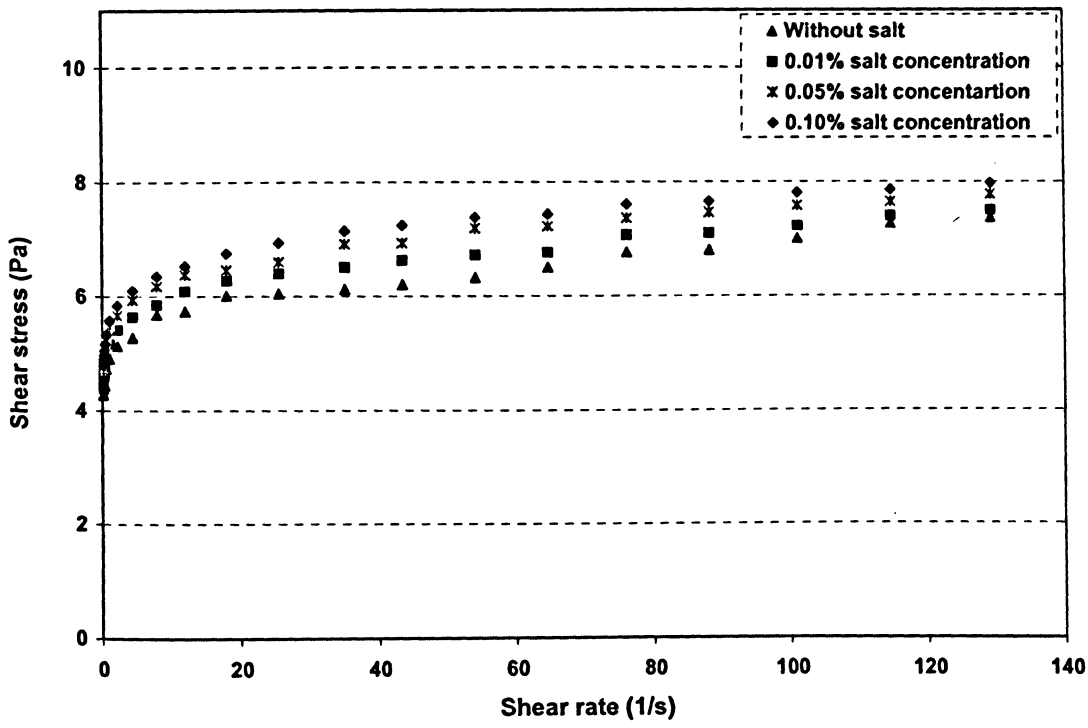

Fig. 4.7. Effect of salt addition on 0.5% xanthan concentration.

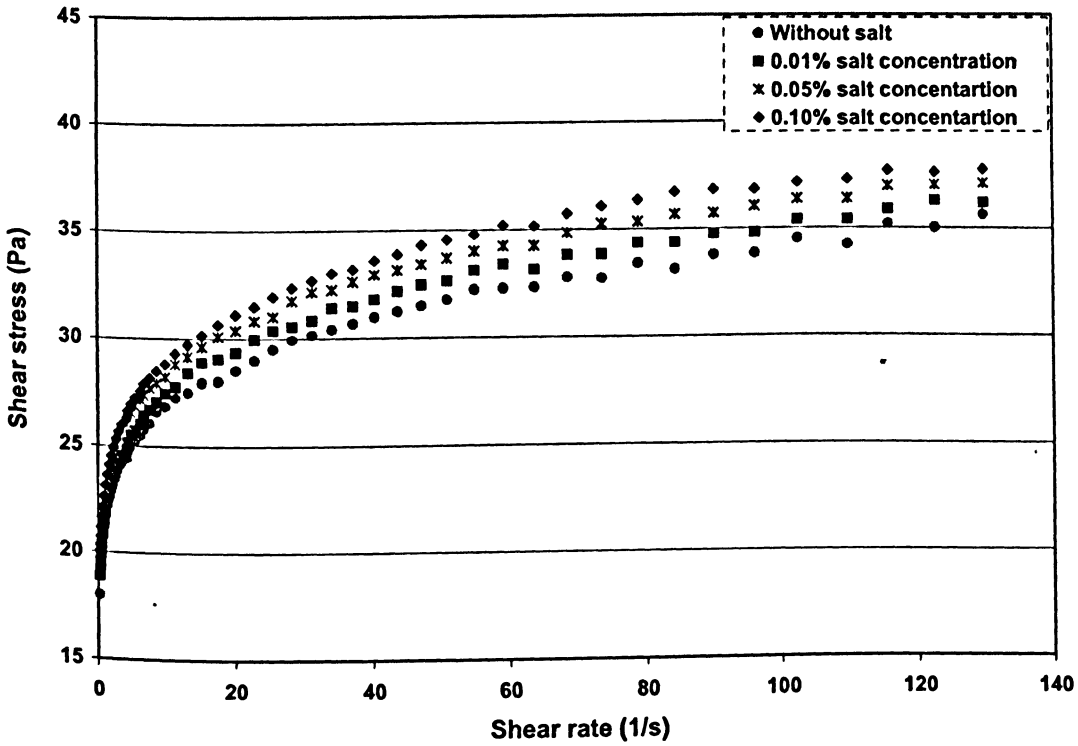

Fig. 4.8. Effect of salt addition on 1.5% xanthan concentration.

4.4 Experimental Procedure

4.4.1 Solution Preparation

Test fluids for both experimental and CFD analysis were three xanthan gum solutions with concentration of 0.5%, 1.0%, and 1.5% as shown in Table 4.1. Each batch was prepared by dissolving the appropriate amount of xanthan in tap water. Great care had to be taken to avoid air bubbles formation, once formed; it is very difficult to remove them. For all experiments, the solution within the tank was allowed to sit overnight to reach the desired temperature and eliminate possible air bubble.

4.4.2 Cavern Measurements

The data collection and the image reconstruction were made online and the temporal resolution was 4 s/frame. Before measurements could be taken it was necessary to calibrate the instrument current source (15mA) and gain map. Prior to collecting data, the referenced state was measured to eliminate the effects of the stirrer and other internal structures. At about 10–12 frames after starting the measurement, 30ml of 5% saline solution (secondary liquid) was injected to the solution volume using a plastic syringe near the impeller hub through a 10mm o.d. injection tube. The injection took about 2-3sec for all experiments. A conductivity meter (PC10 portable meter, Oakton instruments, USA) was used to take an independent conductivity measurement before each experiment run to be sure that the conductivity of the solutions are the same for a set of experiments and also care was taken to ensure that both the vessel contents and tracer were at the same temperature. For each experiment, taking the measurements continued for 50 frames, and the dimension of the cavern was measured 10 frames after injection once the cavern size remained unchanged. The cavern boundary was determined as a position at which the tracer concentration was zero. The tracer concentration distributions (expressed as a concentration of NaCl, *g/L*) can be obtained from the conductivity distribution using the following equation (ITS, 2006):

$$\alpha_s = 0.0687\sigma_{mc} - 0.1087 \quad (4.5)$$

where α_S is the concentration of NaCl (g/L) and σ_{mc} is the reconstructed measured conductivity, mS/cm.

4.4.3 Mixing Time Measurements

To measure the mixing time in the mixing tank, 50ml of 10% saline solution was added (10cm below liquid surface on the plane 1≈ pixel 58) to the mixing tank. Then, using ERT system, solution conductivity or concentration was measured dynamically by two methods: first using 4 measuring planes (1,264 pixels), and second using 4 selected pixels (pixel 38 on plane 1, pixel 231 on plane 2, pixel 264 on plane 3, and pixel 76 on plane 4). The measurement procedure was repeated like previous Section (4.4.2) but the temporal resolution was 1.42 s/frame and current source has been changed to 75mA (it was found that in high speed higher current injection can increase signal to noise ratio). The mixing time was defined as the required time for the concentration or conductivity to reach 95% of the steady state value. Fig. 4.9 shows the transient response of four sensing planes in mixing tank to the injection tracer while Fig. 4.10 shows the transient response for four pixels (each from one plane).

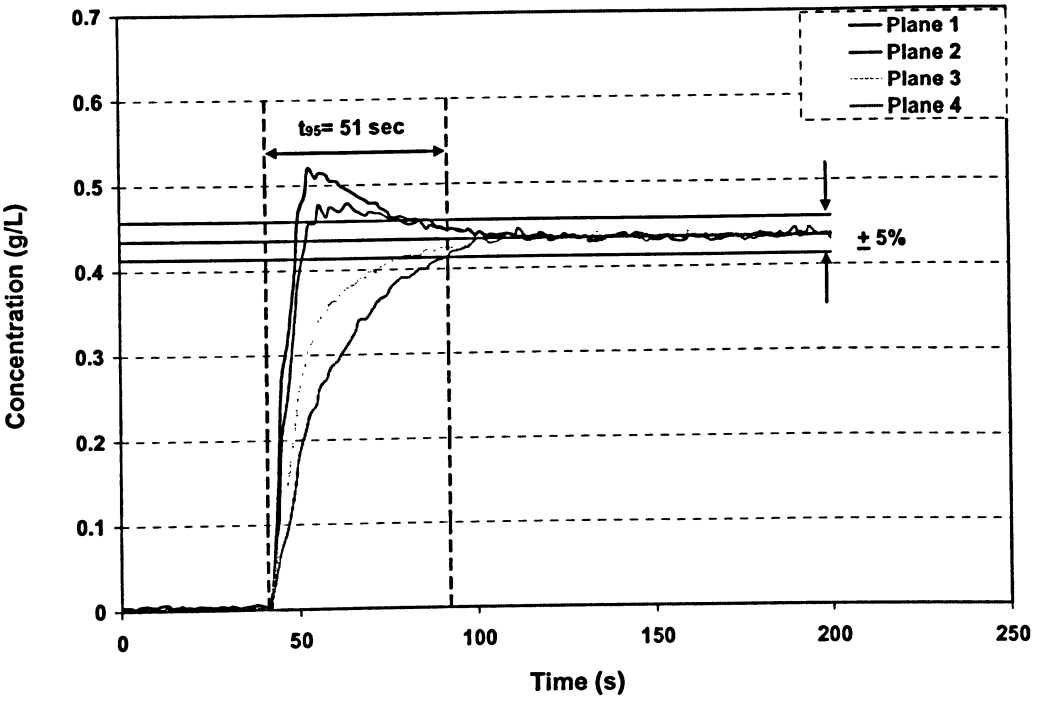

Fig. 4.9. Mixing time measured using 4 planes.

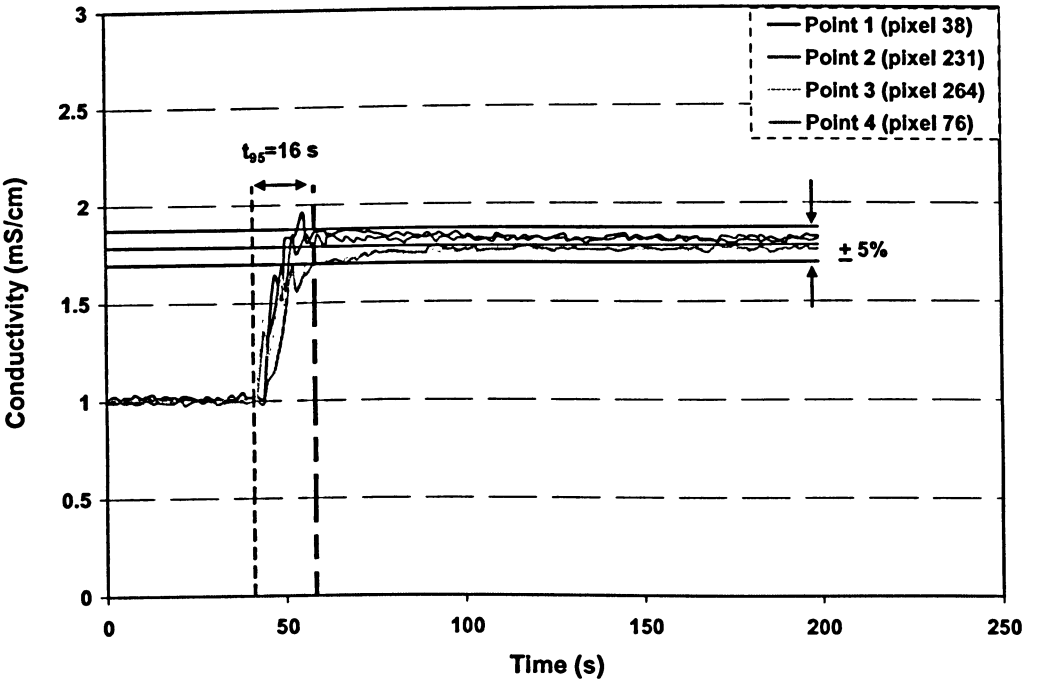

Fig. 4.10. Mixing time measured using 4 pixels.

4.5 Experimental Conditions

The effect of rheological properties (especially yield stress) and impeller rotational speeds on the mixing of xanthan solutions agitated by a Scaba 6SRGT impeller was studied in terms of the impeller flow pattern, cavern formation (size and shape), and mixing time. The experimental conditions are summarized in Table 4.3.

Table 4.3. Experimental conditions

Xanthan concentration	Impeller rotational speed for:	
	Cavern measurements	Mixing time measurements
0.5%	10-100 rpm	185-350 rpm
1.0%	10-160 rpm	250-350 rpm
1.5%	10-220 rpm	340-425 rpm

5. CFD MODEL DEVELOPMENT

5.1 Introduction

Computational Fluid Dynamics is a tool that is becoming popular to study complex fluid flow such as those typically found in mixing vessels. The main advantage of this approach is in its potential for reducing the number of experiments required to describe such types of flow. This chapter is organized in two sections: first section reviews the general information about governing equations, numerical methods, and methods of discretizing the equations as well as grid generation and other relevant information and the second section of the chapter is devoted to the current CFD model development.

The Commercial CFD package FLUENT 6.3.27 (Fluent Inc., Lebanon, NH) was used to numerically solve the Navier-stokes equations. GAMBIT, the meshing tool package with FLUENT CFD software, was used to generate a 3D geometrical model and mesh of the mixing tank.

5.2 Governing Equations

The principle equations of fluid dynamics are based on the conservation laws, i.e. mass, momentum and energy conservations (Blazek, 2005). For the case of three-dimensional motion, the flow field is specified by the velocity vector ($v=u_i+v_j+w_k$), the pressure p, density ρ, and the temperature T as functions of the space coordinates and time t. It is obvious that these six quantities (u_i, v_j, and w_k, p, ρ, and T) need six equations to be determined. These six equations (Bird *et al.*, 2002) are the continuity equation (conservation of mass), the three equations of motion (conservation of momentum), the energy equation (conservation of energy), and the thermodynamic equation of state $p=p(\rho, T)$.

Since the mixing process in this study occurs in an isothermal condition, the flow field can be solved by considering mass conservation (continuity equation) and momentum

equations only. For incompressible fluids (without density variations), there is no relation between the energy equation and the mass conservation and momentum equations, i.e. there is no need for an equation of state.

5.2.1 Continuity Equation

For the unsteady flow of a compressible fluid, the conservation of mass applied to a fluid passing through a fixed control volume (*Eulerian approach*) yields the following equation of continuity (Patankar, 1980; Ranade, 2002; Fluent, 2006):

$$\frac{\partial \rho}{\partial t} + \nabla.(\rho \vec{v}) = \frac{D\rho}{Dt} + \rho(\nabla.\vec{v}) = 0 \qquad (5.1)$$

The first term in above equation represents the dynamic change of density in the control volume and the second term shows the rate of mass flux passing through the control volume per unit volume.

The symbol $D\rho/Dt$ denotes the substantive derivative, which consists of the local contribution in unsteady flow $\partial\rho/\partial t$ and the convective contribution $v.(\nabla \rho)$.

A flow in which the density of each fluid element remains constant is called incompressible (Shyy *et al.*, 1997). Then eq. (5.1) reduces to eq. (5.3) for steady or unsteady incompressible flow:

$$\frac{D\rho}{Dt} = 0 \qquad (5.2)$$

then,

$$\nabla.\vec{v} = \frac{\partial v_i}{\partial x_i} = 0 \qquad (5.3)$$

5.2.2 Momentum Equation

The momentum equation is derived from Newton's second law ($\vec{F} = m\vec{a}$) of motion (Batchelor, 1967). Newton's second law says that the net force on the fluid element equals its mass times the acceleration of the element. There are two sources for the force: (1) forces acting directly on the mass of the fluid element or volume (e.g., gravitational forces) known as body forces, and (2) forces acting on the surface of the fluid element or volume (e.g., pressure and friction) known as surface forces.

$$\frac{\partial}{\partial t}(\rho\vec{v}) + \nabla\cdot(\rho\vec{v}\vec{v}) = -\nabla p + \nabla\cdot\left(\bar{\bar{\tau}}\right) + \rho\vec{g} + \vec{F} \tag{5.4}$$

where p is the statistic pressure, ρg is the gravitational body force, F is the external body force and $\bar{\bar{\tau}}$ is the stress tensor, created from the friction between the fluid and the surface of the fluid element in accordance with Fluent (2006):

$$\bar{\bar{\tau}} = \mu\left[(\nabla\vec{v}) + (\nabla\vec{v}^{T}) - \tfrac{2}{3}\nabla.\vec{v}I\right] \tag{5.5}$$

where μ is the molecular viscosity, I is the unit tensor, and the second term on the right hand side is the effect of volume dilation (Bird *et al.*, 2002). For incompressible fluids, the expression for the stress tensor is given by eq. (5.5) with the last term omitted:

$$\bar{\bar{\tau}} = \mu\left[(\nabla\vec{v}) + (\nabla\vec{v}^{T})\right] \tag{5.6}$$

where

$$\mu\left[(\nabla\vec{v}) + (\nabla\vec{v}^{T})\right] = \mu\bar{\bar{D}} \tag{5.7}$$

where $\overline{\overline{D}}$ is the rate-of-strain tensor. The generalized Newtonian fluid model is obtained by simply replacing the constant viscosity μ. The non-Newtonian viscosity η is a function of the shear rate $\dot{\gamma}$, which is related to the second invariant of $\overline{\overline{D}}$ and is defined as (Bird, 2002):

$$\dot{\gamma} = \sqrt{\frac{1}{2}\left(\overline{\overline{D}} : \overline{\overline{D}}\right)} \tag{5.8}$$

Therefore, we have:

$$\rho\left(\frac{\partial v_i}{\partial t} + v_i \frac{\partial v_i}{\partial x_i}\right) = -\frac{\partial p}{\partial x_i} + \frac{\partial}{\partial x_i}\left[\eta\left(\frac{\partial v_i}{\partial x_j} + \frac{\partial v_j}{\partial x_i}\right)\right] + F_i, \quad (i,j = 1, 2, 3) \tag{5.9}$$

In eq. (5.9) , the convection terms are on the left. The terms on the right-hand side are pressure gradient (source term); the divergence of the stress tensor (diffusion of the momentum); the gravitational force (source term) and other generalized forces (source terms). These well-known differential equations form the basis of fluid mechanics, and are known as the Navier-Stokes/ Euler equations (Blazek, 2005).

5.3 Boundary Conditions

The equations given above govern the flow of a fluid. Their solution can be determined when the boundary and initial conditions (for unsteady cases) are specified. In fact, the boundary conditions, which are different for each case, specify the particular solutions to be obtained from the governing equations. Commonly used boundary conditions are discussed below:

1. Inlet; At inlet boundaries, information about the velocity or pressure (refereed to momentum equation, when the normal component of the velocity is known at the boundary, boundary condition for pressure is not required because the velocity field

depends on the pressure gradient and not on the absolute value of pressure), mass flows, and scalars such as temperature, species concentrations, physical properties and so on should be known.

2. Outlet; Generally, at outlet boundaries, the gradients in the direction normal to the outlet surface are zero for all variables except pressure (Ranade, 2002). When the gradients at the outlet boundary are not zero then use of this boundary condition is not suitable.

3. Walls; At the wall boundaries of the domain, a 'no slip' boundary condition can be used (Patankar, 1980). This means that the transverse fluid velocity is equal to that of the surface of the wall and the normal velocity is zero. In mass or heat transfer applications, binary diffusivities, and thermal properties need to be defined as well.

4. Symmetry; At the symmetry surface, the normal velocity is set to zero (no flow across the symmetry surface) and the normal gradients of all variables except normal velocity are set to zero (no flux across the symmetry surface). It means that there is no convective or diffusive flux across the boundary (Versteeg and Malalaskera, 1995).

The component material transport properties, such as density, viscosity, and heat capacity, need to be prescribed as constant or selected from a database and can be functions of temperatures, pressure or any other variables of state. Fluids can be modeled as being either compressible or incompressible. The viscosity of the fluid can be either Newtonian or non-Newtonian.

5.4 Numerical Techniques

The governing equations are complex partial differential equations for which no analytical solution (applicable only to some simplified flow problems) can be found (Garg, 1998). A numerical solution of a differential equation consists of a set of numbers

from which the distribution of the dependent variable can be formed. On the other hand, the numerical solution requires some discretization of the field into a collection of points or cells which is called discretization of the domain or grid generation. There are a number of numerical techniques available for solving the flow field. In general, there are three main methods of numerical solution: finite difference (Smith, 1985), finite element and finite volume (Patankar, 1980 and Ranade, 2002) method.

The idea of all three methods is to replace the partial derivatives in the governing equations with algebraic expressions, resulting in a system of algebraic equations which can be solved for the variables at the discrete grid cells in the flow.

All three techniques have the following steps (Versteeg and Malalaskera, 1995):

1. Approximation of the unknown variables.
2. Discretization by substitution of the approximations into governing equations.
3. Solution of the algebraic equations.

The three techniques are different from each other in the first and second steps above.

5.4.1 Finite Difference Method (FDM)

FDM is applied to the differential form of the governing equation. Finite difference representations of the partial derivatives are based on Taylor's series expansions. Therefore, the partial derivatives in the governing equations are replaced by the difference quotients, leading the system of algebraic equations for the dependent variables at each grid point. For simple geometry and structured grids (grid types are discussed latter in this chapter, Section 5.4.3.1), not physical in industry, the FDM is relatively simple and straightforward to easily obtain high-order approximations (Blazek, 2005). This limitation to simple geometry is very important disadvantage (Ranade, 2002).

5.4.2 Finite Element Method (FEM)

FEM divides the continuum field, or domain into cells or elements (triangular or a quadrilateral form in 2-D or tetrahedral or hexahedral form in 3-D) which can be rectilinear or curved. The grids are unstructured ones, which give the most important advantage of the method in compared with FDM. A finite element method provides simple functions (linear or quadratic) valid on elements to describe the local variations of unknown flow variables. The approximation functions are defined at specified points called nodes. Nodes usually are located on the element boundaries to which the adjacent elements are connected. Now the nodal field variables become the new unknowns of algebraic equations. As is well known the governing equation is satisfied by the exact solution of the variables, which is not possible by substituting the approximation functions for variables and therefore a residual is defined to measure the errors. Next, the residuals are minimized in some sense by multiplying them by a set of weighting functions and integrating. By minimizing the residual, a set of non-linear algebraic equation is obtained. It is believed that this method is particularly suitable for the non-Newtonian fluids (Blazek, 2005).

5.4.3 Finite Volume Method (FVM)

The finite volume method was originally developed as a special finite difference formulation. FVM is a method by which the integral formulation of the conservation laws is discretized directly in the physical space, i.e., this approach employs numerical balances of a conserved variable over small control volumes (control volume integration), thereby ensuring that the basic quantities like mass, momentum, and energy remain conserved at the discrete level. This distinguishes the finite volume method from all other CFD techniques. The Finite volume method is combination of the best from the FEM, i.e., the geometric flexibility, and the best from the FDM, i.e., the flexibility in defining the discrete flow field (Garg, 1998). The advantage of the FVM is that the resulting solution would imply that the integral conservation of quantities such as mass, momentum, and energy should exactly satisfy over control volumes. This behaviour

exists for any number of grid points. Therefore, even the coarse-grid solution has exact integral balance. On the other hand, FVM has difficulty in derivatives substitution (Patankar, 1980). The substitution from Taylor series as FEM is not possible because of non-equally spaced cells in computational grids. In addition, there is no mechanism like FEM to convert high-order derivatives (higher than second order) into lower ones.

Like the FEM, a grid or mesh is used to break the domain into a set of cells that can be triangles or quadrilaterals in 2D domains or tetrahedral, prisms, pyramids or hexahedra in 3D domains (Blazek, 2005) as shown in Fig. 5.1.

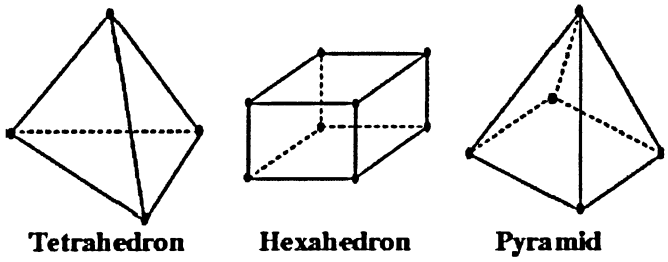

Fig. 5.1. Three element types that can be used in computational grids

The numerical technique used by FLUENT is the finite volume method, which is the most well established technique (Versteeg and Malalaskera, 1995).

5.4.3.1 Grid Generation

As mentioned, numerical solution of partial differential equations needs some discretization of the domain into a set of points or elemental volumes (cells). The differential equations are approximated as a set of finite volume algebraic equations, which are then solved for the discrete values of the variables on the grids. The grids are the organized or unorganized distribution of points and cells. The former leads to a structured grid evaluated by Thompson *et al.* (1985), while the latter leads to an unstructured grid updated by Choo (1995) and Carey (1997). In the unstructured grids, increasingly in use these days, the grids are fine near elements where the gradients of

pressure, velocity, and temperature are very large (e.g., impellers, baffles, tank walls) and coarser (Since there are no small changes in flow behaviour to be captured, it is a waste to have a fine grid in such regions) in areas where the gradients of velocity and temperature are small (Blazek, 2005). The cost and accuracy of the solution are directly coupled to the quality of the grid. In Laminar flows, the grid near boundaries should be refined to allow the solution to capture the boundary layer flow detail (Paul *et al.*, 2004).

5.4.3.2 Discretization

The main step of the finite volume method is the integration of the governing equation over a control volume to give a discretized equation at its nodal point. The general transport equation for a dependent variable ϕ in a Cartesian co-ordinate system can be written as (Ranade, 2002):

$$\frac{\partial}{\partial t}(\rho\phi)+\nabla\cdot(\rho\vec{v}\phi)=\nabla\cdot(\Gamma_{\phi}\nabla\phi)+S_{\phi} \tag{5.10}$$

where ρ= density, $\vec{V}$ =velocity vector, Γ_{ϕ}= the effective diffusivity (equal to the viscosity in the momentum equations), and S_{Φ}= source of ϕ per unit volume.

The transient term, $\frac{\partial}{\partial t}(\rho\phi)$ accounts for the accumulation of ϕ in the concerned control volume. The convection term, $\nabla.(\rho\vec{v}\phi)$ accounts for the transport of ϕ due to the existence of the velocity field. The diffusion term[1], $\nabla\cdot(\Gamma_{\phi}\nabla\phi)$ accounts for the transport of ϕ due to its gradients. The source term, S_{Φ} accounts for any sources or sinks that either create or destroy ϕ. Any extra terms that cannot be as the convection or diffusion terms are considered as source terms. The dependent variable ϕ can stand for different quantities, such as the mass fraction of a chemical species, the enthalpy or the

[1] The word diffusion is used here in a generalized form, representing chemical-species diffusion flux, heat flux, viscous stress, etc. (Patankar, 1980).

temperature, a velocity component, the turbulent kinetic energy, or a turbulent length scale. Eq. (5.10) is then integrated in space, and time (for unsteady case) and discretized according to the discretization scheme chosen. The steady-state conservation equation for can be written in integral form any control volume as follows:

$$\int_A \rho\phi\vec{v}.d\vec{A} = \int_A \Gamma_\phi \nabla\phi.d\vec{A} + \int_{CV} S_\phi dV \tag{5.11}$$

where $\vec{A}$ = surface area vector. This equation is applied to each control volume, or cell, in the computational domain. Discretization of equation for a given cell yields:

$$\sum_f^{N_{faces}} \rho_f \vec{v}_f \phi_f . \vec{A}_f = \sum_f^{N_{faces}} \Gamma_\phi (\nabla\phi)_n . \vec{A}_f + S_\phi V \tag{5.12}$$

where N_{faces}= number of faces enclosing the cell, ϕ_f= value of ϕ convected through face f, $\rho_f \vec{v}_f . \vec{A}_f$ = mass flux through the face, $\vec{A}_f$ = area of face f, $(\nabla\phi)_n$ = magnitude of $\nabla\phi$ normal to face f and V= cell volume.

Eq.(5.12) as the general form is solved by FLUENT. By default, FLUENT stores discrete values of the scalar ϕ at the cell centers (Fluent, 2006). Here four following terms should be considered:

1. The diffusion term in above equation is central differenced and is always second-order accurate.

2. Face values ϕ_f are required for the convection terms in eq. (5.12) and must be interpolated from the cell center values. This is accomplished using an upwind scheme. Unwinding means that the face value ϕ_f is derived from quantities in the cell upstream, or "upwind," relative to the direction of the normal velocity v_n in eq. (5.12). FLUENT allows

one to choose from several upwind schemes such as first-order upwind, second-order upwind, power law, and QUICK (Fluent, 2006) which will be discussed in Section 5.4.3.2.2.

3. The pressure gradient term forms the main momentum source term in most cases. Pressure is also stored at cell centers. Therefore, an interpolation scheme is required to compute the face values of pressure from the cell values. For this purpose, FLUENT provides several schemes such as first-order, linear, second-order, body-force-weighted and PRESTO scheme (Fluent, 2006), which will be explained in Section 5.4.3.2.1.

4. Another important issue is the role played by the pressure appearing in the momentum equation as the source term, but there is no equation for pressure individually. Several methods have been proposed to estimate the pressure field. Then the pressure field should be estimated. The most widely used methods for incompressible flows, implicit or semi implicit pressure correction methods, such as SIMPLE, SIMPLEC, and PISO (Fluent, 2006) which will be discussed in Section 5.4.3.2.3.

In general, eq. (5.12) is non-linear with respect to an unknown scalar variable ϕ at the cell center as well as the unknown values in surrounding neighbour cells. A linearized form of equation can be written as:

$$a_p \phi_p = \sum a_{nb} \phi_{nb} + S_\phi \tag{5.13}$$

where the subscript 'p' denotes the node at which governing equation is approximated and the 'nb' refers to neighbour cells, and a_p and a_{nb} are the linearized coefficients for ϕ_p and ϕ_{nb}, and S_φ is the source term.

5.4.3.2.1 Pressure Interpolation Scheme

Referring to (3) in pervious section, an interpolation scheme is required to compute the face values of pressure from the cell values. For driving the interpolation scheme, we shall use the three-grid-point set shown in Fig. 5.2. "*P*" shows the general nodal point and its neighbours in a one-dimensional geometry, *W* and *E* specify the nodes to the west and east, respectively. The west and east side faces of the control volume are specified by "*w*" and "*e*" respectively. The distances between the nodes *W* and *P*, and between nodes *P* and *E*, are specified by δx_{WP} and δx_{PE} respectively.

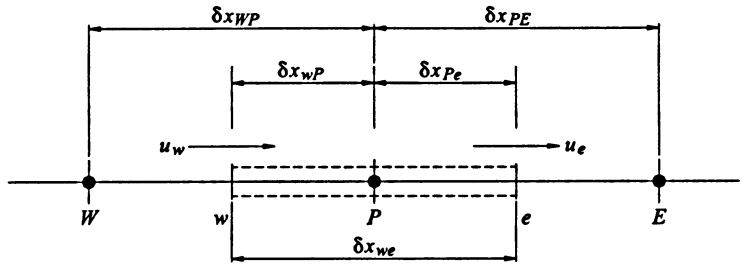

Fig. 5.2. One dimensional control volume (source: Versteeg and Malalasekera, 1995)

5.4.3.2.1.1 The First-order or Standard Interpolation Scheme

The first order or standard scheme interpolates the pressure values at the faces using first-order accurate (with a first order Taylor's series truncation error).

$$\left(\frac{\partial p}{\partial x}\right)_e \approx \frac{p_E - p_e}{\delta x_{PE}} \tag{5.14}$$

5.4.3.2.1.2 The Linear Interpolation Scheme

The linear scheme computes the face pressure as the average of the pressure values in the adjacent cells.

$$\left(\frac{\partial p}{\partial x}\right)_e \approx \frac{\frac{p_E + p_P}{2}}{\delta x_{PE}} \tag{5.15}$$

5.4.3.2.1.3 The Second-order Interpolation Scheme

The second-order scheme reconstructs the face pressure in the manner used for second-order accurate (with a second order Taylor's series truncation error) convection terms (Section 5.4.3.2.2.3). This scheme may provide some improvement over the standard and linear schemes, but it may have some trouble if it is used at the start of a calculation and/or with a bad mesh (Fluent, 2006).

$$\left(\frac{\partial p}{\partial x}\right)_e \approx \frac{p_E - p_P}{2\delta x_{PE}} \tag{5.16}$$

5.4.3.2.1.4 The Body-force-weighted Interpolation Scheme

The body-force-weighted scheme computes the face pressure by assuming that the normal gradient of the difference between pressure and body forces is constant. This works well if the body forces are known a priori in the momentum equations (Fluent, 2006).

5.4.3.2.1.5 The PRESTO Interpolation Scheme

The PRESTO (PREssure STaggering Option) scheme uses the discrete continuity balance for a "staggered" control volume about the face to compute the "staggered" (i.e., face) pressure (Fluent, 2006). The PRESTO scheme is available for all types of meshes (tetrahedral, triangular, hexahedral, quadrilateral, and hybrid meshes).

The Staggered control volume can be explained as follows:
If the velocities and pressures are both defined at the same node, highly non uniform pressure field can act like a uniform filed in the discretized momentum equations. This means that the influence of pressure is properly not shown in the momentum. To solve

this problem, Harlow and Welch (1965) introduced a staggered grid for the velocity components. In their case, all scalar variables are evaluated at normal nodal point while the velocity components are calculated on staggered grids centered on the cell faces.

5.4.3.2.2 Discretization Schemes for Convective Terms

In practical calculations, the numerical results will only be physically realistic when the discretization scheme has certain fundamental properties or it can be said that the accuracy, numerical stability, and boundness of the solution depend on the numerical scheme used for convective terms (Patankar, 1980). Therefore, the following four crucial properties of the discretization schemes can be highlighted: conservativeness, boundedness, transportiveness and accuracy.

1. Conservativeness; The finite volume approach guarantees local conservation of a fluid property ϕ for each control volume. Numerical schemes, which possess the conservativeness property, also ensure global conservation of the fluid property for the entire domain. This is very important physically and is achieved by means of consistent expression for fluxes of ϕ through the cell faces of adjacent control volumes. This means that the flux of ϕ leaving a control volume through particular face must be equal to the flux of ϕ entering the next control volume through the same face.

2. Boundedness; This property is attached to stability and requires that solution (in the linear problem) is bounded by the maximum and minimum boundary values of the flow variable (Scarborough, 1958). This means numerical method does not increase the errors (such a method is said to be stable). It can be achieved by placing restrictions on the magnitude and signs of the coefficients of the algebraic equations. If the flow problems are non-linear, it is important to study the boundedness of a finite volume scheme for closely related linear problems. If the discretization scheme does not satisfy the boundedness requirements, the solution may not converge at all (Versteeg and Malalasekera, 1995).

3. Transportiveness; All flow processes contain effects due to convection and diffusion. Convective phenomena act only in the flow direction so that a point experiences effects due to changes only at upstream locations. Finite volume schemes with the transportiveness property must account for the direction of fluid in terms of the relative strength of convection and diffusion. The non-dimensional cell Peclet number (P_e) as a measure of the relative strengths of convection and diffusion is:

$$P_e = \frac{F}{D} = \frac{\rho \vec{v}}{\Gamma / \delta x} \tag{5.17}$$

where

$$D \equiv \frac{\Gamma}{\delta x} \tag{5.18}$$

and

$$F \equiv \rho \vec{v} \tag{5.19}$$

where F indicates the strength of the convection (or flow), D is the diffusion conductance, and δx is characteristic length (cell width). D always remains positive, and F can be either positive or negative depending on the direction of the fluid flow.

4. Accuracy; The accuracy of a discretized scheme depends on its truncation error. Hence the first order approximation takes the first two terms in the Taylor series while the second order approximation uses the first three terms of the Series and the third order approximation takes the first four terms of the Taylor series.

The effect of discretization scheme on the simulation of flow in stirred vessels has been investigated in very few works such as Sahu and Joshi (1995), Brucato *et al.* (1998), and Aubin *et al.* (2004).

5.4.3.2.2.1 The First Order Upwind (FOU) Scheme

This method was first introduced by Courant *et al.* (1952) and subsequently by Gentry *et al.*, (1966), Barakat and Clark (1966), and Runchal and Wolfshtein (1969). It is also known as the upwind-difference scheme, the upstream-difference scheme, and the donor-cell method.

Hence the convection term is calculated from the following assumption: The quantities at cell faces ($\phi_f : \phi_e \text{ or } \phi_w$) are determined by assuming that the cell-center values represent a cell-average value and hold throughout the entire cell; the face quantities are equal to the cell quantities. Thus, when first-order upwinding is selected, the face value ϕ_f is set equal to the cell-center value of the upstream cell (Versteeg and Malalasekera, 1995):

$$\phi_e = \phi_P \quad \text{if } (\vec{v}.\vec{n})_e > 0 \text{ or positive direction} \tag{5.20}$$

and

$$\phi_e = \phi_E \quad \text{if } (\vec{v}.\vec{n})_e < 0 \text{ or negative direction} \tag{5.21}$$

The value of ϕ_w can be defined similarly.

This method uses consistent expressions to find fluxes through cell faces: thus, the formulation is conservative. The method satisfies the requirements for boundedness, since the coefficients of the discretized equation are always positive. The scheme accounts for the direction of the flow (eq. (5.20) and (5.21)) so transportiveness in considered in formulation. The scheme is only first order based on the Taylor series truncation error (considering two terms of Taylor series).

5.4.3.2.2.2 The Power-law Scheme

The power-law differencing scheme, which is described by Patankar (1980) interpolates the face value of a variable($\phi_f : \phi_e$ *or* ϕ_w) using the exact solution to a one-dimensional convection-diffusion equation:

$$\frac{d}{dx}(\rho\vec{v}\phi) = \frac{d}{dx}\left(\Gamma\frac{d\phi}{dx}\right) \tag{5.22}$$

where $\rho\vec{v}$ and Γ are constant across the interval δx. Eq. (5.22) can be integrated to yield the solution describing how ϕ varies with x in terms of the Peclet number eq. (5.17). The power-law expressions (Patankar, 1980) can be written as:

$$\text{For } P_e < -10, \quad \frac{D_e - \frac{F_e}{2}}{D_e} = -P_e \tag{5.23}$$

$$\text{For } -10 \le P_e < 0, \quad \frac{D_e - \frac{F_e}{2}}{D_e} = (1 + 0.1P_e)^5 - P_e \tag{5.24}$$

$$\text{For } 0 \le P_e \le 0, \quad \frac{D_e - \frac{F_e}{2}}{D_e} = (1 - 0.1P_e)^5 \tag{5.25}$$

$$\text{For } P_e > 10, \quad \frac{D_e - \frac{F_e}{2}}{D_e} = 0 \tag{5.26}$$

where D_e is the diffusion conductance eq. (5.18) and F_e indicates the strength of the convection (eq. (5.19)) on the face.

Therefore, it can be said that when the flow is dominated by convection (no diffusion), interpolation can be accomplished by simply letting ϕ_f be set equal to its "upwind" or upstream value as the first-order scheme.

The scheme is conservative and because the coefficients are always positive like first order it is also bounded. It satisfies the transportiveness requirements by using an upwind formulation for large values of the Peclet number. The scheme is stable and accurate.

5.4.3.2.2.3 The Second-order Upwind Scheme

The accuracy of the first order and power-law is only first order in terms of Taylor series truncation error (Versteeg and Malalasekera, 2007). The errors can be minimized by using high order discretization such as second order. The higher order schemes involve more neighbour points and reduce the errors. In second-order scheme, quantities at cell faces are computed using a multidimensional linear reconstruction approach (Barth and Jespersen, 1989). Thus when second-order upwinding is selected, the face value ϕ_f is computed by means of:

$$\phi_f = \phi + \nabla\phi.\Delta\vec{r} \tag{5.27}$$

where ϕ is the cell-centered value and $\nabla\phi$ represents the best estimate of the solution gradient in the cell computed from surrounding centroid data, and $\Delta\vec{r}$ is the displacement vector from the upstream cell centroid to the face centroid. This formulation requires the determination of the gradient $\nabla\phi$ in each cell. In the literature, there are several methods for this purpose such as least-squares gradient reconstruction (Versteeg and Malalasekera, 2007). This gradient can be computed using the divergence theorem[1], which in discrete form is written as:

$$\nabla\phi = \frac{1}{V}\sum_{f}^{N_{faces}} \tilde{\phi}_f \vec{A} \tag{5.28}$$

[1] The divergence theorem is a conservation law, which states that the volume total of all sinks and sources, the volume integral of the divergence, is equal to the net flow across the volume's boundary (Montiel and Ros, 2005).

where the face values $\tilde{\phi}_f$ are computed by averaging ϕ from the two cells adjacent to that face and V is cell volume. The scheme shows significant improvement in comparison with first order and provides suitable accuracy for many industrial cases of interest (Barth and Jespersen, 1989).

5.4.3.2.2.4 The Quadratic Upwind Difference Scheme: The Quick Scheme

QUICK scheme (Leonard, 1979; Han *et al*, 1981; Pollard and Siu, 1982; Hayase *et al.*, 1992 and Leonard and Mokhtari, 1990) is based on a weighted average of second-order-upwind and central interpolations of the variable, i.e. it uses a three-point (two surrounding the face and one on the upstream side) upstream quadratic interpolation for cell face values. Therefore, the QUICK scheme calculates the value ϕ_e at the east cell face of a general node as:

$$\phi_e = \frac{3}{8}\phi_E + \frac{6}{8}\phi_P - \frac{1}{8}\phi_W \tag{5.29}$$

The scheme is conservative since it uses reliable quadratic profiles, i.e. the cell face values of fluxes are always obtained by quadratic interpolation between two neighbouring nodes and an upstream node (Versteeg and Malalasekara, 2007). The method's accuracy in terms of the Taylor series truncation error is third order. The transportiveness property is based on three nodal values as mentioned before. It is less computationally stable because of negative main coefficients.

5.4.3.2.3 The Pressure-velocity Coupling Algorithms in Steady Flows

Transport equations for velocity components (momentum equations) can be derived from the general transport equation (eq. (5.12)) by replacing the variable ϕ by velocity. Then the obtained velocity field must satisfy the continuity equation. The real difficulty in the calculation of the velocity field is the unknown pressure field (the pressure gradient term

forms the main momentum source term). Therefore, the momentum equations can be solved only when the pressure field is estimated. Unless the correct pressure field is employed, the resulting velocity field will not satisfy the continuity equation. The aim is to find a way to improve the estimated pressure, and subsequently the resulting velocity field will get gradually closer to satisfying the continuity equation.

FLUENT provides three methods for the pressure-velocity coupling: SIMPLE, SIMPLEC, and PISO for steady-state calculations.

The performance of the pressure-velocity coupling has been investigated in some works such as Ranade and Joshi (1989), Gjesdal and Lossius (1997), Xu and Zheng (1999), Moukalled and Darwish (2002 and 2004) and Darwish *et al.* (2004).

5.4.3.2.3.1 The SIMPLE Algorithm

The SIMPLE algorithm (Semi-Implicit Method for Pressure-Linked Equation) is a guess-and -correct method for the calculation of the pressure (Patankar and Spalding, 1972). To start the SIMPLE calculation process, a pressure field is estimated. Consequently, the discrete momentum equations are solved to yield the velocity field. If the pressure field is not estimated correctly, the obtained velocity values will not satisfy the continuity equation. Then a pressure correction equation, deducted from the continuity equation (Ranade, 2002), is solved to obtain a pressure correction field which is in turn used to update the velocity and pressure fields for next iteration.

Based on the discretized versions of the momentum equation, nodal velocity corrections depend in part in velocity corrections at neighbouring nodes (eq. (5.30)) and unless some approximations are made, it is not possible to obtain the desired pressure correction equations.

$$a_p u_p = \underbrace{\sum a_{nb} u_{nb}}_{\text{Velocity corrections at neighbouring nodes}} - V\left(\frac{\delta P}{\delta x}\right) \tag{5.30}$$

where V is the cell volume. In the SIMPLE algorithm, the velocity corrections at the neighbouring nodes are neglected:

$$u_p = -\frac{V}{a_P}\left(\frac{\delta P}{\delta x}\right) \tag{5.31}$$

5.4.3.2.3.2 The SIMPLEC Algorithm

Van Doormal and Raithby (1984) developed a variation of SIMPLE, called SIMPLEC. This method follows the same steps as the SIMPLE algorithm with the difference that the SIMPLEC velocity correction equations neglect terms that are less important than those neglected in the SIMPLE algorithm. In fact in this method, instead of omitting the first term of the right hand side of eq. (5.30), i.e. the effect of neighbouring nodes, it is assumed that the order of magnitude of the velocity corrections at the neighbouring nodes will be the same as that of the node under consideration (Ranade, 2002). Based on this assumption, the following equation for velocity correction is obtained:

$$u_p = -\frac{V}{(a_P - \sum a_{nb})}\left(\frac{\delta P}{\delta x}\right) \tag{5.32}$$

For quite uncomplicated problems such as laminar flows in which convergence is limited by the pressure-velocity coupling, it can be often obtained a converged solution more quickly using SIMPLEC (Fluent, 2006). As SIMPLEC is more consistent, thus, it reduces the need for under-relaxing the pressure, therefore in FLUENT, with SIMPLEC, the pressure-correction under-relaxation factor is generally set to 1.0, which aids in convergence speed-up. In some problems, increasing the pressure-correction under-relaxation to 1.0 can lead to instability due to high grid skewness. For such cases, it is

required to use a slightly more conservative under-relaxation value (up to 0.7), or use the SIMPLE algorithm (Fluent, 2006).

5.4.3.2.3.3 The PISO Algorithm

The PISO (Pressure Implicit with Splitting of Operators) of Issa (1986) is a two-step corrector algorithm. This method has one predictor step and two corrector steps, which the first corrector step is the same as that of the SIMPLE algorithm. Then the corrected velocity and pressure fields are used to derive the second correction equation. For the second step, the first term in the right hand side of eq.(5.30) is calculated using the first correction step (Versteeg and Malalasekara, 1995).

This method is a pressure-velocity calculation procedure developed originally for the non-iterative computation of unsteady compressible flows (Ranade, 2002). The PISO algorithm with neighbour correction is highly recommended for all transient flow calculations, especially for a large time step (Fluent, 2006). For steady-state problems, PISO with two-step correction procedure does not provide any advantage over the other methods such as SIMPLE or SIMPLEC with optimal under-relaxation factors (Fluent, 2006). As this method solves the pressure correction equation twice, so the method requires additional storage for calculations.

5.4.3.3 Solution of Discretized Equation

With the grid created, the boundary conditions, and the physical properties specified, the calculations can be started. The differential equations are approximated as a set of finite volume equations on the grid, and the resulting set of algebraic equations is then solved for the discrete values of the variables. Because of nonlinearity of the equations that govern the fluid flow and related processes, an iterative solution procedure is required.

FLUENT provides two numerical methods: segregated or coupled solver. In a segregated solution approach, one variable at a time is solved all over the domain and the iteration of

the solution is complete when the variable has been solved on the entire domain. In a coupled solution approach, all variables are solved at the same time in a particular cell before the solver moves to the next cell.

As mentioned before, FLUENT will solve the governing integral equations for the conservation of mass and momentum, and (when appropriate) for energy and other scalars such as turbulence and chemical species. In both cases (segregated or coupled), a control-volume-based technique is used.

In both the segregated and coupled solution methods, the non-linear governing equations are linearized to produce a system of equations for the dependent variables in all computational cells. This process may take an "implicit" or "explicit" form with respect to the dependent variable of interest.

1. **Implicit;** For a given variable, the unknown value in each cell is computed using a relation that has both existing and unknown values from neighbouring cells. Thus each unknown variable will appear in more than one equation in the system, and these equations must be solved simultaneously to give the unknown quantities.

2. **Explicit;** For a given variable, the unknown value in each cell is computed using a relation that includes only existing values. Therefore, each unknown will appear in only one equation in the system and the equations for the unknown value in each cell can be solved one at a time to give the unknown quantities.

By considering above information, segregated approach solves for a single variable field in all cells, and then solves for the next variable field by considering again all cells at the same time, and so on. Therefore, there is no explicit option for the segregated solver. However, in coupled solution method, there is a choice of using either an implicit or an explicit linearization of the governing equations. The coupled implicit approaches solves for all variables in all cells at the same time, while the coupled explicit approaches solves for all variables in one cell at a time.

In the segregated solution method, each discrete governing equation is linearized implicitly with respect to that equation's dependent variable. This will result in a system of linear equations with one equation for each cell in the domain. Because there is only one equation per cell, this is sometimes called a "scalar" system of equations. A point implicit (Gauss-Seidel) linear equation solver is used in conjunction with an algebraic multigrid (AMG) method to solve the scalar system of equations for the dependent variable in each cell (Fluent, 2006).

5.4.3.3.1 Gauss-Seidel[1] in Conjunction with an Algebraic Multigrid (AMG)

Iterative methods are based on repeating of a simple algorithm until convergence obtained after a number of repetitions (Versteeg and Malalasekera, 1995). A well-known example is the Gauss-Seidel point-by-point iteration method.

5.4.3.3.1.1 The Gauss-Seidel Method

The Gauss-Seidel method is a technique used to solve a linear system of equations (Versteeg and Malalasekera, 2007). The Gauss-Seidel iterative method (for solving sets of linear equations, $Ax=b$, with A assumed to have dimensions $M\times M$) can be described as follows: The iterative scheme carries on at regular intervals throughout the elements of unknowns, X_j for $j=1, 2, \ldots, M$, finding one single X_j at time. Therefore, it is assumed that all X_i, $i\neq j$, are known from previous steps. Therefore, X_j can be expressed as (Husoy, 2003):

$$X_j = \frac{1}{a_{j,j}}\left[b_j - \sum_{i=1,(i\neq j)}^{M} a_{j,i}X_i\right] \tag{5.33}$$

where $a_{i,j}$ is element (i,j) of A and b_j is element j of b.

[1] The method is named after the German mathematicians Carl Friedrich Gauss and Philipp Ludwig von Seidel.

In numerical linear algebra, one cycle through j=1, 2,..., M is referred to as one iteration. It is clear that for computing X according to eq. (5.33), the X_i's with $i<j$ are available from previous steps of the current iteration, whereas the X_i's with $i>j$ are available from the previous iteration, therefore:

$$X_j^{(k)} = \frac{1}{a_{j,j}}\left[b_j - \sum_{i=1}^{j-i} a_{j,i} X_i^{(k)} - \sum_{i=j+1}^{M} a_{j,i} X_i^{(k-1)}\right] \tag{5.34}$$

While this scheme rapidly takes out the local errors in the solution, the global errors are reduced at a rate inversely connected to the grid size (Versteeg and Malalasekera, 2007). Thus, for a large number of nodes, the residual reduction rate becomes low (Fluent, 2006). To solve this problem, FLUENT uses a multigrid scheme to accelerate the convergence of the solution by computing corrections on a series of coarse grid levels and therefore reduce the number of iterations and specifically the CPU time when the model has a large number of control volumes.

5.4.3.3.1.2 The Basic Concept in Multigrid Scheme

Multigrid methods (Shyy *et al.*, 1997) were originally developed by Brandt (1977). The basic idea is to accelerate the convergence speed of the iterative scheme (e.g. Gauss-Seidel iteration) by updating the corrections to the solution on coarser grids (Press *et al.*, 1992). The idea is that the low frequency components of the errors (global error) can be smoothed out more rapidly on the coarser grids. Thus, the success of this scheme depends on good damping of the errors.

The process starts from the original grid where the problem is defined, or the finest grid. A few iterations are carried out on the finest grid to reduce the high frequency errors. This step is called pre-relaxation step because they are performed before moving to the next coarser grid level. Then the residual errors, controlling the accuracy of the solution on all coarse grids are injected into the coarser grids. The process of smoothing and

injection continues down to a lowest grid, the coarsest one. Here the correction to the solution can be found rapidly and can be interpolated back up until the finest grid is reached again. Next iterations are carried on the fine grids to remove the high-frequency errors formed on the coarse grids by the multigrid cycles. These iterations are referred to post-relaxation sweeps because they are performed after returning from the coarser grid level.

5.4.3.3.2 Under Relaxation

As mentioned before (Section 5.4.3.2) the linear algebraic equations (eq.(5.13)) are approximate forms of the original non-linear discretized equations. The overall iterative procedure of repeatedly solving linearized equations to obtain solutions of non-linear equations is often desirable to divergence, especially when these are coupled with equations of other variables (Fluent, 2006). In order to control the change of ϕ during each iteration, a under relaxation factor, α is introduced:

$$\phi = \phi_{old} + \alpha \Delta\phi \tag{5.35}$$

Therefore, the new value of the variable within a cell depends upon the old value (ϕ_{old}), the computed change in ϕ ($\Delta\phi$), and the under-relaxation factor (α). The under relaxation factor is between zero and one. Lower values of under-relaxation factor lead to more stable but slower convergence. There is no rule to find the optimum value for α, depending on the nature of the problem, the grid number and spacing, and the iterative method (Patankar, 1980). The value of α can be changed (not a fixed value) during the computation (from iteration to iteration).

5.4.3.3.3 Solution Convergence

Independent of the method used, equations must be solved until the error of the solution is reduced to a reasonably small value (Garg, 1998). The convergence criteria are preset

conditions for the residuals that determine when an iterative solution is converged (Paul *et al.*, 2004).

Usually a measure of how closely each discretized equation is balanced is used for convergence criteria (Ranade, 2002). Therefore, the imbalance in the governing equations is summed over the entire domain, which is called the residual, and for a general conservation, equation can be written as:

$$R^{\phi} = \sum_{all\,nodes} \left| \sum_{nb} a_{nb}\phi_{nb} + S_{\phi} - a_p\phi_p \right| \tag{5.36}$$

As mentioned, the residuals for each of the governing equations need to be reduced to a small value. The amount of decrease in the residual, which is necessary for convergence, may be problem dependent and can be determined through experiences (Garg, 1998).

R^{ϕ} is known as the "unscaled " residual. The convergence evaluation using unscaled residual is a difficult task since no scaling is employed (Fluent, 2006). FLUENT scales the residual using a scaling factor representative of the flow rate of ϕ over the entire domain. The "scaled" residual is defined as

$$R_s^{\phi} = \frac{\sum_{all\,nodes} \left| \sum_{nb} a_{nb}\phi_{nb} + S_{\phi} - a_p\phi_p \right|}{\sum_{all\,nodes} |a_P\phi_P|} \tag{5.37}$$

It should be noted that for the momentum equations, term ϕ is replaced by velocity $\vec{v}$, where $\vec{v}_P$ is the magnitude of the velocity at cell P.

For the continuity equation, the unscaled residual for the segregated solver is defined as (Fluent, 2006):

$$R^c = \sum_{all\ nodes} |rate\ of\ mass\ reaction in\ cell\ P| \tag{5.38}$$

and the segregated solver's scaled residual for the continuity equation is defined as:

$$\frac{R^c_{iteration\ N}}{R^c_{iteration\ 5}} \tag{5.39}$$

The denominator is the largest absolute value of the continuity residual in the first five iterations (Fluent, 2006).

5.5 CFD-Based Modeling of the Stirred Tanks

Flow in baffled stirred tanks has been modeled by employing four general approaches as: black box, sliding mesh, multiple reference frames, and snapshot approach shown schematically in Fig. 5.3.

5.5.1 The Black Box Approach

This approach requires boundary conditions on the impeller swept surface, which need to be determined experimentally (Ranade, 1995). Therefore, this approach is limited by the availability of experimental data. When the explained data are available for an impeller in a specific geometry, it does not mean that this impeller generates the same flow field for all alternative mixing systems (Rutherford *et al.,* 1996). Extension of such an approach to more complex mixing processes such multiphase flows and to industrial-scale reactors is not feasible because it is not an easy task to obtain the boundary conditions for such systems. On the other hand, this approach cannot evaluate the flow between the impeller blades (Fig. 5.3 a).

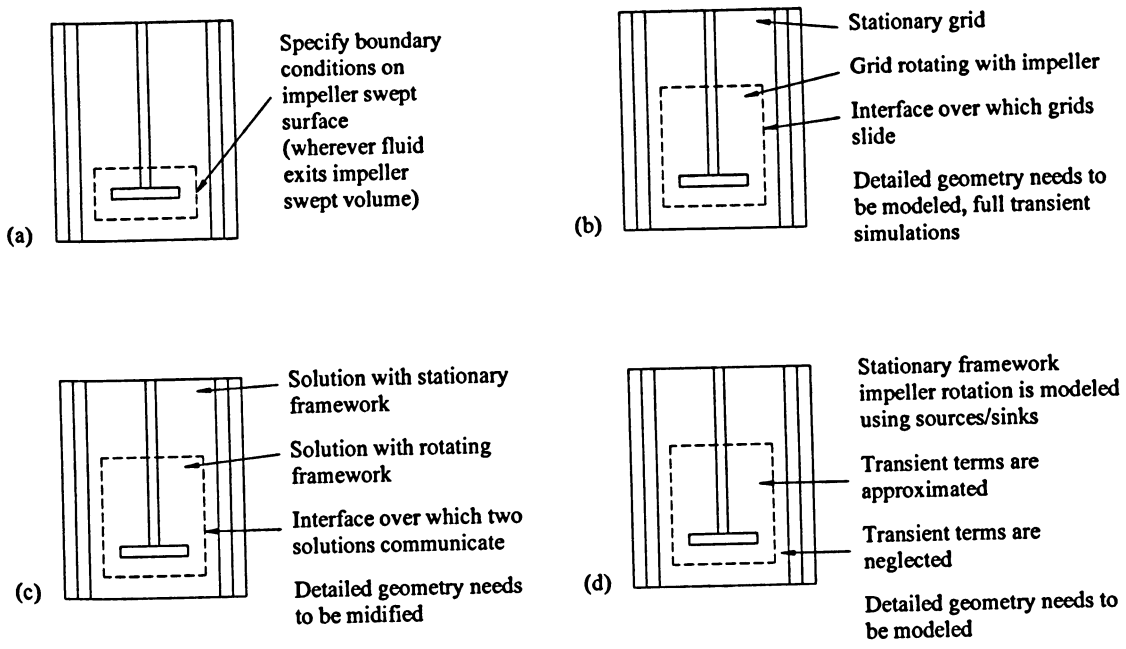

Fig. 5.3. Approaches to modeling flow in stirred tanks. (a) black box approach, (b) sliding mesh approach, (c) multiple reference frame, (d) snapshot approach.(Source: Ranade, 2002)

5.5.2 The Sliding Mesh Approach

In the sliding mesh approach (Luo *et al.*, 1993; Perng and Murthy, 1993; Harris *et al.*, 1996; Ranade *et al.*, 1997), the dynamic simulations (the most important advantage of this approach) are carried out using two grid zones; one is attached to the baffles and tank wall while the other is attached to the rotating impeller (Fig. 5.3 (b)). As the impeller rotates in time relative to the baffles, so does the grid in the impeller region, while the baffle region does not move. To evaluate the motion of the grid, the solution method must be time-dependent (there is no steady-state solution of the impeller(s) and baffle(s) when this model is used). Without any experimental data (compared with black-box approach), this approach can provide useful information which can be used as a design tool. As this approach depends on unsteady-state solution in a stirred vessel, computational requirements are greater than those required by the steady-state simulations. Therefore, use of such an approach as a design tool to evaluate the mixing performance becomes difficult. The extreme computational requirements make some limitations on number of computational cells that can be used for the simulations. Another important issue is that

the results from this approach are not yet sufficiently validated (Harris *et al.,* 1996). On the other hand, knowledge of the full unsteady-state flow field (which repeats after some impeller rotations) may not be necessary when qualitative comparison of the flow field generated by different impellers may be useful in industry, which can be performed by steady-state approaches such as multi reference frame.

5.5.3 The Multi Reference Frame (MRF) Approach

When the MRF model (Luo *et al.,* 1994) is used, two regions are created within the mixing tank; one region around the impeller with distance above and below it. This impeller grid region is stationary, but the conservation equations are solved in a rotating frame. The rotation angular velocity of this region is the same as that of the impeller and shaft. Thus, the velocity of these elements is zero relative to the rotating frame. The second region is associated with the outside walls of the tank (including the top surface) as well as the baffles. The conservation equations in this grid region are solved in the stationary frame. Thus, no motion is applied to the tank wall, the liquid surface, or the baffles. Values of the conserved quantities are matched at the interface between these two grid regions, i.e. rotating and stationary frames.

5.5.4 The Snapshot Approach

This approach is based on taking a snapshot of flow in a stirred tank in which the relative position of a impeller and baffles is fixed (Ranade, 2002). Ranade and Dommeti (1996) introduced such an approach, in which impeller blades are modeled as solid walls and flow is simulated using stationary frame in a fixed blade position. Simulations are performed at different blade positions and then the averaged results are obtained. Like MRF the entire domain is divided into two regions. In the impeller region, time-dependent terms are approximated in terms of spatial derivatives. In the outer region, time derivative terms are usually small enough compared with the other terms in the governing equations and can be neglected.

The two models, available in FLUENT for simulating the action of the impellers in the mixing tank, are multiple reference frame (MRF) and sliding mesh model.

5.6 Model Description

FLUENT is a CFD software package that solves the Navier-Stokes equations using a finite volume method. In this research, Fluent V6.3 (Fluent Inc., 2006) was used to solve the conservation of mass and momentum (and other relevant quantities) and generate steady-state flow fields through 3-D depictions of the stirred tank.

5.6.1 Computational Models

5.6.1.1 Geometry

A specialized pre-processor for mixing applications, MixSim[1] version 2.1.10 (Fluent Inc., 2006) was used for defining the mixing tank configuration shown in Fig. 5.4 (explained in Chapter 4).

Vessel	Cylindrical
Diameter (m)	0.4
Height (m)	0.61
Fluid height (m)	0.4
Impeller	
Diameter (m)	0.18
Blade number	6
Off-bottom distance (m)	0.17 and 0.21
Baffles	
Width (m)	0.04
Number	4

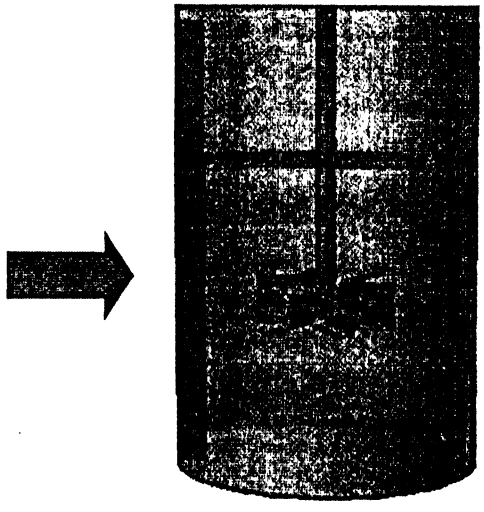

Fig. 5.4. Geometry

[1] MixSim is a comprehensive analysis tool for complete hydrodynamic simulation of agitated mixing vessels (MixSim, 2006).

5.6.1.2 Impeller Model

Between two available numerical approaches, sliding mesh (Luo *et al.*, 1993; Lane and Koh, 1997) and multi reference frame (Luo *et al.*, 1994; Tabor *et al.*, 1996), reviewed and compared by Brucato *et al.*, (1998), multiple reference frame (MRF) method was utilized (Fig. 5.5). This technique is a steady-state approximation suitable if the distance between the impeller blades and baffles is sufficient such that the flow near the impeller is unaffected by the rest of the tank and can be time-independent with respect to the impeller. This method has been shown to save the computational time of a factor of about 10, while providing a similar degree of accuracy to the sliding mesh method (Luo *et al.*, 1994; Tabor *et al.*, 1996). A complete analysis of the different modeling approaches for different types of mixing systems conducted by Brucato *et al.* (1998), showed that the MRF method provides reasonable results compared with full unsteady computations and measurements.

The literature review on CFD modelling of baffled stirred tanks highlights several works using MRF method (Kukukova *et al.*, 2005; Aubin *et al.* 2004; Sommerfeld and Decker, 2004; Ricard *et al.*, 2005; Buwa *et al.*, 2006; and Lane *et al.*, 2001).

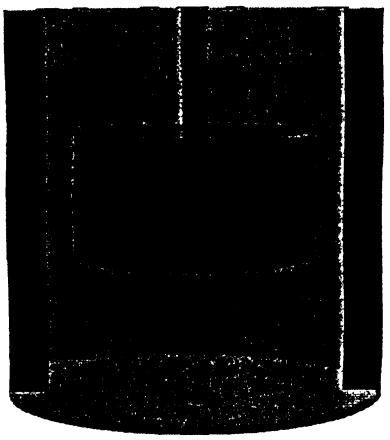

Fig. 5.5. MRF modeling flow in the stirred tank.

5.6.1.3 Flow Model

Since all simulations were conducted in the laminar and transitional regimes, the flow was modelled as laminar. On the other hand, with highly viscous solutions, turbulence strength will be driven away significantly by the time the fluid reaches the tank wall or baffles (Ford *et al.*, 2006). As it has been seen in several studies such as Kelly and Humphrey (1998), Zalc *et al.* (2001), Letellier *et al.* (2002), Alvarez *et al.* (2002), Kelly and Gigas (2003), Alliet-Gaubert *et al.* (2006), and Ford *et al.* (2006), the macro-instabilities that may happen at the transient flow range close to the laminar regime, can be neglected and consequently flow can be modeled using laminar equations.

5.6.1.4 Physical Properties

The fluid rheologies (Table 4.1) were modeled as Hershel-Bulkley fluids. In numerical modeling, the Bingham and Hershel-Bulkley models are discontinuous since at small shear rates, the non-Newtonian viscosity becomes unbounded (Ford, 2004). This discontinuous behaviour causes major difficulties in numerical analysis. Thus, it can be assumed that for low shear rates ($\dot{\gamma} \leq \tau_y / \mu_0$), the solution acts like a very viscous fluid with viscosity μ_0. As the shear rate is increased and the yield stress (τ_y) is overcome, the fluid behaviour is described by a power-law model (Fluent, 2006). Fig. 5.6 shows how shear stress (τ) varies with shear rate ($\dot{\gamma}$) for the Herschel-Bulkley model. Hence, a two-viscosity model can be used to overcome the discontinuity (eq.(5.41 b)) as follow:

$$\eta = \mu_0 \qquad For\ \tau \leq \tau_y \tag{5.40 a}$$

$$\eta = \frac{\left[\tau_y + K\left[\dot{\gamma}^n - \left(\frac{\tau_y}{\mu_0}\right)^n\right]\right]}{\dot{\gamma}} \qquad For\ \tau \rangle \tau_y \tag{5.41 b}$$

where μ_0 is yielding viscosity. Therefore, the fluid rheologies were modeled as Herschel-Bulkley fluids based on the parameters in Table 5.1.

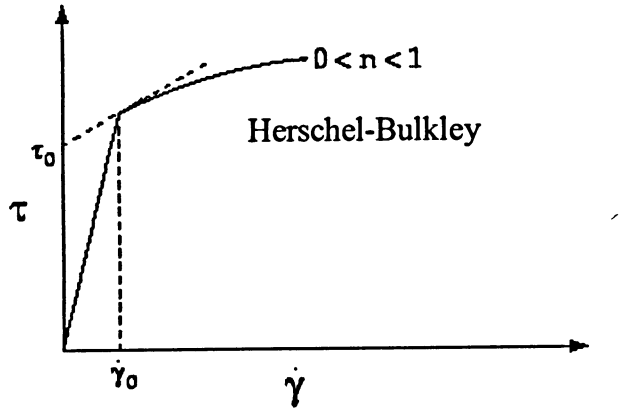

Fig. 5.6. Shear stress vs. shear rate according to eq. (5.41 b)

Table 5.1. Fluid rheological parameters.

Xanthan Concentration	K (Pa s^n)	n -	τ_y (Pa)	μ_0 (Pa.s)
0.5%	3	0.11	1.789	13.30
1.0%	8	0.12	5.254	22.61
1.5%	14	0.14	7.455	32.36

5.6.2 Grid Generation

A pre-processor, GAMBIT[1] version 2.2.30 (Fluent Inc., 2006) was used to descretize the flow domain with an unstructured tetrahedral mesh consisting of 331,772 cells shown in Fig. 5.7. The quality of the grid has been checked using a grid histogram (Fig. 5.8) for the equiangle skewness (Q). The equiangle skewness is a normalized measure of skewness that is an indication of how close the cell is to a perfect tetrahedral element (for this study), i.e. Skewness=0, describes the perfect tetrahedral element and skewness=1, indicates a poorly shaped element. In the majority of simulations performed, around 96% of cells had a Q less than 0.6 confirming a good quality for the mesh generated, and less than 0.01% had a Q between 0.8 and 0.85 (as a fair quality).

[1] GAMBIT is the geometry and grid generator that MixSim can use when the model is ready (Fluent, 2006).

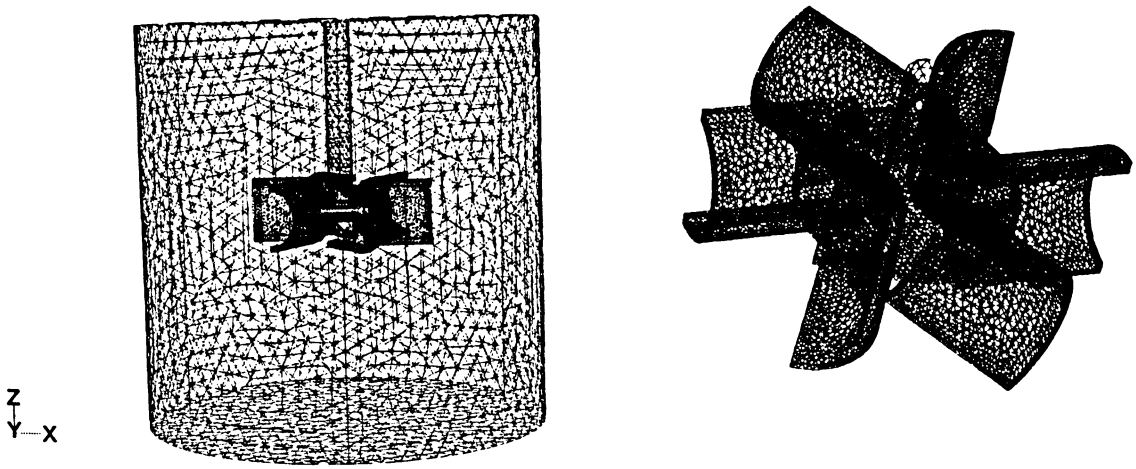

Fig. 5.7. Numerical grid (Unstructured tetrahedral mesh).

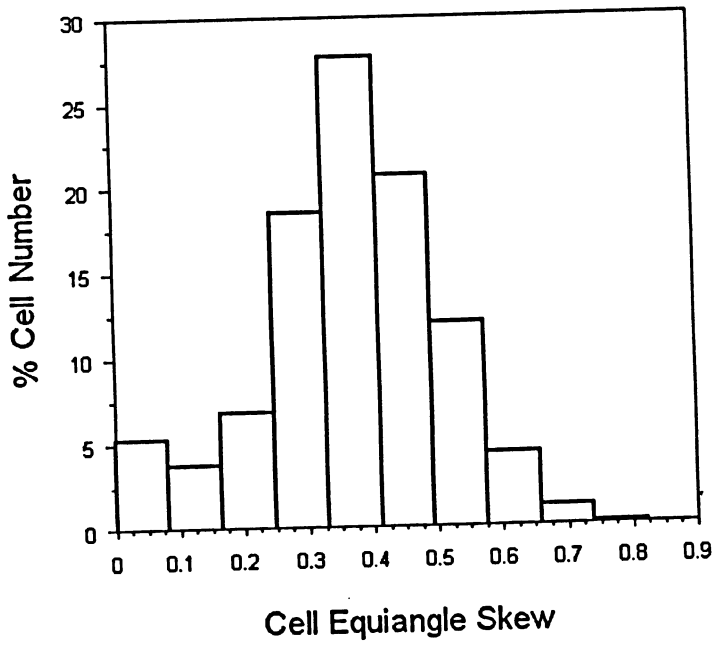

Fig. 5.8. Grid histogram.

5.6.2.1 Grid Independence

Grid independence studies were performed and demonstrated that the number of grids used is sufficient to capture most of the important features of the flow. The number of grid nodes, especially in the regions of high gradient around the blades (the discharge region), were systematically increased throughout the vessel such that three grids were generated (221879 as a coarse grid, 331772 as a medium grid, and 391538 as a fine grid) for Reynolds number (*Re*) = 24. Significant differences were not found in the calculated power number for all three grids (< 0.1%).

A further requirement was that the additional grids did not change the calculated velocity profiles in regions of high-velocity gradients. Fig. 5.9 shows the radial and tangential velocity profiles as functions of horizontal positions, where large transport gradients in the flow exist, (impeller is a radial flow one). It can be seen that the fine and medium grids give very similar profiles of radial and tangential velocity. The radial velocity profile for the coarse grid is clearly different from those of the fine and medium meshes. The discrepancy between them can be qualified in terms of the root-mean-square (RMS) deviation (Arratia *et al.*, 2006):

$$RMS = \frac{\left[\frac{1}{n}\sum_{1}^{n}(u_1 - u_2)^2\right]^{1/2}}{\left[\frac{1}{n}\sum_{1}^{n}(u_2)^2\right]^{1/2}} \tag{5.42}$$

where n is the number of nodes in the velocity field. Here the RMS values between the coarse grid and the medium grid are 4.22 % and 1.82 %; and between the medium grid and the fine grid are 3.32 % and 1.85 % for radial and tangential velocity, respectively. As the difference between the radial velocity profiles for the coarse grid and the medium grid simulations is more than 4% and for the medium grid and the fine grid is less than 4%, therefore 331,772 control volumes were considered suitable for this problem and were used for all simulations.

A Literature review on the grid independency evaluation is shown in Table 5.2.

Table 5.2. Grid independency evaluation (review)

Research	Cell number	Evaluated by
Gentic *et al.*, 2005	233,000 463,000	Radial profiles of axial velocity, turbulent kinetic energy, and turbulent dissipation rate
Brucato *et al.*, 1998	2,646 9,240 29,106 97,440	Radial profile of axial velocity, axial profile of radial velocity, The power number
Barailler *et al.*, 2006	178,000 410,000	-
Alliet-Gaubert *et al.*, 2006	160,000 505,000	-
Letellier *et al.*, 2002	75951 & 35644 at 90 rpm 58053 & 104153 at 70 rpm 182501 & 216598 at 50 rpm	Power
Kelly and Humphrey, 1998	2000 to 26000	Average axial velocity
Aubin *et al.*, 2004	76,000 155,000 350,000	Radial profile of turbulent kinetic energy
Buwa *et. al.*, 2006	22,498 46,953 93,440 175,661	Profiles of mean velocity components and turbulent kinetic energy
Kelly and Gigas, 2005	4 cells 8 cell 16 cells at 2 mm of impeller surface	Power number Angle discharge Average strain rate near impeller surface (s^{-1})

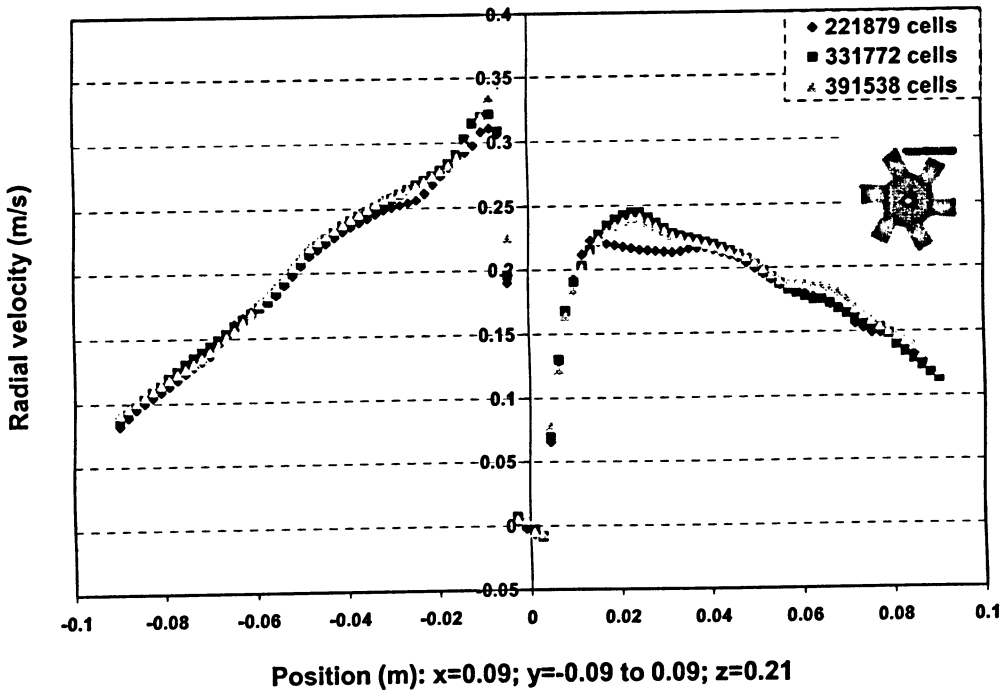

(a)

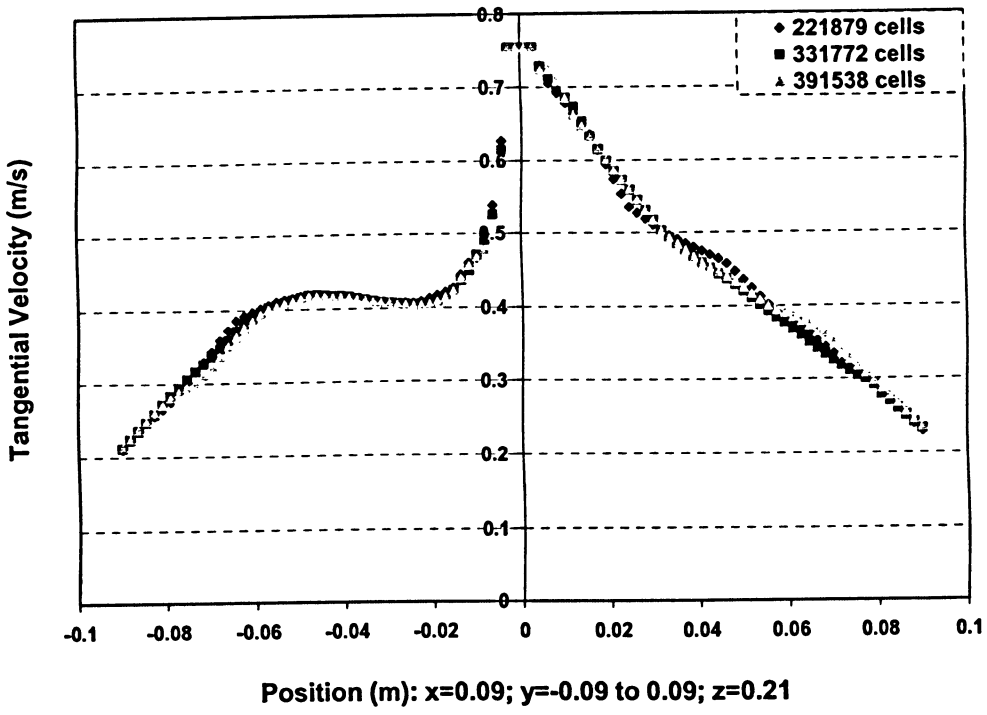

(b)

Fig. 5.9. Effect of grid numbers on: (a) radial velocity, and (b) tangential velocity, in horizontal position.

5.6.3 Performing the Calculation

After defining the mixing model and generating the grid, solutions can be started. The numerical scheme selected in FLUENT was the segregated solver. Using this approach, the governing equations are solved sequentially.

In the segregated algorithm, the individual governing equations for the solution variables are solved one after another (Fluent, 2006). Each governing equation, while being solved, is segregated from other equations. Therefore, the segregated algorithm is memory-efficient, but relatively slow. Each iteration consists of the following steps (Fluent, 2006):

1. Update fluid properties.
2. Solve the momentum equations, one after another, using the recently updated values of pressure and face mass fluxes.
3. Solve the pressure correction equation using the recently obtained velocity field and the mass-flux.
4. Correct face mass fluxes, pressure, and the velocity field using the pressure correction obtained from step 3.
5. Check for the convergence.

These steps are continued until the convergence criteria are reached.

The governing equations are discretized using the finite-volume method. The convective terms of the governing equations are discretized using the second-order upwind differencing scheme. A first order upwind scheme was initially used for the momentum equations and after several iterations, when the convergence ($<1\times10^{-2}$) was reached; the solution was used as the initial conditions for the calculation of a second order upwind scheme. It is important to note that this scheme is more accurate than first order and power law as the first order accurate scheme (Aubin *et al.*, 2004) and more stable than QUICK. The pressure interpolation scheme selected was also second order accurate. The pressure-velocity coupling method used was SIMPLEC.

Convergence was monitored dynamically by checking the residuals for each conservation variable: mass, x-velocity, y-velocity, and z-velocity. Simulations were considered converged when the scaled residuals dropped below 1×10^{-5}.The under relaxation factors for momentum and pressure were set at 0.3 and 0.7 (default) respectively.

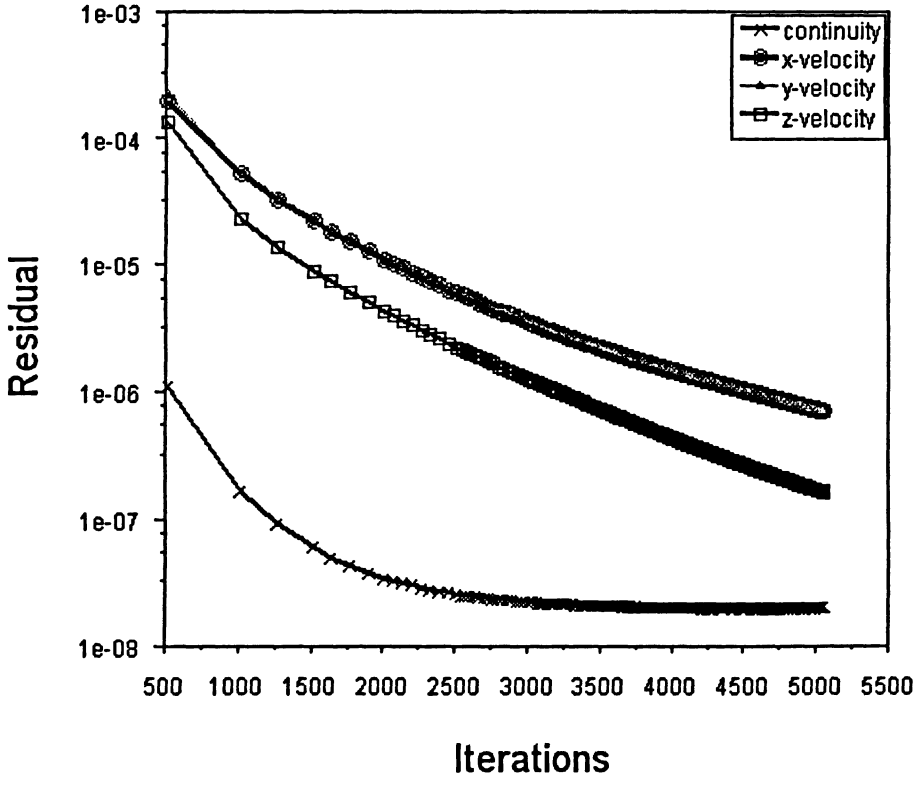

Fig. 5.10. Typical convergence history of the scaled residuals.

A no-slip boundary condition is imposed on all walls. The free liquid surface is modeled with no vortex, flux and stress conditions.

Most problems required 5000-7000 iterations for convergence. All computations were performed on a platform comprising Intel Pentium 4 equipped with 2.00 Gbytes RAM at 3.60 GHz. The CPU time varied between 6 and 8 hours.

5.6.4 Species Transport

After the flow fields had been calculated, the calculations were switched to transient and simulations for the tracer homogenization were performed. The tracer, having the same physical properties as the bulk (xanthan solutions), was added 10cm under the liquid surface (Fig. 5.11) and stretched to a quarter-circle adjacent the first probe. In all simulations, the value of mass fraction of the injected tracer was set to 1.

The tracer mass fraction in the vessel was recorded during the time-dependent simulation. The virtual probes were placed at four points (Fig. 5.11), at the same positions as the experimental probes, i.e. the four pixels selected on each ERT plane. The time step adopted for the simulation was equal to 0.1s refers to Section 5.6.4.1. The value of species residual for a converged solution was set equal to 10^{-7}. The CPU time varied between 6 and 8 hours.

To model the flow of the tracer, the following species transport equation needs to be solved:

$$\frac{\partial}{\partial t}(\rho w)+\nabla.(\rho \bar{v} w)=\nabla.\rho D_m \nabla \phi \qquad (5.43)$$

where w is the local mass fraction of the tracer, $\bar{v}$ is the mean velocity vector, ρ is the fluid density, D_m is the molecular diffusivity of the tracer in the mixture which is assumed to be 10^{-9} as a typical value for liquids (Montante *et al.*, 2005).

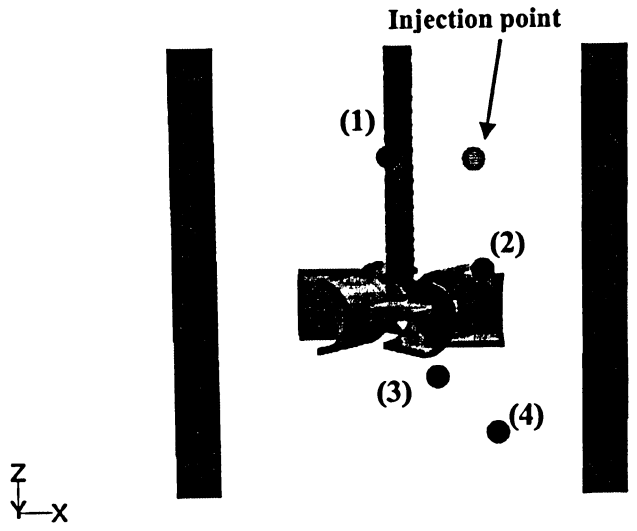

Fig. 5.11. The location of the injection point and monitoring locations known as probes; all locations are specified by their x, y, z coordinates in (m). Injection point: 0.07, 0.11, 0.295; Probes location: (1): -0.01, 0.13, 0.295; (2): 0.07,-0.07, 0.21; (3): 0.03, -0.11, 0.125; and (4): 0.09, 0.09, 0.04.

5.6.4.1 Influence of Time Step on the Simulation

The influence of the time step on the tracer concentration profiles was checked by performing the simulations with time steps of 0.01, 0.1, 1, and 1.5s. Fig. 5.12 presents the calculated profiles corresponding to each probe. These figures show that the tracer concentration at points 3 and 4 is almost unaffected by the time step. Although the differences can be observed in the traced concentration at the beginning of its dispersion inside the vessel, the predicted mixing times (t_{95}) are almost the same for 0.01 and 0.1s (see Fig. 5.13 and Table 5.3). On the other hand, the computational time required to reach the homogonous level using the time step of 0.01s was more than 24 hours while the computational time required to achieve homogeneity using the time step of 0.1s was 6-7 hours. Fig. 5.12, Fig. 5.13, and Table 5.3 demonstrate that the concentration profiles and corresponding mixing times predicted using time steps of 1s and 1.5s differ substantially from the other profiles estimated using time steps of 0.1s and 0.01s. Therefore, the time step used in the rest of the simulations was set to 0.1s.

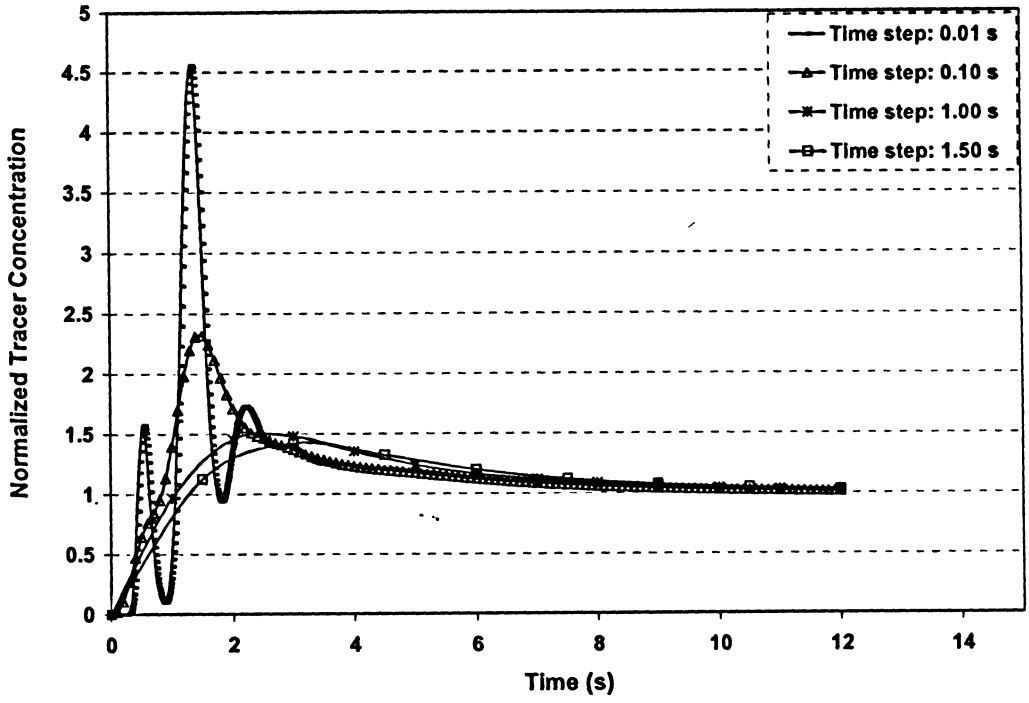
Time step: 0.01 s
Time step: 0.10 s
Time step: 1.00 s
Time step: 1.50 s
Normalized Tracer Concentration
Time (s)
0
0.5
1
1.5
2
2.5
3
3.5
4
4.5
5
0
2
4
6
8
10
12
14

(a)

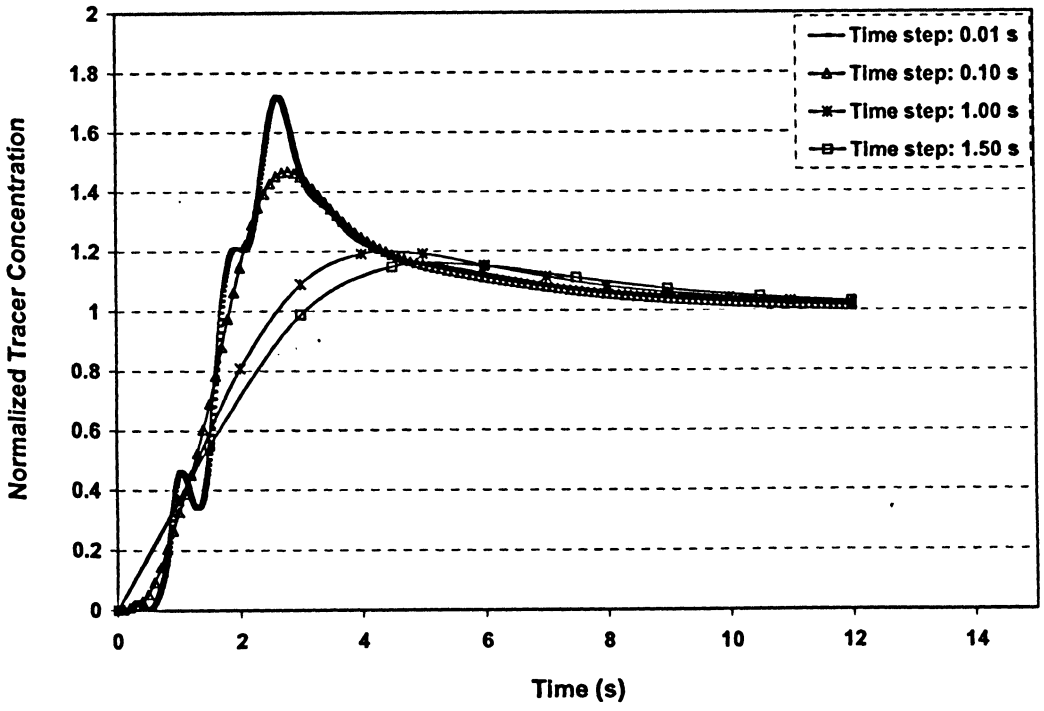
Time step: 0.01 s
Time step: 0.10 s
Time step: 1.00 s
Time step: 1.50 s
Normalized Tracer Concentration
Time (s)
0
0.2
0.4
0.6
0.8
1
1.2
1.4
1.6
1.8
2
0
2
4
6
8
10
12
14

(b)

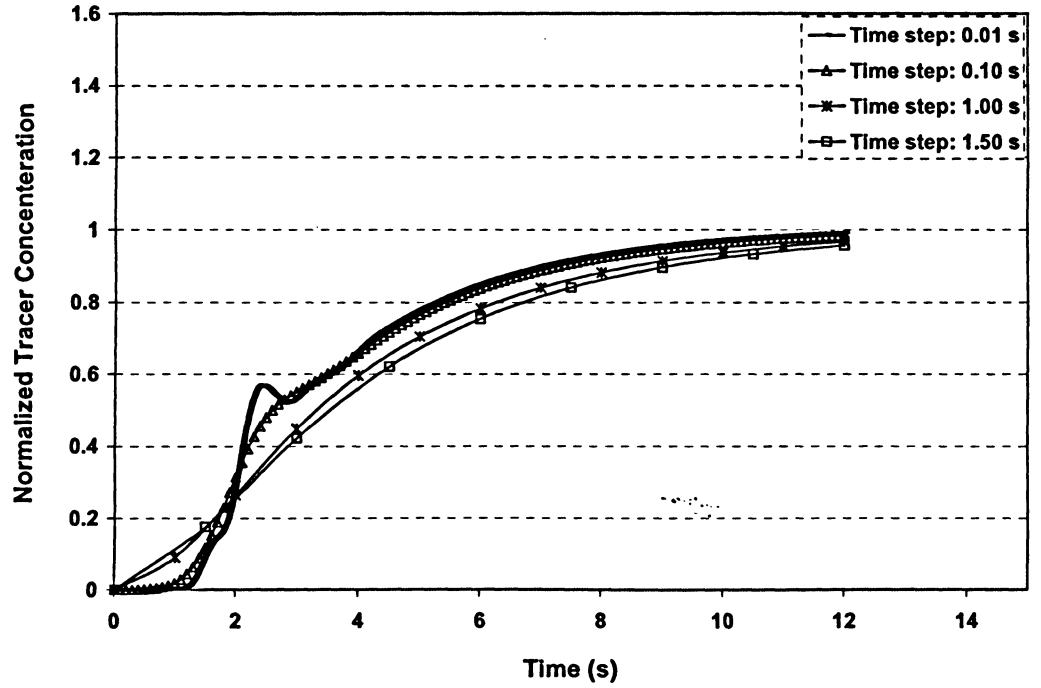

(c)

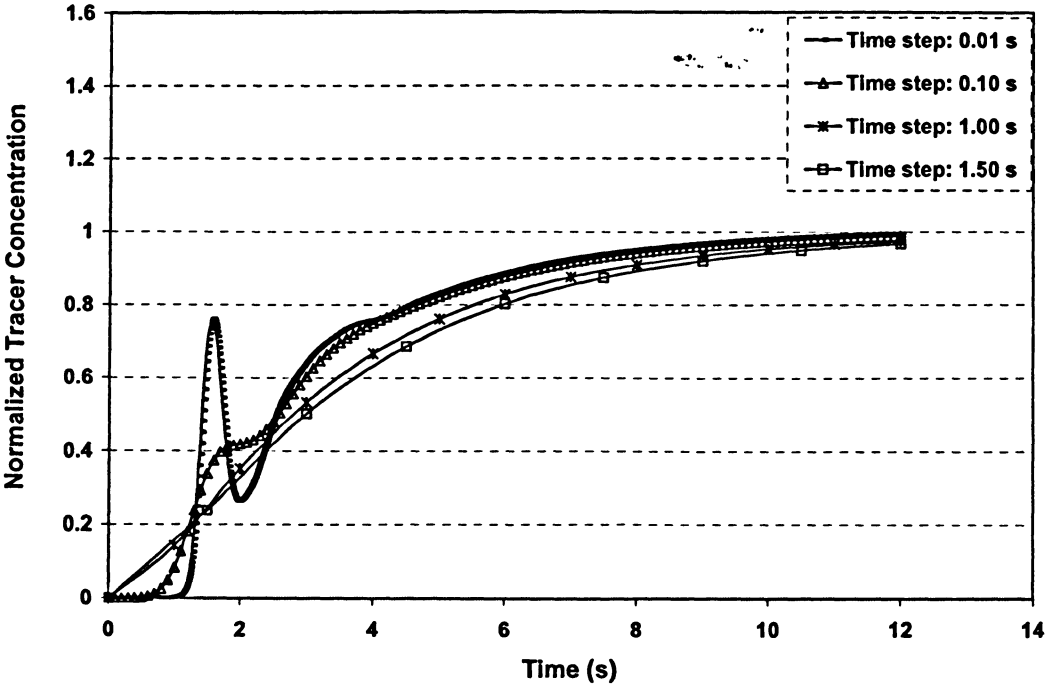

(d)

Fig. 5.12. Comparison of dimensionless tracer concentration at: (a) point 1 (x=-0.01, y=0.13 and z=0.295), (b) point 2 (x=0.07, y=-0.07 and z=0.21), (c) point 3 (x=0.03, y=-0.11 and z=0.125), and (d) point 4 (x=0.09, y=0.09 and z=0.04), vs. time for various time steps. (For 1.0% xanthan solution agitated at 282 rpm).

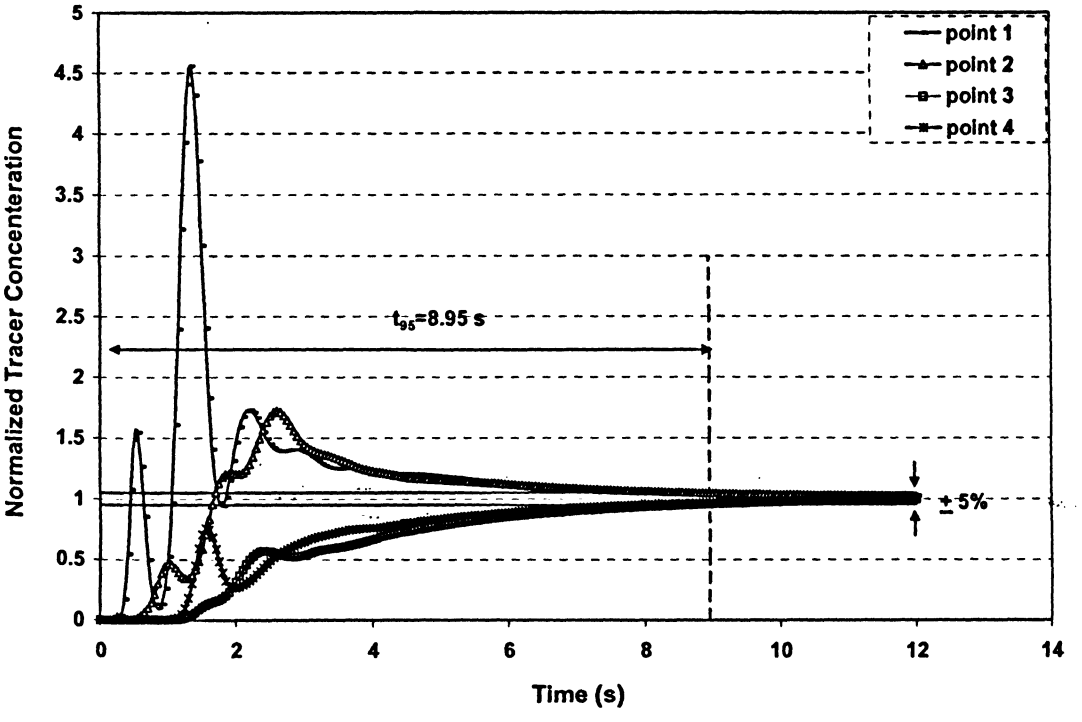
point 1
point 2
point 3
point 4
t_{95}=8.95 s
± 5%
Normalized Tracer Concenteration
Time (s)

(a)

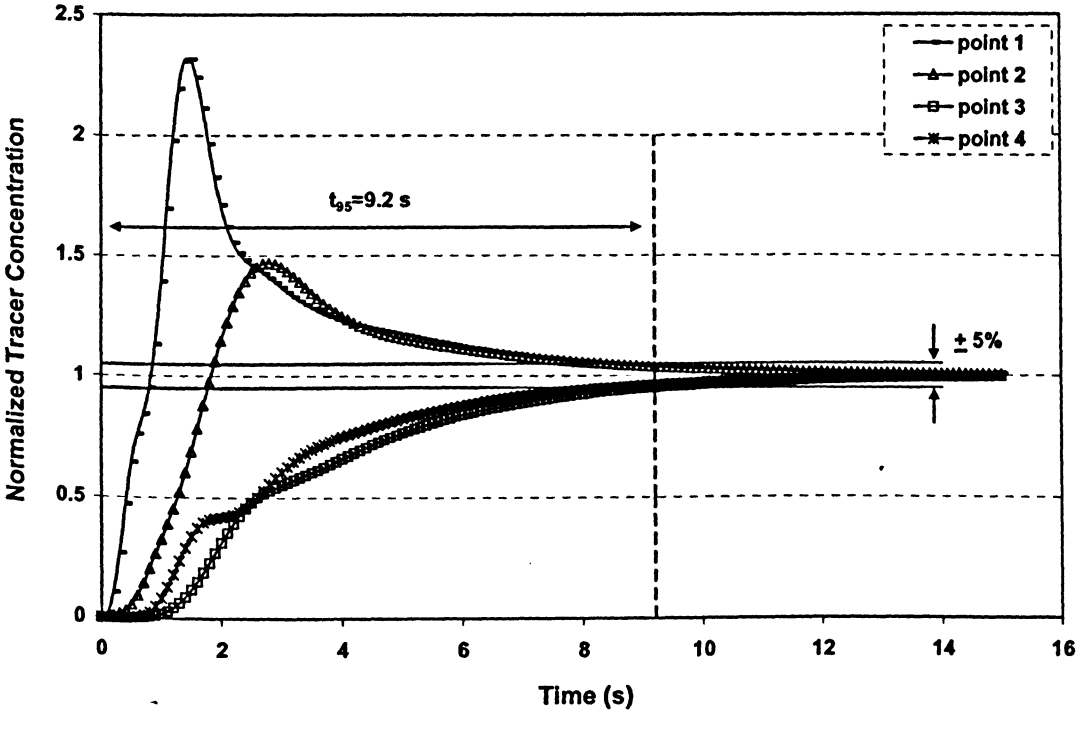
point 1
point 2
point 3
point 4
t_{95}=9.2 s
± 5%
Normalized Tracer Concentration
Time (s)

(b)

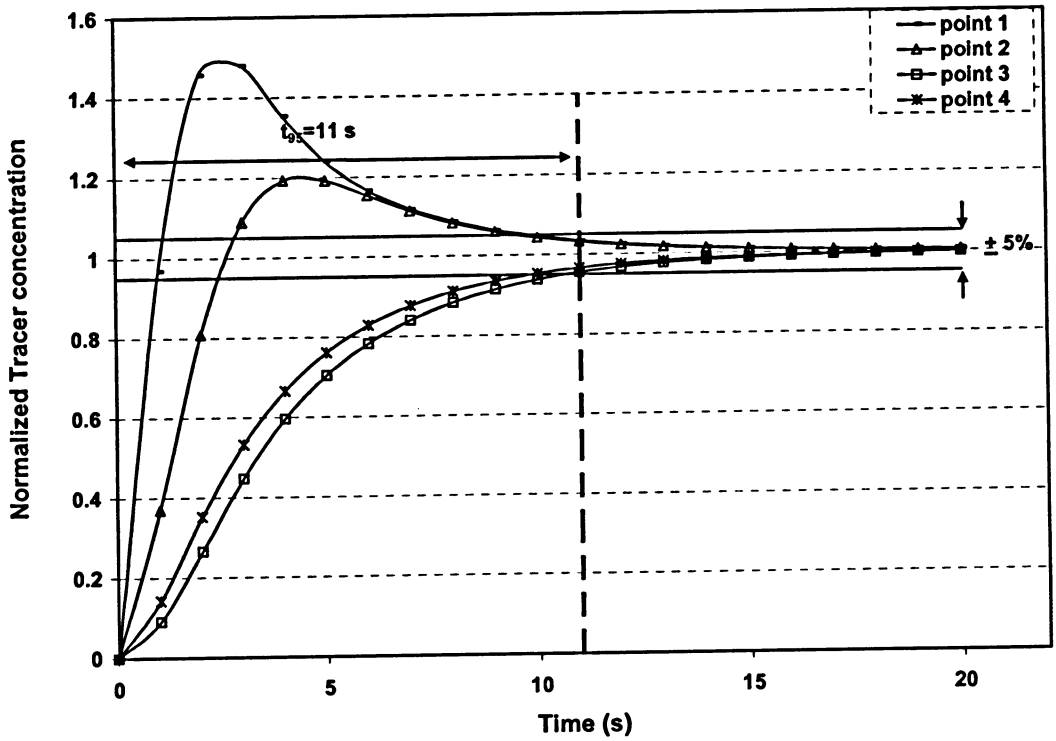

(c)

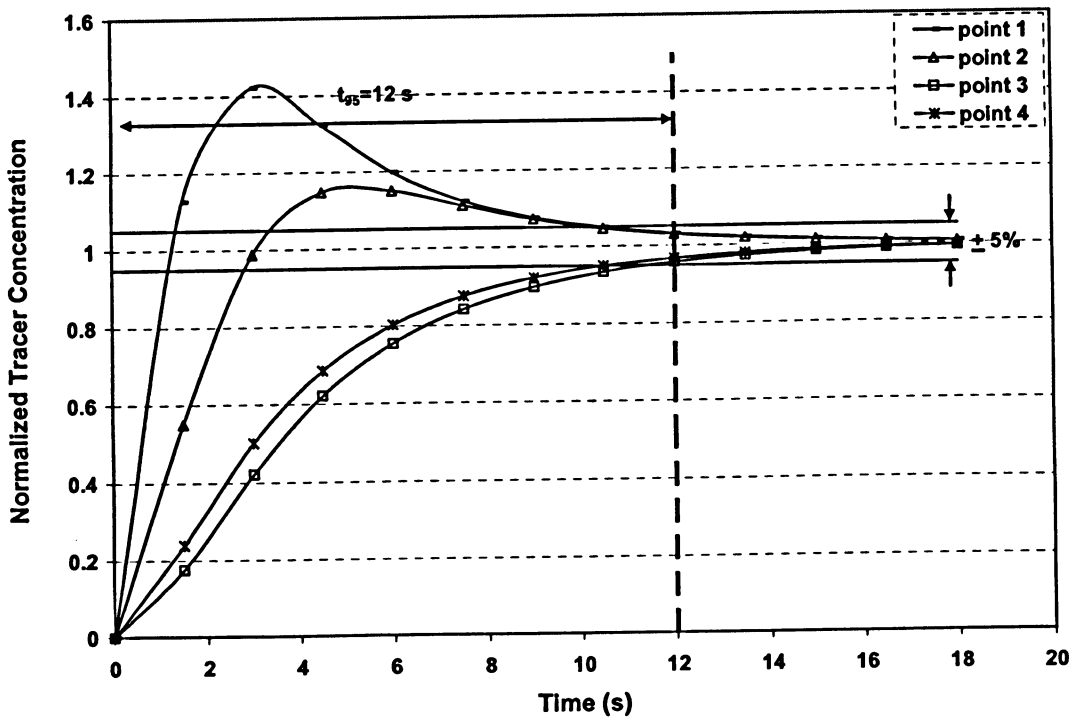

(d)

Fig. 5.13. Comparison of dimensionless tracer concentration vs. time for 1.0% xanthan solution agitated at 282 rpm using different time steps: (a) time step: 0.01s; (b) time step: 0.1s ; (c) time step: 1s; and (d) time step: 1.5s. (For point 1: x=-0.01, y=0.13 and z=0.295, point 2: x=0.07, y=-0.07 and z=0.21, point 3: x=0.03, y=-0.11 and z=0.125, and point 4: x=0.09, y=0.09 and z=0.04).

Table 5.3. Mixing time for 1.0% xanthan solution agitated at 282 rpm.

Time step (s)	t_{95} (s)
0.01	8.95
0.1	9.2
1	11
1.5	12

5.6.4.2 The Influence of the Number of the Probes on Mixing Time

The influence of the number of the probes on mixing time was evaluated by performing simulations for 4 probes, 10 probes (see Fig. 5.14) and four planes, same as ERT planes (see Fig. 5.15) under the same conditions (time step: 0.01s). Only negligible differences can be seen in the profiles (refer to Fig. 5.16) and the resulting mixing times (see Table 5.4).

Fig. 5.17 shows a series of CFD horizontal cut planes (same as ERT planes) for 1.0% xanthan solution agitated at 282 rpm. After 9s, the contours show that all four measuring planes reach the 95% of the final concentration.

It can be concluded that the number of the probes is not critical in CFD for mixing times measurements. This can be considered as one of the limitations of CFD simulations. Therefore, in this study, four virtual probes were placed at four points same as four selected pixels from four ERT planes (each pixel on each plane).

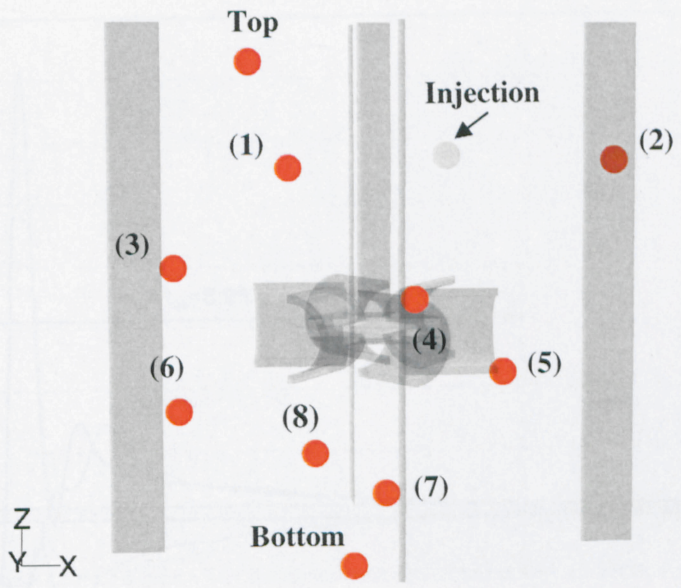

Fig. 5.14. The location of the injection point and monitoring locations known as probes; all locations are specified by their x, y, z coordinates in (m).Injection point: 0.07, 0.11, 0.295; Probes location: (1): 0.07, -0.07, 0.295; (2): 0.19, 0.03, 0.295; (3): -0.15, 0.07, 0.21; (4): 0.01,-0.17, 0.21; (5): 0.11, 0.07, 0.125; (6): -0.15, -0.11, 0.125; (7) 0.01, 0.01, 0.04; (8) -0.03, 0.19, 0.04; Top: -0.09, 0.09, 0.37; and Bottom: -0.03, -0.15, 0.02 .

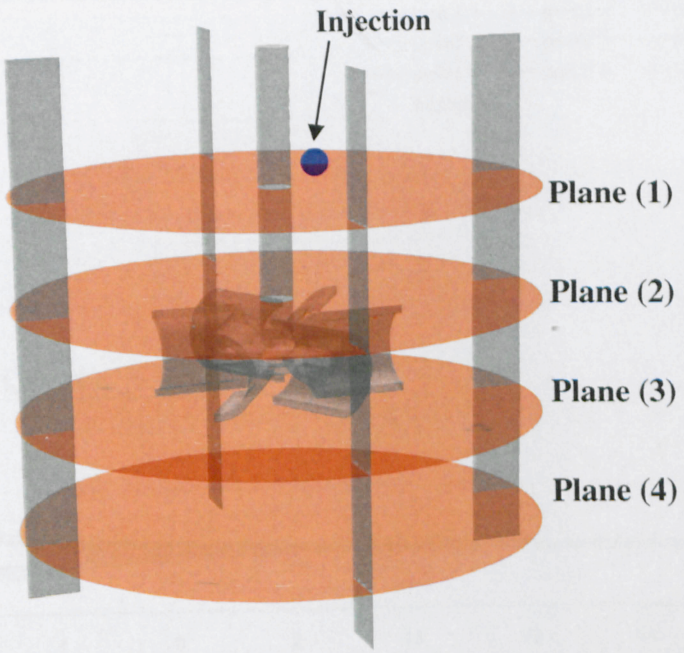

Fig. 5.15. The location of the injection point and monitoring planes; all planes are horizontal specified by their z coordinate in (m). Injection point: x=0.07, y=0.11, z=0.295; Planes location: (1): 0.295; (2): 0.21; (3): 0.125; and (4): 0.04.

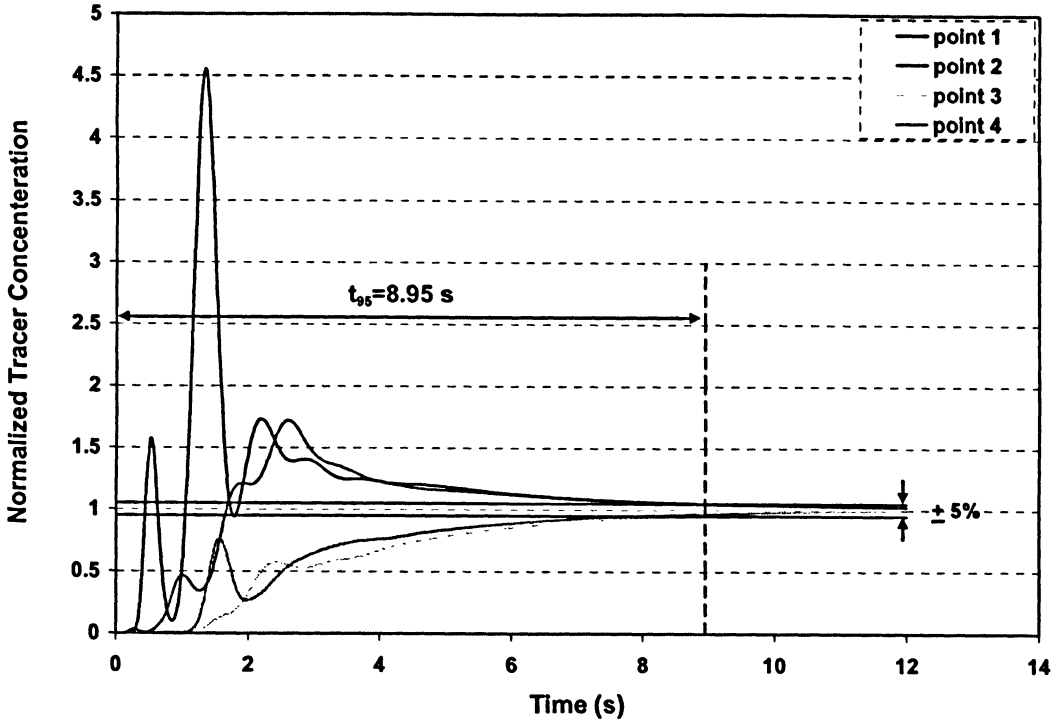
Normalized Tracer Concenteration
Time (s)
point 1
point 2
point 3
point 4
t_{95}=8.95 s
± 5%
0
0.5
1
1.5
2
2.5
3
3.5
4
4.5
5
0
2
4
6
8
10
12
14

(a)

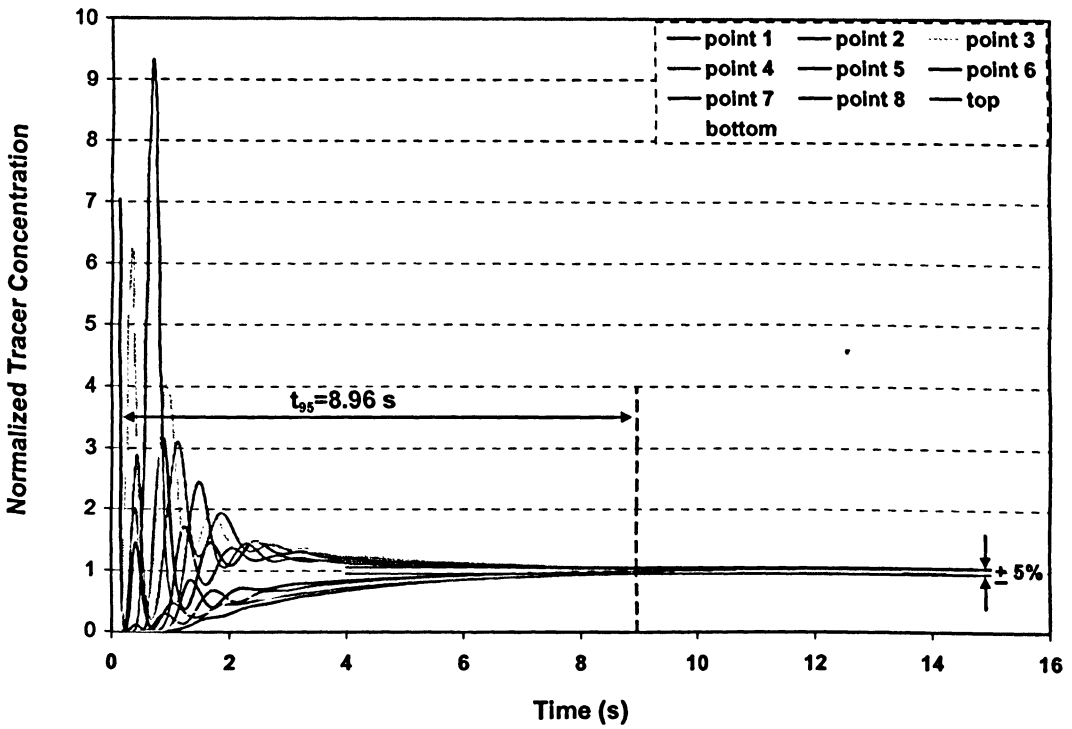
Normalized Tracer Concentration
Time (s)
point 1
point 2
point 3
point 4
point 5
point 6
point 7
point 8
top
bottom
t_{95}=8.96 s
± 5%
0
1
2
3
4
5
6
7
8
9
10
0
2
4
6
8
10
12
14
16

(b)

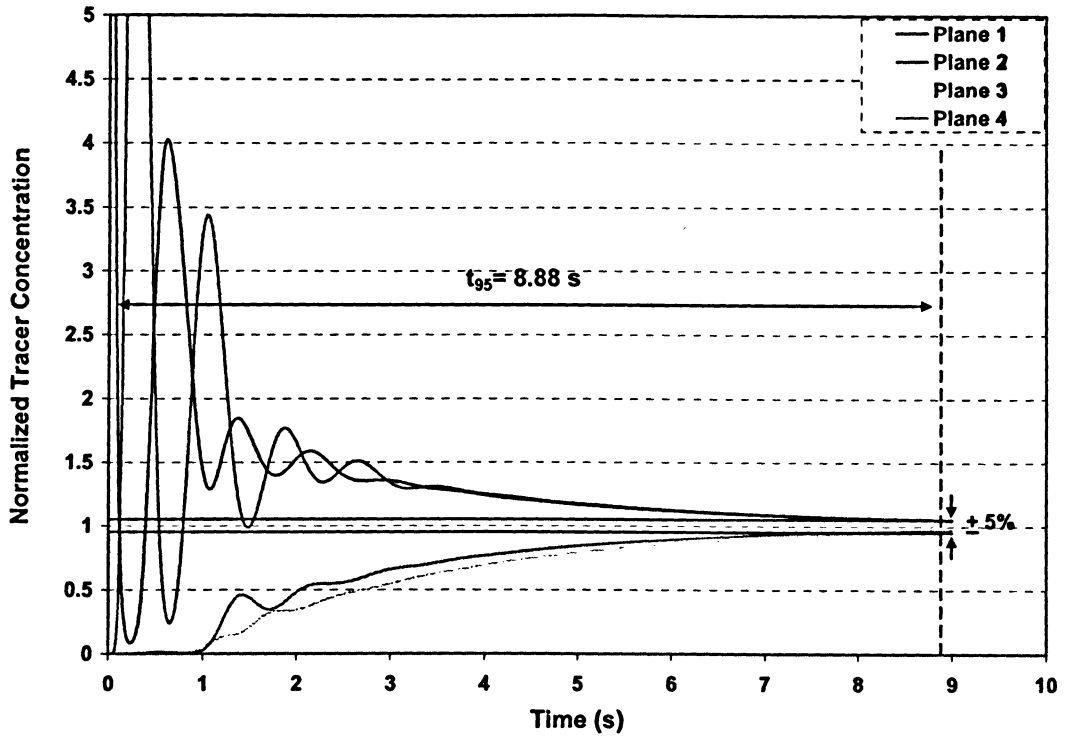

(c)

Fig. 5.16. Comparison of dimensionless tracer concentration vs. time obtained using different number of probes for 1.0% xanthan solution agitated at 282 rpm using 0.01s as a time step (a) 4 points: (point 1: -0.01, 0.13, 0.295; point 2: 0.07,-0.07, 0.21; point 3: 0.03, -0.11, 0.125; and point 4: 0.09, 0.09, 0.04); (b) 10 points: (point 1: 0.07, -0.07, 0.295; point 2: 0.19, 0.03, 0.295; point 3: -0.15, 0.07, 0.21; point 4: 0.01,-0.17, 0.21; point 5: 0.11, 0.07, 0.125; point 6: -0.15, -0.11, 0.125; point7: 0.01, 0.01, 0.04; point 8: -0.03, 0.19, 0.04; point at top: -0.09, 0.09, 0.37 and point at bottom -0.03, -0.15, 0.02); and (c) 4 horizontal planes (Plane 1: z=0.295m; Plane 2: z= 0.21m; Plane 3: z=0.125m; and Plane 4: z=0.04m).

Table 5.4. Comparison of mixing time obtained using different number of probes for 1.0% xanthan solution (CFD results).

	Mixing time t_{95} (s)		
	4 point probes	10 point probes	4 planes
282 rpm	8.95	8.96	8.88

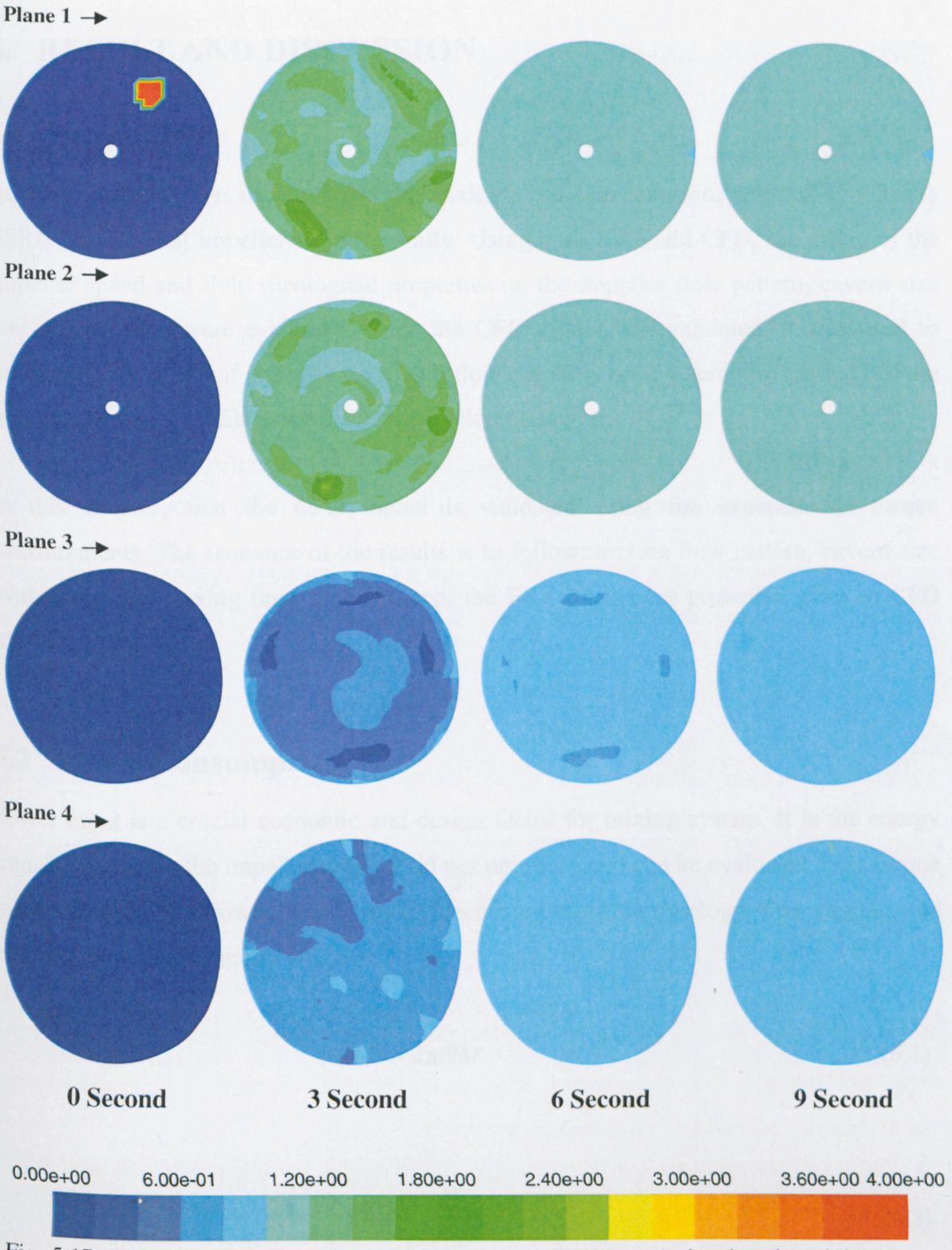

Fig. 5.17. Sequence of CFD contours (based on normalized tracer) showing the mixing process for 1.0% xanthan solution agitated at 282 rpm (Plane 1: z=0.295m; Plane 2: z= 0.21m; Plane 3: z=0.125m; and Plane 4: z=0.04m).

6. RESULT AND DISCUSSION

6.1 Introduction

In this study, ERT was used to study the mixing of xanthan solutions agitated by a Scaba 6SRGT as a radial impeller experimentally. Using both ERT and CFD, the effect of the impeller speed and fluid rheological properties on the impeller flow pattern, cavern size and mixing time were evaluated. Once the CFD model was validated, it was used to investigate the effect of impeller speed and fluid rheology on the pumping capacity of the impeller, velocity profiles, and discharged velocity angles.

In this chapter, first the CFD model is validated using the experimental torque measurements. The sequence of the results is as follow: mixing flow pattern, cavern size evaluation, and mixing time. In each step, the ERT results are presented prior to CFD results.

6.2 Power Consumption

Power input is a crucial economic and design factor for mixing system. It is the energy transformed from the impeller to the fluid per unit time and can be evaluated from torque measurements. The power consumption depends on the fluid rheology, flow regime, and tank and impeller geometry.

$$P = 2\pi NM \tag{6.1}$$

$$P_o = \frac{P}{\rho N^3 D^5} \tag{6.2}$$

where M, N, ρ, P_o, and D are torque, rotational speed, fluid density, power number, and impeller diameter respectively.

According to Metzener and Otto approach (Metzener and Otto, 1957), the effective average shear rate can be related to the impeller speed by:

$$\dot{\gamma}_{av} = k_S N \tag{6.3}$$

where k_s is a weak function of impeller type. Since the exact value of k_s is not known for Scaba impeller, a value of 11.5, found for disc turbines, was taken (Calderbankand Moo-young, 1959). For Herschel-Bulkley type fluid, with:

$$\eta = \frac{\tau}{\dot{\gamma}_{av}} = \frac{\tau}{k_S N} \tag{6.4}$$

The Reynolds number is defined as:

$$\mathrm{Re} = \frac{k_S N^2 D^2 \rho}{\left[\tau_y + k(k_S N)^n\right]} \tag{6.5}$$

where η, τ, $\dot{\gamma}_{av}$, N, D, ρ, τ_y, and k and n are non-Newtonian viscosity, shear stress, averaged shear rate, impeller rotational speed, impeller diameter, fluid density, fluid yield stress, and shear rate independent constants respectively.

6.2.1 Experimental Results for Power Measurements

6.2.1.1 Evaluation of the Torque Sensor Precision

The random error of the torque sensor (type 0170/01MS20RAU, Staiger Mohilo, Germany), caused by electronic fluctuations, mechanical play, and friction can be defined using standard deviation (eq. (6.6)):

$$\sigma = \sqrt{\frac{1}{N}\sum_{i=1}^{N}(M_i - \overline{M})^2} \tag{6.6}$$

where N is the number of measurements, and M is the torque variable and $\overline{M}$ is the mean value of the torque measurements. The spread of the torque about the mean value is indicated by the error bar (using standard deviation as the error amount) as shown in Fig. 6.1. It is clear that the errors are small enough ($\sigma < 1.5\%$) to accept that the torque measurements are error independent.

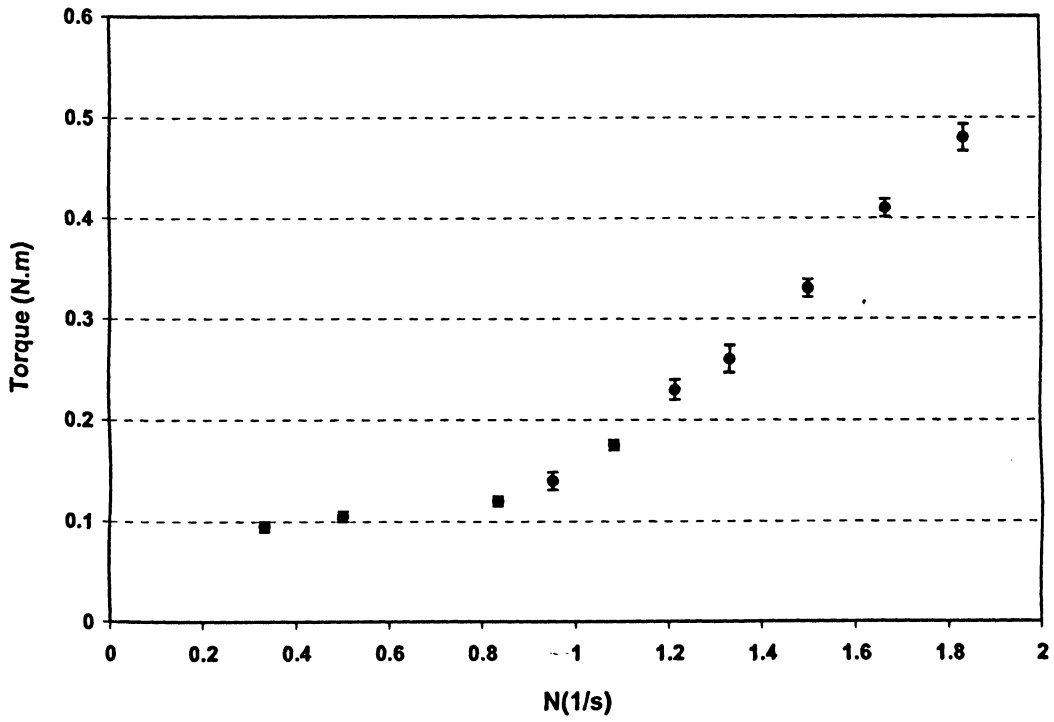

Fig. 6.1. Torque measurements for 1.5% xanthan solution agitated by Scaba 6SRGT.

Fig. 6.2 presents the power number (P_o) plotted versus the Reynolds number (Re) for the Scaba impeller in three xanthan gum solutions.

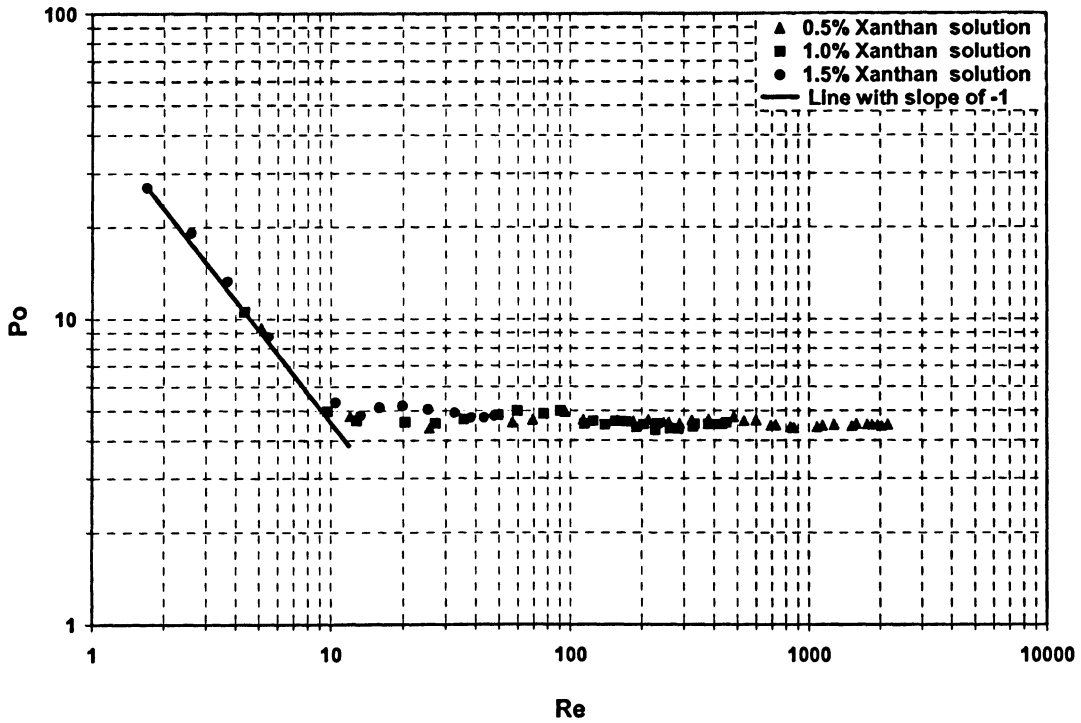

Fig. 6.2. Experiment results for power number versus Reynolds number for xanthan solutions agitated by a Scaba impeller.

The trend in the power number curves for all concentrations are similar to the typical "power curve" such as those reported by Galindo and Nienow (1993) for the Scaba 6SRGT impeller. At Reynolds Number (Re) below 10, $P_o \propto \mathrm{Re}^{-1}$, which is in good agreement with literature (Galindo and Nienow, 1992 and 1993; Amanullah, 1998). It can be seen that lines with slopes of -1 fit the low Re data quite well. Therefore, we can say that in laminar flows, P_oRe is constant.

In laminar regime, the highest values of power number were found for the most concentrated xanthan solution (1.5%). The power number was up to 75% higher between the lowest and the highest xanthan concentrations. Thus, for a given Re, the higher levels of viscoplasticity (Table 4.1) correlate with the higher P_o values. In the transitional

regime, power number changes slightly with *Re* whereas in turbulent flows, P_o is almost constant. It can be seen that no effect of the fluid concentration on the turbulent power number could be determined. At Reynolds in excess of 200, *Po* remains practically constant at a value of 4.5. This value is in good agreement with 4.4 obtained for this impeller (Paul *et al.*, 2004) and is different with that obtained (1.8) by Galindo and Nienow (1993). This large difference is mainly due to the different concave blade shapes (see Fig. 6.3). In this study, a concave-blade impeller with 1/2 pipe blades (Fig. 6.3 (a)) were used while Galindo and Nienow (1993) used a hollow-blade impeller with the asymmetric parabolic blade shape (Fig. 6.3 (b)), which has smaller projected vertical area.

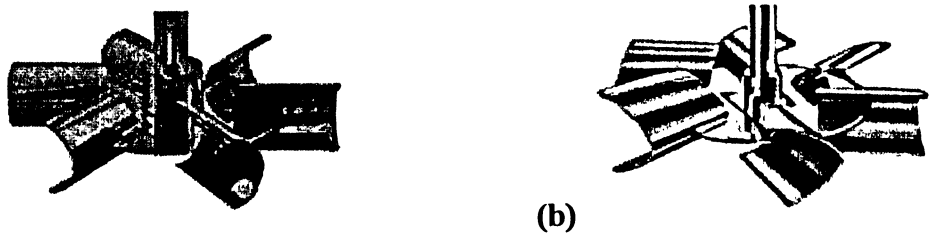

(a) (b)

Fig. 6.3. Two hollow-blade impellers with a) 1/2 pipe blades, and b) asymmetric parabolic blades.

6.2.2 CFD Results for Power Measurements

Fig. 6.4 shows the power number (P_o) versus Reynolds number (*Re*) plot, which has two distinct zones. The power number data lie along the line with slope -1 at low *Re* number (Re<10). As shown here, at Re> 50, the power data tend to converge to about 4.7.

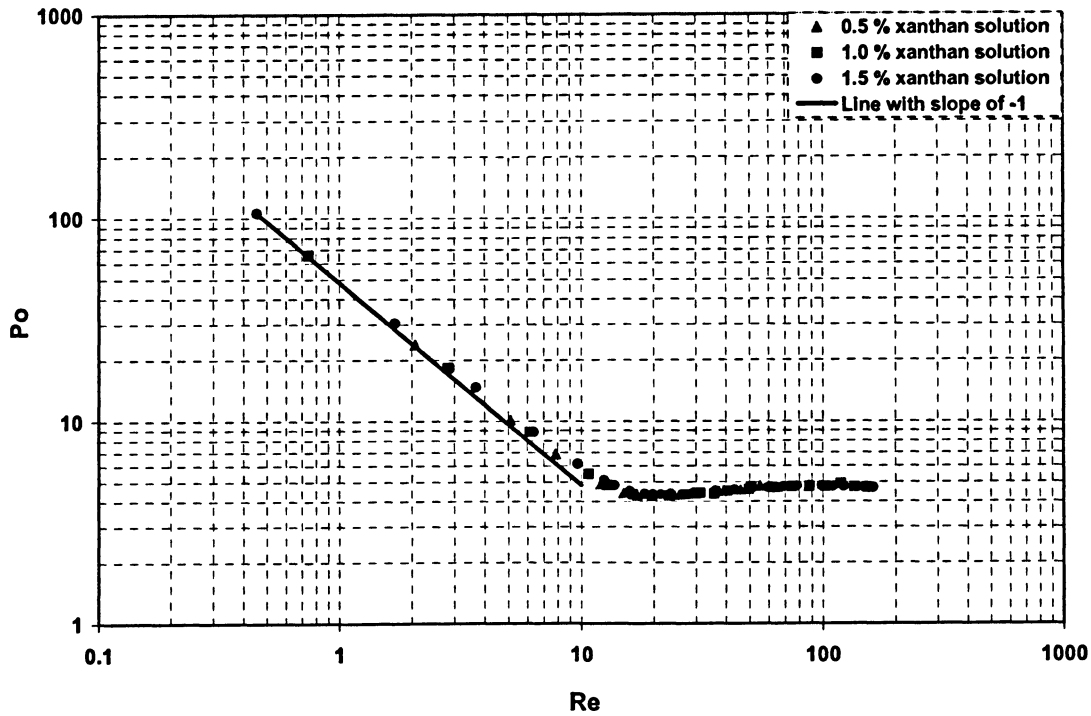

Fig. 6.4. CFD results for power number versus Reynolds number for xanthan solutions agitated by the Scaba impeller.

6.2.3 Comparison between CFD and Experiment Results

Fig. 6.5 to Fig. 6.7 show the comparison between the CFD and experimental power consumption. For lower impeller Reynolds numbers, the calculated power numbers by CFD match the experimentally determined values very well for all three concentrations. When the rotational speed is ramped up; it is also shown a rise of the power consumption which is however more pronounced in the case of the experimental data. The reasons may be a result of a laminar-flow model being employed in a transitional-flow regime for CFD, and/or inadequate grid resolution not capturing all of the small local recirculation zones and swirls near the blade tip. The Scaba 6SRGT impeller, because of its hollow-blades, creates more of this local swirling.

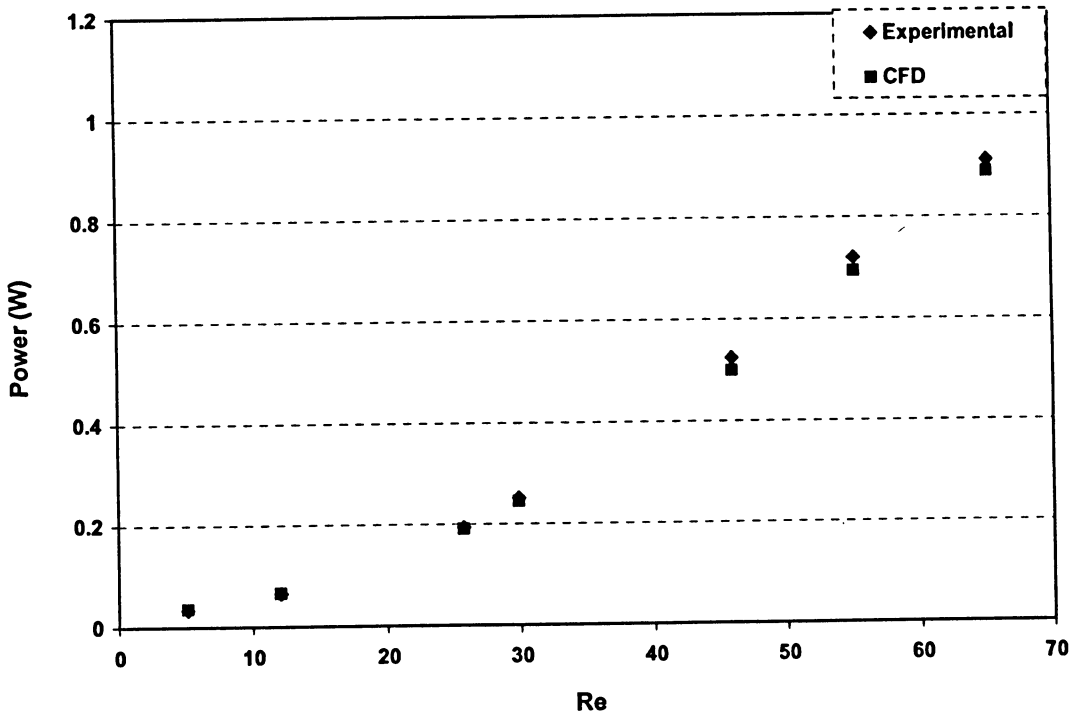

Fig. 6.5. CFD and experimental power consumption versus Reynolds number for 0.5% xanthan solution agitated by the Scaba 6SRGT impeller.

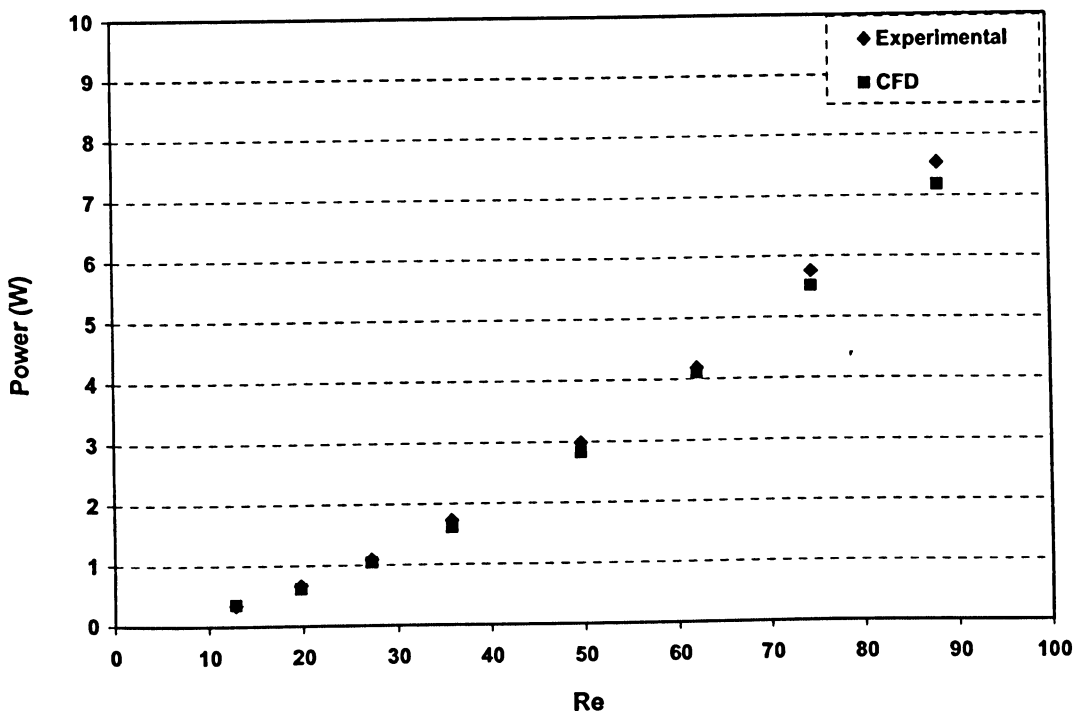

Fig. 6.6. CFD and experimental power consumption versus Reynolds number for 1.0% xanthan solution agitated by the Scaba 6SRGT impeller.

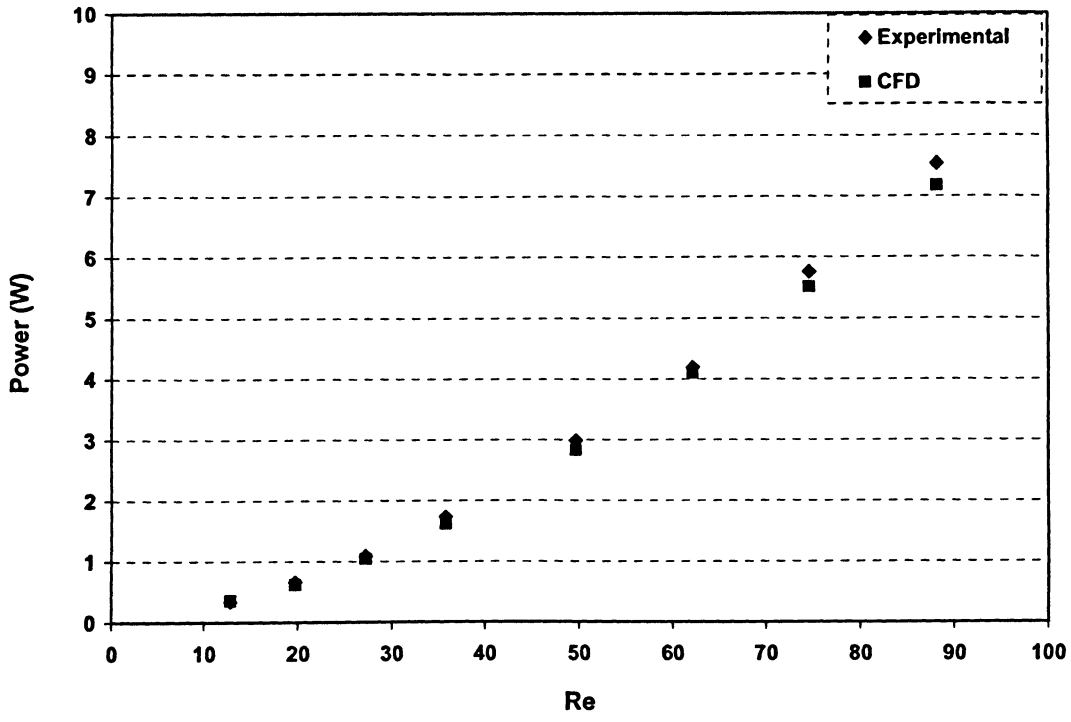

Fig. 6.7. CFD and experimental power consumption versus Reynolds number for 1.5% xanthan solution agitated by the Scaba 6SRGT impeller.

6.3 Estimation of Flow Shear Rate Coefficient (K_S) by CFD

Shear rate of the flow in a mixing vessel is an important parameter in industry (Wu *et al.*, 2006). Metzner and Otto method assumes that the average shear rate in the mixing tank is linearly related to the impeller speed (eq. (6.3)). Therefore, the constant of this relation, K_S, is a function of the impeller geometry but not the fluid rheology.

Fig. 6.8 shows local average shear rate profile near the Scaba blade for all three xanthan concentrations in laminar regime. The average shear rate was calculated from a converged CFD solution using the area-weighted average over an area surrounding the impeller with a height equal to 0.13m ($\frac{z}{H} = 0.325$) and a diameter equal to 0.25m ($\frac{2r}{T} = 0.625$).

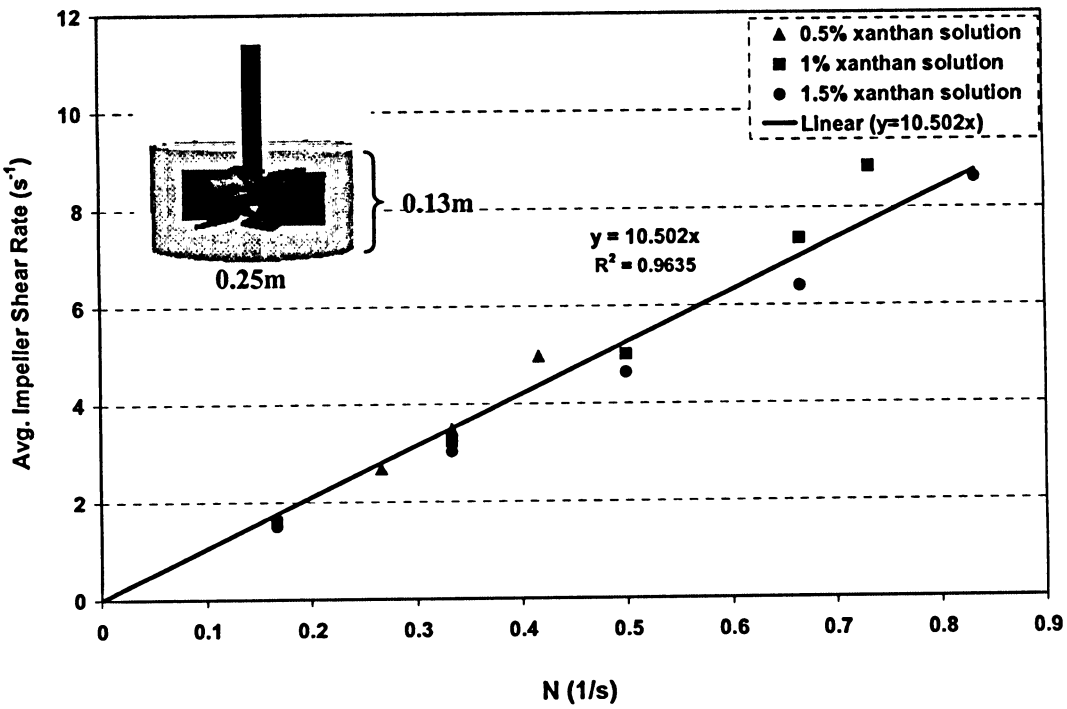

Fig. 6.8. Average shear rate (CFD) versus impeller speed (s^{-1})

This figure indicates that the relation between near-impeller average shear rate and impeller rotational speed (s^{-1}) is linear for the Scaba impeller. The results suggest that the K_S value for Scaba impeller as 10.5, which is lower than 11.5 from experimental data for disc turbine (Calderbank and Moo-Young, 1959) but the agreement, is reasonable with a relative error of 8.7%.

Torrez and Andre (1998) performed both CFD and experimental studies on the velocity profiles of a Rushton turbine mixing Newtonian and shear thinning fluids. Their experimental data suggested value of 12.1, while their CFD result showed a lower value of 9.6.

6.4 Pumping and Circulation Flow Rates

Another important concept for any agitation system is the pumping capacity of the impeller. In order to assess the pumping capacity of the impeller at different operating conditions, the flow number was evaluated. The flow number is calculated from the

integral of axial velocities on a plane below impeller (for axial impellers) or from the integral of radial velocity on a plane around impeller (for radial impeller).

The volumetric flow rate of fluid (Q_r) passing through an area surrounding the impeller with a height equal to that of the impeller blade and a diameter equal to impeller diameter at blade tip was calculated by CFD. The impeller pumping capacity and flow number were defined by (Lamberto, 1999):

$$Pumping\ Capacity = Q_r = \pi D \int_{blade} V_r dz \tag{6.7}$$

$$N_Q = \frac{Q_r}{ND^3} \tag{6.8}$$

Fig. 6.10 shows the CFD measurements of flow number (N_Q) for three xanthan solutions (0.5, 1, and 1.5 %) agitated by the Scaba 6SRGT impeller in different impeller speeds. It is clear that the higher the xanthan solution concentration, the lower is the flow number. This Figure indicates that viscoplasticity generally tends to decrease flow number (N_Q), as expected, in fact, it reduces the amount of flow being pump by the agitator, and therefore N_Q reduces with decreasing impeller speed, attaining values close to 0.06 at very low impeller speeds.

Fig. 6.11 shows that the pumping capacity goes through a maximum moving from the shaft to the wall of the tank. The position of this maximum moves outwards radially as the impeller speed is increased. This trend is in good agreement with literature (Lamberto, 1999).

The circulation flow rate in the tank is the total volumetric turnover rate occurring in the tank. As the impeller is radial flow, the circulation flow defined as the flow rate of fluid returning to the impeller in the axial direction above and below the impeller (see Fig. 6.9). In fact, the volumetric flow rates of fluid (Q_c) passing through two horizontal planes

above and below the impeller with diameter equal to the impeller diameter were calculated by CFD for 1.5% xanthan solution. The circulation flow rate can be given by the sum of the flow rate returning to the impeller in the axial direction (above and below the impeller).

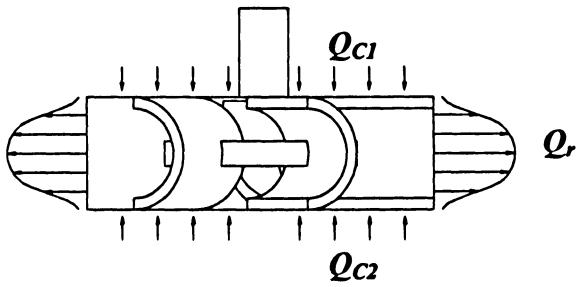

$$Q_r = Q_{C1} + Q_{C2}$$

Fig. 6.9. Scaba 6SRGT Impeller control volume

Fig. 6.12 shows the CFD measurements of the flow number (N_Q) and the circulation number (N_C) for 1.5% xanthan solutions agitated by Scaba 6SRGT in different impeller speeds. This figure indicates that the flow rate discharged from the impeller in radial direction is relatively equal (with a relative error <12%) to the flow returned back to the impeller in axial directions.

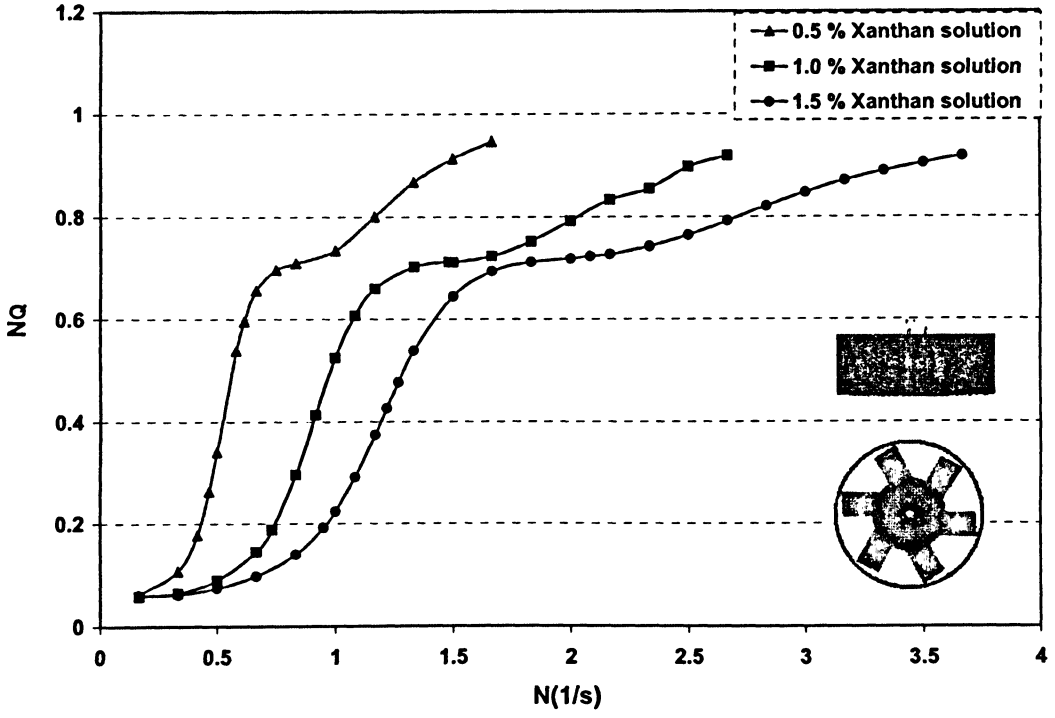

Fig. 6.10. CFD results for flow number for xanthan solutions agitated by a Scaba impeller.

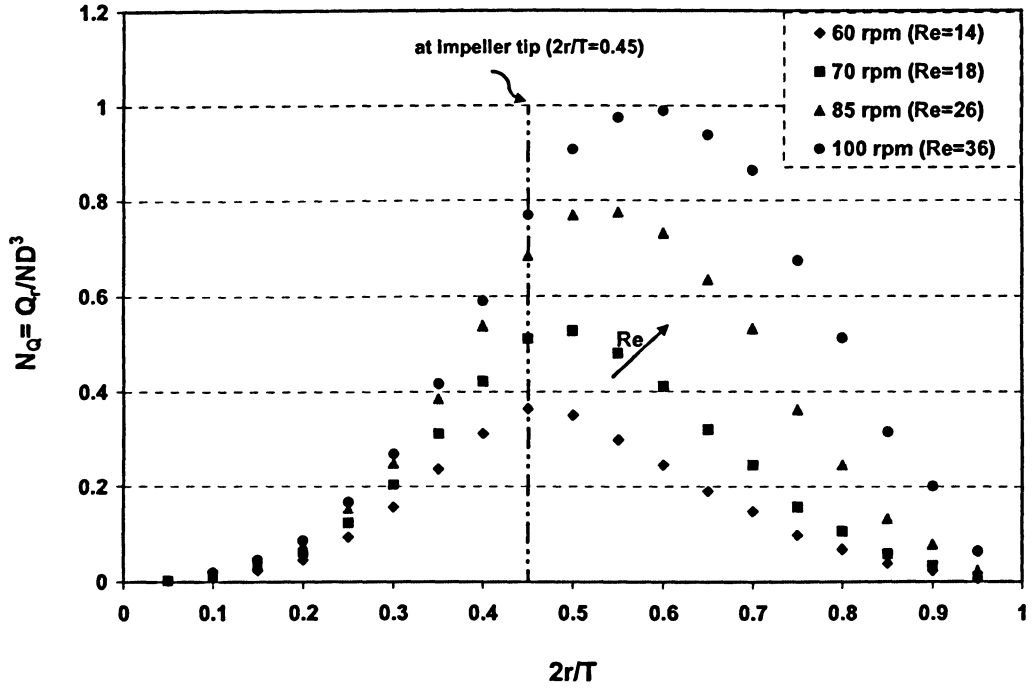

Fig. 6.11. Radial profile of impeller flow number as a function of Re number for 1.5% xanthan concentration.

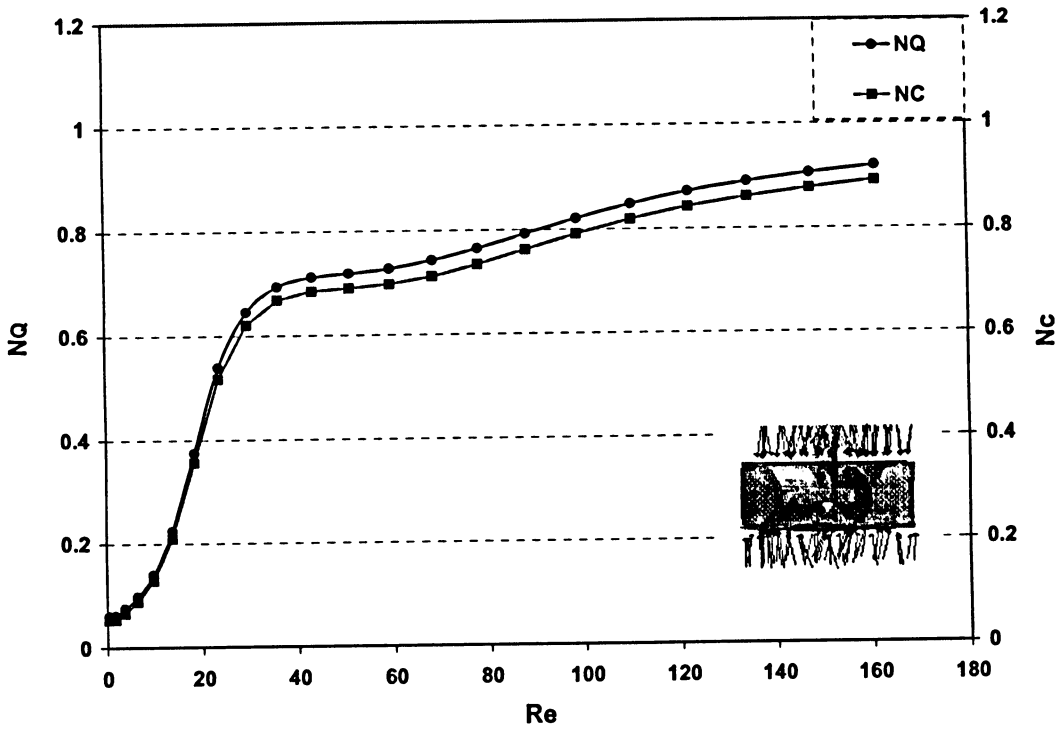

Fig. 6.12. Comparison of the flow number and the circulation number for 1.5% xanthan solution agitated by a Scaba impeller.

6.5 General View of the Flow Pattern

The mixing performance is a function of the flow pattern generated by the impeller. Parameters such as impeller geometry, impeller rotational speed and liquid viscosity have effects on the flow pattern generated by the impeller (Paul *et. al.*, 2004). Since one impeller has been used in this study, the former parameter, i.e. impeller geometry has not been evaluated.

6.5.1 ERT Results for Flow Pattern

One of the main advantages of ERT is to display images that allow the user to study the distribution of electrical conductivity across the measured volume, useful to control and monitor the process. Therefore, ERT can visualize key features of a mixing process while optical and visual access is not possible for example, ERT can show the flow pattern of a non-Newtonian fluid, which is opaque.

6.5.1.1 Effect of Baffles on the Flow Pattern

When a fluid is stirred in a vessel without baffles, an air-core vortex is formed around the shaft due to the swirling motion of fluid induced by the impeller. Installing baffles destroys the vortices and forms a flow pattern that leads to good mixing in the tank. On the other hand, in high viscous fluid agitated at low impeller speed, the presence of baffles in the tank may cause poor mixing around the baffles especially in regions far from impeller (the bottom of the tank and the surface of the fluid).

Fig. 6.13 shows effect of the baffles on mixing profiles using reconstructed tomograms after injection of the tracer. Fig. 6.13a shows a low conductivity region behind the baffles as there was no motion or no tracer (poor mixing). This phenomenon was observed more in the plane 4 (close to the tank bottom) where there was not enough motion especially in the flow direction behind the baffles. On the other hand, Fig. 6.13b shows another tomogram in which the tracer was trapped behind the baffles, i.e. a high conductivity region was observed there. This phenomenon was observed more in plane 1, where the tracer was injected and motion was not enough to disperse the tracer in whole tank. As these low- and high-conductivity regions did not change during the experiment, it seemed reasonable to assume that these regions were due to dead zones behind the baffles.

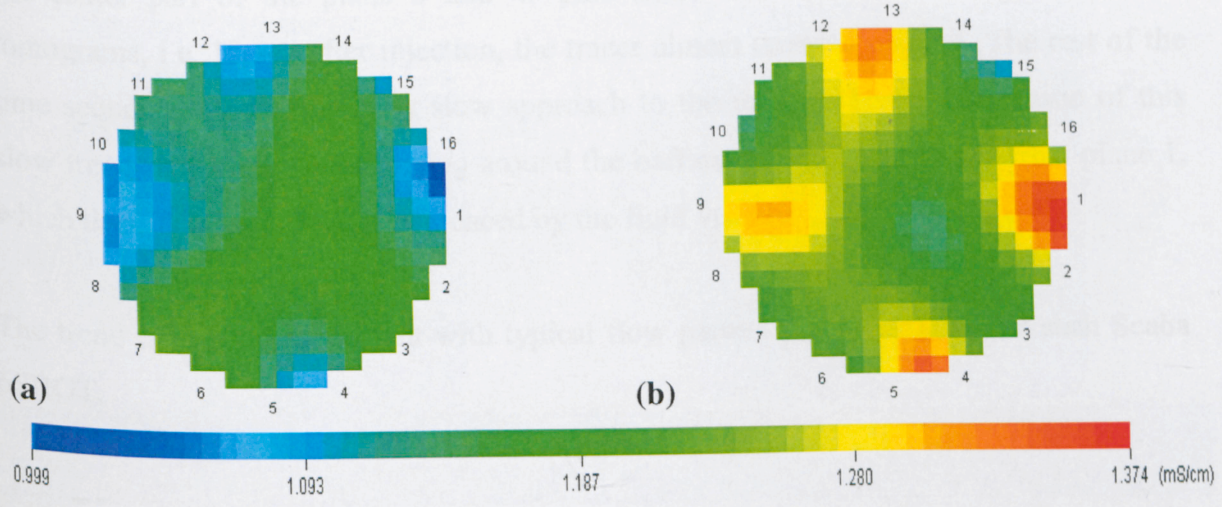

Fig. 6.13. Effect of the baffles on the flow in the stirred tank. (Note: The baffles are located between electrode 1and16, 4and 5, 8and9, and 12and13).

6.5.1.2 Radial Impeller Flow Pattern

ERT has been shown to be an efficient technique to visualize the flow pattern inside a mixing tank (Holden *et al.*, 1998). Fig. 6.14 illustrates the corresponding tomograms obtained when the 50ml of brine solution was injected into 1 % xanthan solution (on plane 1) agitated in 250 rpm.

After 2s, the tracer "cloud" was observed on the plane 1 and partially plane 2. After 3s, it could be easily seen that the tracer was being swept in a clockwise direction because of strong swirl flow around the impeller. This behaviour was more prominent in plane 1 where the tracer injected, and plane 2, which was exactly above the impeller. After a further 2 s, the brine "cloud" enlarged and reached the impeller and the brine was being discharged out toward the tank walls by the strong radial outflow. The tracer was spited downwards and upwards in a narrow region near the wall and reached plane 3 and partially plane 4 in its downward flow. The more concentrated brine could be observed mainly in plane 1 and 2, confirming the effect of injection position in mixing performance. After a further 5s, the tracer covered the entire plane 3 and there was no low conductivity in this plane. This step also shows that the tracer was derived back to the impeller in the central part of the tank as relatively high conductivity region indicated in the center part of the plane 3 and 4. This trend was continued as shown in next tomograms, i.e. 12 sec after injection, the tracer almost covered plane 4. The rest of the time sequence shows relatively slow approach to the uniform level. The reason of this slow trend may be the poor mixing around the baffles in plane 4 and somewhat plane 1, which these dead zones were influenced by the fluid viscosity.

The trend is in good agreement with typical flow pattern for radial impeller such Scaba 6SRGT.

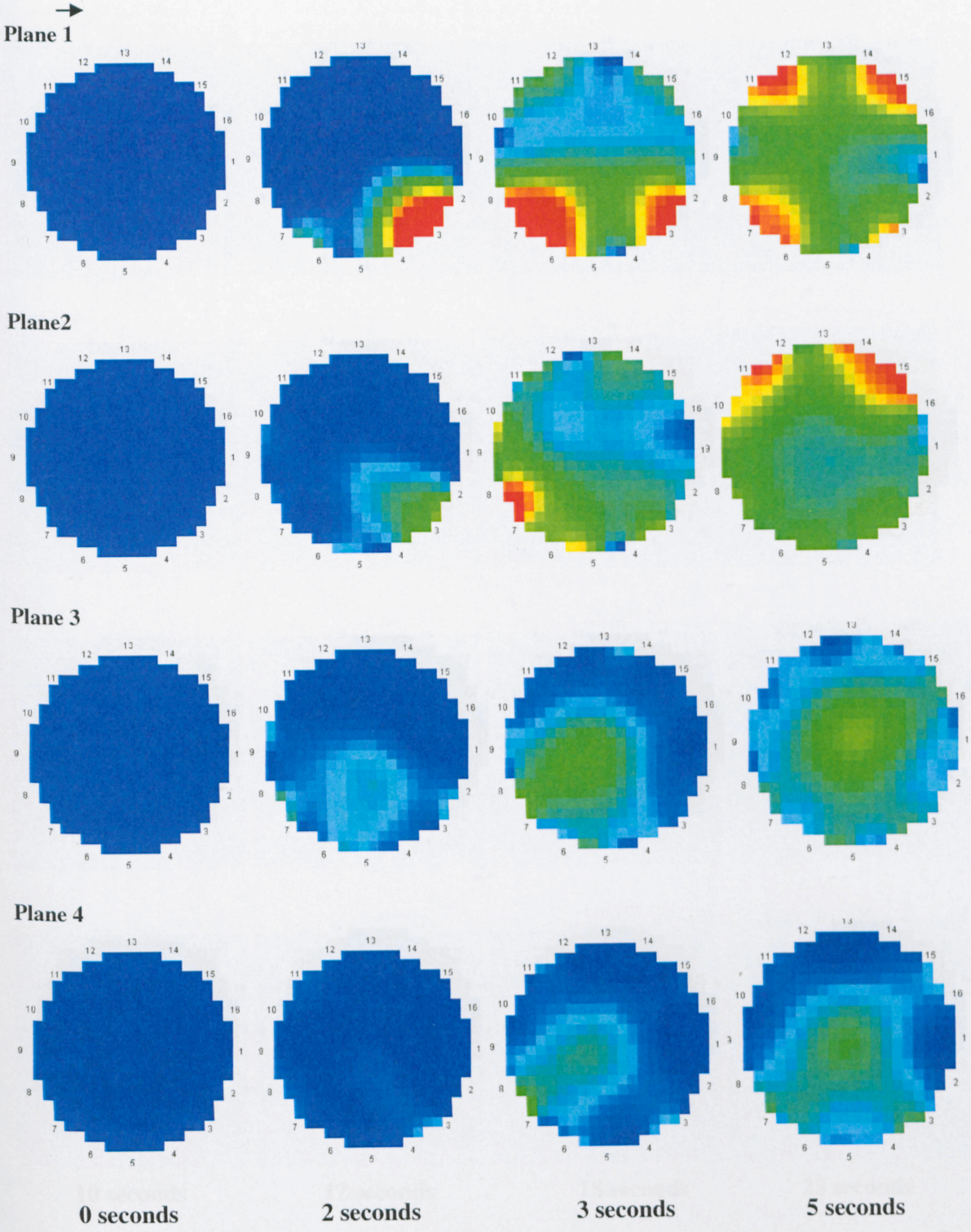
Plane 1
Plane2
Plane 3
Plane 4
0 seconds
2 seconds
3 seconds
5 seconds

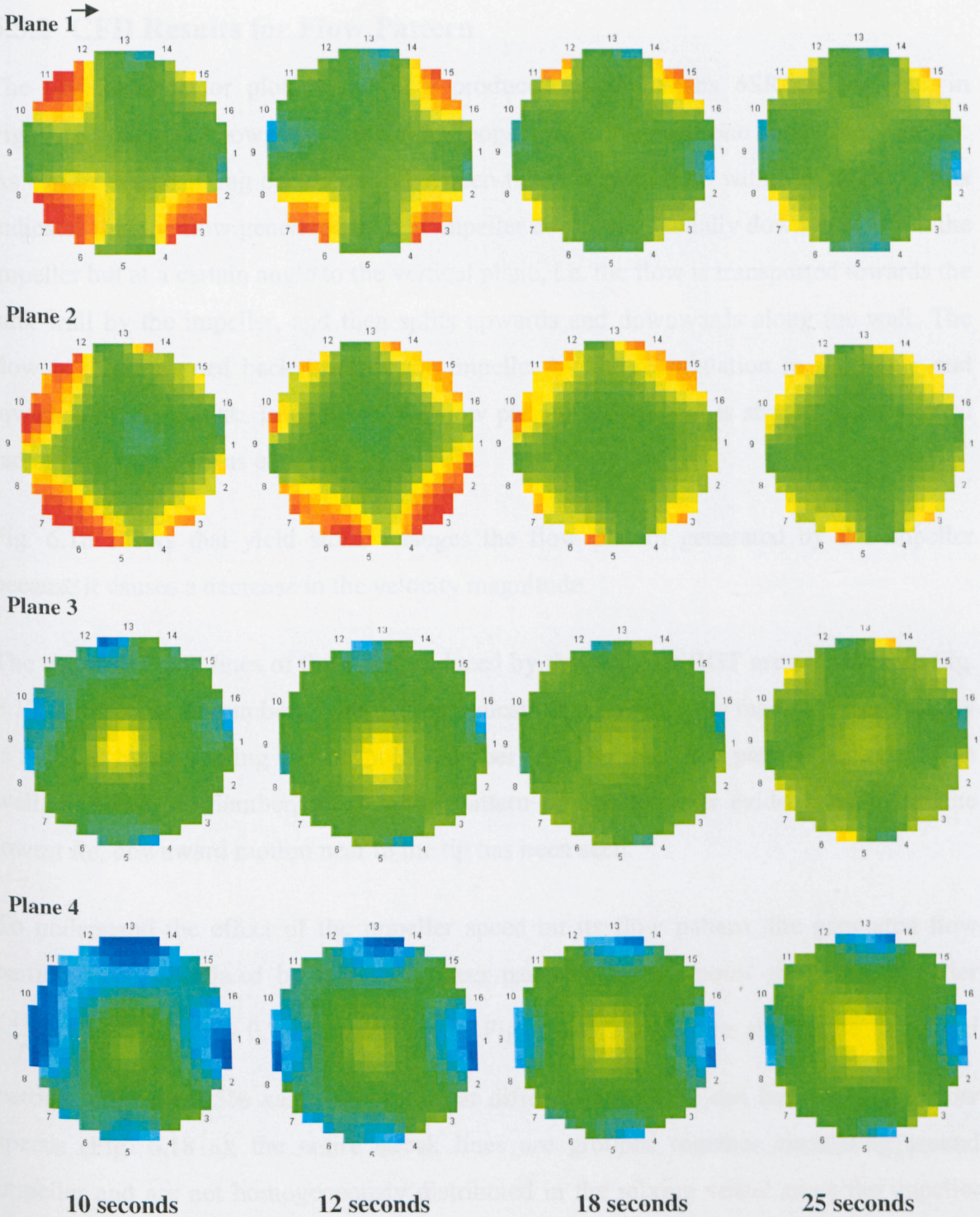

Fig. 6.14. Tomograms following an injection of brine solution into the 1.0% xanthan solution agitated by the Scaba 6SRGT impeller at 250 rpm.

6.5.2 CFD Results for Flow Pattern

The simulated vector plot of the flow produced by the Scaba 6SRGT is shown in Fig. 6.15. The plot shows two circulating loops, one below, and one above the impeller. As can be seen, mixing occurs more between the two loops than within each loop. This indicates that the flow generated by this impeller does not go axially down or up from the impeller but at a certain angle to the vertical plane, i.e. the flow is transported towards the tank wall by the impeller, and then splits upwards and downwards along the wall. The flow is then returned back towards the impeller by the recirculation in the upper and lower parts of the tank. In addition, the flow pattern shown here is similar to the typical radial flow impellers as expected.

Fig. 6.16 shows that yield stress changes the flow pattern generated by the impeller because it causes a decrease in the velocity magnitude.

The simulated path lines of the flow produced by the Scaba 6SRGT are presented in Fig. 6.17 at different *Re* numbers. These plots indicate that not only the magnitude of velocity is reduced by decreasing the Reynolds number (*Re*), but the flow pattern is changing as well. For high *Re* number, the familiar pattern of two loops is evident, while for the lowest *Re*, downward motion near to the tip has been seen.

To understand the effect of the impeller speed on its flow pattern, the generated flow particle lines, simulated by releasing tracer particles from a point above the impeller ($\frac{2r}{T} = 0.66$ and $\frac{z}{H} = 0.73$) are shown in Fig. 6.18. This figure shows the simulated particle lines for 1.5% xanthan solution at different speeds. It can be seen that in low speeds (Fig. 6.18 a), the entire streak lines are grouped together circulating around impeller and are not homogeneously distributed in the mixing vessel since the impeller speed is not adequate. As impeller rotational speed increases, this problem can be overcome. This suggests that possible increase in the impeller rotational speed might improve the extent of mixing. Thus, CFD models can provide very useful information about the mixing behaviour of stirred vessels and can be used as an evaluation tool.

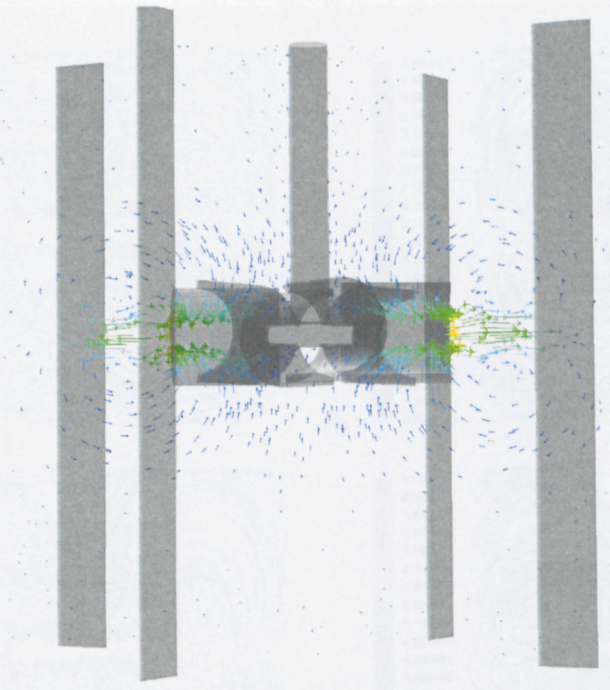

Fig. 6.15. Vector plot in a vertical cross-sectional plane aligned with the impeller blades for 1.0% xanthan solution agitated by the Scaba 6SRGT impeller at 80 rpm.

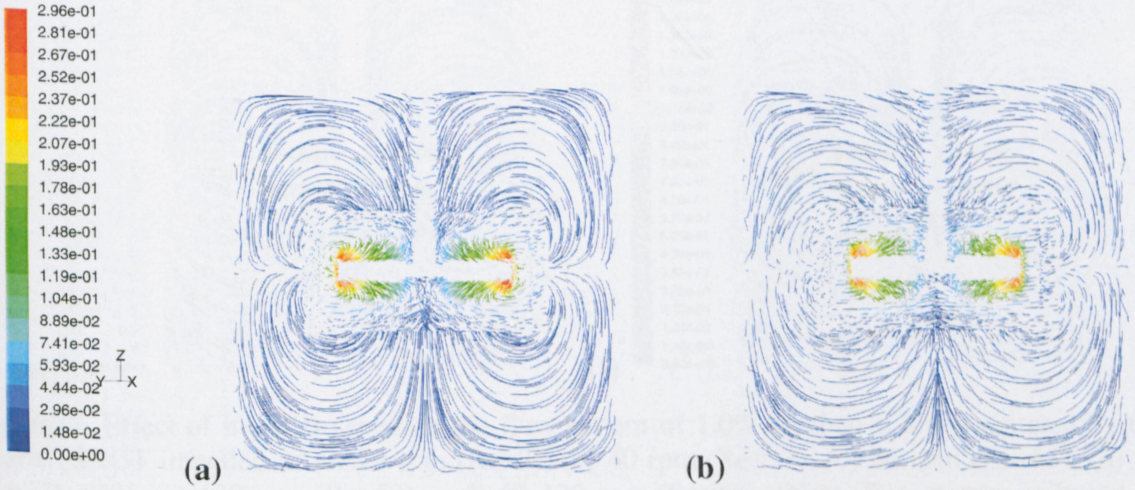

Fig. 6.16.Effect of viscoplasticity on the flow pattern generated by the Scaba 6SRGT impeller for; (a) 0.5% xanthan solution, and (b) 1.5% xanthan solution at 30 rpm. (Note: flow pattern is based on velocity magnitude, m/s).

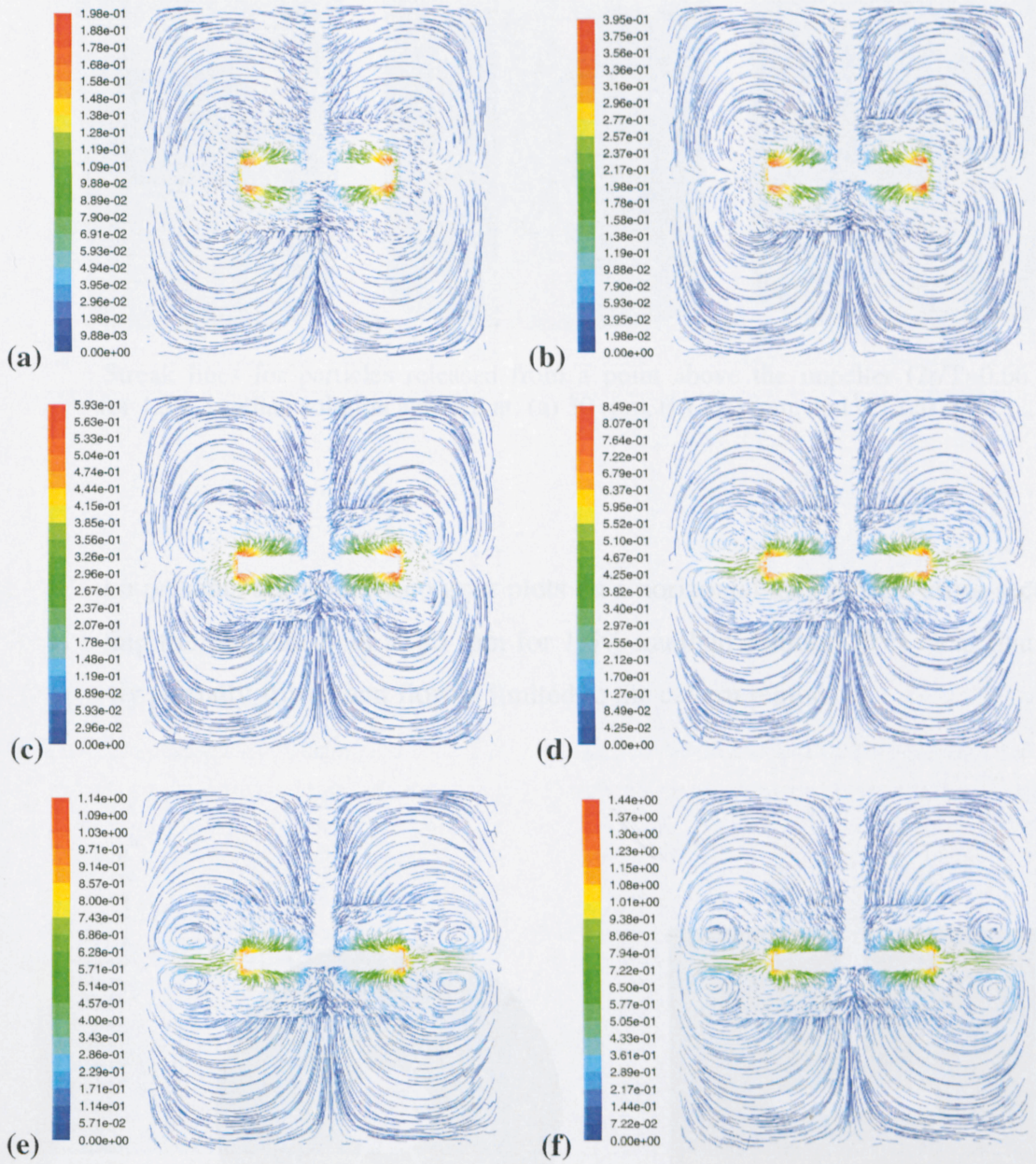

Fig. 6.17. Effect of impeller speed on the flow pattern of 1.0% xanthan solution agitated by the Scaba 6SRGT impeller at; (a) 20 rpm (Re≈3), (b) 40 rpm (Re≈11), (c) 60 rpm (Re≈23), (d) 80 rpm (Re≈40), (e) 100 rpm (Re≈62), and (f) 120 rpm (Re≈88). (Note: flow pattern is based on velocity magnitude, m/s).

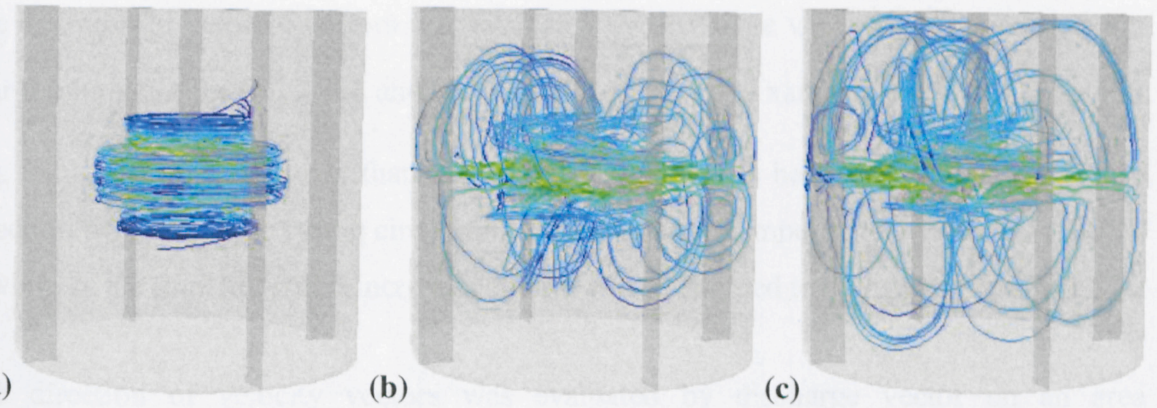

Fig. 6.18. Streak lines for particles released from a point above the impeller (2r/T=0.66 and z/H=0.73) for 1.5% xanthan solution agitated at: (a) 30 rpm, (b) 170 rpm, and (c) 220 rpm.

Fig. 6.19 *a,b* presents the velocity contour plots on a horizontal and vertical cross-section planes cutting the impeller both at 80 rpm for 1.5% xanthan solution. It is clear that the vessel is only partially stirred and flow is limited to the cavern region.

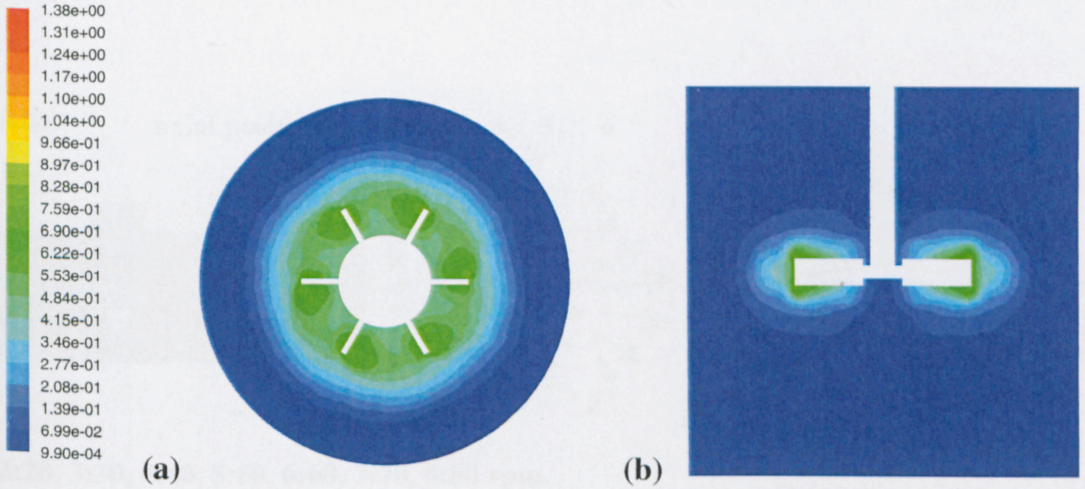

Fig. 6.19. Velocity (m/s) contour plots on: (a) horizontal, and (b) vertical cross-section planes cutting the impeller both at 80 rpm for 1.5% xanthan solution

The direction of velocity vectors was evaluated by discharge vector on an axial position near the impeller tip ($\frac{2r}{T}$ = 0.6 and $\frac{z}{H}$ = 0.3-0.55) for 1.5% xanthan solution is shown in Fig. 6.20. This figure shows that at low speed the flow is being swept in a clockwise direction because of the strong circulating flow around the impeller as shown in Fig. 6.18 a, while as the impeller speed increases, the flow is discharged towards the vessel wall.

The direction of velocity vectors was evaluated by discharge vector on an area surrounding the impeller (height: impeller blade and diameter: impeller diameter) for three concentrations is shown in Fig. 6.21. This figure shows the effect of viscoplasticity and speed on the flow pattern generated by the impeller in terms of discharging velocity vector around the impeller blade tip. In low speeds, all three concentrations show circulation flow around impeller as expected (Fig. 6.18a) as impeller rotational speed increases, flow is discarded radially (velocity vector towards the mixing tank), occurred for 0.5, 1 and 1.5% xanthan solution at 60, 100, and 140 rpm , respectively. This confirms the effect of rheological properties of the solutions on the flow pattern generated by an impeller.

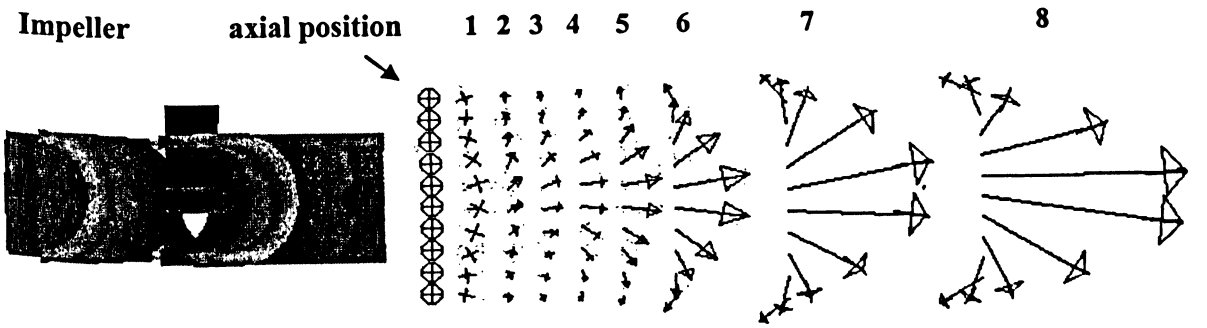

1:10, 2:20, 3:30, 4:40, 5:50, 6:60, 7:70, 8:80 rpm.

Fig. 6.20. Direction of velocity vectors discharged from impeller on an axial position (2r/T=0.6 and z/H=0.3-0.55) for 1.5% xanthan solution.

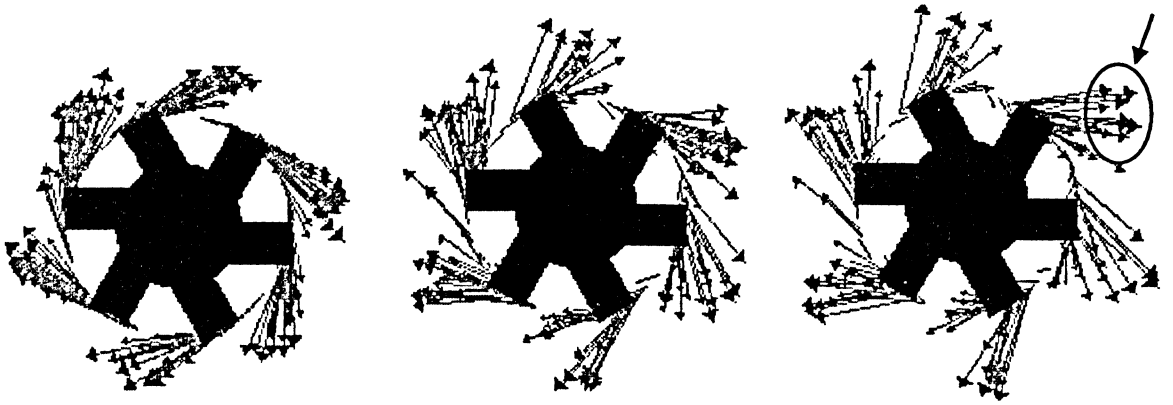

(a) 0.5 % xanthan solution: 20, 40, and 60 rpm

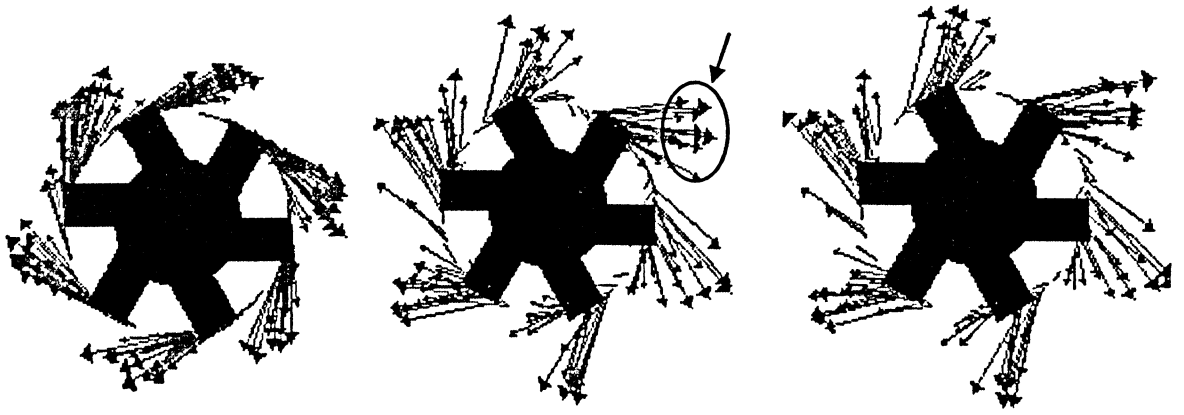

(b) 1 % xanthan solution: 20, 100, and 160 rpm

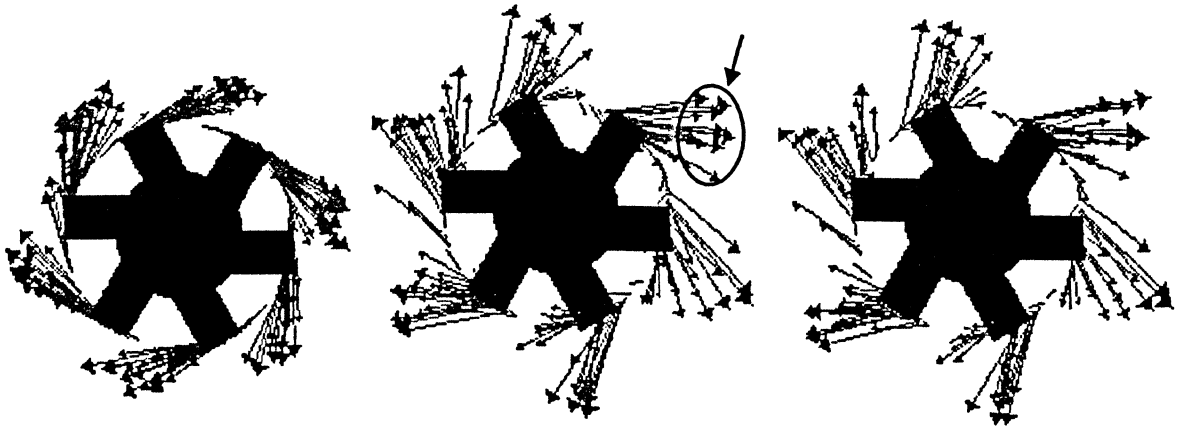

(c) 1.5 % xanthan solution: 20, 140, and 200 rpm

Fig. 6.21. Direction of velocity vectors discharged from impeller for (a) 0.5%, (b) 1.0%, and (c) 1.5% xanthan solution in different speed.

Fig. 6.23- Fig. 6.25 present the axial, radial, and tangential velocities as a function of axial and radial position (see Fig. 6.22), for 1.5 % xanthan solution at *Re*=18.4 (70 rpm). Flow is characterized by the following behaviour:

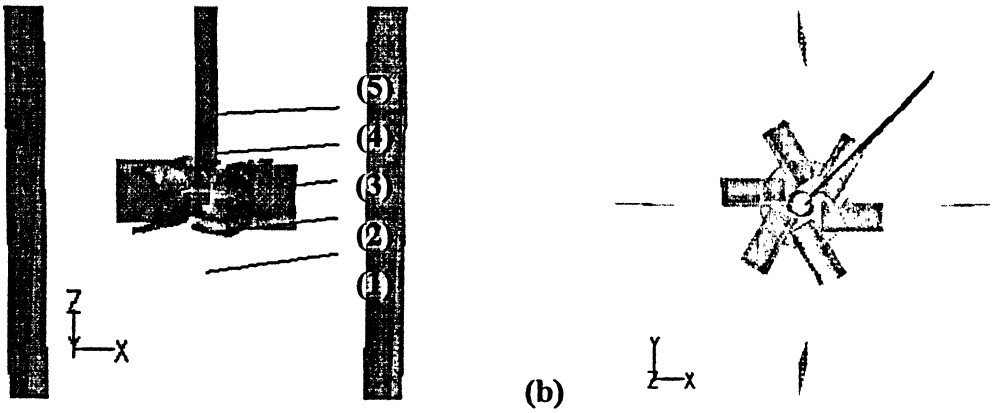

Fig. 6.22. Axial and radial positions r: (0-0.09), θ=45 deg and (1): z=0.13m (z/H=0.325), (2): z=0.17m (z/H= 0.425), (3): z=0.21m (z/H=0.525), (4):z=0.25m (z/H=0.625), and (5):z=0.29m (z/H= 0.725) in (a): Z-X plane and (b): X-Y plane.

As can be seen (Fig. 6.23), there is a very small axial flow (equal to zero) outwards from the center part of the impeller (z/H=0.525), as expected since the impeller is a radial-flow one. Above and bellow the impeller, there is a small axial flow reaching a maximum value above and bellow blades at a dimensionless radius of 0.293. At these points, the flow is downward and upwards into the impeller. The discharge stream turns upwards and downwards before reaching the vessel walls with respect to the two loops and then downwards and upwards respectively before reaching the liquid surface and tank bottom as can be seen in Fig. 6.23. The maximum axial velocity is observed above and below the impeller for each loop giving a value of about 0.1 U_{tip} at about $\frac{2r}{T} = 0.293$.

Fig. 6.24 shows the radial velocity as a function of axial and radial position. There is a radial flow outwards from the center part of impeller (discharge stream), which vanishes with increasing radial distance. It is clear that the maximum radial velocity occurs at z/H= 0.525, which is the centerline (refers to Fig. 6.22). The flow from the lower part of the blades is slightly greater than that from the upper part. Above and below the impeller,

there is a small radial flow inwards (negative magnitude) as expecting. This figure shows that the flow is almost symmetrical above and below the Scaba impeller, which is completely in agreement with the flow pattern generate by this impeller.

Fig. 6.25 shows the tangential velocity around the impeller as a function of radial and axial position. As can be observed the maximum tangential velocity in centerline (z/H=0.525) occurs before impeller tip, i.e. between two blades (the distance between impeller hub and blades tip). The velocity in this direction is much greater than either the radial and axial velocity, reaching almost the impeller tip speed at the blade tip on the centerline of the impeller blades (2r/T=0.45, z/H=0.525). This result is in good agreement with the assumption in the Elson's model or cylindrical model (eq. (2.23)) that the flow in the cavern is mainly tangential and was justified by experimental results for Rushton turbine (radial flow impeller) by Moore *et al.* (1995).

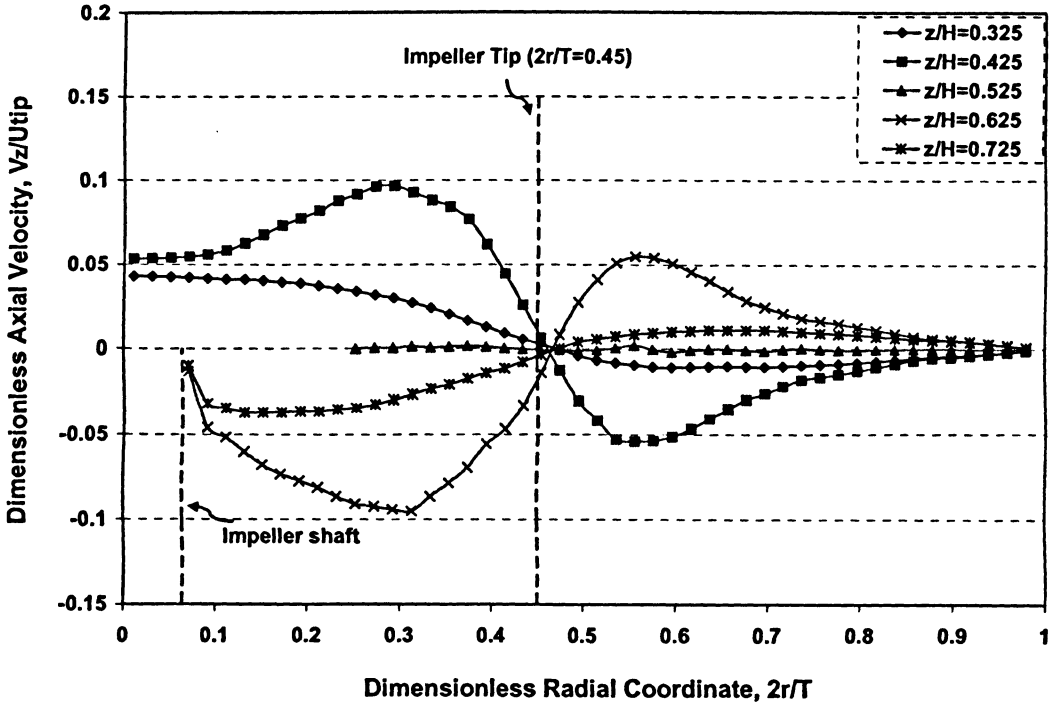

Fig. 6.23. Axial and radial distribution of axial velocity for 1.5 % xanthan solution agitated at 70 rpm (Re=18.4).

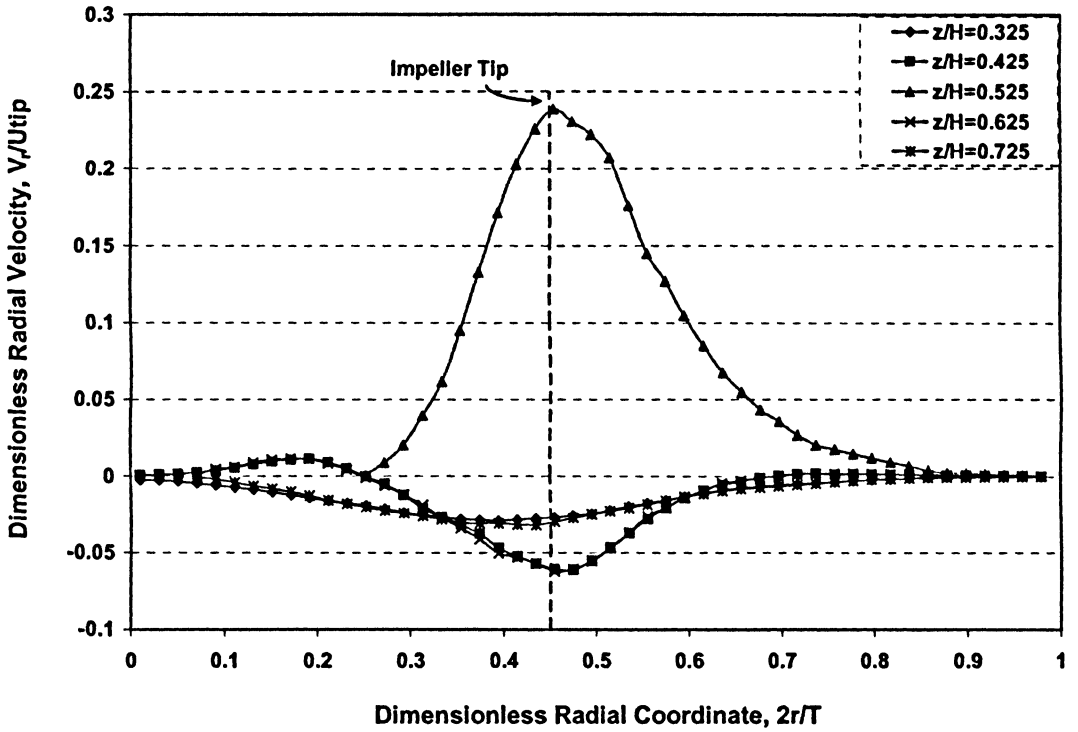

Fig. 6.24. Axial and radial distribution of radial velocity for 1.5 % xanthan solution agitated at 70 rpm (Re=18.4).

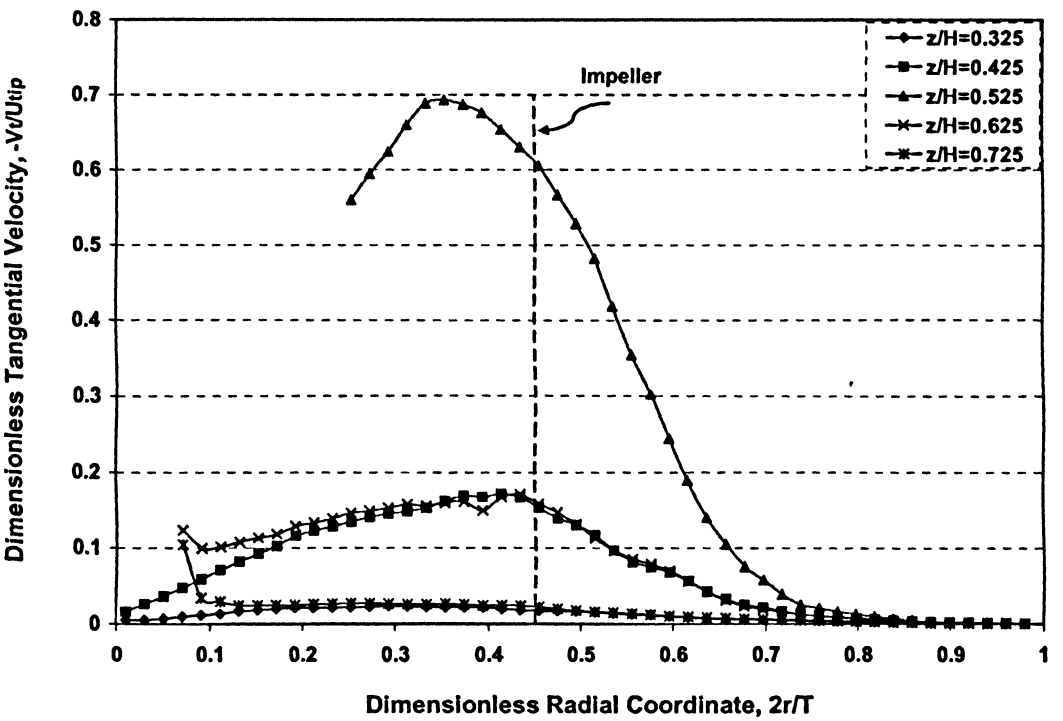

Fig. 6.25. Axial and radial distribution of tangential velocity for 1.5% agitated at 70 rpm (Re=18.4).

Fig. 6.26 and Fig. 6.27 show radial and tangential velocities on the impeller centerline for 1.5% xanthan solution agitated at different impeller speeds. Fig. 6.26 shows the effect of impeller speed and as a result, Re number on the radial velocity profile as the higher the Re, the higher the magnitude of radial velocity attained. It can be seen that the tangential velocity of the fluid (Fig. 6.27) at the blade tip is almost equal the tip velocity. However, for lower speeds, i.e. in laminar regime, the tangential velocity reaches zero slower than that expected, but this figure still confirms the existence of cavern at low impeller speeds. Since the tangential velocity is the major velocity in centerline compared with axial and radial velocities (explained above); this figure shows the cavern growth using 0.001 (m/s) as a velocity on the cavern boundary[1]. It shows that at 20, 40, 60, 80 and somewhat 100 rpm, the tangential velocity is less than the cavern boundary velocity before reaching the tank wall, i.e. the cavern does not touch the vessel wall.

Fig. 6.28 and Fig. 6.29 show the effect of xanthan concentration and as a result, viscoplasticity on the radial and tangential velocity at the same speed and in a radial profile respectively. These figures show that for 1.5% xanthan solution, both velocities (radial and tangential) reach zero value before touching the vessel wall at 80 rpm, which confirms the existence of the cavern.

[1] Boundary velocity for cavern will be explained in Section6.6.2.1.

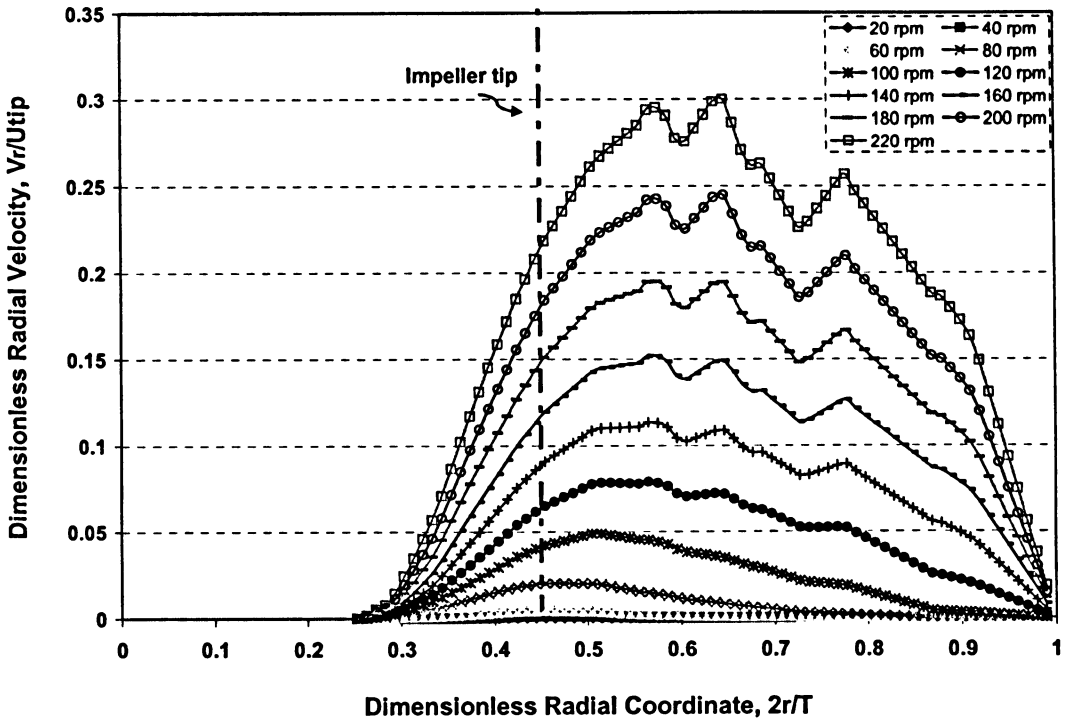

Fig. 6.26. Radial distribution of radial velocity at z= 0.21m (z/H=0.525: impeller centerline) for 1.5 % agitated at different speeds.

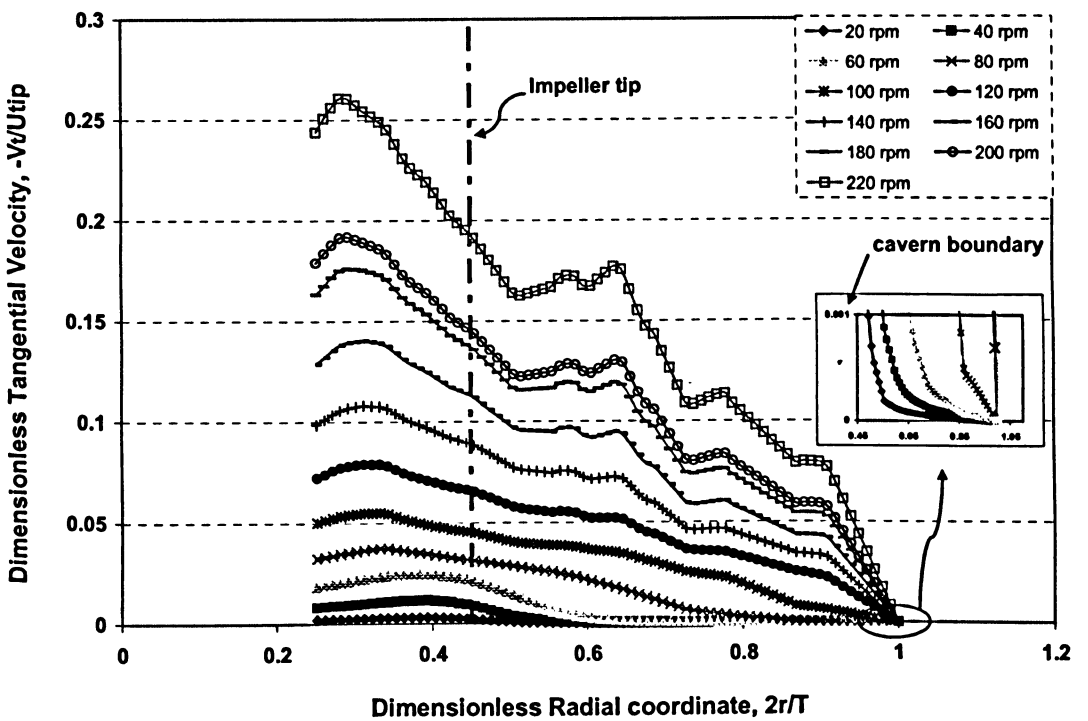

Fig. 6.27. Radial distribution of tangential velocity at z= 0.21m (z/H=0.525: impeller centerline) for 1.5 % agitated at different speeds.

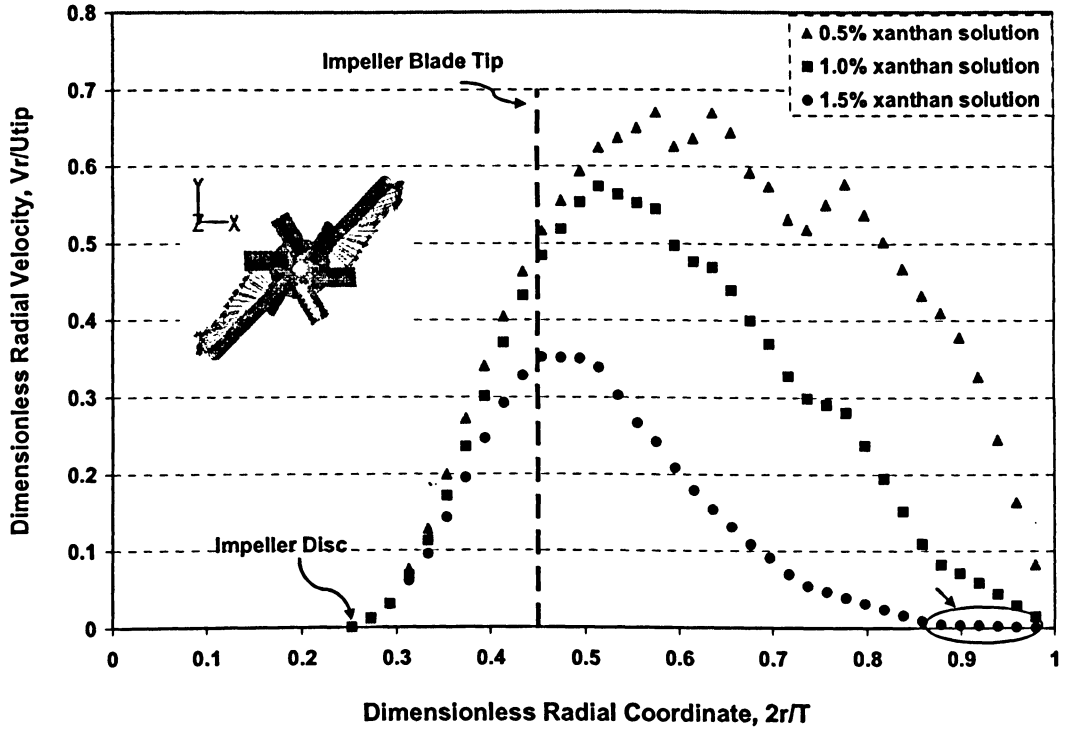

Fig. 6.28. Radial distribution of radial velocity at z=0.21m (z/H=0.525: impeller centerline) for 0.5, 1 and 1.5 % xanthan solutions agitated at 80 rpm.

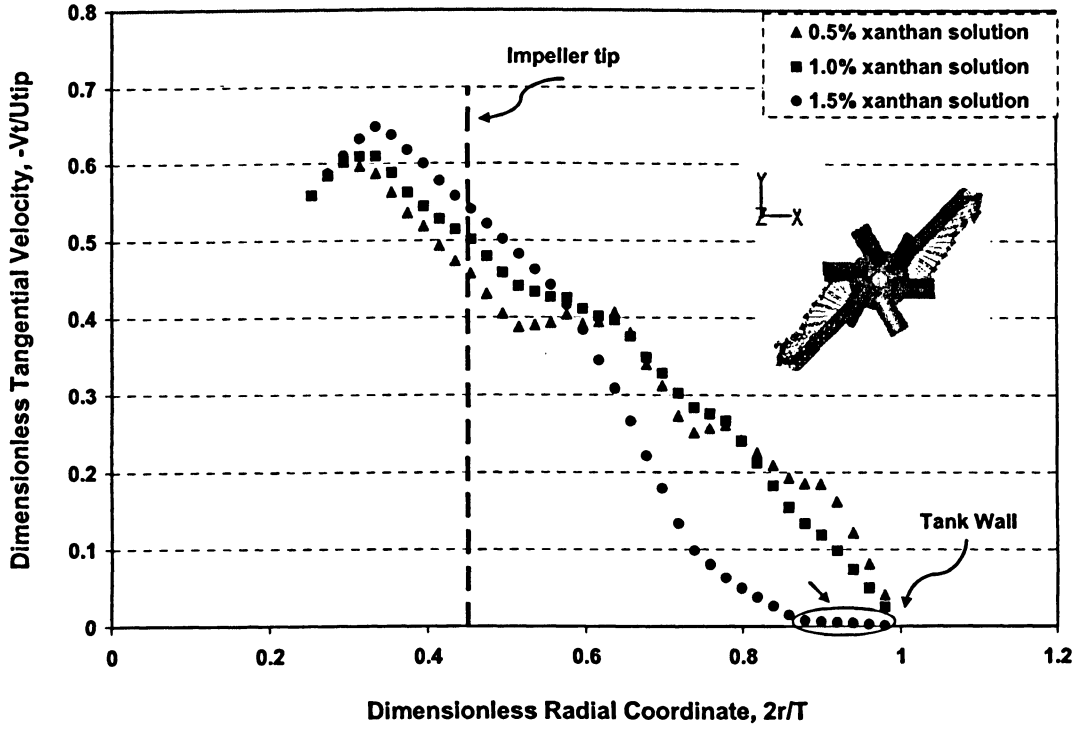

Fig. 6.29. Radial distribution of tangential velocity at z=0.21m (z/H=0.525: impeller centerline) for 0.5, 1 and 1.5 % xanthan solutions agitated at 80 rpm.

6.6 Cavern Size

Several experimental methods have been applied to investigate the formation of cavern such as coloring with dye and taking pictures (Wichterle and Wein 1975, 1981), traversing hot film anemometer (Solomon *et al.*, 1981), taking X-ray photographs (Elson *et al.*, 1986 and Elson, 1988), and using laser Doppler anemometer (Hirata and Aoshima, 1994).

In this work, the electrical resistance tomography (ERT) technique has been adopted to evaluate the cavern formation, shape, and dimension as an experimental device.

6.6.1 Using ERT to Predict the Cavern Diameter

The study of the images obtained provides valuable insight into the vessel behaviour. From ERT tomograms, one can clearly observe that the tracer distribution is limited to a region, a well-mixed zone. A clear layer between this well mixed impeller zones and the rest of the tank is presented in Fig. 6.30.

The cavern boundary was determined as a position at which the tracer concentration was zero. The tracer concentration distributions (expressed as a concentration of NaCl, g/L) can be converted from the conductivity distribution using the following equation (ITS, 2006):

$$\alpha_s = 0.0687\sigma_{mc} - 0.1087 \qquad (6.9)$$

where α_S is the concentration of NaCl (g/L) and σ_{mc} is the reconstructed measured conductivity, mS/cm. It should be noted that outside the cavern boundary, the fluid is not completely stagnant, which is clearly understood from eq. (2.23).

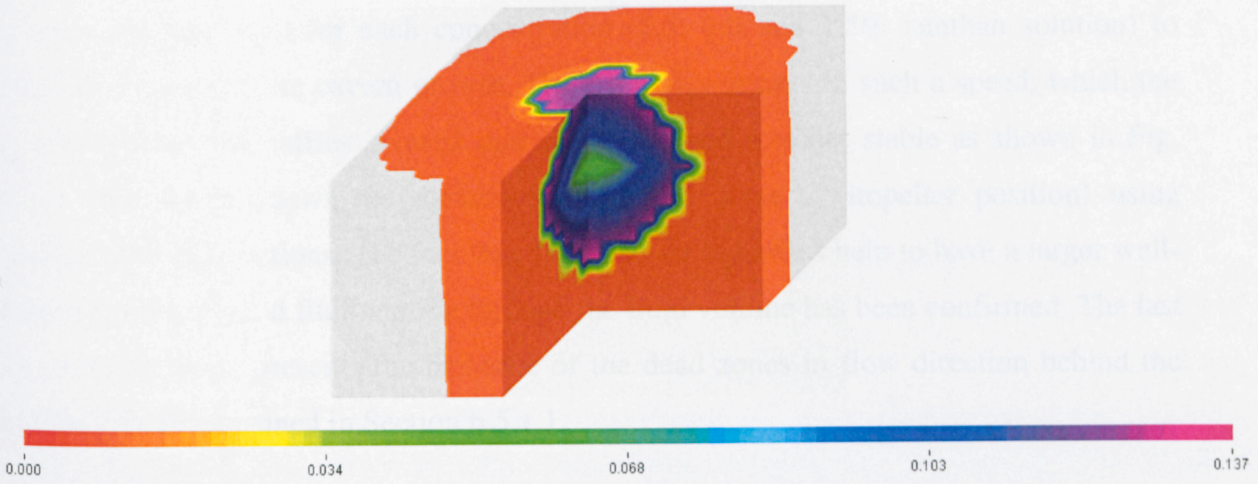

Fig. 6.30. Cavern formed in agitation of 0.5% xanthan solution in 3-D solid body format.

Fig. 6.31 shows the effect of viscoplasticity on the size of the cavern formed in agitation of xanthan solutions using the 2-D format. In comparing Fig. 6.31(a) with Fig. 6.31(b), it is immediately clear that the cavern diameter is higher for 1.0% xanthan solution, which has a less yield stress in compared with 1.5% xanthan solution.

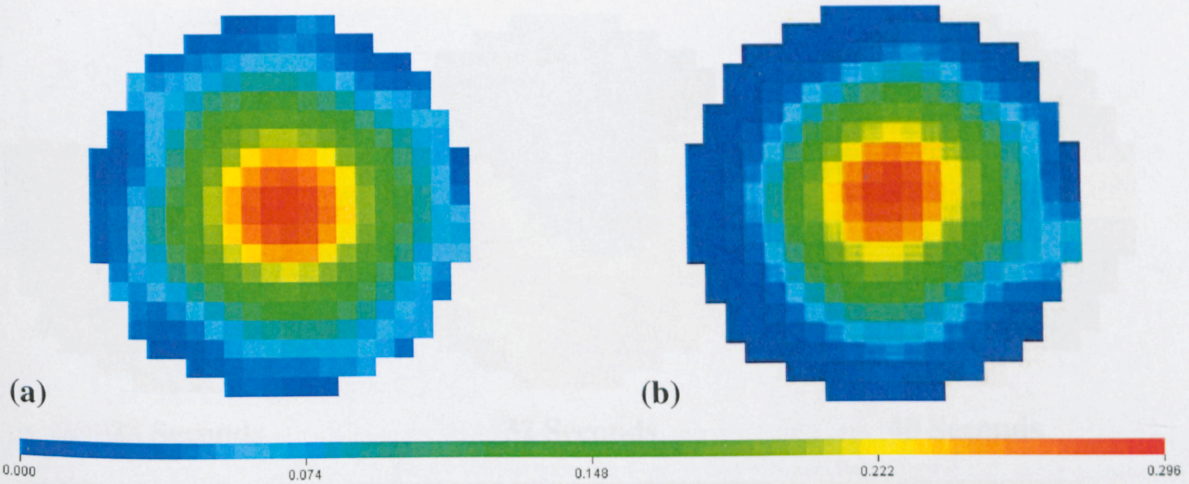

Fig. 6.31. Cavern formed in (a) 1.0%, and (b) 1.5% xanthan solution agitated by Scaba at 73 rpm using impeller plane.

The stirrer rotational speed was varied over a range between *Re*=10 and when the cavern reaches the tank wall for each concentration (0.5, 1.0 and 1.5% xanthan solution) to evaluate the rate of the cavern growth. The dynamics images in such a speed, which the cavern touches the baffles showed that cavern formed was not stable as shown in Fig. 6.32. This figure shows the dynamic changes of plane 2 (impeller position) using conductivity distributions. The fact that the presence of baffles help to have a larger well-mixed cavern or good fluid motion through the fluid volume has been confirmed. The last image (after 40 s) presents the presence of the dead zones in flow direction behind the baffles, which explained in Section 6.5.1.1.

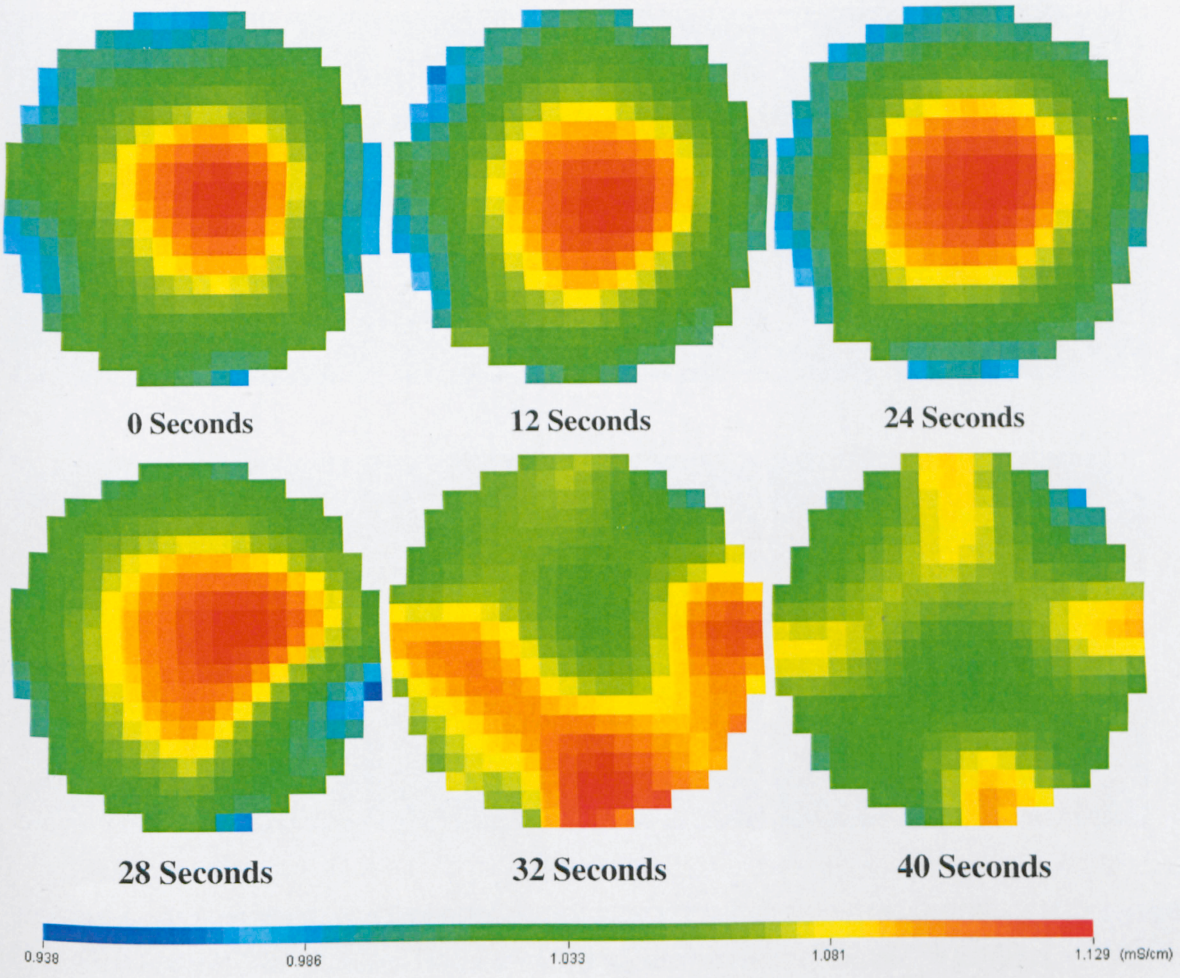

Fig. 6.32. Dynamics images of cavern formed for 1.0% xanthan solution agitated at 90 rpm.

Fig. 6.33 presents some illustrative results showing the effect of impeller speed on the size of the cavern for 0.5% xanthan solutions. The images show the results in the format of the four tomograms, one for each sensing plane. Plane 2 presents the impeller position and consequently cavern diameter. As can be easily seen, the size of the cavern increases by increasing the impeller speed. The solid-body images, representation for the volume of cavern formed in the yield stress fluids for all three concentrations will be shown in appendix A.

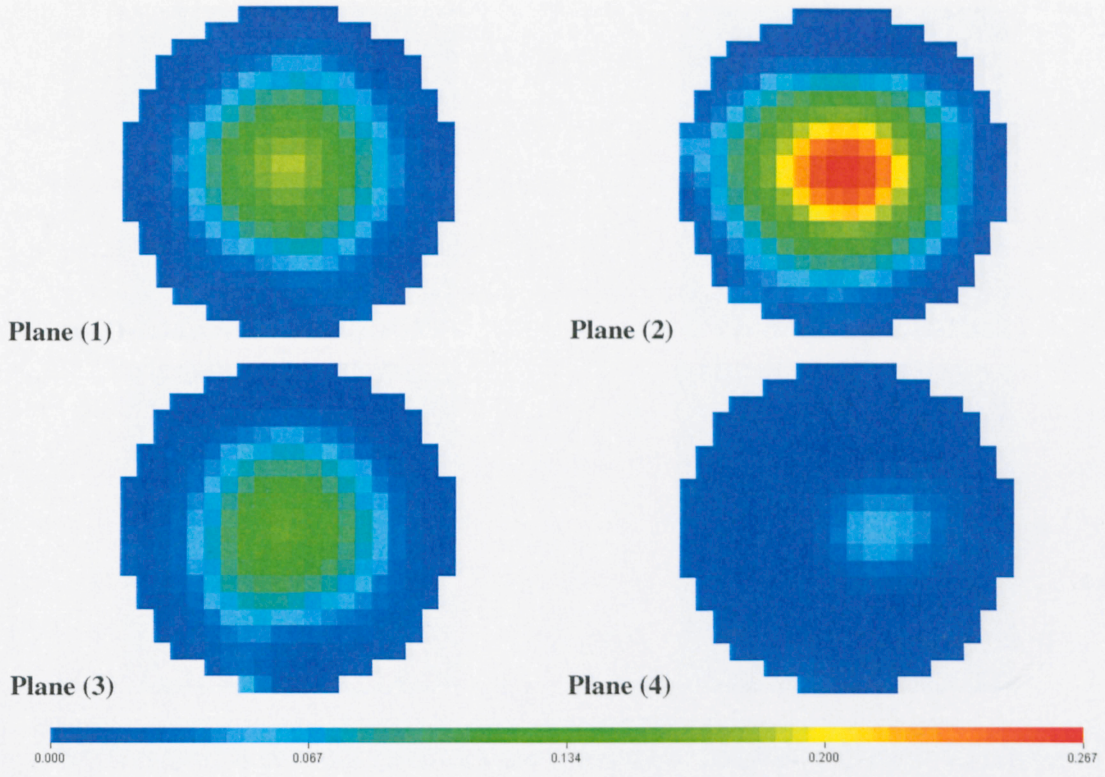
Plane (1)
Plane (2)
Plane (3)
Plane (4)
0.000
0.067
0.134
0.200
0.267

(a)

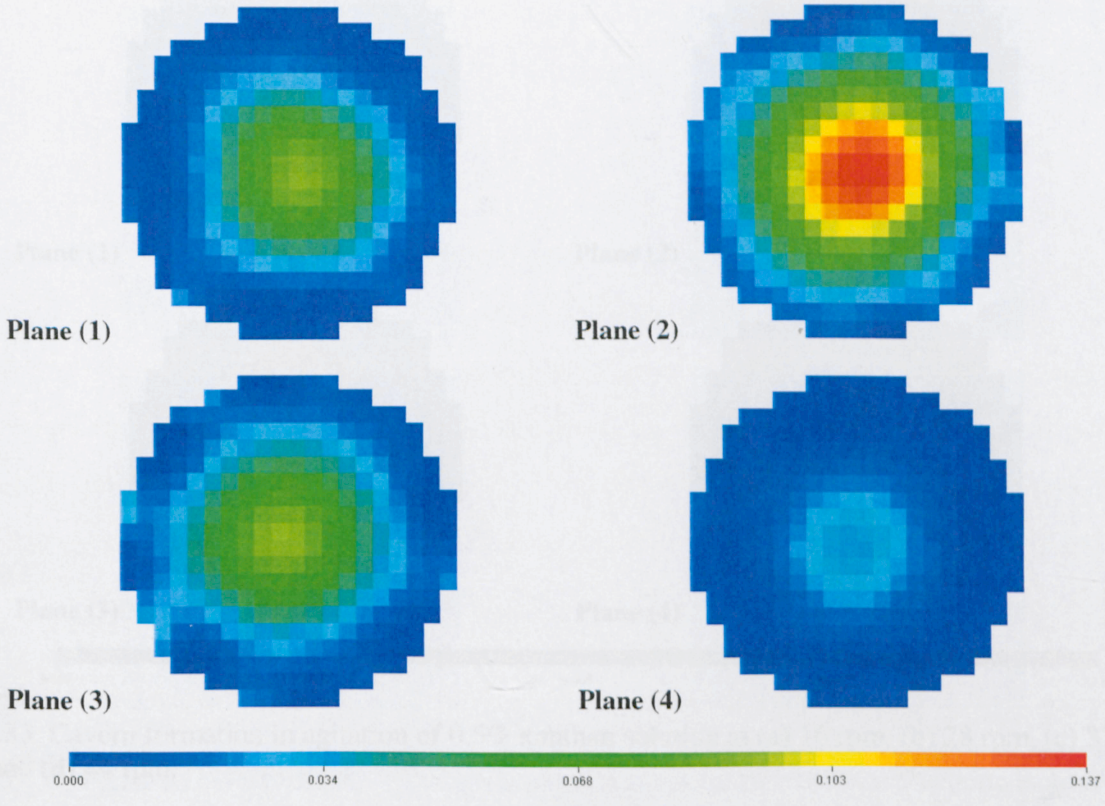
Plane (1)
Plane (2)
Plane (3)
Plane (4)
0.000
0.034
0.068
0.103
0.137

(b)

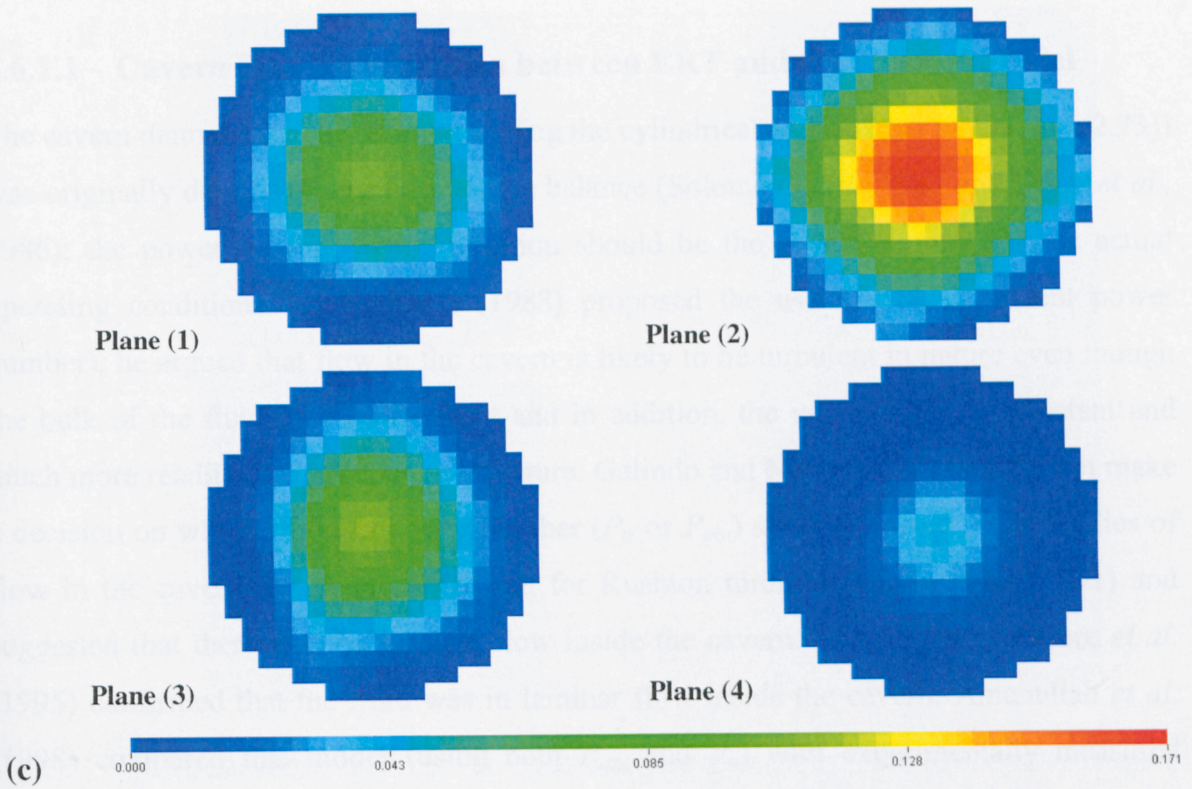

(c)

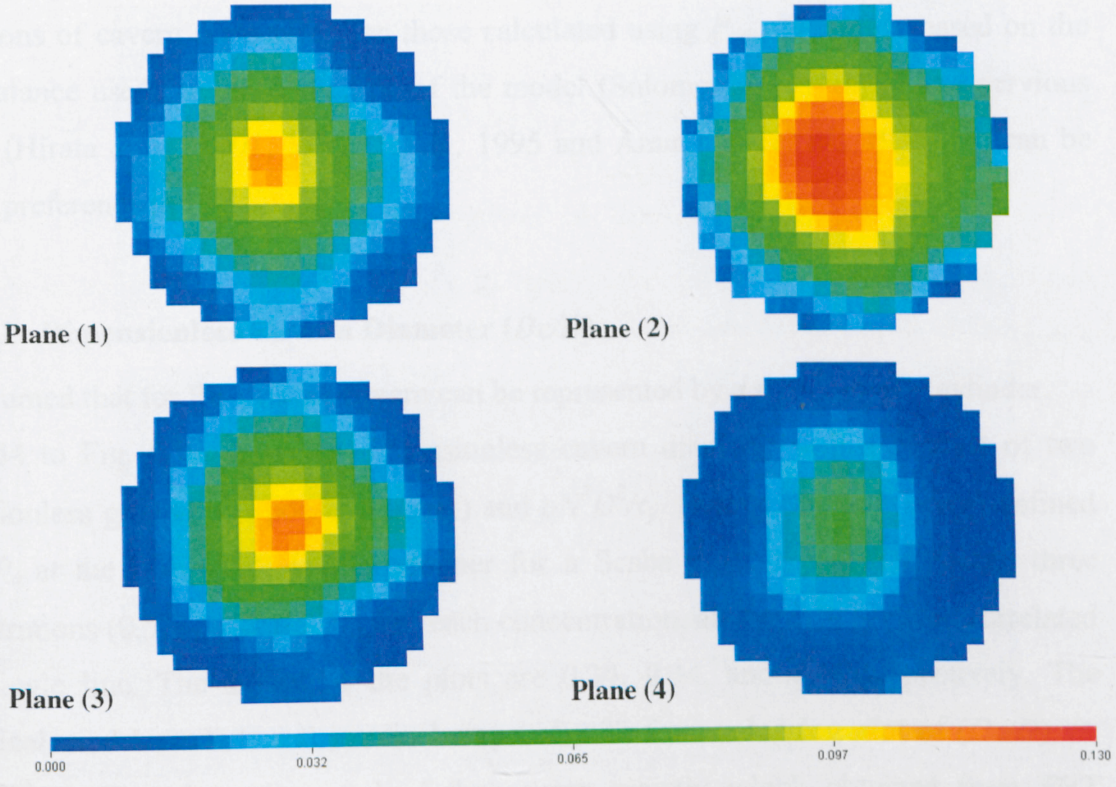

(d)

Fig. 6.33. Cavern formation in agitation of 0.5% xanthan solution at (a) 16 rpm, (b) 28 rpm, (c) 37 rpm, and (d) 44 rpm.

6.6.1.1 Cavern Size: Comparison between ERT and Cylindrical Model

The cavern diameter can be estimated using the cylindrical model. This model (eq. (2.23)) was originally derived, based on a torque balance (Solomon *et al.*, 1981 and Elson *et al.*, 1986); the power number in the equation should be the power number for the actual operating conditions. Later, Elson (1988) proposed the use of P_{otu} (turbulent power number), he argued that flow in the cavern is likely to be turbulent in nature even though the bulk of the fluid may be stagnant and in addition, the value of P_{otu} is constant and much more readily available in the literature. Galindo and Nienow (1992) could not make a decision on which value of power number (P_o or P_{otu}) should be used. LDA studies of flow in the cavern has been carried out for Rushton turbines (Hirata *et al.*, 1991) and suggested that there may be laminar flow inside the cavern. The results of Moore *et al.* (1995) confirmed that the fluid was in laminar flow inside the cavern. Amanullah *et al.* (1998) compared this model (using both P_{otu} and P_o) with experimentally measured cavern diameters. They pointed out that *Re* dependant P_o gives relatively more accurate predictions of cavern diameters than those calculated using P_{otu}. Therefore based on the force balance used for the derivation of the model (Solomon *et al.*, 1981) and pervious studies (Hirata *et al.*, 1991, Moore *et al.*, 1995 and Amanullah *et al.*, 1998), P_o can be used in preference to P_{otu}.

6.6.1.1.1 Dimensionless Cavern Diameter (*Dc/D*)

It is assumed that for Re >10 the cavern can be represented by a right circular cylinder. Fig. 6.34 to Fig. 6.36 show the dimensionless cavern diameter versus product of two dimensionless groups, P_o (power number) and $\rho N^2D^2/\tau_y$ (Reynolds yield stress) defined using P_o at the relevant Reynolds number for a Scaba 6SRGT impeller for all three concentrations (0.5, 1, and 1.5 %). For each concentration, all the data are well correlated by a single line. The slopes of the plots are 0.34, 0.34, and 0.36 respectively. The cylindrical model predicts a theoretical slope of 0.33 from a log-log plot of (*Dc/D*) vs. ($P_o\rho N^2D^2/\tau_y$). Therefore, the trend of the cavern growth, which obtained from ERT tomograms, is in good agreement with theory.

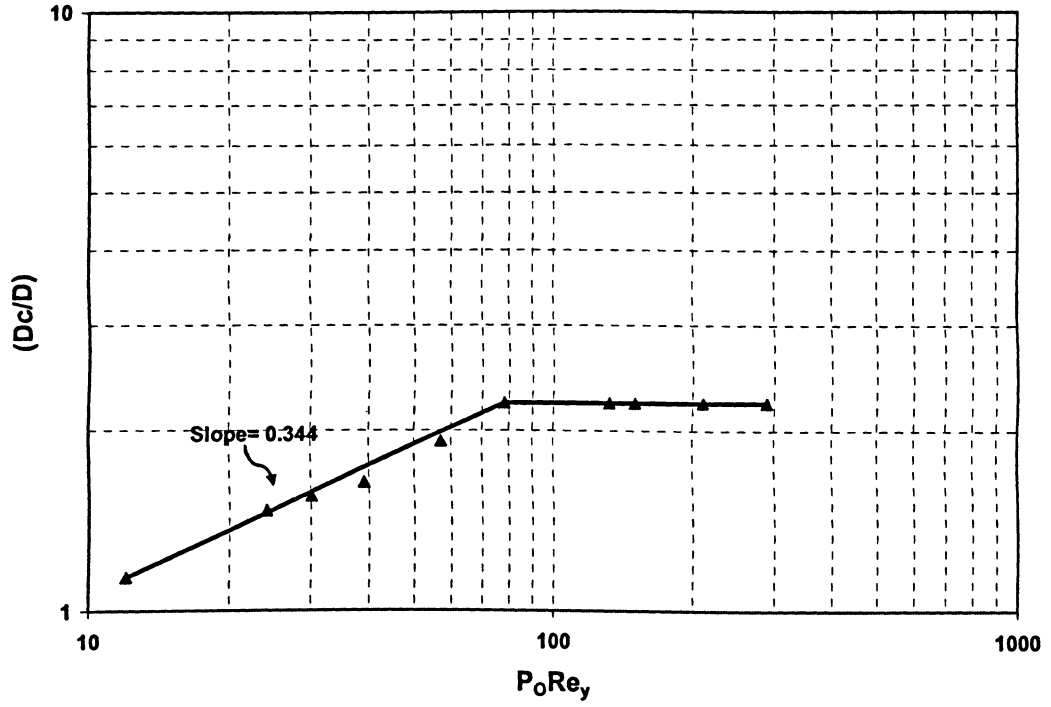

Fig. 6.34. ERT results for dimensionless cavern diameter versus dimensionless stress (P_oRe_y) for 0.5% xanthan solution agitated by a Scaba impeller.

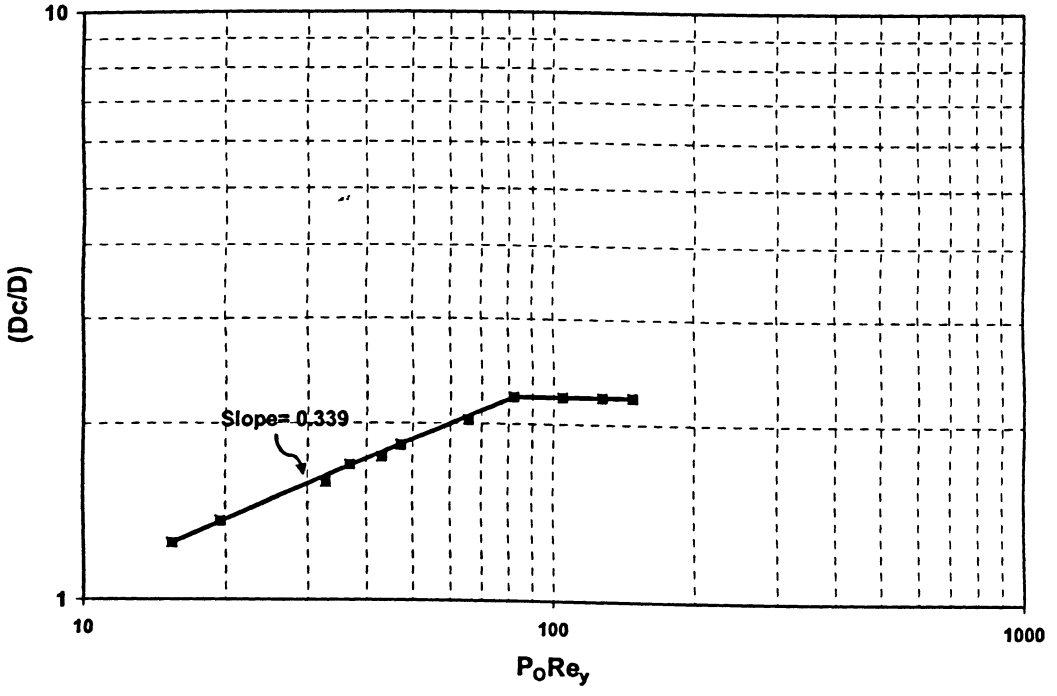

Fig. 6.35. ERT results for dimensionless cavern diameter versus dimensionless stress (P_oRe_y) for 1.0% xanthan solution agitated by a Scaba impeller.

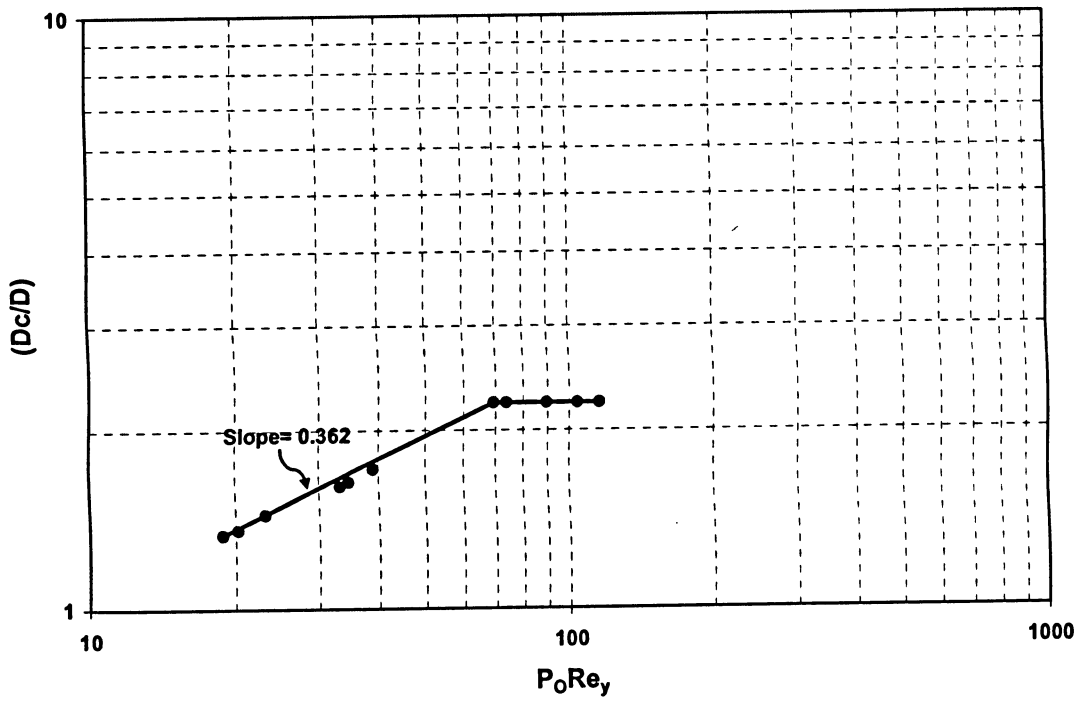

Fig. 6.36. ERT results for dimensionless cavern diameter versus dimensionless stress (P_oRe_y) for 1.5% xanthan solution agitated by a Scaba impeller.

6.6.2 Using CFD to Predict the Cavern Dimensions

6.6.2.1 Cavern-Defining Velocity, Velocity on the Cavern Boundary

The value of the cavern-defining velocity, v_o, used in the present analysis was maintained constant at 0.00099 ms^{-1} which is 0.01 U_{tip} of the lowest impeller speed (10 rpm) within a data set. However, it is obvious that the predicted diameter of the cavern is dependent on the value of v_o. Fig. 6.37 shows the effect of cavern-defining velocity (v_o) on the cavern diameter for 1.5% xanthan solution. It is shown that the most variation can be found in the range of 10^{-1}-10^{-2} ms^{-1} and in this range the cavern diameter varies by approximately 7-30%, in the range of 10^{-2}-10^{-3} ms^{-1} the increase in size is small (1-2%) and for the range of 10^{-3}-10^{-5} ms^{-1} there is no change in cavern size. Therefore, it can be concluded that the cavern diameter is less sensitive to the cavern defining velocity as reported by Amanullah *et al.*, (1998) and 0.00099 ms^{-1} was considered suitable in this study and was used for all simulations.

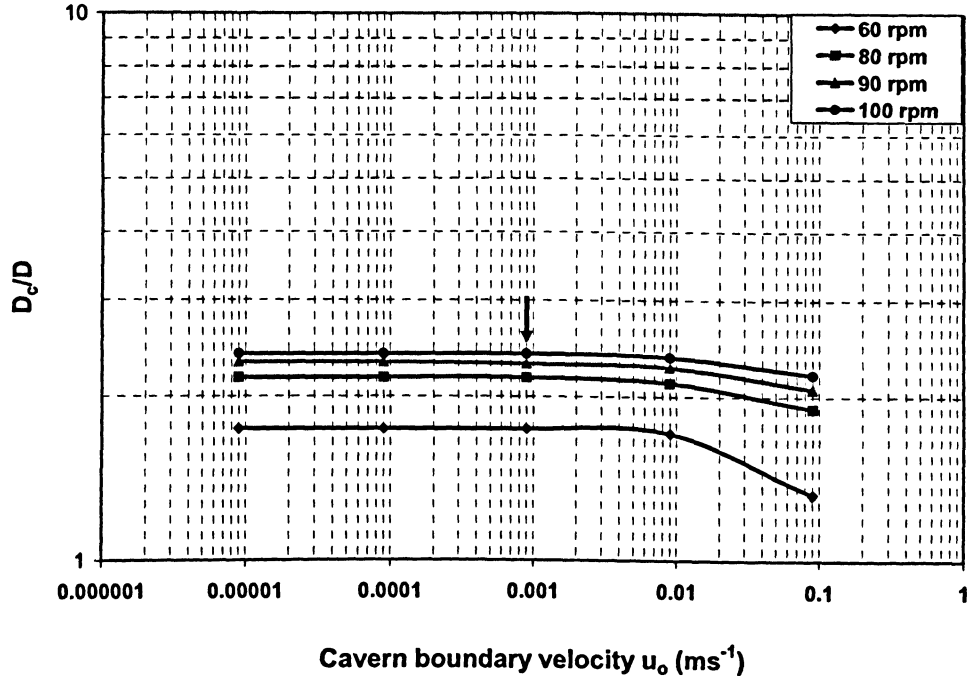

Fig. 6.37. Effect of cavern boundary velocity (1.5% xanthan) on cavern diameter.

6.6.2.2 Effect of Yield Stress on the Formation and Size of Cavern

Fig. 6.38 shows the effect of the xanthan concentration (and thus viscoplasticity) on the formation and size of the cavern. The presence of the yield stress may lead to form the stagnant region around the cavern in which the shear stress falls below the fluid's yield stress. Therefore, as the yield stress increases, the cavern diameter decreases. It can be said that the boundary of the cavern is defined by the surface where the local shear stress equals the fluid yield stress. This figure is based on velocity contour (ms^{-1}) and the cavern-defining velocity was fixed on 0.00099 ms^{-1} as mentioned before.

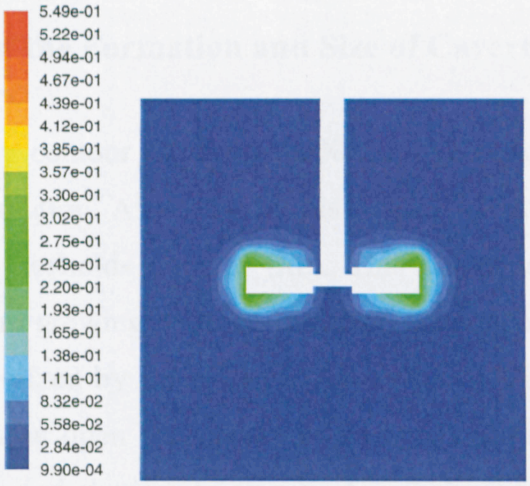

(a) 0.5 % xanthan solution

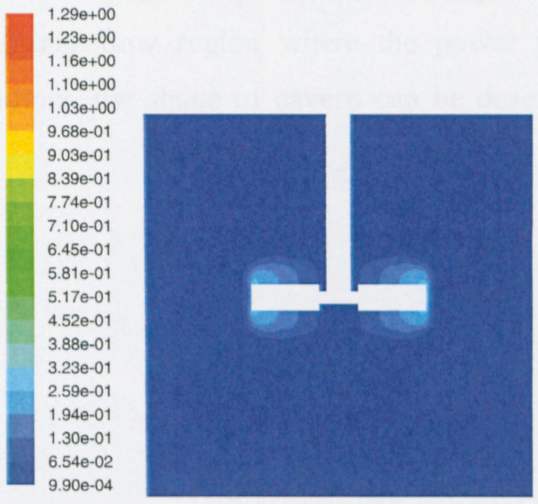

(b) 1.0 % xanthan solution

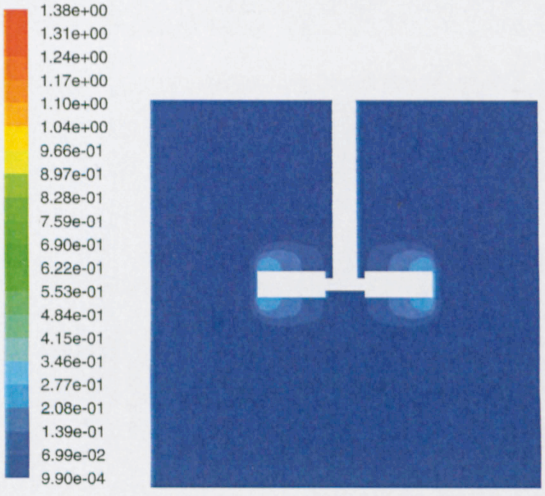

(c) 1.5 % xanthan solution

Fig. 6.38. Velocity contour plots (vertical cross-sectional planes cutting the impeller at 30 rpm) for three xanthan concentrations, v_o=0.00099 ms^{-1}.

6.6.2.3 Effect of Impeller Speed on the Formation and Size of Cavern

Fig. 6.39Fig. 6.39 shows CFD velocity contour plots for 0.5% xanthan concentration[1], formed on agitation of xanthan gum solution. As shown in this figure, the cavern shape and size change with increasing the Reynolds number (*Re*). This clearly shows that regions with significant fluid motion are growing with increasing impeller speed. Cavern growth around the impeller is characterized by three shapes, as shown in Fig. 6.39. It starts with a torus-shaped cavern with an open center part in low *Re*, continues with a torus-shaped cavern with closed center and changes to cavern of oval-shaped in *Re* >10. At low Reynolds numbers in the laminar flow region where the power number is inversely proportional to Reynolds number, the shape of cavern can be described by a torus.

[1] CFD velocity contour plots for 1.0 and 1.5% xanthan concentration are placed in Appendix B.

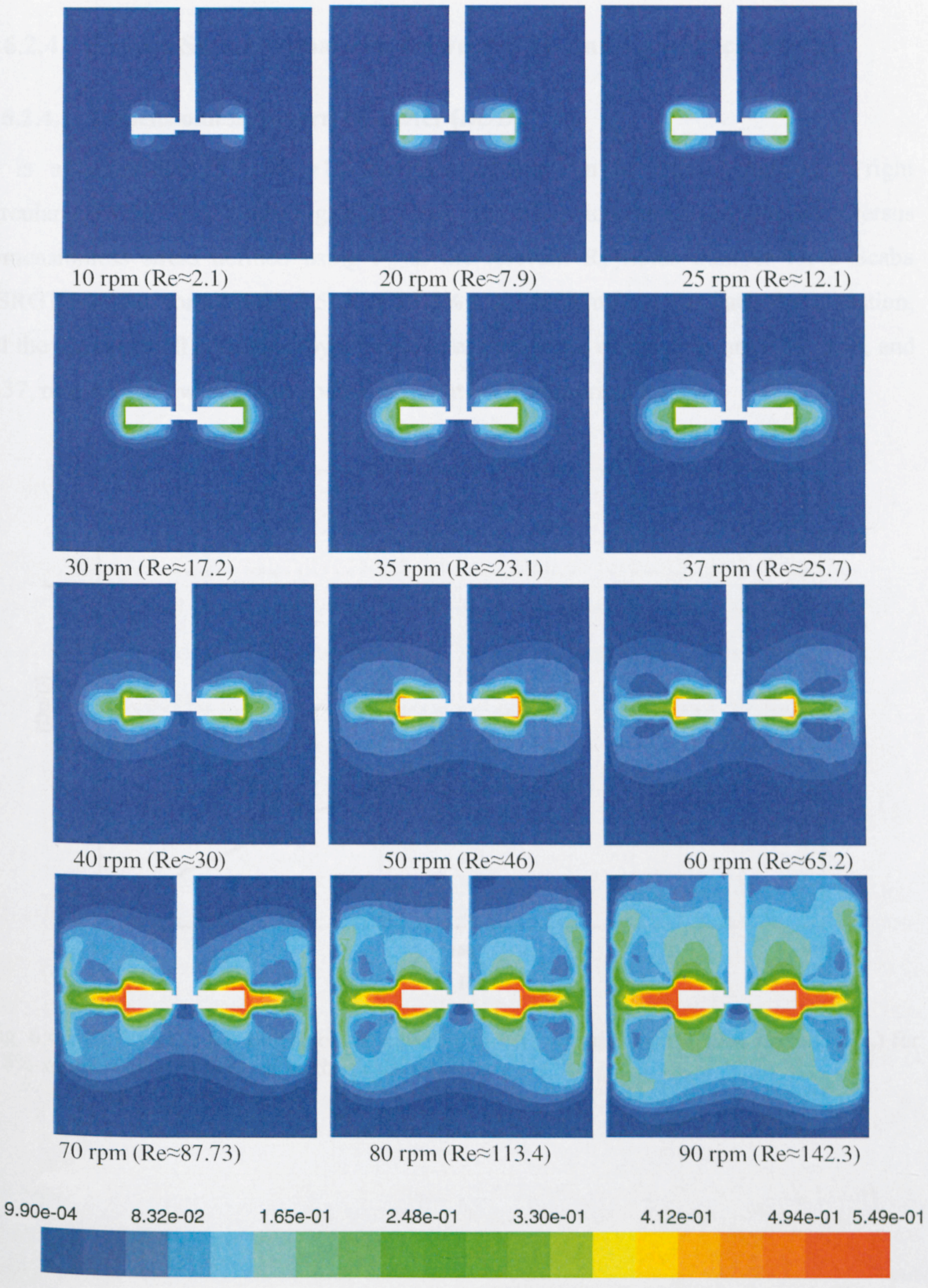

Fig. 6.39. CFD velocity (ms^{-1}) contour plots for 0.5% xanthan concentration, v_o=0.00099 ms^{-1}.

6.6.2.4 Cavern Size: Comparison between CFD and Cylindrical Model

6.6.2.4.1 Dimensionless Cavern Diameter (*Dc/D*)

It is assumed that for *Re* >10 the oval cavern can be represented by a right circular cylinder. Fig. 6.40- Fig. 6.42 show the dimensionless cavern diameter versus dimensionless stress defined using P_o at the relevant Reynolds number for a Scaba 6SRGT impeller for all three 0.5, 1 and 1.5% xanthan solutions. For each concentration, all the data are well correlated by a single line. The slopes of the plots are 0.38, 0.35, and 0.37, respectively, which is in good agreement with cylindrical model.

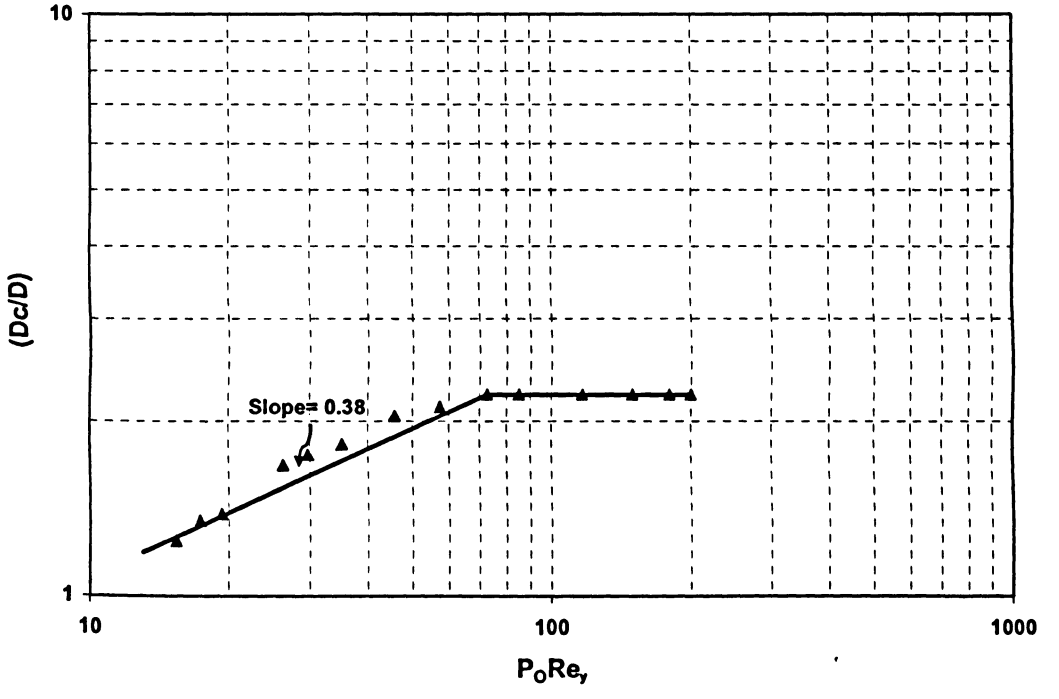

Fig. 6.40. CFD results for dimensionless cavern diameter versus dimensionless stress (P_oRe_y) for 0.5% xanthan solution agitated by the Scaba impeller

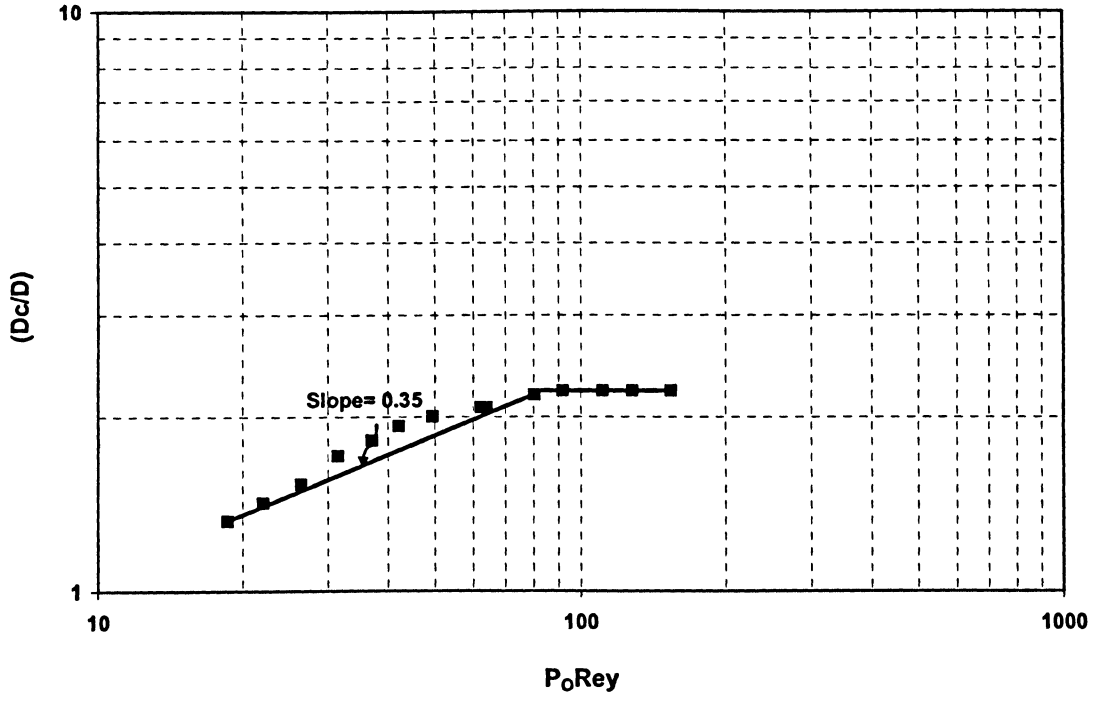

Fig. 6.41. CFD results for dimensionless cavern diameter versus dimensionless stress (P_oRe_y) for 1.0% xanthan solution agitated by the Scaba impeller.

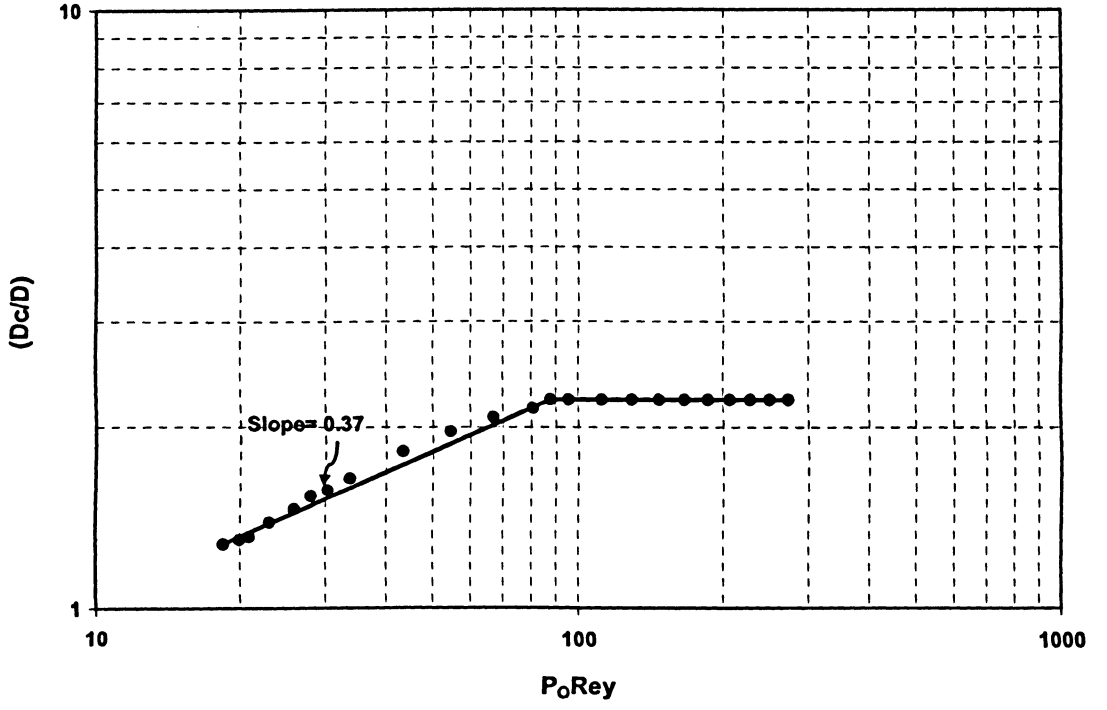

Fig. 6.42. CFD results for dimensionless cavern diameter versus dimensionless stress (P_oRe_y) for 1.5% xanthan solution agitated by the Scaba impeller.

6.6.2.4.2 Cavern Height to Diameter Ratio *(Hc/Dc)*

Before the cavern reaches the wall, the ratio *Hc/Dc* is almost constant for each type of the impeller (see Table 6.1). This term varies with the type of impeller, ranging from 0.4 for a radial-flow Rushton turbine to 0.75 for an axial-flow Marine propeller as reported in the literature (Table 6.1).

Elson *et al.* (1986) also indicated that after cavern reached the vessel walls (D_C=T), the height of the cavern increases with the stirring speed such that,

$$\frac{H_C}{D_C} \propto N \tag{6.10}$$

Subsequent re-analysis of above equation by Elson (1988) and new data for other impellers indicated that the dependence of H_C on N was weaker than originally given by eq.(6.10). The rate at which the height of the cavern increased with impellers speed thereafter was expressed as:

$$\frac{H_C}{D_C} = N^p \tag{6.11}$$

where p is a weak function of impeller type, varying from 0.88 for the radial flow impellers to 0.76 for axial flow impellers, while a value of 0.53 and 0.54 has been found for a lightning A315 (Galindo and Nienow, 1992) and a Scaba 6SRGT impeller (Galindo and Nienow, 1993), Table 6.1. It is clear that p is the slope of the log-log plot of (*Hc/Dc*) versus N after cavern touches the tank.

Fig. 6.43-Fig. 6.45 show *Hc/Dc* versus impeller speed. It can be seen that increasing impeller speeds, both height and diameter of caverns were found to increase in such a manner that their ratio (*Hc/Dc*) remained approximately constant at 0.473, 0.463, and 0.478 for 0.5, 1 and 1.5% xanthan solution respectively until the cavern touched the tank

wall or baffles. This result is similar to that reported (*Hc/Dc* ≈0.48) by Galindo and Nienow (1993). Once the wall was reached, the cavern heights increased directly with the power of impeller speed with exponent of 0.583, 0.603, and 0.578 for 0.5, 1, and 1.5% concentration respectively. The obtained slope values (*p*) are upper than the value of 0.54 quoted by Galindo and Nienow (1993). Theses differences probably are due to the different concave blade shapes of the impeller employed in their study (as explained in Section 6.2.1).

Table 6.1. Summery of Cavern studies using different impellers.

Impeller type	Reference	*D/T*	*H/T*	Mean H_C/D_C	*p*
Rushton turbine	Solomon *et al.*, 1981 Elson, 1988	0.6-0.25	1	0.40±0.05	0.88
Pitched blade turbine	Solomon *et al.*, 1981 Elson, 1988	0.5-0.33	1	0.55±0.10	0.86
Two blade paddle	Elson, 1988	0.5	1	0.45±0.05	0.88
Marine propeller	Elson, 1990	0.56	1	0.75±0.05	0.76
Lightnin A315	Galindo and Nienow, 1992	0.49	1	0.58±0.05	0.53
Scaba 6SRGT	Galindo and Nienow, 1993	0.48	1	0.48±0.02	0.54
Scaba 3SHPI	Amanullah *et al.*, 1997	0.33-0.49	1	0.46±0.02	-

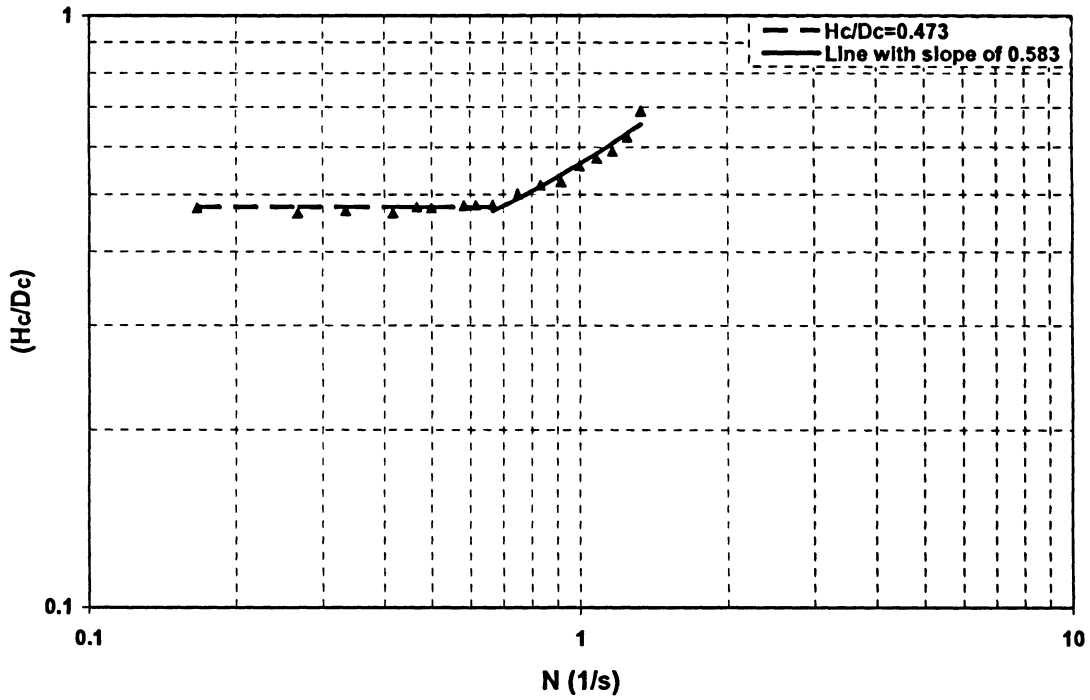

Fig. 6.43. CFD results for cavern height to diameter ratio versus Scaba impeller speed for 0.5% xanthan solution.

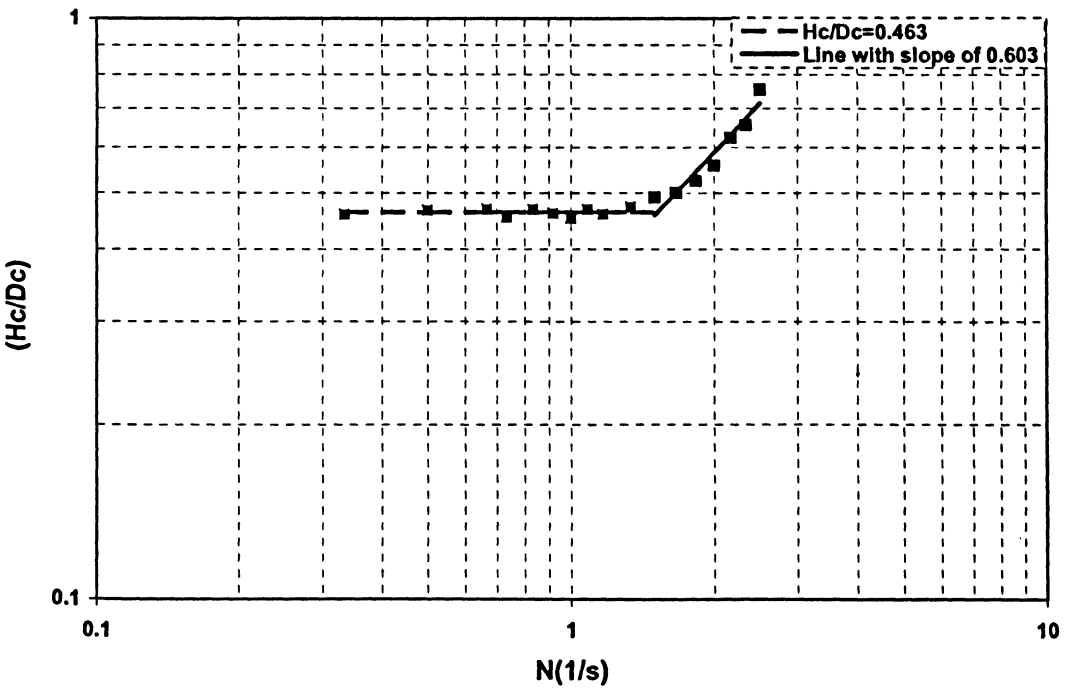

Fig. 6.44. CFD results for cavern height to diameter ratio versus Scaba impeller speed for 1.0% xanthan solution.

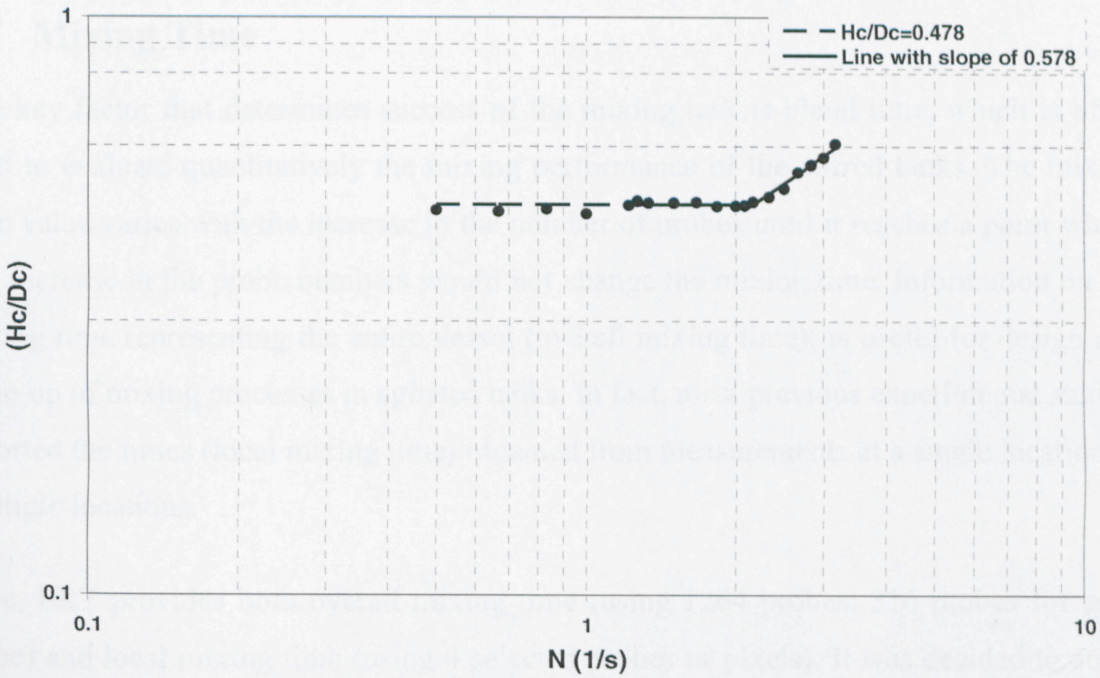

Fig. 6.45. CFD results for cavern height to diameter ratio versus Scaba impeller speed for 1.5% xanthan solution.

Fig. 6.46 presents two horizontal cut-planes obtained from ERT and CFD simulation. The ERT tomogram based on the distribution of the tracer concentration is in good agreement with the CFD velocity contour. It is obvious that the cavern touches the baffles but the shape of the cavern is stable.

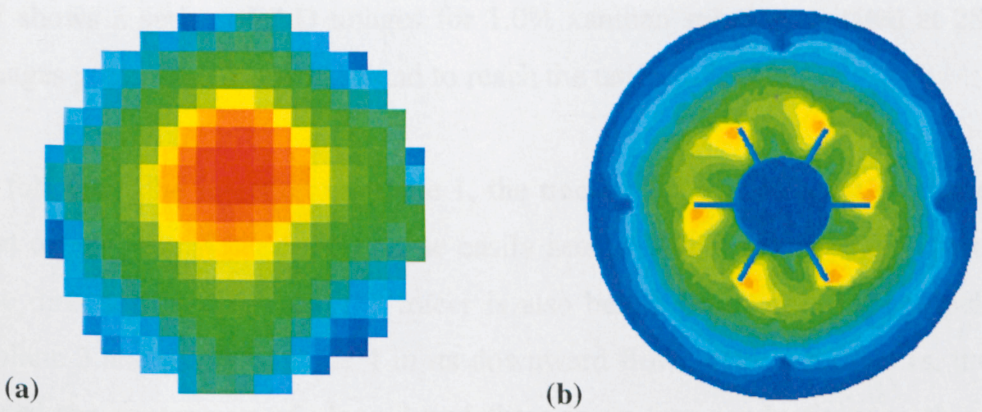

Fig. 6.46. Sample cavern diameter comparison for 0.5% xanthan solution agitated in 44 rpm; (a) ERT tomogram (plane 2: impeller position) based on concentration, g/L, and (b) CFD horizontal impeller cut-plane, velocity contour.

6.7 Mixing Time

The key factor that determines success of the mixing task is blend time, which is often used to evaluate quantitatively the mixing performance of the stirred tanks. The mixing time value varies with the increase in the number of probes until it reaches a point where any increase in the probe numbers would not change the mixing time. Information on the mixing time representing the entire vessel (overall mixing time), is useful for design and scale-up of mixing processes in agitated tanks. In fact, most previous experimental studies reported the times (local mixing time) obtained from measurements at a single location or multiple locations.

Here, ERT provides both overall mixing time (using 1264 probes: 316 probes for each plane) and local mixing time (using 4 selected probes or pixels). It was decided to study t_{95} (both for experiments and CFD simulations), which is the time required to reach 95% of homogeneity, since the 100% uniform distribution from experiments can never be reached due to measurement noises.

6.7.1 ERT Results for Mixing Time

For the effective prediction of homogenization (overall mixing time), the time dependence of tracer concentration (i.e. concentration curve) is presented in this study. Fig. 6.47 shows a series of 2-D images for 1.0% xanthan solution agitated at 282 rpm. These images pursue the following trend to reach the uniform level:

After 3s following the injection on plane 1, the tracer has been detected on plane 1 and somewhat on plane 2. After 5s, it can be easily seen that the tracer is being swept in a clockwise direction. In this step, the tracer is also being dispersed by the impeller and reaches plane 3 and partially plane 4 in its downward flow. After a further 1s, the tracer has covered the center part of plane 3 and there is no low conductivity in this region, confirming that the tracer is derived back to the impeller in the central part of the tank. This trend is continued and after 11s, the tracer has almost covered plane 2.

The remainder of the time sequence shows a relatively slow approach toward the final uniform level. After 42s, the images show that all four measuring planes reach the 95% of the final concentration, except for the small regions behind the baffles (Section 6.5.1.1).

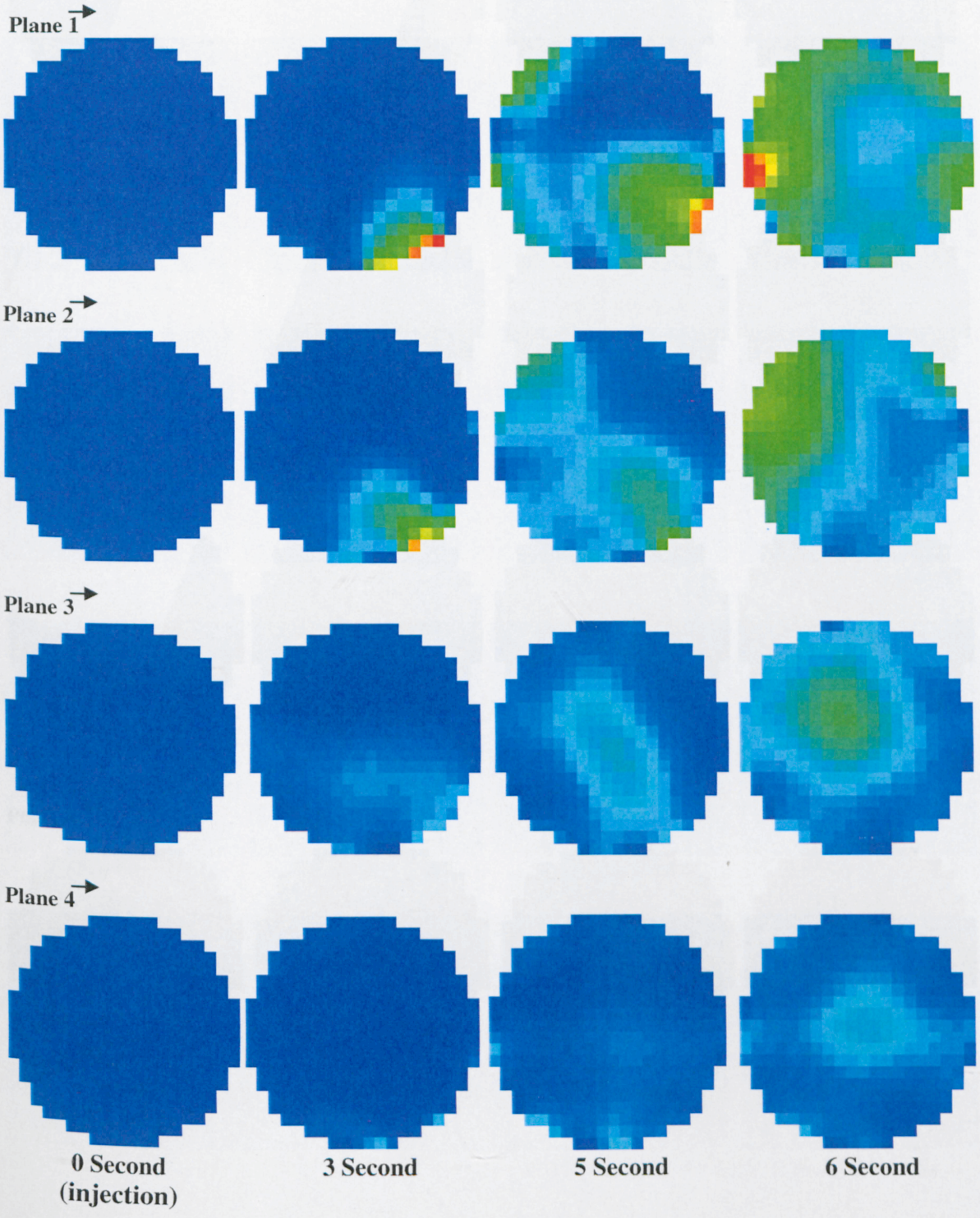

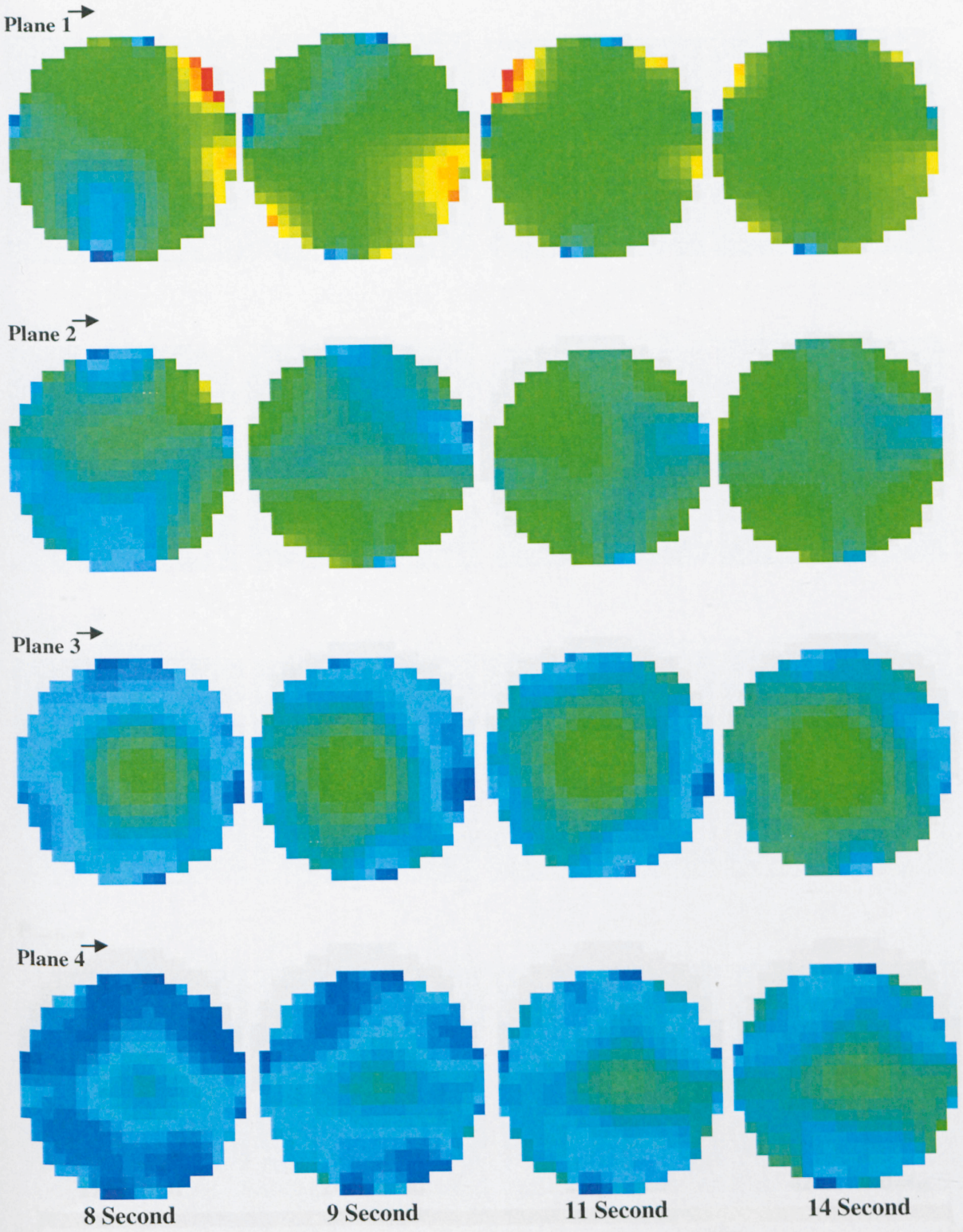
Plane 1
Plane 2
Plane 3
Plane 4
8 Second
9 Second
11 Second
14 Second

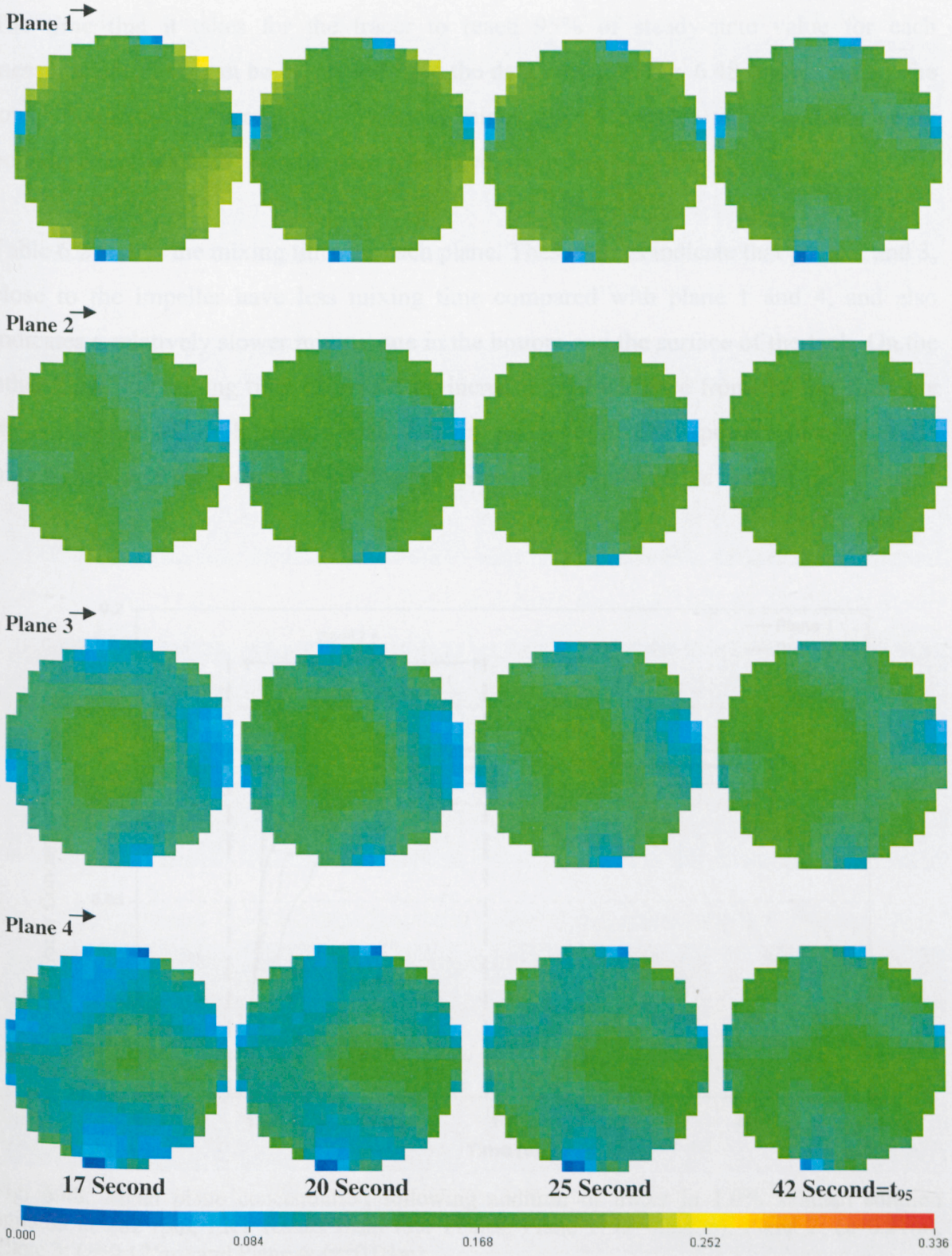

Fig. 6.47. Sequence of reconstructed ERT images (based on tracer concentration, g/l) showing the mixing process for 1.0% xanthan solution agitated at 282 rpm (Plane 1: (z=0.295m), Plane 2: (z=0.21m), Plane 3: (z=0.125m) and Plane 4: (z=0.04m)).

The time that it takes for the tracer to reach 95% of steady-state value for each measurement plane can be calculated from the data shown in Fig. 6.48. In this figure, the lower boundary is average (steady state) minus 5% of average value and the upper boundary represents the average plus 5% of average value.

Table 6.2 shows the mixing time for each plane. These values indicate that plane 2 and 3, close to the impeller have less mixing time compared with plane 1 and 4, and also indicates a relatively slower mixing rate in the bottom and the surface of the tank. On the other hand, the mixing time decreases by increasing the distance from the top since the tracer concentration dilutes as it passes down. At some impeller speeds, plane 4 has the highest mixing time because of dead zones (poor mixing) around the baffles.

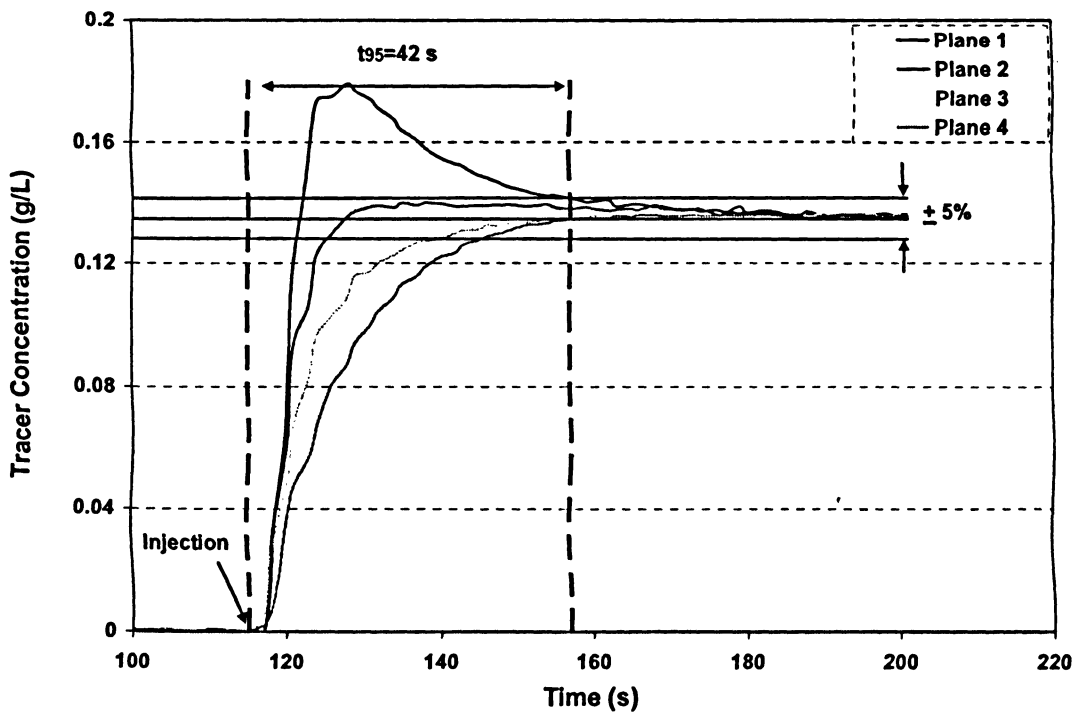

Fig. 6.48. Mean plane concentration following addition of tracer in 1.0% xanthan solution agitated at 282 rpm; ERT results from four Planes: Plane 1: (z=0.295m), Plane 2: (z=0.21m), Plane 3: (z=0.125m) and Plane 4: (z=0.04m).

Table 6.2. Mixing time within each measurement plane form ERT for 1.0% xanthan solution agitated at 282 rpm.

Plane number	Time tracer appears* (s)	Time tracer disappears (s)
1	3	42
2	5	11
3	6	25
4	6	31

* The time origin is the injection time.

It has already been demonstrated (Section 4.4.3) that electrical tomography can be used to construct mixing curves (based on conductivity, mS/cm) for any pixel in any of the four sensing planes fitted to our tank. For each experiment, the injection pixel (58) on plane 1 corresponds to the following location: x=0.07, y=0.11 and z=0.295m. Fig. 6.49 shows mixing time detections at pixels 38 in plane 1 (x=-0.01, y=0.13, and z=0.295m), 231 in plane 2 (x=0.07, y=-0.07, and z=0.21m), 264 in plane 3 (x=0.03, y=-0.11, and z=0.125m) and 76 in plane 4 (x=0.09, y=0.09, and z=0.04m) for 1.0% xanthan solution agitated at 282 rpm. The mixing time obtained here is significantly smaller than that from four planes, i.e. 1264 pixels. This confirms the effect of the probe numbers on the mixing time. As mentioned before, these mixing times are the local mixing times, which are just approximations.

It is expected that increasing the impeller rotational speed should decrease the mixing time. This behaviour is verified well with literature (Buwa *et al.*, 2006). Fig. 6.50 shows the expected trend for all three concentrations. The experiments were repeated 3 times and a single result is an average from three mixing time values. Using standard deviation as the error amount, the error bars as shown in Fig. 6.51 indicates the spread of the mixing time about the mean value for 1% xanthan solution. The maximum standard deviation was found about 2%, confirming the high accuracy of the ERT system in mixing time measurements.

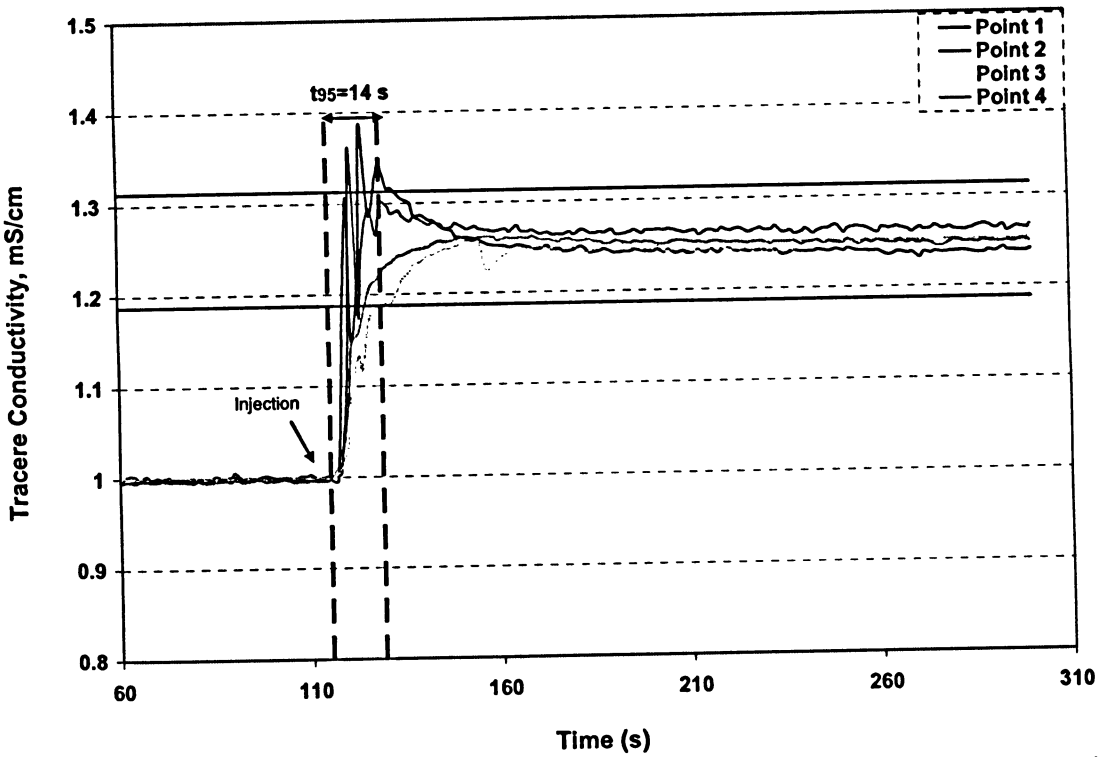

Fig. 6.49. Mean pixel conductivity following addition of tracer in 1.0% xanthan solution agitated at 282 rpm; ERT results form four pixels (Points): Point 1: (x=-0.01, y=0.13, and z=0.295m), Point 2: (x=0.07, y=-0.07, and z=0.21m), Point 3: (x=0.03, y=-0.11, and z=0.125m) and Point 4: (x=0.09, y=0.09, and z=0.04m).

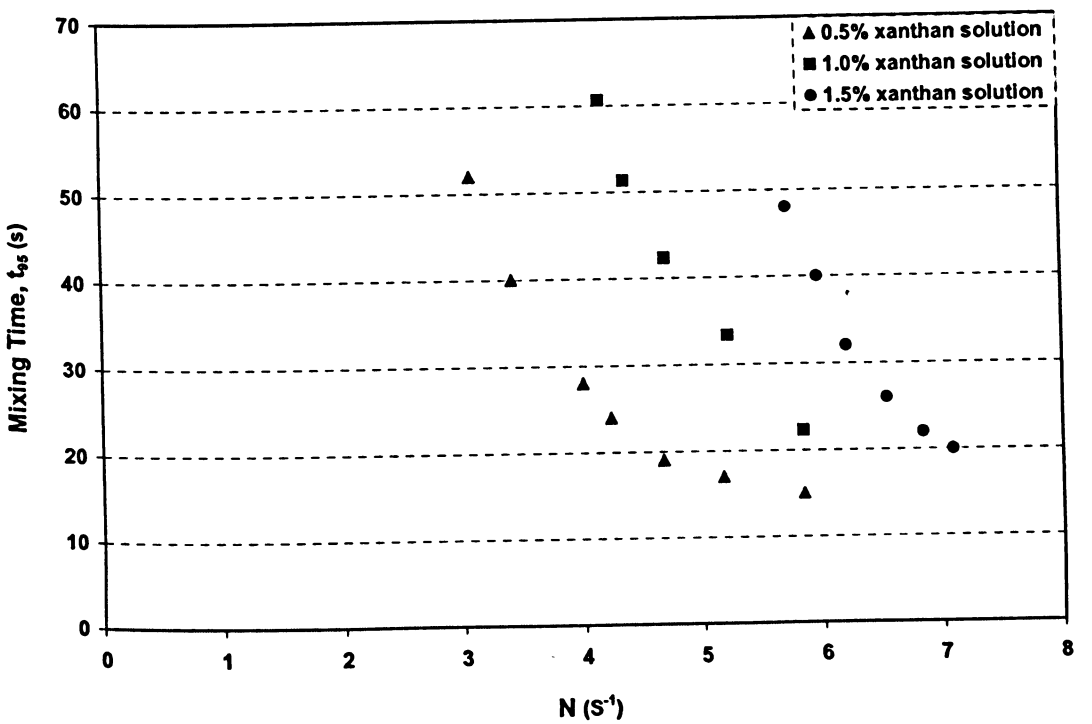

Fig. 6.50. Overall mixing time (ERT results from 4 planes) as a function of the impeller speed for 3 xanthan concentrations (0.5, 1 and 1.5 %).

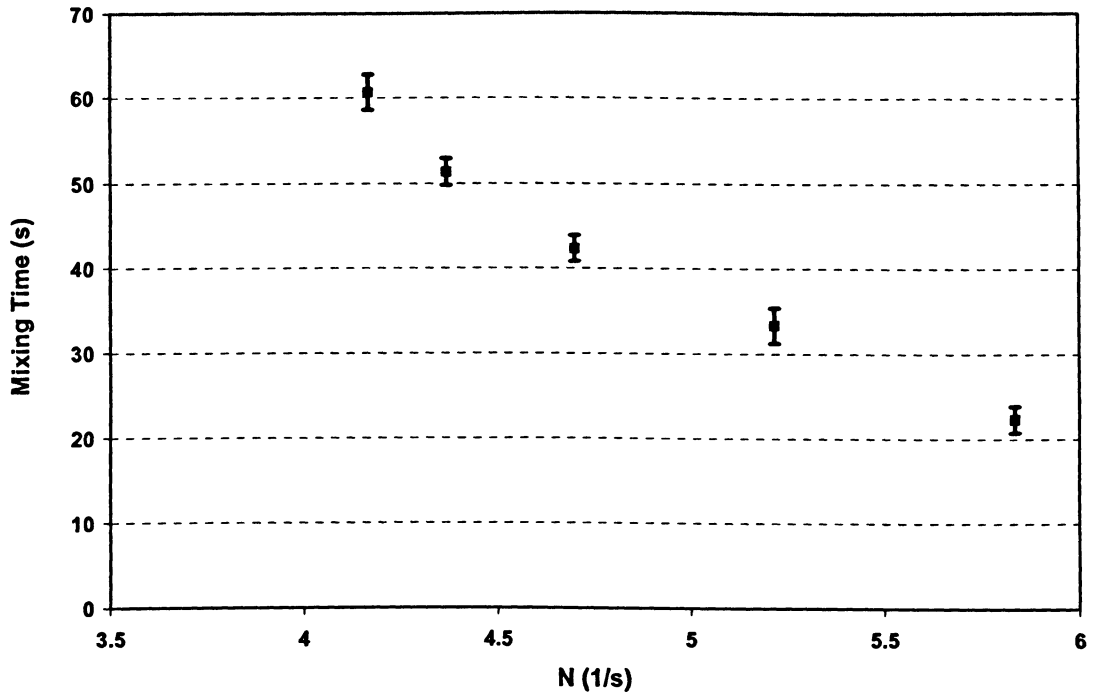

Fig. 6.51. Overall mixing time (ERT results from four planes) as a function of the impeller speed for 1.0% xanthan.

6.7.1.1 Comparison of Mixing Time with Correlations

In order to quantitatively assess the accuracy of the overall experimental mixing times (from four planes), the results were also compared with empirical correlations available from the literature (Section 2.7.2) as follows:

The results have been correlated in a dimensionless form using Moo-Young *et al.* (1972) relation:

$$N.t_m = a\,\mathrm{Re}^b \tag{6.12}$$

The variation of the dimensionless mixing time ($N.t_m$) vs. Reynolds number (Re) is shown in Fig. 6.52. As expected the dimensionless mixing time ($N.t_m$) decreases by increasing the Reynolds number. In order to evaluate if this trend can be correlated by eq. (6.12), the regression coefficients a and b should be obtained. The coefficients a and b in the

Reynolds range of 350-700 (from all three concentrations) were found as 1.20×10^5 and -1.0453581 with R^2=0.92. The correlation coefficient (R^2) is a measure of how well the equation correlates the data. A value of 1.0 would indicate a perfect correlation.

For *Re* number >10^3, the dimensionless mixing times remain constant at 87. It should be noted that as this work has been carried out in the transition regime, there are not too many measurements in *Re*>10^3.

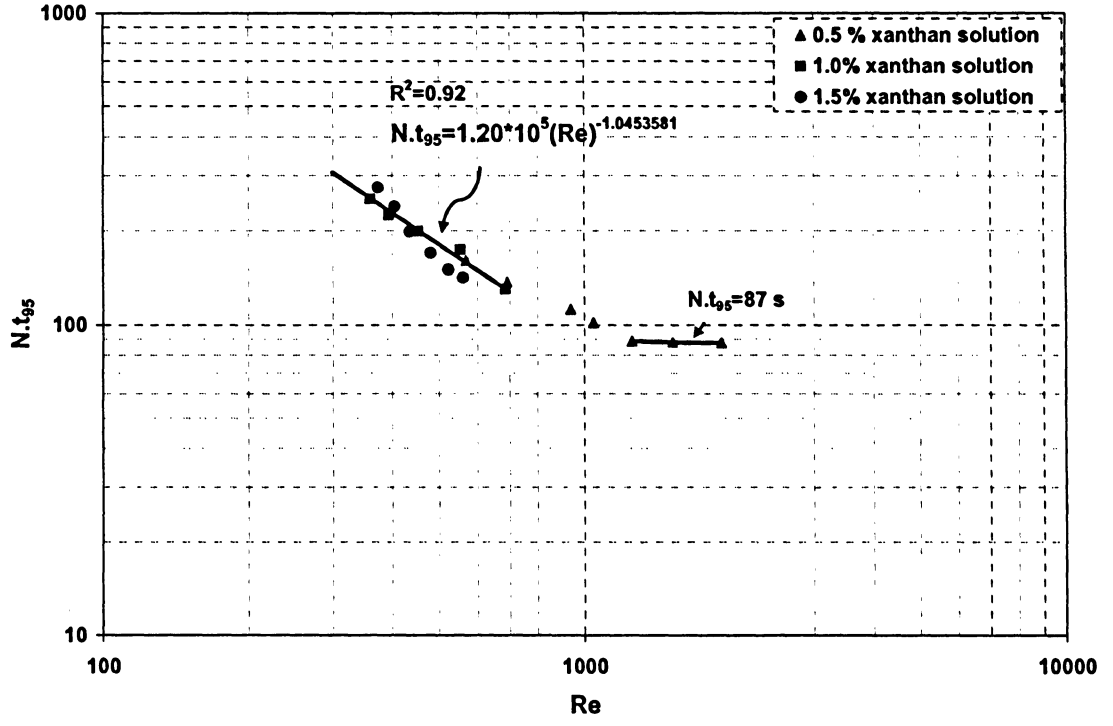

Fig. 6.52. Dimensionless overall mixing time (ERT results from four planes) vs. Re number

The coefficients *a* and *b* for the dimensionless mixing time trendlines are shown in Table 6.3 for each concentration. It shows that the dimensionless mixing times are correlated well with Re for each concentration.

Table 6.3. Coefficients of mixing time correlation ($N.t_m=aRe^b$) with xanthan solutions.

solution	Range of *Re*	*a*	*b*	R^2
0.5% xanthan solution	500-1000	1.64×10^4	-0.73072	0.997
1.0% xanthan solution	350-700	7.61×10^4	-0.97109	0.984
1.5% xanthan solution	350-600	5.43×10^6	-1.67454	0.983

The mixing time is often correlated with data power consumption in order to obtain the efficiency of the mixing system. A unique equation exists between the mixing time and power consumption per unit volume and is given by the following equation (Moo-Young *et al.*, 1972; Nienow, 1997):

$$t_m = c\left(\frac{P}{V}\right)^d \tag{6.13}$$

The exponent on the *P/V* term can be seen to be -1/3 in most studies (refer to Section 2.7.2), which performed in turbulent regime. The main difference between previous studies is in value of "*c*" depending on the impeller and vessel geometry.

The variation of the overall mixing time (t_m) with *P/V* (specific power consumption) is presented in Fig. 6.53, which shows the specific power required to obtain the specified homogenization effectiveness. The regression coefficients *c* and *d* are shown in Table 6.4. The values of "*d*" are bigger (in magnitude) than 0.33. This is mainly due to transition regime in which experiments have been performed. However, the exponents are not the same as the reported value; the correlation coefficients (R^2) show that the obtained data (for all three concentrations) is well correlated with eq. (6.13).

On other hand, the value of -0.33 reported in literature were often obtained with local mixing times using one or few probes. This can be confirmed in Fig. 6.54 showing the variation of the local mixing time (ERT results from four pixels) with *P/V*. The regression coefficients *c* and *d* are 120.2136 and -0.314532.

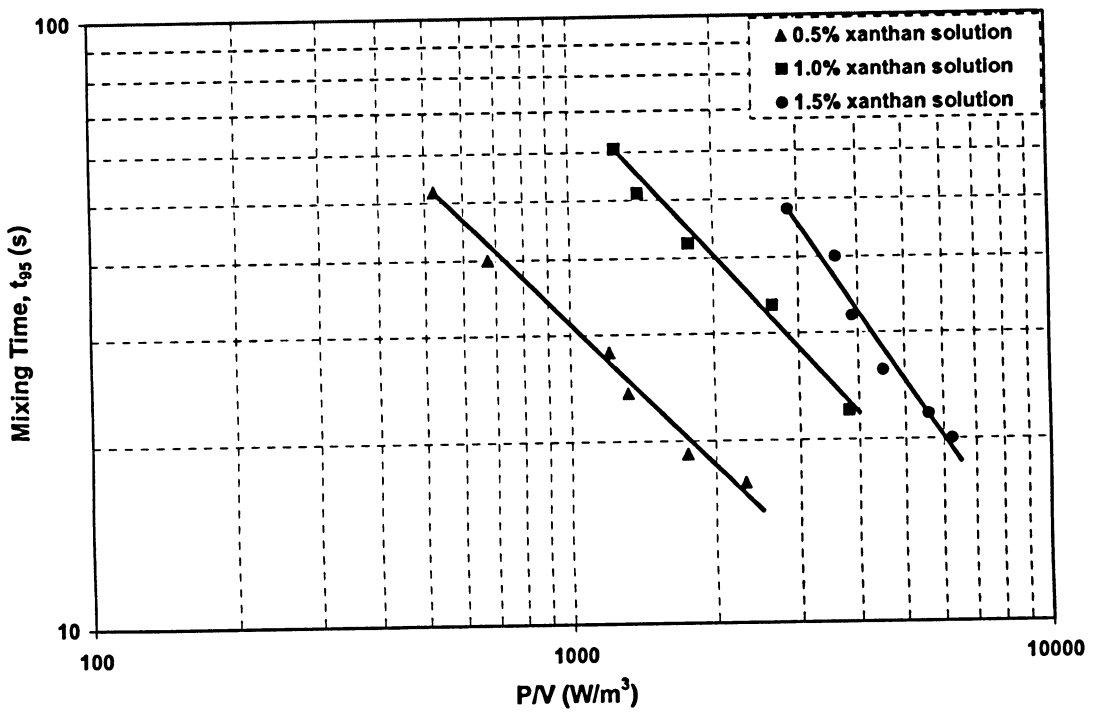

Fig. 6.53. Overall mixing time (ERT results from four planes) versus power consumption per unit volume.

Table 6.4. Coefficients of the overall mixing time correlation ($t_{95}=c(P/V)^d$) with xanthan solutions.

solution	Range of *Re*	*c*	*d*	R^2
0.5% xanthan solution	500-1500	5.95×10^3	-0.77241	0.971
1.0% xanthan solution	350-700	2.36×10^4	-0.84081	0.985
1.5% xanthan solution	350-600	5.69×10^5	-1.17821	0.971

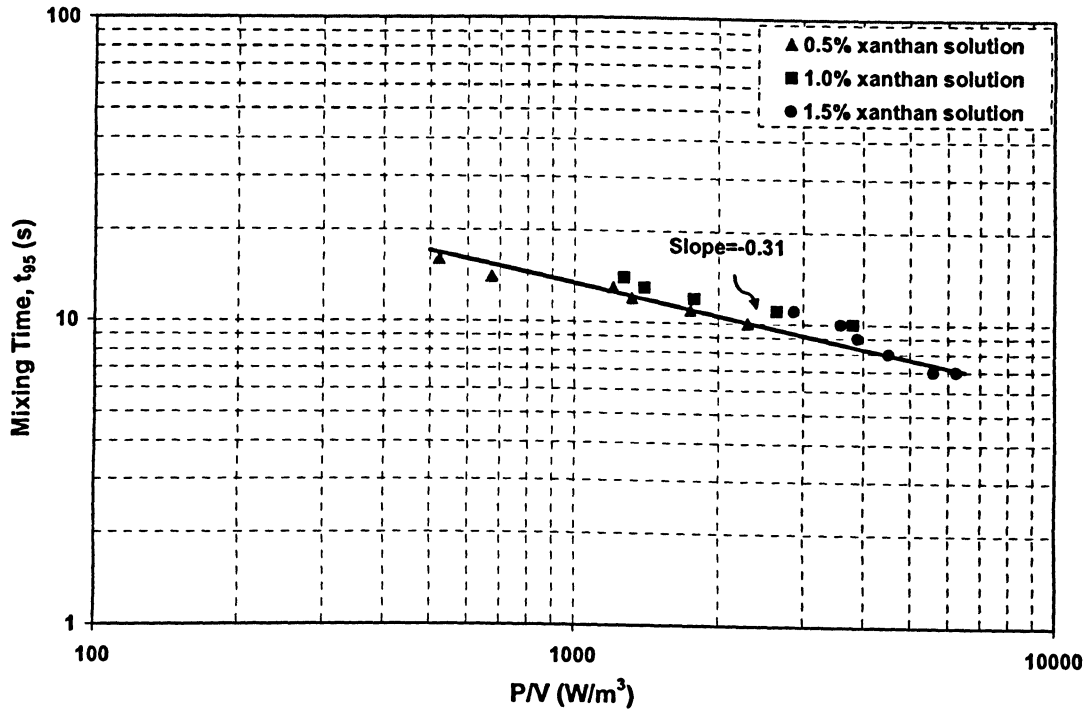

Fig. 6.54. Local mixing time (ERT results from four pixels) versus power consumption per unit volume.

6.7.2 CFD Results for Mixing Time

The numerical simulations were performed to understand the effects of impeller rotational speed and rheological properties of solution (three different xanthan solutions with different rheological properties) on the mixing time. The local mixing times were obtained from the simulated dimensionless tracer concentration profiles as explained in Section 5.6.4. As checked before (refer to Section 5.6.4.2), the number of probes did not have significant effect on the mixing times in CFD approach and consequently it was decided to use four virtual probes providing local mixing times. Here again the time that it takes the tracer reaches 95% of steady state value was defined as the mixing time. All the simulations provide a reasonable trend of the mixing time as a function of impeller speed, shown in Fig. 6.55 to Fig. 6.57. It is clear that as the impeller speed increases, the mixing time decreases.

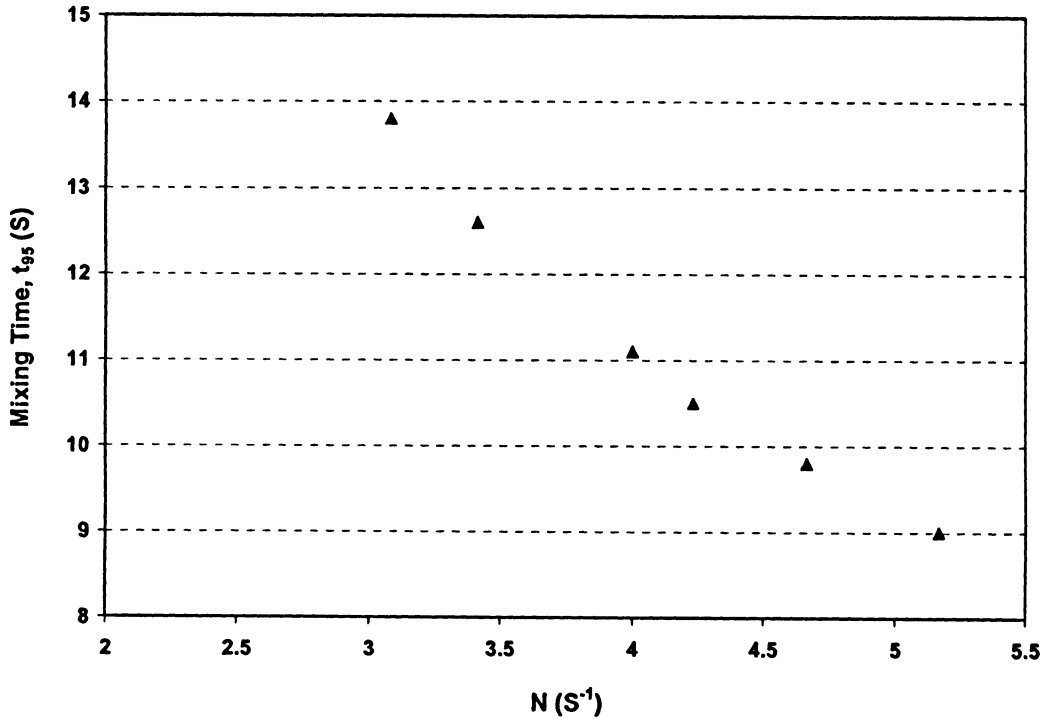

Fig. 6.55. Local mixing time (CFD results from four points) as a function of impeller speed for 0.5% xanthan concentration.

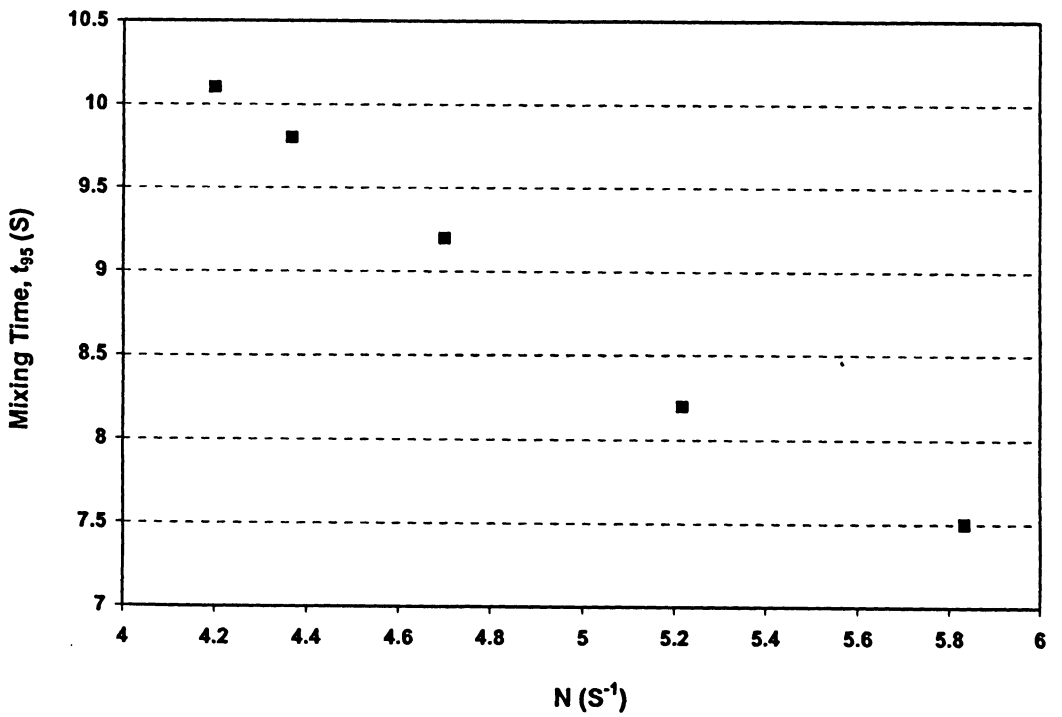

Fig. 6.56. Local mixing time (CFD results from four probes) as a function of impeller speed for 1.0% xanthan concentration.

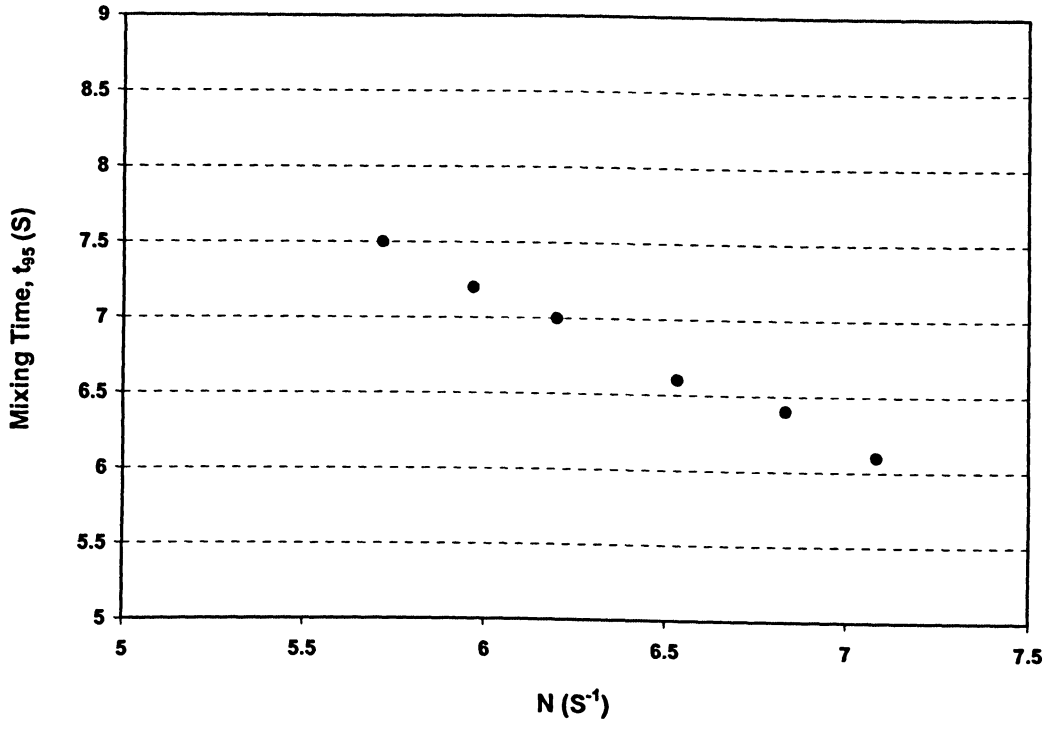

Fig. 6.57. Local mixing time (CFD results from four probes) as a function of impeller speed for 1.5% xanthan concentration.

The variation of the local mixing time (t_m) with P/V (specific power consumption) can be observed in Fig. 6.58, which shows the specific power required to obtain the specified homogenization effectiveness. The regression coefficients c and d are 113.2695 and -0.3301264. It can be observed that mixing time varies inversely with the cube root of the power consumed per unit volume of the liquid, which is in good agreement with the literature (Nere *et al.*, 2003). This confirms our previous conclusion that the value -0.33 for the exponent can be obtained from local mixing times.

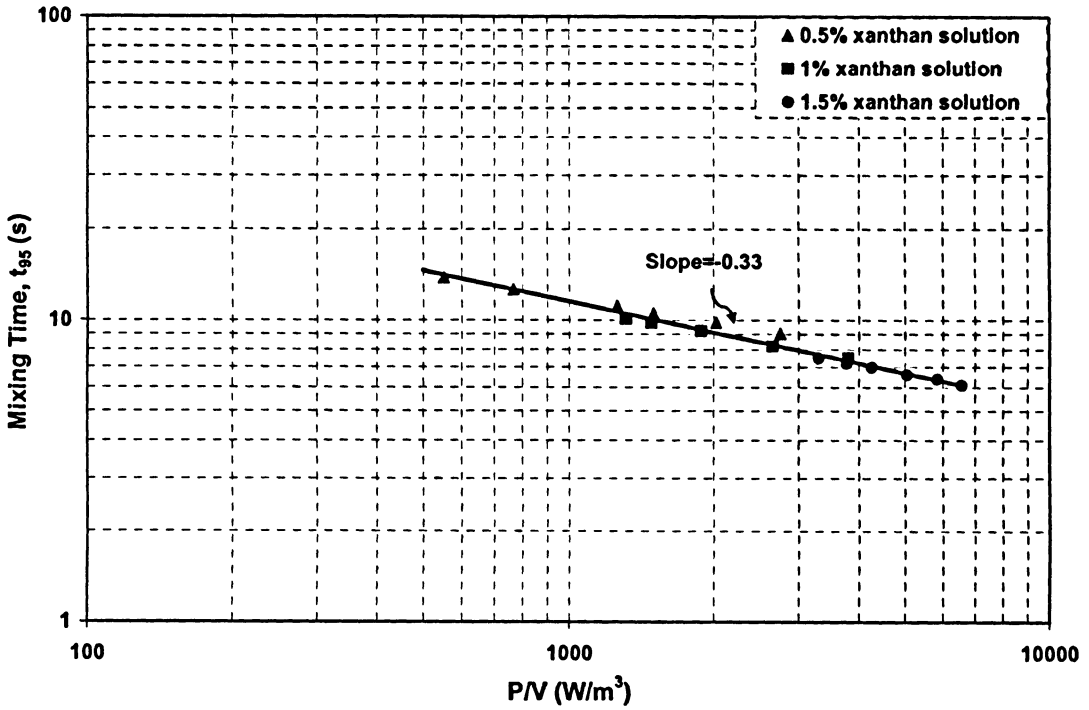

Fig. 6.58. Local mixing time (CFD results from four points) versus power consumption per unit volume.

As mentioned ERT has the ability to predict local mixing time by defining some pixels from measuring planes. These pixels were selected as CFD virtual probes. Fig. 6.59 shows the CFD and experimental mixing times. The magnitude of the difference between the predicted and measured mixing times varies with impeller speed and solution concentration such as the error for 0.5% xanthan solution is <16%, while for 1.0% and 1.5% xanthan solutions are <50%. These discrepancies indicate that CFD simulations are not able to predict the mixing times very well. The reasons may be a result of a laminar-flow model being employed in a transitional-flow regime for CFD, MRF method as a steady state technique adopted for the flow field before switch to transient simulations for mixing time, and/or inadequate grid resolution not capturing all of the small local recirculation zones and swirls near the blade tip. Thus, it can be observed that the mixing time predictions depend on the accuracy of the predicted flow pattern, i.e. the simulation flow with laminar model and MRF do not yield accurate flow predictions of the transition and turbulent flow field. The discrepancy between CFD and experimental data for

measuring mixing time has been commonly reported in the literature such as Jaworski *et al.*, 2000 and Bujalski *et al.*, 2002.

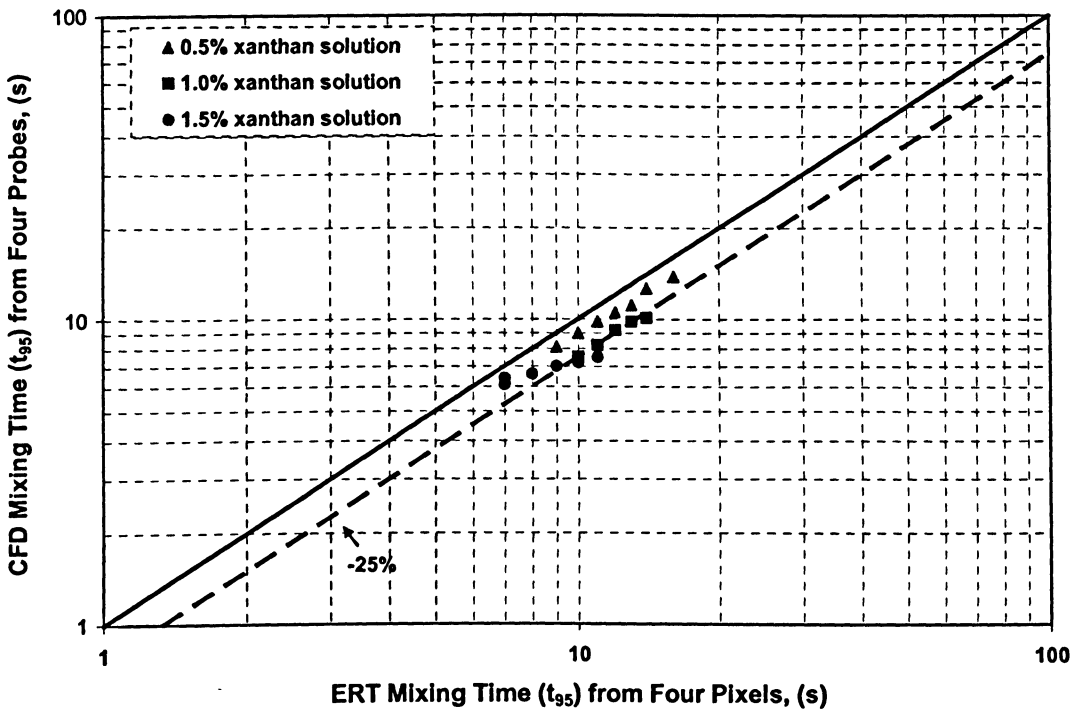

Fig. 6.59. Comparison of experimental data (ERT results from four pixels) and CFD predictions (form four virtual probes) for the local mixing time in xanthan solutions.

7. CONCLUSIONS

Using electrical resistance tomography (ERT) and computational fluid dynamics (CFD), this study reports various important features of mixing performance of the yield-pseudoplastic fluids, which hopefully will contribute to the better understanding of non-Newtonian fluids mixing.

An ERT system using 4-plane set of peripheral sensing electrodes, each containing 16 electrodes has been used to study the mixing performance of the xanthan solutions agitated by a Scaba 6SRGT impeller and the following main conclusions were drawn:

- The ability of the ERT system to distinguish the flow pattern of the impeller and monitor the mixing processes was demonstrated by monitoring the distribution of the tracer concentration as 2-D tomograms and 3-D solid body images

- It is believed that this is the first application of ERT for measuring and monitoring the cavern formation in yield stress fluids. Using ERT, the formation and characteristics of cavern formed in mixing of xanthan solutions have been successfully monitored and measured. The images have clearly shown the presence of well-agitated zones (cavern) with growth in size by increasing agitator speed. Under the condition where cavern does not meet the tank wall, the cavern diameters are well correlated with the cylindrical model (eq.(2.23)).

- Using ERT, the overall mixing times were measured using 1,264 probes in the four different axial positions, two upper and two lower than impeller positions for three xanthan solutions in the transition regime. The trend of mixing times by increasing impeller speed was reasonably good for all three concentrations, as impeller speed increases the mixing time decreases. An attempt was made to plot the dimensionless mixing time ($N.t_m$) versus Re number and Moo-Young coefficients were found, confirming the acceptable trend for mixing time as a function of Re number.

The CFD simulations were also performed and following the CFD validation by the experimental torque measurements, the following main conclusions were drawn:

- The power curves of the Scaba 6SRGT in the agitation of non-Newtonian fluids with yield stresses have been determined using CFD simulations as well the experimental results. The power input calculated using CFD simulations matched the experimentally determined values well. This provided a validation for CFD results. Both results showed that P_o was decreased by increasing Re number and for $Re \leq 10$, $P_o \approx Re^{-1}$.

- The pumping capacity of the impeller was evaluated by introducing flow number. It was found that as the impeller speed was reduced, the impeller flow number was reduced as well, and also viscoplasticity generally tends to decrease flow number (N_Q), as expected, in fact it reduces the amount of flow being pumped by the agitator. It was shown that the flow rate discharged from the impeller in radial direction was relatively equal to the flow returned back to the impeller in axial directions.

- The velocity vectors obtained from the CFD simulations agreed qualitatively with the typical flow pattern of a Scaba as a radial-flow impeller. Using CFD, the valuable information about the flow field generated by Scaba was obtained, such as velocity angle and velocity profile.

- It was shown that the cavern diameter is less sensitive to the cavern defining velocity. The simulations have clearly shown the presence of well-agitated caverns with growth in size with increasing agitator speed. Outside of these caverns, the fluid is stagnant because of its yield stress. Considerable cavern growth in a yield stress fluid took place in transitional regime. Under the condition where the cavern did not reach the tank wall, the cavern diameter was well correlated with the cylindrical model (eq. (2.23)). When the cavern reached the wall, its height increased with agitation speed as expected.

- The local mixing times predicted from CFD simulations agreed well with the literature in a way that mixing times varied inversely with the cube root of the power

consumed per unit volume of the solution. CFD under predicted the local mixing times measured using ERT by 11-47%.

7.1 Recommendations for Future Work

The results from experimental work and numerical simulations in this study drew attention to the areas for future considerations as follow:

- Further work can be made to evaluate the effect of the impeller type and position in the mixing tank.

- Since xanthan solutions are produced in the fermentors, the mixing performance can be evaluated in the presence of oxygen using CFD and ERT. Both techniques have the ability to provide valuable information about two-phase (gas-liquid) mixing performance.

- The temporal resolution used in this study for ERT can be reduced to give the more accurate dynamic changes following the tracer injection, especially in the case of mixing time evaluations.

- The spatial resolution used in this study for ERT tomograms can be improved using an iterative algorithm based on the sensitivity conjugate gradient method.

- Flow was modeled as laminar for all simulations; applying turbulent models in the transient regime may improve the simulation results for this regime. This will allow us to determine the quality of the laminar model used in this study.

- The Hercshel-Bulkley model was used as an approximation of the rheological behaviour of xanthan solutions. Using the other rheological models (refer to Section 2.2) may improve the accuracy of the CFD model development.

- The CFD model may be improved by applying the sliding mesh method as an unsteady approach. Although an unsteady approach requires more computational time compared with MRF, but it will provide information about the accuracy of the steady state approach.

- The boundary conditions used in this model can be improved by including the modelling of the free surface. This can be performed by considering the multiphase modeling in order to include the interface of xanthan and air in the computational domain.

- The velocity profiles obtained using CFD can be examined by experimental results. ERT can be used to measure the velocity, however it will be a difficult task, but it can be used as a validation for CFD simulations.

Nomenclature

a	constant, dimensionless (eq.(2.10))
a	constant in an empirical given by Moo-Young (Table 2.2), dimensionless
a_p *and* a_{nb}	linearized coefficients (eq.(5.13))
$\vec{A}$	surface area vector, m^2
A_S	swept surface, m^2
b	constant, dimensionless (eq. (2.10))
b	constant in an empirical given by Moo-Young (Table 2.2), dimensionless
b_0, b_1, b_2, b_3	constants in an empirical given by Biggs (Table 2.2), dimensionless
B_A	blade angle, rad
c	constant, dimensionless (eq. (2.32))
C	impeller clearance from the base of the vessel, m
C	constant, dimensionless (eq. (2.10))
C_d	an arbitrary radial distance from the tip of the blade (eq. (2.18))
d	constant, dimensionless (eq. (2.32))
D	impeller diameter, m
$\overline{\overline{D}}$	rate of strain tensor, s^{-1}
D	diffusion conductance, m^2s^{-1}
D_e	diffusion conductance on the face "e",
Dc	cavern diameter, m
D_m	molecular diffusivity of the tracer, m^2s^{-1}
E	the east node
f	friction factor in an empirical given by Fox and Gex (Table 2.2), dimensionless
F	strength of the convection,
F_e	strength of the convection on the face "e", N
$\vec{F}$	external (body) force, N
F_z	axial force imparted by the impeller, N

g	gravitational acceleration, ms^{-2}
H	height of fluid in vessel, m
H_c	cavern height, m
i, I	current, mA
I	unit tensor
k_s	Metzener–Otto constant for calculating shear rate, dimensionless
K_p	proportionality constant of the power number, dimensionless
FK	fluid consistency coefficient, Pa s^n
m	constant in the cross model (Table 2.1), dimensionless
M	torque, N.m
$\overline{M}$	mean torque, N.m
M	number of measurements (eq.(3.2) and eq. (3.3))
$\vec{n}$	normal vector
n	power-law index, dimensionless
n	number of nodes
n_b	number of baffles
N	impeller rotational speed, rot s^{-1}
N	constant in the Carreau model (Table 2.1), dimensionless
N	number of electrodes (eq. (3.2))
N_f	axial force number, dimensionless
N_{faces}	number of faces enclosing the cell
N_Q	impeller flow number, dimensionless
p	constant describing the rate of axial fluid expansion once the cavern touches the vessel wall (eq. (6.11))
p	pressure, Pa
P	power, W
P	general nodal point
P_o	power number, dimensionless
Q	volumetric flow rate of fluid, m^3s^{-1}

Q	equiangle skewness (Section 5.6.2)
r	radial coordinate, m
R	nonlinear functional
$2r/T$	dimensionless radial coordinate
$R^{c}_{iteration\ N}$	unscaled continuity residual
$R^{c}_{iteration\ 5}$	continuity residual in the first five iteration
R^{Φ}	unscaled residual
R^{Φ}_{s}	scaled residual
S_{φ}	generalized source term, variable unit
t_c	circulation time, s
t	time, s
T	tank diameter, m
T	temperature, ◦C
v_o	fluid velocity at cavern boundary, ms^{-1}
U_{tip}	impeller tip speed, ms^{-1}
$\bar{v}$	mean velocity, ms^{-1}
$\vec{v}$	velocity vector, ms^{-1}
u_i, v_j, w_k	cartesian velocity component normal to face, ms^{-1}
V	fluid volume, m^3
V	cell volume in (eq. (5.12)), m^3
V	voltage, v
V_C	volume of a cavern, m^3
w	local mass fraction of the tracer, dimensionless
W	impeller blade height, m
W	west node
z	axial coordinate, m
z/H	dimensionless axial coordinate

Greek letters

a	proportional constant (eq. (2.14))
α	ellipse parameter, dimensionless (eq. (2.30))
α	under-relaxation factor (eq.(5.35))
α_c	time constant in cross model (Table 2.1), s
α_S	concentration of NaCl, (g/l)
β	ratio of ellipse major axis to minor axis, dimensionless (Eq. (2.31))
$\dot{\gamma}$	shear rate, s^{-1}
$\dot{\gamma}_{av}$	average shear rate in the mixing vessel, s^{-1}
δ	distinguishability, dimensionless
δx	characteristic length (cell width), m
δx_{WP}	distance between nodes W and P, m
δx_{PE}	distance between nodes P and E, m
$\Delta\vec{r}$	displacement vector from the upstream cell centroid to the face centroid, m
Γ	free source inhomogeneous domain, dimensionless
Γ_φ	generalized diffusion coefficient, variable unit
ε	proportional constant, dimensionless (eq. (2.27))
ε	precision of measurement, dimensionless (eq. (3.1))
ε_v	τ_{av} in (eq. (2.23)) may be expressed in terms of the average dissipation rate per volume
η	non-Newtonian viscosity, Pa.s
λ_c	time constant, s (Table 2.1)
μ	Newtonian viscosity, Pa.s
μ_0	zero shear viscosity, Pa.s (Table 2.1)
μ_{app}	apparent viscosity, kg $m^{-1}s^{-1}$
μ_∞	infinite shear viscosity, Pa.s (Table 2.1)
ρ	fluid density, Kg/m^3
σ	surface tension of liquid, dyes.cm^{-1}
σ_{mc}	conductivity, ms/cm

τ	shear stress, Pa
$\bar{\bar{\tau}}$	viscous stress tensor, Pa
τ_{av}	average shear stress, Pa
τ_d	representative shear stress in the dissipating zones, Pa
τ_y	yield stress, Pa
υ	kinematic viscosity of the liquid, m^2s^{-2}
Φ	generalized conserved quantity, variable unit
$\tilde{\phi}_f$	averaged Φ at face, variable unit
Φ_{old}	old value of variable in iteration, variable unit

Subscripts

av	average
c, C	axial and radial circulation
c	cavern
cv	control volume
d	dissipating
e	referred to east (Chapter 5)
f	face
in	in zone entering
m	general mixing time
n	normal to a surface
nb	neighbour cell
out	out zone leaving
p	the general nodal point
r, R	radial component
s	swept (surface)
t, T	tangential component
tip	impeller tip

tu	turbulent flow
w	at vessel wall
w	referred to west (chapter 5)
y	yield stress
z, Z	axial component
95	95% mixing times

Dimensionless Numbers

Fr	Froude number, dimensionless
Pe	Peclet number, dimensionless
Re	Reynolds number, dimensionless
Re_y	yield stress Reynolds number, dimensionless
$N.t_m$	dimensionless mixing time

Abbreviations

ADC	analogue digital converter
AMG	algebraic multigrid
API	active pharmaceutical ingredient
CFD	computational fluid dynamics
CMMR	common-mode rejection ratio
CPU	central processing unit
DAC	digital analogue converter
DAS	data acquisition system
ECT	electrical capacitance tomography
EIT	electrical impedance tomography
ERT	electrical resistance tomography
FDM	finite difference method
FEM	finite volume method
FVM	finite volume method
GFM	ground floating measurement

HWA	hot wire anemometry
LBP	linear back projection
LC	liquid crystal
LCT	liquid-crystal thermography
LDA	laser Doppler anemometry
LDV	laser Doppler velocimetry
MRF	multiple reference frame
MNR	modified Newton-Raphson
MUX	multiplexer
NRRL	northern regional research laboratories
pH	potential of hydrogen
PRESTO	PREssure STaggering Option
PISO	pressure implicit with splitting of operators
PIV	particle image velocimetry
pLIF	planner laser induced fluorescence
PM	parametric model
RAM	random access memory
RMS	root-mean-square
SCG	sensitivity conjugate gradient
SNR	signal to noise
SIMPLE	semi-Implicit Method for Pressure-Linked Equation
SIMPLEC	*SIMPLE* consistent
UV	ultraviolet
VCCS	voltage controlled current source
XRF	X-ray fluorescence

Operations

$\frac{\partial}{\partial x}$	partial derivative with respect to space

$\frac{\partial}{\partial t}$	partial derivative with respect to time
$\frac{D}{Dt}$	substantive derivative
∇	Del or nabla operator

Bibliography

Abdullah M. Z. "Electrical Impedance Tomography for Imaging Conducting Mixtures in Hydrocyclone Separators." PhD Thesis University of Manchester (1993).

Adams L. W. and Barigou M. "CFD Analysis of Caverns and Pseudo-Caverns Developed During Mixing of Non-Newtonian Fluids." Chem. Eng. Res. Des., 85 (A5) (2006): 598-604.

Ahmad J., Ramaswamy H. S., and Ngadi M. O. "Rheological Characteristics of Arabic Gum in Combination with Guar and Xanthan Gum Using Response Surface Methodology: Effect of Temperature and Concentration." Int. J. Food Prop., 8 (2) (2005): 179-192.

Alliet-Gaubert M., Sardeing R., Xuereb C., Hobbes P., Letellier B., and Swaels P. "CFD Analysis of Industrial Multi-Staged Stirred Vessels." Chem. Eng. Process., 45 (2006): 415-427.

Alvarez M., Zalc J., Shinbort T., Arratia P., and Muzzio F. "Mechanisms of Mixing and Creation of Structure in Laminar Stirred Tanks." AIChE J., 48 (10) (2002): 2135-2148.

Amanullah A., Hjorth S. A., and Nienow A. W. "Cavern Sizes Generated in Highly Shear Thinning Viscous Fluids by Scaba 3SHP1 Impeller." Trans. IChem. E., (part-C) 75 (1997):232-238.

Amanullah A., Hjorth S. A., and Nienow A. W. "A New Mathematical Model to Predict Cavern Diameters in Highly Shear Thinning, Power Law Liquids Using Axial Flow Impellers." Chem. Eng. Sci., 53 (3) (1998): 455-469.

Armenante P. M. and Chou C. "Velocity Profiles in a Baffled Vessel with Single or Double Pitched Blade Turbines." AIChE J., 42 (1996): 42-54.

Armenante P. M., Luo C., Chou C. C., Fort I., and Medek J. "Velocity Profiles in a Closed, unbaffled Vessel: Comparison between Experimental LDV data and Numerical CFD Prediction." Chem. Eng. Sci., 52 (20) (1997): 3483-3492.

Arratia P. E., Kukura J., Lacombe J., and Muzzio F. J. "Mixing of Shear-Thinning Fluids with Yield Stress in Stirred Tanks." AIChE J., 52 (7) (2006): 2310-2322.

Ascanio G., Brito-Bazan M., Brito-De La Fuente E., Carreau P. J., and Tanguy P. A. "Unconventional Configuration Studies to Improve Mixing Times in Stirred Tanks." Can. J. Chem. Eng., 80 (2002): 558-565.

Ascanio G., Foucault S., and Tanguy P. A. "Performance of a New Mixed Down Pumping Impeller." Chem. Eng. Technol., 26 (8) (2003): 908-911.

Aubin J., Fletcher D. F., and Xuereb C. "Modeling Turbulent Flow in Stirred Tanks with CFD: the Influence of the Modeling Approach, Turbulence Model, and Numerical Scheme." Exp. Thermal and Fluid Sci., 28 (2004): 431-445.

Bakker A. and Gates L. E. "Properly Choose Mechanical Agitators for Viscous Liquids", Chem. Eng. Prog., 91 (1995): 25-34.

Barailler F., Heniche M., and Tanguy P. A. "CFD Analysis of a Rotor-Stator Mixer with Viscous Fluids." Chem. Eng. Sci., 61 (2006): 2888-2894.

Barber C. D. and Brown B. H. "Applied Potential Tomography." J. of Phys. E: Sci. Instrum 17 (9) (1984): 723-733.

Barber C. D., Brown B. H., and Freeston I. L. "Imaging Spatial Distributions of Resistivity Using Applied Potential Tomography." Electron. Lett., 19 (1983):933-935.

Barakat H. Z. and Clark J. A. "Analytical and Experimental Study of Transient Laminar Natural Convection Flows in Partially Filled Containers." Proc. 3rd Int. Heat Transfer Conf., 57 (1966): 152-162.

Batchelor G. K. "An Introduction to Fluid Dynamics." Cambridge Univ. Press, Cambridge, England, (1967).

Beck M. S., Campogrande E., Morris M. A., Williams R. A., and Waterfall R. Tomography Techniques and Processes Design and Operation. Computational Mechanics Publications, (1993).

Biggs R. D. "Mixing Rates in Stirred Tanks." AIChE J., 9 (5) (1963): 636-640.

Bird R. B., Dai G. C., and Yarusso B. J. "The Rheology and Flow of Viscoplastic Materials." Rev. Chem. Eng., 1 (1982): 1-70.

Bird R. B., Stewart W E., and Lightfoot E. N. "Transport Phenomena." 2nd ed. New York: John Wiley & Sons. Inc, (2002).

Blazek J. "Computational Fluid Dynamics: Principles and Applications." 2nd ed. Amsterdam: Elsevier Inc., (2005).

Bolton G. T. "A Review of Linear Electrical Tomography Probes for Monitoring the Behaviour of Multiphase Mixing Processes." 12th European Conference on Mixing, Bologna, (2006).

Bolton G. T., Hooper C. W., Mann R., and Stit E. H. "Flow Distribution Velocity Measurement in a Radial Flow Fixed Bed Reactor Using Electrical Resistance Tomography." Chem. Eng. Sci., 59 (2004): 1989-1997.

Bolton G. T. and Primrose K. M. "An Overview of Electrical Topographic Measurement in Pharmaceutical and Related Applied Areas." AAPS PharmSciTech., 6 (2) (2005): E137-E143.

Bradshaw I. J., Nisbet B. A., Kerr M. H., and Sutherland I. W. "Modified Xanthan-Its Preparation and Viscosity." Carbohydr. Polym., 3 (1983): 23–38.

Brennan D. J. and Lehrer I. H. "Impeller Mixing in Vessels. Experimental Studies on the Influence of Some Parameters and Formulation of a General Mixing Time." Trans. IChem. Eng., 3 (1976): 139-152.

Brandt A. "Multi-level adaptive solutions to boundary-value problems," Math. of Comput., 31 (1977): 333-390.

Brodkey R. S. "The Phenomena of Fluid Motions." Reading, MA: Addison-Wesley Co., (1967).

Brucato A., Ciofalo M., Crisfi F., and Micale G. "Numerical Prediction of Flow Fields in Baffled Stirred Vessels: A comparison of Alternative Modeling Approaches." Chem. Eng. Sci., 53 (1998): 3653-3684.

Bruun H. H. "Hot-Wire Anemometry Principles and Signal Analysis." New York: Oxford UP, (1995).

Bujalski W., Jaworski Z., and Nienow A. W. "CFD Study of Homogenization with Dual Rushton Turbines-Comparison with Experimental Results Part II: The Multiple reference Frame." Chem. Eng. Res. Des., 80 (2002):97-104.

Burns D. H. "Optical Tomography for Three-Dimensional Spectroscopy." Appl. Spectroscopy, (1994): 12A-19A.

Buwa V., Dewan A., Nasser A. F., and Durst F. "Fluid Dynamics and Mixing of Single-Phase Flow in a Stirred Vessel with a Grid Disc Impeller: Experimental and Numerical Investigations." Chem. Eng. Sci., 61 (2006): 2815-2822.

Calderbank P. H. and Moo-Young M. B. "The prediction of Power Consumption in the Agitation of Non- Newtonian fluids." Trans IChem E. 37 (1959):26-33.

Carey G. F. "Computational Grids, Generation, Adaptation, and Solution Strategies." Bristol: Taylor & Francis, (1997).

Casson N. "A Flow Equation for Pigment-Oil Suspensions of the Printing Ink Type. in Rheology of Disperse Systems." ed. C.C. Mill. New York: Pergamon P, (1959): 82-104.

Chhabra R. P. and Richardson J. F. "Non- Newtonian Flow in the Process Industries." 1st ed. Butterworth Heinemann, (1999).

Choo Y. K. "Surface Modeling, Grid Generation, and Related Issues in Computational Fluid Dynamics (CFD) Solution." OH: NASA CP-3291: Cleveland, (1995).

Chung F. H. and Smith D. K. "Industrial Application of X-Ray Diffraction." CRC PRESS, (2000).

Costes J. and Couderc J. P. "Study by Laser Doppler Anemometry of the Turbulent Flow Induced by a Rushton Turbine in a Stirred Tank: Influence of the Size of the Units -I. Mean Flow and Turbulence." Chem. Eng. Sci., 43 (1988): 2751-2764.

Courant R., Isaacson E., and Rees M. "On the Solution of Non-Linear Hyperbolic Differential Equations by Finite Differences." Comm. Pure Appl. Math. 5 (1952): 243-255.

"Customer's Guide Documentation." Chemineer Inc., (1998).

Darwish M., Asmar D., and Moukalled F. "A Comparative Assessment within a Multigrid Environment of Segregated Pressure-Based Algorithm for Fluid Flow at All Speeds." Numerical Heat Transfer, 45 (B) (2004): 49-74.

Delaplace G., Bouvier L., Moreau A., Guerin R., and Leuliet J. C. "Determination of Mixing Time by Colorimetric Diagnosis- Application to a New Mixing System." Exp. in Fluids, 36 (2004): 437-443.

Delaplace G., Thakur R. K., Bouvier L., Andre C., and Torrrez C. "Dimensional Analysis for Planetary Mixer: Mixing Time and Reynolds Number." Chem. Eng. Sci., 62 (2007): 1442-1447.

Drain L. E. "The Laser Doppler Technique." New York: John Wiley & Sons Ltd, (1980).

Dickin F. and Wang. M. "Electrical Resistance Tomography for Process Applications." Meas. Sci. Technol., 7 (1996): 247-260.

Distelhoff M. F. W., Marquis, A. J., Nouri, J. M., and Whitelaw, J. H. "Scalar Mixing Measurements in Batch Operated Stirred Tanks." Can. J. Chem. Eng., 75 (1997): 641-652.

Doraiswamy D., Grenville R. K., and Etchells A. W. "Two-Score Year of the Metzner-Otto Correction." Ind. Eng. Chem. Res. 33 (1994): 2253-2258.

Dyakowski, T. "Process Tomography Applied to Multi-Component Measurement." Meas. Sci. Techn. (1996): 343-353.

Dyakowski T., Wang S. J., Geldart D. and Beck M. S. "Tomographic Studies of Flow Patterns within a Circulating Fluidised Bed." Chem. Eng. Commun., 175 (1999): 117-130.

Elliot J. H. "Some Rheological Properties of Gum Solutions." Extracellular Microbial PolysaccharidesACS Symp., 45, (1977): 144–159 Washington, DC.

Elson T. P., and Cheesman, D. J. "X-Ray Studies of Cavern Sizes and Mixing Performance with Fluids Possessing a Yield Stress." Chem. Eng. Sci., 41 (10) (1986): 2555-2562.

Elson T. P. "Mixing of Fluids Possessing a Yield Stress." Proc. 6th European Conf on Mixing, Pavia. Italy, Organized by AIDIC-Associazione Italian di Ingegeneria Chemica (1988): 485-492.

Elson T. P. "The Growth of Caverns Formed around Rotation Impellers during the Mixing of a yield stress Fluid." Chem. Eng. Commun., 96 (1990): 303-391.

Etchells A. W., Ford W. N., and Short D. G. R. "Mixing of Bingham Plastics on an Industrial Scale." Fluid Mixing III, Ins. Chem. Eng. Symp., 10 (8) (1987):8-10.

Industrial Tomography System Ltd. "ERT Sensor Design Guidelines." Industrial Tomography System Ltd., (2005).

Foucault S., Ascanio G., and Tanguy P. A. "Mixing Time in Coaxial Mixers with Newtonian and Non-Newtonian Fluids." Ind. Eng. Chem. Res., 45 (2006): 352-359.

Ferguson J. and Kemblowski Z. "Applied Fluid Rheology." New York: Elsevier Applied Science, (1991).

Fluent Inc, "Fluent 6.3 User's Guide Documentation." FLUENT Inc, (2006).

Ford C. "CFD Simulation of Mixing Dynamics in Agitated Pulp Stock Chests." MASc Thesis, University of British Columbia, (2004).

Ford C., Ein-Mozaffari F., Bennington C. P. J., and Taghipour F. "Simulation of Mixing Dynamics in Agitated Pulp Stock Chests Using CFD." AIChE J., 52 (10) (2006): 3562-3569.

Fox E. A. and Gex, V. E. "Single Phase Blending of Liquids." AIChE J., 2 (4) (1956):539-544.

Fransolet F., Crine M., Marchot P., and Toye D. "Analysis of Gas Holdup in Bubble Columns with Non-Newtonian Fluid Using Electrical Resistance Tomography and Dynamic Gas Disengagement Technique." Chem. Eng. Sci., 60 (2005): 6118-6123.

Galindo E. and Nienow A. W. "Mixing of Highly Viscous Simulated Xanthan Fermentation Broths with the Lightnin A-315 Impeller." Biotechnol. Prog. 8 (3) (1992): 223-239.

Galindo E. and Nienow A. W. "The Performance of the Scaba 6SRGT Agitator in the Mixing of Simulated Xanthan gum Broths." Chem. Eng. Technol., 16 (1993):102-108.

Galindo E., Torrestiana B., and García-Rejón A. "Rheological characterization of xanthan fermentation broths and their reconstituted solutions." Bioproc. Eng. 4 (1989): 113-118.

Gentric C., Mignon D., Bousquet J., and Tanguy P. A.. "Comparison of Mixing in Two Industrial Gas-Liquid Reactors Using CFD Simulations." Chem. Eng. Sci., 60 (2005): 2253-2272.

Gentry, R. A., R. E. Marthin, and B. J. Daly. "An Eulerian Differencing Method for Unsteady Compressible Flow Problems." J. Comput. Phys. 1 (1966): 87-118.

García-Ochoa F. and Casas J. A. "Apparent Yield Stress in Xanthan Gum Solution at Low Concentration." Chem. Eng. J., 53 (1994): B41–B46.

Gracia-Ochao F., Casas J. A., and Mohedan A. F. "Precipitation of Xanthan Gum." Sec Sci Technol., 28 (1993): 1303-1313.

Gracia-Ochao F., Santos V. E., Casas J. A., and Gomes E. "Xanthan Gum: Production, Recovery, and Properties." Biotechnol. Adv., 18 (15) (2000): 549-579.

Garg V. K. "Applied Computational Fluid Dynamics." Marcel Dekker, Inc. (1998): 118.

Gisser D. G., Issacson D., and Newell J. "Current Topics in Impedance Imaging." Clin. Phys. Physiol. Meas., 8 (A) (1987): 36-46.

Gjesdal T. and Lossius M. E. H. "Comparison of Pressure Correction Smoothers for Multigrid Solution of Incompressible Flow." Int. J. Numer. Meth. Fluids, 25 (1997): 393-405.

Hackl A. and Wurian H. "Determination of Mixing Time." Ger. Chem. Eng. 2 (1979): 103.

Hannote M., Flores F., Torres L., and Galindo E. "Apparent Yield Stress Estimation in Xanthan Gum Solution and Fermentation Broths by a Low-Cost Viscosimeter." Chem. Eng. J., 45 (1991): B49–B56.

Harlow F. H. and Welch J. E. "A Numerical Calculation of Time Dependent Viscous Incompressible Flow of Fluid with Free Surface." Phys. Fluids, 8 (1965): 2182-2189.

Harnby N., Edwards M. F., and Nienow A. W. "Mixing in the Process Industries." Reed Educational and Professional Publishing Ltd., (1992).

Harris C. K., Roekaerts D., and Rosendal F. J. J. "Computational Fluid Dynamics for Chemical Reactor Engineering." Chem. Eng. Sci., 51 (10) (1996): 1569-1594.

Hassler R. A. and Doherty D. H. "Genetic Engineering of Polysaccharide Structure: Production of Variants of Xanthan Gum in Xanthamonoas campestris." Biotechnol. Prog. 6 (1990): 182-187.

Hayase T., Humphrey J. A. C., and Greif R. "A Consistency Formulated QUICK Scheme for Fast and Stable Convergence Using Finite Volume Iterative Calculation Procedures." J. Comput. Phys., 98 (1992): 108-118.

Herschel W. E. and Bulkley R. "Measurements of Consistency as Applied to Rubber-Benzene Solutions." Proc. Am. Soc. Test. Mat, 26 (part 2) (1926): 621-633.

Hirata Y. and Aoshima Y. "Flow Characteristics and Power Consumption in an Agitated Shear-Thinning Plastic Fluid." IChem. E., 136 (1994): 415-422.

Hirata Y. and Aoshima Y. "Formation and Growth of Cavern in Yield Stress Fluids Agitated Under Baffled and Non-Newtonian Conditions." Trans. IChem. E. 74 (part-A) (1996): 438-444.

Hirata Y., Nienow A. W., and Moore I. P. "LDA Studies of Velocity Distributions and Cavern Sizes in a Yield Stress Fluid Agitated by a Rushton turbine." Proc. 7th Euro. Conf. Mixing., Brugge, Belgium; KVIV: Belgium (1991):167-172.

Hirata Y., Nienow A. W., and Moore I. P. Estimation of Cavern Sizes in a Shear-Thinning Plastic Fluid Agitated by a Rushton Based on LDA Measurements." J. Chem. Eng. Jpn., 27 (1994): 235-237.

Holland F. A. and Chapman F. S. "Liquid Mixing and Processing." New York: Reinhold Pub. Corp., (1966).

Holden P. J. and Mann R. "Turbulent 3-D Mixing in a Stirred Vessel: Correlation of a Network-of-Zones Image Reconstruction Approach with Point wise Measurements." Inst. Chem. Eng. Symp., 140 (1996): 167-179.

Holden P. J., Wang M., Mann R., Dickin F. J., and Edwards R. B. "Imaging Stirred-Vessel Macromixing Using Electrical Resistance Tomography." AIChE J., 44 (1998): 780-790.

Holden P. J., Wang M., Mann R., Dickin F. J., and Edwards R. B. "On Detecting Mixing Pathologies inside a Stirred Vessel Using Electrical Resistance Tomography." Trans IChem E., 77(part –A) (1999):709-712.

Holmes D. B., Voncken, R. M. and Dekker, J. A. "Fluid Flow in Turbine Stirred, Baffled Tanks-I. Circulation Time." Chem. Eng. Sci., 19 (1964): 201-208.

Hoogendoorn C. J., Den Hartog A. P. "Model Studies on Mixers in the Viscous Flow Regime." Chem. Eng. Sci., 22 (1967):1689-1699.

Hoyle B. S. and Jia X. "Generic Reality Visualization Modelling From Process Tomography Sensor Data in Process Design." Meas. Sci. Techn., 15 (2004): 1355-1365.

Hua P., Woo E J., Webster J. G., and Tompkins W. J. "Using Compound Electrodes in electrical impedance tomography." IEEE Trans.Biomed. Eng., 40 (1993): 29-34.

Huang S. M., Plaskowski A., Xie C. G., and Beck M. S. "Design of Sensor Electronics for Electronics for Electrical Capacities Tomography." J of Phys: E Sci. Instrum. 22 (1989): 173-177.

Huang S. M., Xie C. G., Plaskowski A., Thorn R., Williams R. A., Hunt A., and Beck M. S. "Process Tomography for Identification, Design and Measurement in Industrial Systems." Powder Technol., 69 (1992): 85-92.

Ihejirika I. and Ein-Mozaffari F. "Using CFD and Ultrasonic Velocimetry to Study the Mixing of Pseudoplastic Fluids with a Helical Ribbon Impeller." Chem. Eng. Technol., 30 (5) (2007): 606-614.

Industrial Tomography System Ltd. "Operating Manual." Industrial Tomography System Ltd, (2005).

Iranshahi A., Heniche M., Bertrand F., and Tanguy P. A. "Numerical Investigation of the Mixing Efficiency of the Ekato Paravisc Impeller." Chem. Eng. Sci., 61 (2006): 2609-2617.

Issa R. I. "Solution of the Implicitly Discretized Fluid Flow Equations by Operator Splitting." J. Comput. Phys., 62 (1986): 40-65.

Jaworski Z., Bujalski W., Otomo N., and Nienow A. W. "CFD Study of Homogenization with Dual Rushton Turbines-Comparison with Experimental Results. Part I: Initial Studies." Chem. Eng. Res. Des., 78 (2000): 327-333.

Jaworski Z. and Nienow A. W. "An LDA Study of the Hydrodynamics of Caverns Formed in a Yield Stress Fluid Agitated by a Hydrofoil Impeller." CHISA (1993a).

Jaworski Z. and Nienow A. W. "LDA Measurements of Flow Fields with Hydrofoil Impellers in Fluids with Different Rheological Properties." Proc. 8th Euro. Conf. Mixing, (Cambridge 21 23 Sep., IChem. E. 136 (1993b): 105-112.

Jaworski Z. and Nienow A. W. "On Flow Close to Cavern Boundaries in Yield Stress Fluids." Chem. Eng. Sci., 49 (1994): 3321-3324

Jaworski Z., Nienow A. W., and Dyster K. N. "An LDA Study of the Turbulent Flow Field in a Baffled Vessel Agitated by an Axial, Down-Pumping Hydrofoil Impeller." Can. J. Chem. Eng. 74 (1996): 3-15.

Joshi J. B., Pandit A. B., and Sharma, M. M. "Mechanically Agitated Gas-Liquid Reactors." Chem. Eng. Sci., 37 (1982): 813-844.

Kagoshima M., and Mann R. "Interactions of Precipitation and Fluid Mixing with Model Validation by Electrical Tomography." Chem. Eng. Res. Des. 83 (part –A7) (2005): 806-810

Kaminoyama M., Taguchi S., Misumi R., and Nishi K. "Monitoring Stability of Reaction and Dispersion States in a Suspension Polymerization Reactor Using Electrical Resistance Tomography Measurements." Chem. Eng. Sci., 60 (2005): 5513-5518.

Kang K. S. and Pettit D. J. "Xanthan, gellan, wellan, and rhamsan." In: Whistler, RL and BeMiller, JN, Editors, 1993. Industrial gums, Academic Press, New York, (1993): 341-398.

Kawase Y., Shimizu K., Araki T., and Shimodaira T. "Hydrodynamics in Three-Phase Stirred Tank Reactors with Non-Newtonian Fluids." Ind. Eng. Chem. Res., 36 (1997): 270-276.

Khang S. J. and Levenspiel O. "New Scale Up and Design Method for Stirrer Agitated Batch Mixing Vessels." Chem. Eng. Sci., 31 (1976): 569-577.

Kelly W. and Gigas, B. "Using CFD to Predict the Behaviour of Power Law Fluids near Axial-Flow impellers operating in the transitional flow regime." Chem. Eng. Sci., 58 (2003): 2141-2152.

Kelly W. and Humphrey A. E. "Computational Fluid Dynamics Model for Predicting Flow of Viscous Fluids in a Large Fermentor with Hydrofoil Flow Impellers and Internal Cooling Coils." Biotechnol. Prog. 14 (1998): 248-258.

Kim S., Nkaya A. N., and Dyakowski T. "Measurement of Mixing of Two Miscible Liquids in a Stirred Vessel with Electrical Resistance Tomography." Int. Commun. in Heat and Mass Transfer, 33 (2006): 1088-1095.

Komori S. and Murakami, Y. "Turbulent Mixing in Baffled Stirred Tanks with Vertical Blade Impellers." AIChE J. 34 (1988): 932-937.

Kramers H., Baars G. M., and Knoll W. H. "A Comparative Study on the Rate of Mixing in Stirred Tanks." Chem. Eng. Sci., 2 (1953): 35-42.

Kukukova A., Mostek M., Jahoda M., and Machon V. "CFD Prediction of Flow and Homogenization in a Stirred Vessel: Part I Vessel with One and Two Impeller." Chem. Eng. Technol., 28 (10) (2005): 1125-1133.

Lahey R T. and Ohkawa K. "An Experimental Investigation of Phase Distribution in an Eccentric Annulus." Int. J. Multiphase Flow, 15 (1989): 447-457.

Lamberto D. J., Alvarez M. M., and Muzzio F. J. "Experimental and Computational Investigation of the Laminar Flow Structure in a Stirred Tank." Chem. Eng. Sci., 54 (7) (1999): 919-942.

Lane G. L., Rigby G. D., and Evans G. M. "Pressure Distribution on the Surface of Rushton Turbine Blades- Experimental Measurement and Predicted by CFD." J. Chem. Eng. Jpn., 34 (5) (2001): 613-620.

Lane G. and Koh P. T. L. "CFD Simulation of a Rushton Turbine in a Baffled Tank." Proc. Int. Conf. on Computational Fluid Dynamics in Mineral and Metal Processing and Power Generation, CSIRO, Melbourne, 3-4 July, (1997): 377-385.

Lee K. C. and Yianneskis, M. "Measurement of Temperature and Mixing Time in Stirred Vessels with Liquid Crystal Thermography." Proc. 9th Europ. Conf. Mixing, (1997): 121-128.

Lee R. E., Finch C. R., and Wooledge J. D. "Mixing of High Viscosity Newtonian and on-Newtonian Fluids." Ind. Eng. Chem., 49 (1957): 1849.

Leonard B. P. "A Stable and Accurate Convective Modeling Procedure Based on Quadratic Upstream Interpolation." Comput. Methods Appl. Mech. Eng., 19 (1979): 59-98.

Leonard B. P. and Mokhtari S. "ULTRA-SHARP Nonoscillatory Convection Schemes for High-Speed Steady Multi dimensional Flow." NASA TM 1-2568 (ICOMP-90-12), NASA Lewis Research Center, (1990).

Letellier B., Xuereb C., Swaels P., Hobbes P., and Bertrand J. "Scale-Up in Laminar and Transient Regimes of a Multi-Stage Stirrer a CFD Approach." Chem. Eng. Sci., 57 (2002): 4617-4632.

Li L. and Wei J. "Three-Dimensional Image Analysis of Mixing in Stirred Vessels." AIChE J., 45 (9) (1999): 1855-1865.

Li M., White G., Wilkinson D., Roberts K. J. "Scale up Study of Retreat Curve Impeller Stirred Tanks Using LDA Measurements and CFD Simulation." Chem. Eng. J. 108 (2005): 81-90.

Lucas G. P., Cory J., Mann R., Dickin F. J., and Edwards R. B. "Measurement of the Solids Volume Fraction and Velocity Distributions in Solids-Liquid Flows Using Dual-Plane Electrical Resistance Tomography." Flow Meas. Instrum. 10 (4) (1999): 249-258.

Loh W. W., Pinheiro P. A. T., Dickin F. J., and Waterfall R. C. "Low Common Mode Error Data Collection Strategy for Electrical Resistance Tomography." Electron. Lett., 34 (15) (1998): 1489-1490.

Luo J. Y., Gosman A. D., Issa R. I., Middleton J. C., and Fitzgerald M. K. "Full Flow Field Computation of Mixing in Baffled Stirred Vessels." Trans IChem E. 71 A (1993): 342-344.

Luo J. Y., Gosman A. D., and Issa R. I. "Prediction of Impeller Induced Flows in Mixing Vessels Using Multiple Frames of Reference." Inst. Chem. Eng. Symp., 136 (1994): 549-556.

Ma L. and Barbosa-Canovas G. V. "Instrumentation for the rheological characterization of foods." Food Sci Technol Int., 1 (1995): 3–17.

Mann R., Dickin F. J., Wang M., Dyakowski T., Williams R. A., Edwards R. B., Forrest A. E., and Holden P. J. "Application of Electrical Resistance Tomography to Interrogate Mixing Process at Plant Scale." Chem. Eng. Sci., 52 (1997): 2087-2097.

Mann R. and Mavros P. "Analysis of Unsteady Tracer Dispersion and Mixing in a Stirred Vessel Using Interconnected Network of Ideal Flow Zones." Proc. 4th Eur. Conf. Mixing (1982): 35-48.

Mann R., Stanley S. J., Vlaev D., Wabo E., and Primrose K. "Augmented Reality Visualization of Fluid Mixing in Stirred Chemical Reactors Using Electrical Resistance Tomography (ERT)." J.of Electronic Imaging, 10 (3) (2001): 620-629.

Mann R., Wang M., Dickin F. J., Dyakowski T., Holden P. J., Forrest A. E. and Edwards R. B. " Resistance Tomography Imaging of Stirred Vessel Mixing at Plant Scale." IChem. Eng. Symp. 140 (1996): 155-162.

Mann R. and Ying P. "Application of 3D Network of Zones Mixing Model to a Stirred Vessel." Proc. 8th Europ. Conf. Mixing, (1994): 317-324.

Marcotte M., Taherian Hoshahili A. R., and Ramaswamy H. S. "Rheological Properties of Selected Hydrocolloids as a Function of Concentration and Temperature." Food Res. Int., 34 (2001): 695-703.

Masiuk S. and Lacki H. "Power Consumption and Mixing Time for Newtonian and Non-Newtonian Liquids Mixing in a Ribbon Mixer." Chem. Eng. J., 52 (1993): 13-17.

Margaritis A. and Zajic J. E. "Biotechnology review: mixing mass transfer and scale-up of polysaccharide fermentations." Biotechnol. Bioeng., 20, (1978): 939–1001.

Mavros P., Mann R., Vlaev S. D., and Bertrand J. "Experimental Visualization and CFD Simulation of Flow Patterns Induced By A Novel Energy- Saving Dual- Configuration Impeller In Stirred Vessels." Trans IChem. E., 79 (part –A) (2001): 857-866.

Mavros P., Xuereb C., and Bertrand J. "Determination of 3-D Flow Fields in Agitated Vessels by Laser-Droppler Velocimetry. Effect of Impeller Type and Liquid Viscosity on Liquid Flow Patterns." Trans IChem. E., 74 (part-A) (1996): 658-668.

Menisher T., Metghalchi M., and Gutoff E. B. "Mixing Studies in Bioreactors." Bioprocess Eng., 22 (2000): 115-120.

Mersmann A., Einenkel, W. D., and Kappel, M. "Design and Scale-up of Agitated Vessels." Int. Chem. Eng., 16 (1976): 590-603.

Metzner A. B. and Otto R. E. "Agitation of Non-Newtonian Fluids." AIChE J., 3 (1957): 3-11.

Milas M., Rinaudo M., and Tinland B. "The Viscosity Dependence on Concentration, Molecular Weight, and Shear Rate of Xanthan Solutions." Polym Bull., 14, (1985):157–164.

Mill C. C. "Rheology of Disperse Systems." New York: Pergamon Press, (1959).

"MixSim User's Guide Documentation." FLUENT Inc, (2003).

Moilanen P., Laakkonen M., and Aittamaa J. "Modeling Aerated Fermenters with Computationla Fluid Dynamics." Ind. Eng. Chem. Res., 45 (2006): 8656-8663.

Montante, G., Moštěk M., Jahoda M., and Magelli F. "CFD Simulation and Experimental Validation of Homogenization Curves and Mixing Time in Stirred Newtonian and Pseudoplastic Liquids." Chem. Eng. Sci., 60 (2005): 2427-2437.

Montiel S. and Ros. A. "Curves and Surfaces." American Mathematical Society, (2005).

Moo-Young M., Tichar K., Dullib A. L. "The Blending Efficiencies of Some Impellers in Batch Mixing." AIChE J., 18 (1972):178.

Moore I. P. T., Cossor G., and Baker M. R. "Velocity Distributions in a Stirred Tank Containing a Yield Stress Fluid." Chem. Eng. Sci., 50 (1995): 2467-2481.

Morris E. R. "Molecular Origin of Xanthan Solutions." Extracellular Microbial Polysaccharides, ACS Symp., 45 (1977): 81-89.

Moukalled F. and Darwish M. "A Comparative Assessment of the Performance of Mass Conservation-Based Algorithms for Incompressible Multiphase Flows." Num. Heat Trans., 42 (part-B) (2002): 259-283.

Moukalled F. and Darvish M., "Pressure -Based Algorithm for Multifluid Flow At All Speeds- Part 1: Mass Conservation Formulation." Num. Heat Trans., 45 (part-B) (2004): 495-522.

Murthy S. S. and Jayanti S. "Mixing of Power-Law Fluids Using Anchors: Metzner-Otto Concept Revisited." AIChE J., 49 (2003a) 1: 30-40.

Murthy S. S. and Jayanti S. "Mixing of Pseudo plastic Fluids Using Helical Ribbon Impellers." AIChE J., 49 (2003b) 11: 2768-2772.

Nere N. K., *Patwardhan A. W., and Joshi J. B.* "Liquid Phase Mixing in Stirred." Ind. Eng. Chem. Res. 42 (12) (2003): 2661-2698.

Nienow A. W. "On Impeller Circulation and Mixing Effectiveness in the Turbulent Flow Regime." Chem. Eng. Sci., 52 (1997): 2557-2565.

Nienow A. W. and Elson T. P. "Aspects of Mixing in Rheologically Complex Fluids." Chem. Eng. Res. Des., 66 (1988): 5-15.

Norton S. S. and Linzer M. "Ultrasonic Reflectivity Tomography." Ultrasonic Imaging, 1 (1979): 154-184.

Norwood K.W. and Metzner A. B. "Flow Patterns and Mixing Rates in Agitated Vessels." AIChE J., 6 (1960):432-437.

Nouri J. M. and Whitelaw J. H. "Flow Characteristics of Stirred Reactors with Newtonian and Non-Newtonian Fluids." AIChE J., 36.4 (1990): 627-629.

Ofoli R. Y., Morgan R. G., and Steffe J. F. "A Generalized Rheological Model for Inelastic Fluid Foods." J. Texture Studies, 18 (1987): 213-230.

Oldshue J. Y. "Fluid Mixing Technology." New York: McGraw-Hill, Inc, (1983).

Ostendorf W., Mewes D., and Mayinger F. "Tomographical Method Using Holographic Interferometery for the Registration of Three-Dimensional Unsteady Temperature Profiles in Laminar and Turbulent Flow." Heat transfer- Proc 8th Int Heat Transfer Conf. Hamispher Publ Corp, New York, USA, 2 (1986): 519-524.

Pandit A. B. and Joshi J. B. "Mixing in Mechanically Agitated Gas-Liquid Contactors, Bubble Columns, and Modified Bubble Columns." Chem. Eng. Sci., 38 (1983): 1189-1215.

Pant H. J., Kundu A., and Nigam K. D. P. "Radiotracer Applications in Chemical Process Industry." Rev. Chem. Eng., 17 (2001):165-252.

Parker D. S., Hawkesworth M. R., Broadbent C. J., Fowles P., Fryer T. D. and McNeal P. A. "Industrial Positron-Based Imaging: Principles and Applications." Nucl. Instr. and Meth., 349 (part-A) (1994): 583-592.

Patankar S. V. "Num. Heat Transfer and Fluid Flow." New York: Hemisphere Publishing Corporation, Taylor & Francis Group, (1980).

Patankar S. V. and Spalding D. B. "A Calculation Procedure for Heat, Mass, and Momentum Transfer in 3-D Parabolic Flows." Int. J. Heat Mass Transfer 15 (1972): 1787-1806.

Patwardhan A. W. and Joshi J. B. "Relation between Flow Pattern and Blending in Stirred Tanks." Ind. Eng. Chem. Res., 38 (1999): 3131-3143.

Paul E. L., Atiemo-Obeng V. A., and Keresta S. M. "Handbook of Industrial Mixing Science and Practice." John Wiley & Sons, Inc., (2004).

Paulson K., Breckon W., and Pidcock M. "Electrode Modeling in Electrical Impedance Tomography." J. Appl. Math, 52 (4) (1992): 1012-1022.

Perng C. Y. and Murthy J. Y. "A Moving Deforming Mesh Technique for Simulation of Flow in Mixing Tanks." AIChE Symp. Ser., 89 (1993): 37-41.

Pinheiro P. A. T., Loh W. W., and Dickin F. J. "Optimal Sized Electrodes for Electrical Resistance Tomography." 34 (1). Electron. Lett., (1998): 69-70.

Pollard A. and Siu A. L. W. "The Calculation of Some Laminar Flows Using Various Discretization Schemes." Comput. Methods Appl. Mech. Eng. 35 (1982): 293-313.

Press W. H., Flannery B. P., Teukolsky S. A., and Velterling W. T. "Num. Recipes-the Art of Scientific (FORTRAN Version)." Cambridge University Press: Cambridge, (1992).

Rahimi M. and Mann R. "Macro-Mixing Partial Segregation and 3-D Selectivity Fields Inside a Semi-Batch Stirred Reactor." Chem. Eng. Sci., 56 (2001): 763-769.

Raghav Rao K. S., M. S., and Joshi, J. B. "Liquid Phase Mixing in Mechanically Agitated Vessels." Chem. Eng. Commun., 74 (1) (1988):1-25.

Ranade V. V. "An Efficient Computational Model for Simulating Flow in Stirred Vessels: a Case of Rushton Turbine." Chem. Eng. Sci., 52 (24) (1997): 4473- 4484.

Ranade V. V. "Computational Fluid Dynamics for Reactor Engineering." Rev. in Chem. Eng., 11 (1995): 229-284.

Ranade V. V. "Computational Flow Modeling for Chemical Reactor Engineering." San Diego: ACADEMIC PRESS, (2002).

Ranade V. V., Bourne, J. R., and Joshi, J. B. "Fluid Mechanics and Blending in Agitated Tanks." Chem. Eng. Sci., 46 (1991):1883-1893.

Ranade V. V. and Dommeti S. M. S. "Computational Snapshot of Flow Generated by Axial Impellers in Baffled Stirred Vessels." Trans. IChem. E., 74 (part A) (1996):476-484.

Ranade V. V. and Joshi J. B. "Flow Generated by Pitched Blade Turbines. I: Measurements Using Laser Doppler Anemometer." Chem. Eng. Commun., 81 (1989): 197-224.

Rao M. A. "Rheology of Fluid and Semisolid Foods Principles and Applications." Maryland: Aspen, Inc, (1999).

Reed X. B., Princz M.and Hartland S. "Laser Doppler Measurements of Turbulence in a Standard Stirred Tank." Proc 2nd Europ. Conf. on Mixing, Cambridge, U.K. (1977): b1-1-b1-26.

Rewatkar V. B. and Joshi J. B. "Effect of Impeller Design on Liquid Phase Mixing in Mechanically Agitated Reactors." Chem. Eng. Commun., 91 (1991): 322-353.

Ricard F., Brechtelsbauer C., Xu X. Y., and Lawrence, C. J. "Monitoring of Multiphase Pharmaceutical Processes Using Electrical Resistance Tomography." Trans IChem E., 83 (part –A7) (2005): 794-805.

Rice M., Hall J., Papadakis G., and Yianneskis. "Investigation of Laminar Flow in a Stirred Vessel at Low Reynolds Numbers." Chem. Eng. Sci., (2006): 2762-2770.

Rivera C., Foucault S., and Heniche M. "Mixing Analysis in a Coaxial Mixer." Chem. Eng. Sci., 61 (2006): 2895-2907.

Rochefort W. E. and Middleman S. "Rheology of Xanthan Gum: Salt, Temperature, and Strain Effects in Oscillatory and Steady Shear Experiments." J.of Rheology, 31 (4) (1987): 337-369.

Ruck B. "Distortion of LDA Fringe Pattern by Tracer Particles." Exp. in Fluids, 10 (1991): 349-354.

Runchal A. K. and Wolfshtein M. "Numerical Integration Procedure for the Steady State Navier-Stokes Equations." J. Mech. Eng. Sci., 11 (1969): 445-452.

Ruszkowski S. "A Rational Method for Measuring Blending Performance and Comparison of Different Impeller Types." Proc. 8th Europ. Conf. Mixing, (1994): 283-292.

Rutherford K., Mahmoudi S. M. S., Lee K. C., and Yianneskis M. "The Influence of Rushton Impeller Blade and Disk Thickness on the Mixing Characteristics of Stirred Vessels." Trans. IChem. Eng., 74 (part-A) (1996): 369-378.

Rzyski E. "Liquid Homogenisation in Agitated Tanks." Chem. Eng. Technol., 16 (4) (1993): 229-233.

Sahu A. K. and Joshi J. B. "Simulation of Flow in Stirred Vessels with Axial Flow Impellers: Effects of Various Numerical Schemes and Turbulence Model Parameters." Ind. Eng. Chem., 34 (1995): 626-639.

Sahu A. K., Kummar P., and Joshi J. B. "Simulation of Flow in Stirred Vessels with Axial Flow Impellers: Zonal Modelling and Optimization of Parameter." Ind. Eng. Chem., 37 (1998): 2116-2130.

Sahu A. K., Kummar P., Patwardhan A. W., and Joshi J. B. "CFD Modelling and Mixing in Stirred Tanks." Chem. Eng. Sci., 54 (1999): 2285-2293.

Sano Y. and Usui H. "Interrelations among Mixing Time, Power Number, and Discharge Flow Rate Number in Baffled Mixing Vessels." J. Chem. Eng. Jpn., 18 (1985): 47-52.

Sasakura T., Kato Y., Yamamuro S., and Ohi N. "Mixing Process in a Stirred Vessel. Int. Chem. Eng., 20 (1980): 251-258.

Saeed S., Ein-Mozaffari F., and Upreti S. R. "Using computational Fluid Dynamics and Ultrasonic Doppler Velocimetry to Study Pulp Suspension Mixing." Ind. Eng. Chem. Res., 46 (2007): 2172-2179.

Satio F., Nienow A. W., Chatwin S., and Moore I. P. T. "Power, Gas Dispersion and Homogenisation Characteristics of Scaba SRGT and Rushton Turbine Impellers." J. Chem. Eng. Jpn., 25 (3) (1992): 281-287.

Seagar A. D., Barber D. C., and Brown B. H. "Theoretical Limits to Sensitivity and Resolution in Impedance Imaging." Clin. Phys. Physiol. Meas, 8 (1987): 13-31.

Sederman A. J. and Gladden L. F. "Transition for Pulsing Flow in Trickle-Bed Reactors Studied Using MRI." AIChE J., 51 (2) (2005): 615-621.

Serrano-Carreon L. and Galindo E. "Studies on Cavern Development in Mixing a Yield Stress Fluid in a Pilot-Scale Proto-Fermenter." Rècents Progerès en Gènie Procèdès 11 (1997): 161-168.

Shaw J. A. "Understanding the Effects of Impeller Types, Diameter, and Power on Mixing Time." Chem. Eng. Prog., 45 (1994): 45-48.

Shekhar S. M. and Jayanti S. "Mixing of Power-Low Fluids Using Anchors: Metzner-Otto Concept Revisited." AIChE J., 49 (2003): 30-40.

Shervin C. R., Raughley D. A., and Romaszewski R. A. "Flow Visualization Scaleup Studies for the Mixing of Viscoelastic Fluids." Chem. Eng. Sci., 46 (1991): 2867-2873.

Shiue S. J. and Wong C. W. "Studies on Homogenization Efficiency of Various Agitators in Liquid Blending." Can. J. Chem. Eng., 62 (1984): 602-609.

Shyy W., Thakur S. S., Ouyang H., Liu J., and Blosch E. "Computational Techniques for Complex Transport Phenomena." New York: Cambridge University Press, (1997).

Sikora M., Kowalski S., Tomasik P., and Sady M. "Rheological and Sensory Properties of Dessert Sauces Thickened by Starch-Xanthan Gum Combinations." J. of Food Eng. 79 (4) (2007): 1144-1151

Skelland A. H. P. "Non-Newtonian Flow and Heat Transfer." New York: Wiley, (1967).

Solomon J., Elson T. P., and Nienow A. W. "Cavern Sizes in Agitated Fluids with a Yield Stress." Chem. Eng. Commun., 11 (1981): 143-164.

Smith G. D. "Numerical Solution of Partial Differential Equations: Finite Difference Methods." 3rd ed. Oxford: Clarendon, (1985).

Smith J. H. and Pace G. W. "Recovery of Microbial Polysaccharides." J. Chem. Technol. Biotechnol., 32 (1982): 119–129.

Sommerfeld M. and Decker S. "State of the Art and Future Trends in CFD Simulation of Stirred Vessel Hydrodynamics." Chem. Eng. Technol., 27 (2004): 215-224.

Stanley S. J. "Tomographic Imaging during Reactive Precipitation in a Stirred Vessel: Mixing with Chemical Reaction." Chem. Eng. Sci., 61 (2006): 7850-7863.

Stanley S. J., Mann R., and Primose K. "Tomographic Imaging of Fluid Mixing in Three Dimensions For Single-Feed Semi-Batch Operation of a Stirred Vessel." Trans. IChem. E., 80 (part –A) (2002): 903-909.

Stanley S. J., Mann R., and Primrose K. "Interrogation of a Precipitation Reaction by Electrical Resistance Tomography (ERT)." AIChE J., 51 (2005): 607-614.

Stanley S. J., Wabo E., Mann R., and Primrose K. "Dual-Validation of Miscible Liquid Mixing in a Stirred Vessel Imaged by Electrical Resistance Tomography." 2nd World Cong. Process Tomography. Hannover, Germany, (2001): 151-158.

Tabor G., Gosman A. D., and Issa R. I. "Numerical Simulation of the Flow in a Mixing Vessel Stirred by a Rushton Turbine." Inst. Chem. Eng. Symp., 140 (1996): 25-34.

Tako M. and Nakamura S. "Rheological Properties of Deacetylated Xanthan in Aqueous Media." Agric Biol Chem., 12 (1984). 2987-2993.

Tanguay P. A., Lacroix R., Choplin L., and Brito-De La Fuente E. "Finite Element Analysis of Viscous Mixing a Helical Ribbon Screw Impeller." AIChE J., 38 (1992): 939-944.

Tapp H. S. and Williams R. A. "Status and Applications of Microelectrical Resistance Tomography." Chem. Eng. Sci., 77 (2000): 119-125.

Tatterson G. B. "Fluid Mixing and Gas Dispersion in Agitated Tanks." New York: McGraw-Hill, Inc, (1991).

Thompson J. F., Warsi Z. U. A., and Mastin C. W. "Numerical Grid Generation, Foundations and Applications." New York: North-Holland, (1985).

Torres L. G., Flores F., and Galindo E. "Apparent Yield Stress of Xanthan Solutions and Broths." Bioprocess Eng., 12 (1995): 41-46.

Torrez C. and Andre C. "Power Consumption of a Rushton Turbine Mixing viscous Newtonian and Shear-thinning Fluid: Comparison between Experimental and Numerical Results." Chem. Eng. Technol., 21 (1998): 599-604.

Torrez C. and Andre C. "Simulation of a Rushton Turbine Mixing Yield Stress Fluids: Application of the Metzner-Otto Concept." Chem. Eng. Technol., 22 (8) (1999): 701-706.

Toye D., Marchot P., Crine M., and L'Homme E. "The Use of Large Scale Computed Tomography for the Study of Hydrodynamics in Trickling Filters." Chem. Eng. Sci., 49 (24b) (1994): 5271-5280.

Van Doormaal J. P. and G. D. Raithby. "Enhancements of the Simple Method for Predicting Incompressible Fluid Flows." Num. Heat Transfer, 7 (1984): 147-163.

Van't Riet K. and Smith J. M. "The Behaviour of Gas-Liquid Mixtures near Rushton Turbine Blades." Chem. Eng. Sci., 28 (1973): 1031-1037.

Versteeg H. K. and Malalasekera W. "An Introduction to Computational Fluid Dynamics the Finite Volume Method." 1st ed. London: Longman Group Ltd, (1995).

Versteeg H. K. and Malalasekera W. "An Introduction to Computational Fluid Dynamics the Finite Volume Method. 2nd ed. London: Longman Group Ltd, (2007).

Viergever M. A. and Todd-Pokropek A. E. "Mathematics and Computer Science in Medical Imaging." Berlin: Springer, (1988).

Vlaev D. S. and Bennington C. P. J. "Using Electrical Resistance Tomography to Image Liquor Flow in a Model Digester." J. of Pulp and Paper Science., 30 (1) (2004): 15-21.

Vlaev D., Wang M., Dyakowski T., Mann R., and Grieve B. D. "Detecting Filter Cake Pathologies in Solid-Liquid Filtration: Semi-Tech Scale Demonstration Using Electrical Resistance Tomography (ERT)." Chem. Eng. J., 77 (2000): 87-92.

Wang M., Dickin F. J., and Williams R. A. "Grouped-Node Technique as a Means of Handling Large Electrode Surfaces in Electrical Impedance Tomography." Physiol. Meas., 16 (part-A) (1995): 219-226.

Wang M., Dorward A., Vlaev D. and Mann R. "Measurement of Gas-Liquid Mixing in a Stirred Vessel Using Electrical Resistance Tomography (ERT)." 1st World Cong. on Ind. Process Tomography, Buxton, Greater Manchester, (1999):14-17.

Wang M., Dorward A., Vlaev D., and Mann R. "Measurement of Gas-Liquid Mixing in a Stirred Vessel Using Electrical Resistance Tomography (ERT)." Chem. Eng. Sci., 77 (2000): 93-98.

Wang M., Jia X., Bennet M., and Williams R. A. "Flow Regime Identification and Optimum Interfacial Area Control of Bubble Columns Using Electrical Impedance Imaging." Proc. 2nd World Cong. on Ind. Process Tomography (2001): 726-734.

Whitcomb P. J. "Rheology of Xanthan Gum." J. of Rheology, 22 (5) (1978): 493-505.

Whitcomb P.T., E. k., B. J., and Macosko C. W. "Rheology of Xanthan Gum Solutions." Extracellular microbial polysaccharides ACS Symp., Washington, DC 45 (1997):160-173.

White R. B. and Doblin C. "An Investigation of Sparged Mixing Tanks Using Electrical Impedance Tomography and Computational Fluid Dynamics." 3th Int. Conf. on CFD in the Minerals and Process Ind., CSIRO, Melbourne Australia, 10-12 December, (2003): 593-598

Wichterle K. and Wein O. "Agitation of Concentrated Suspensions." CHISA (1975): 75, Paper B4.6, Prague, Czechoslovakia.

Wichterle K. and Wein O. "Threshold of Mixing of Non-Newtonian Liquids." Int. Chem. Eng., 21 (1981): 116-120.

Wilkens R. J., Miller J. D., Dietz D. C., and Myers K. J. "New Technique for Measuring and Modeling Cavern Dimensions in a Bingham Plastic Fluid." Chem. Eng. Sci., 60 (2005): 5269-5275.

Wilkes J. O. "Fluid Mechanics for Chemical Engineers, With Microfluidies and CFD." 2nd ed. Pearson Education, Inc., (2006).

Wikstrom T. and Rasmuso A. "The Agitation of Pulp Suspensions with a Jet Nozzle Agitator." Nordic Pulp and Paper Research J. 13 (2) (1998): 88-94.

Williams R. A. and Beck M. S. "Process Tomography: Principles, Techniques, and Applications." Butterworth-Heineman, Oxford, (1995).

Williams R. A., Jia X., West R. M., Wang M., Cullivan J. C., Bond J., Faulks I., Dyakowski T., Wang S. J., Climpson N., Kostuch J. A., and Payton D. "Industrial Monitoring of Hydrocyclone Operation Using Electrical Resistance Tomography." Minerals Eng., 12 (10) (1999): 1245-1252.

Williams R. A., Mann R., Dickin F. J., Ilyas O. M., Ying P. and Edwards R. B. "Application of Electrical Impedance Tomography to Mixing in Stirred Vessels." AIChE J., 10 (1993): 8-15.

Wright B., Matsuda O., and Sugawara Y. "Real Time Imaging of Surface Acoustic Waves on Crystals and Microstructures." Jpn. J. Appl. Phys., 44 (6B) (2005): 4292-4296.

Wu H. and Patterson G. K. "Laser-Doppler Measurements Turbulent-Flow Parameters in a Stirred Mixer." Chem. Eng. Sci., 44 (1989): 2207-2221.

Wu J., Graham L. J., and Mehidi N. N. "Estimation of Agitator Flow Shear Rate." AIChE J., 52 (7) (2006): 2323-2332.

Xu H. and Zhang G. "Study of the Effect of the Non-Orthogonality for Non-Staggered Grids-the Results." Int. J. Numer. Math. Fluids, 29 (1999): 625-644.

Yeh Y. and Cummins H. Z. "Localized Fluid Flow Measurements with An He-Ne Laser Spectrometer." Appl. Phys. Lett., 4 (1964): 176-178.

Yu Z. Z., Peyton A. J., Beck M. S., Conway W.F. and Xu L.A. "Imaging Systems Based on Electromagnetic Tomography (EMT)." Electron. Lett. 29 (7) (1993).

Zalc J. M., Alvarez M. M., and Muzzio F. J. "Extensive Validation of Computed Laminar Flow in a Stirred Tank with Three Rushton Turbine." AIChE J., 47 (10) (2001): 2144-2154.

Zlokarnik M. "Stirring: Theory and Practice." Germany: Wiley-VCH: Weinheim, (2001).

Appendix A

A. Solid body images (based on tracer concentration, g/L) for the cavern formed in 0.5% xanthan solutions agitated by Scaba at different speed

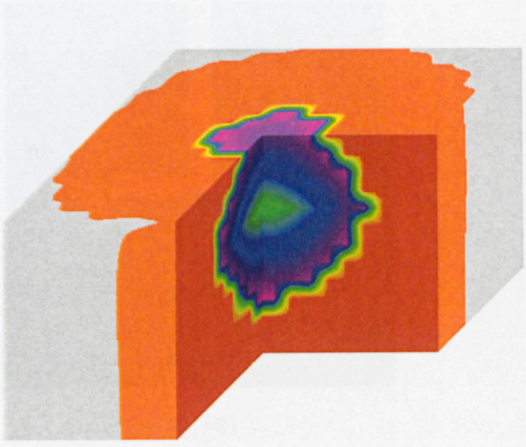

(a) 16 rpm

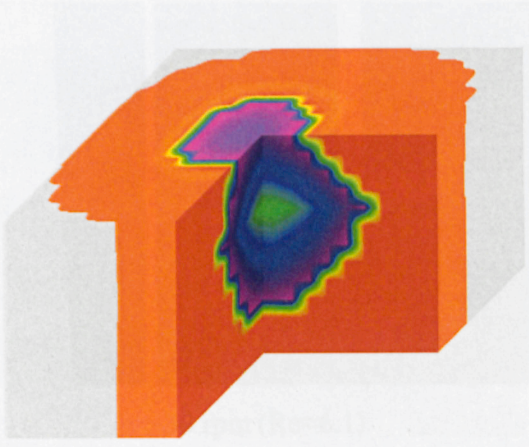

(b) 28 rpm

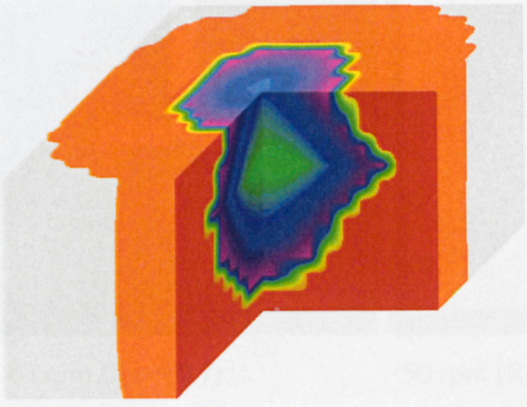

(c) 37 rpm

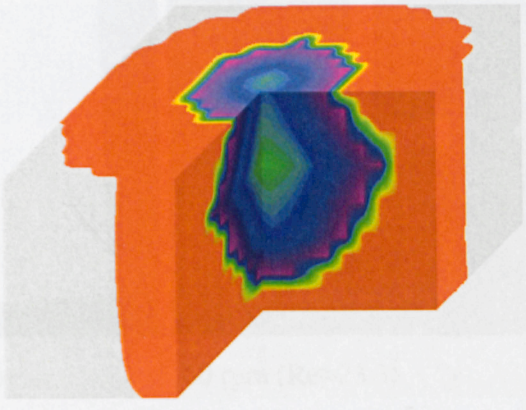

(d) 44 rpm

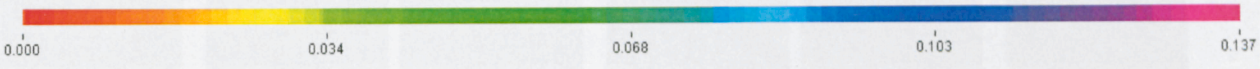

Appendix B

B.1. CFD velocity (ms^{-1}) contours for 1.0% xanthan concentration.

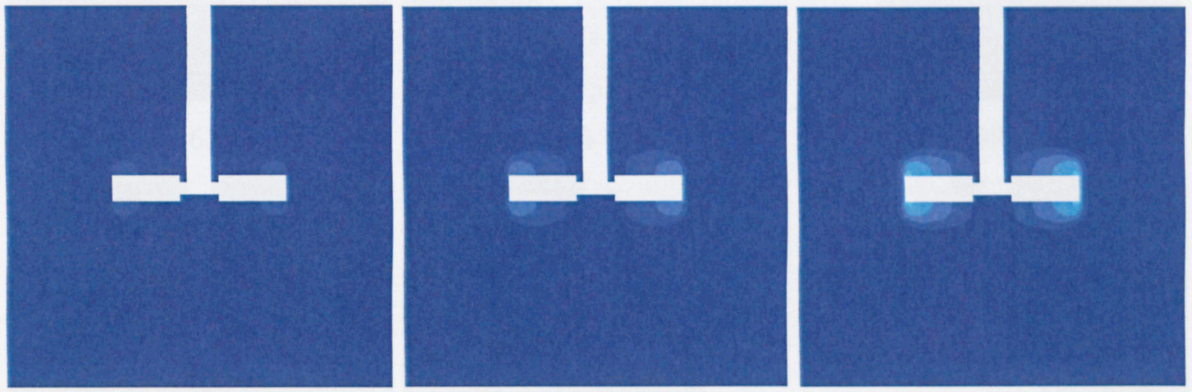

10 rpm (Re≈0.74) 20 rpm (Re≈2.8) 30 rpm (Re≈6.1)

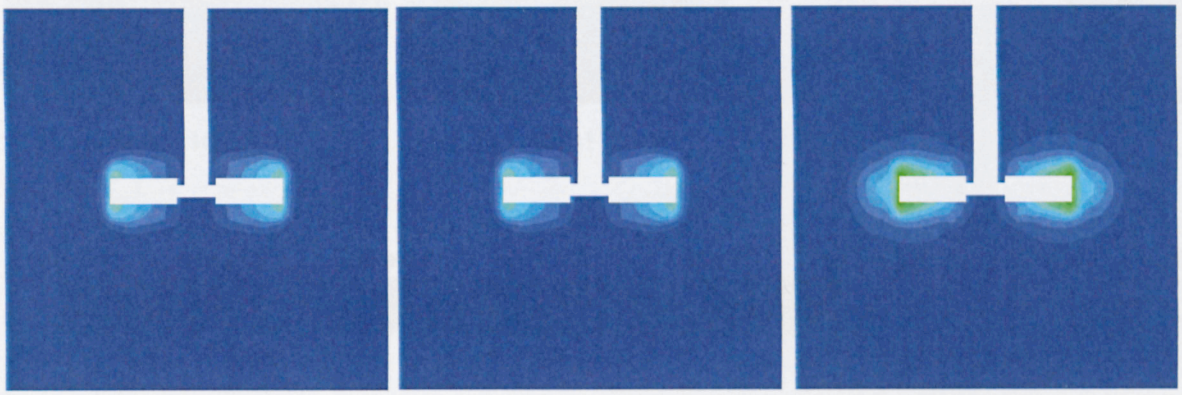

40 rpm (Re≈10.7) 50 rpm (Re≈16.4) 60 rpm (Re≈23.3)

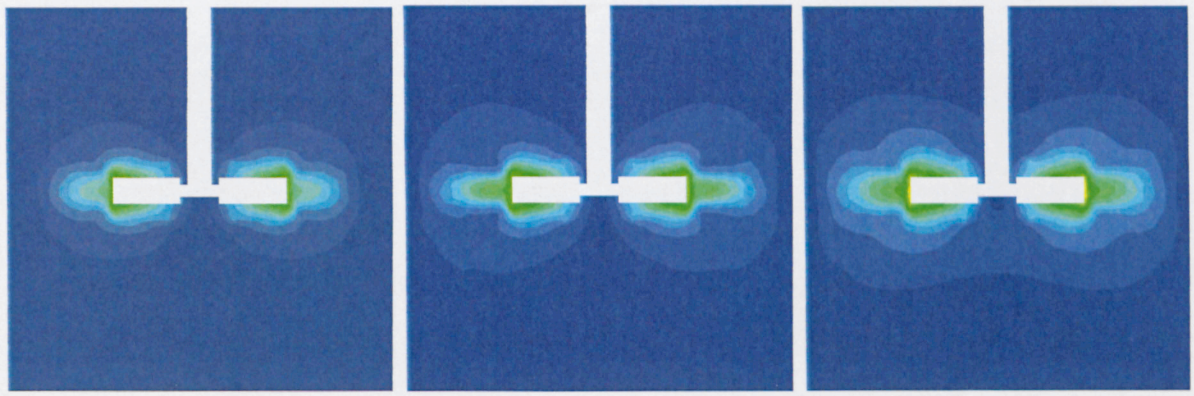

70 rpm (Re≈31.34) 80 rpm (Re≈40.5) 90 rpm (Re≈50.8)

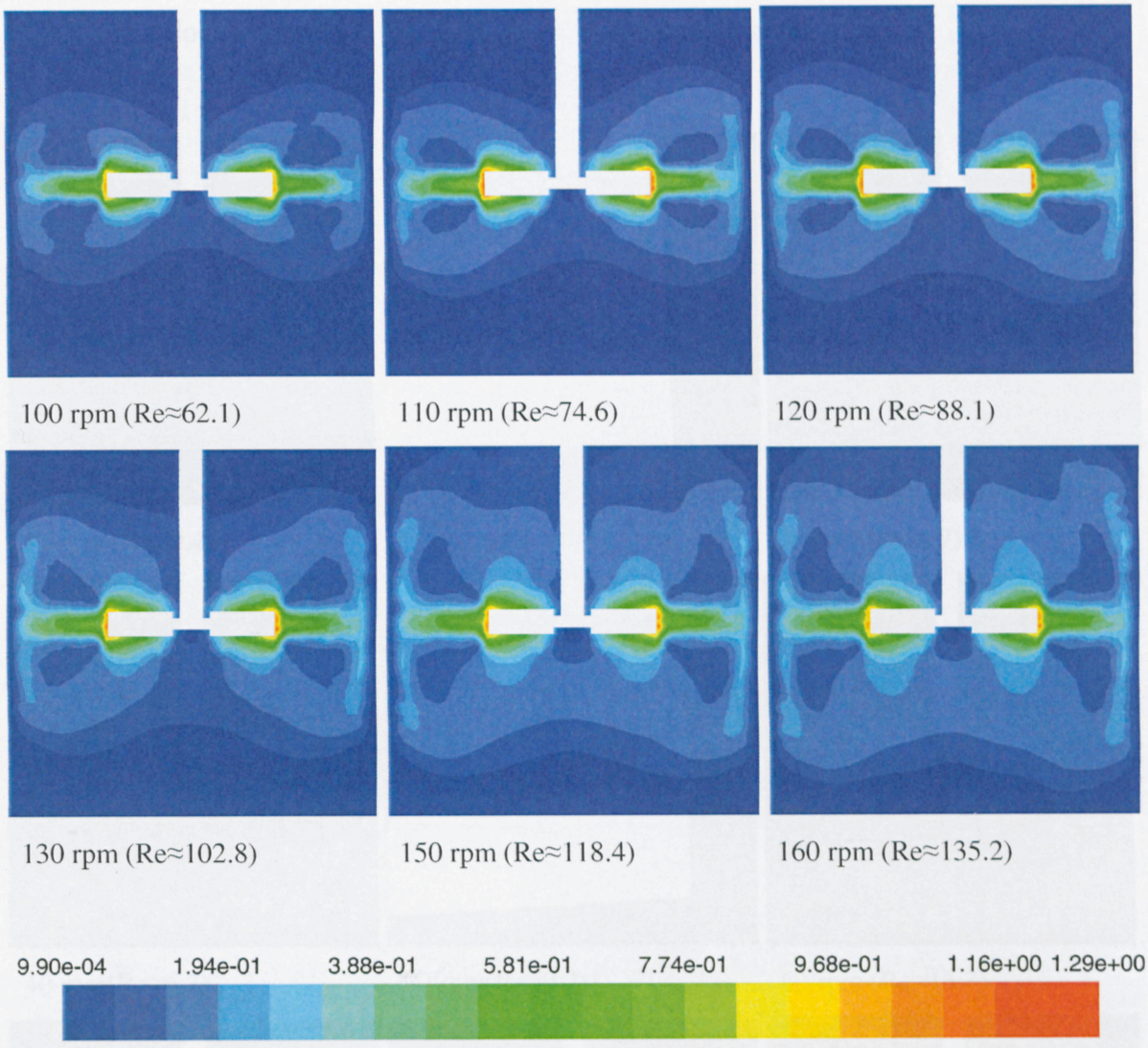
100 rpm (Re≈62.1)
110 rpm (Re≈74.6)
120 rpm (Re≈88.1)
130 rpm (Re≈102.8)
150 rpm (Re≈118.4)
160 rpm (Re≈135.2)
9.90e-04
1.94e-01
3.88e-01
5.81e-01
7.74e-01
9.68e-01
1.16e+00
1.29e+00

B.2. CFD velocity (ms^{-1}) plots for 1.5% xanthan concentration.

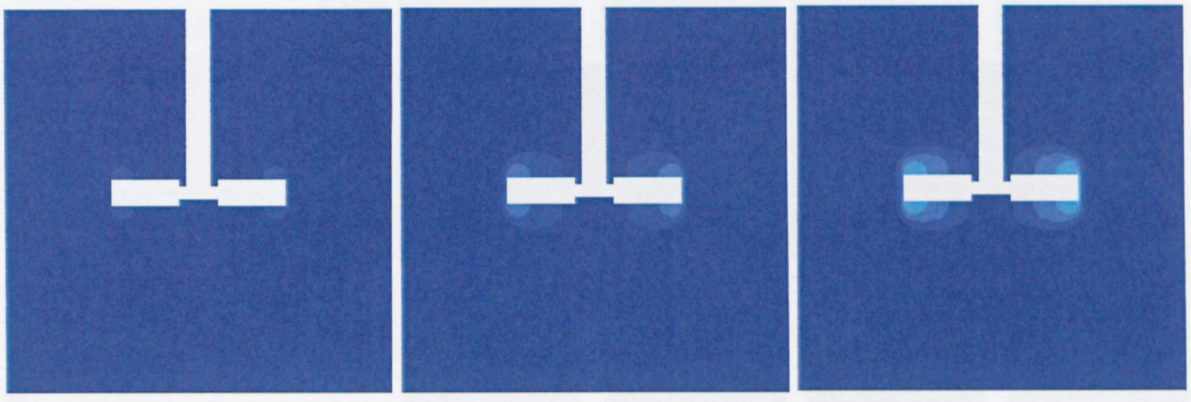

10 rpm (Re≈0.45) 20 rpm (Re≈1.7) 30 rpm(Re≈3.7)

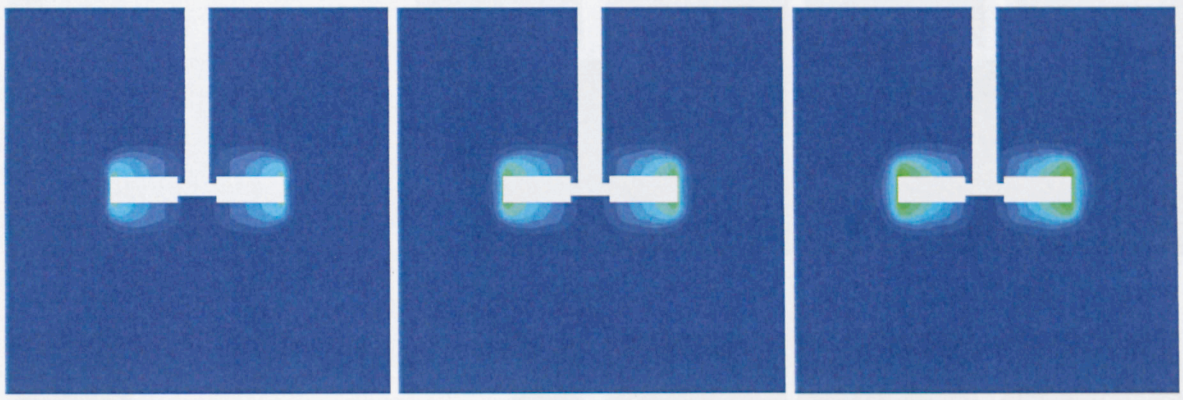

40 rpm(Re≈6.3) 50 rpm(Re≈9.7) 60 rpm (Re≈13.7)

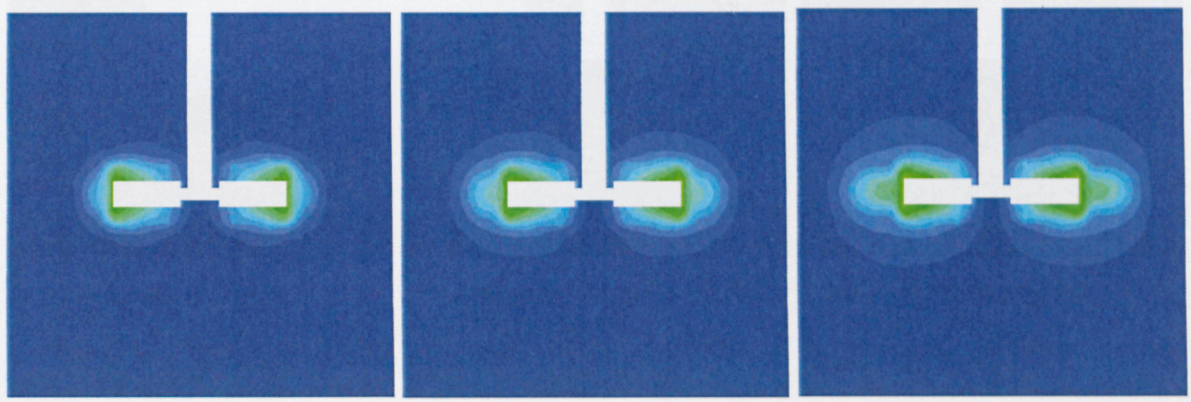

70 rpm (Re≈18.4) 80 rpm (Re≈23.7) 90 rpm (Re≈29.61)

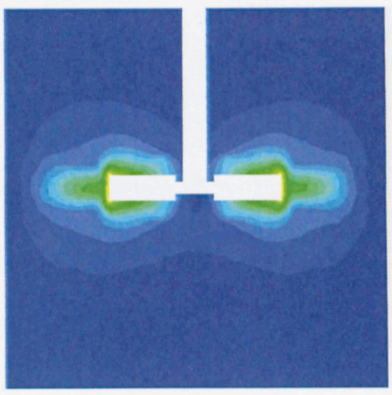

100 rpm (Re≈36.16)

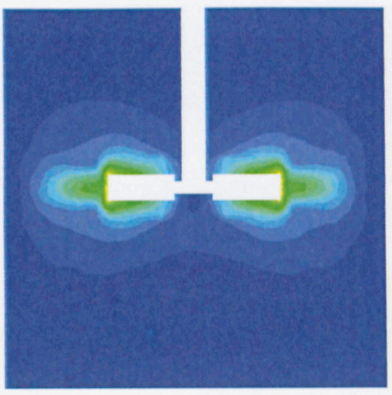

110 rpm (Re≈43.22)

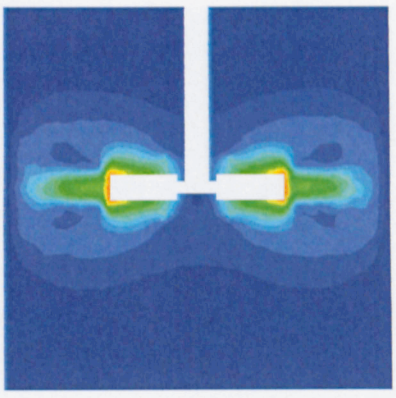

120 rpm (Re≈51.09)

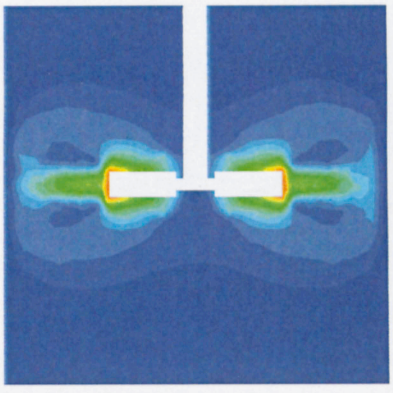

130 rpm (Re≈56.46)

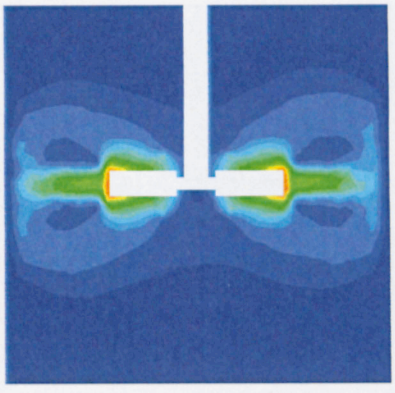

140 rpm (Re≈68.43)

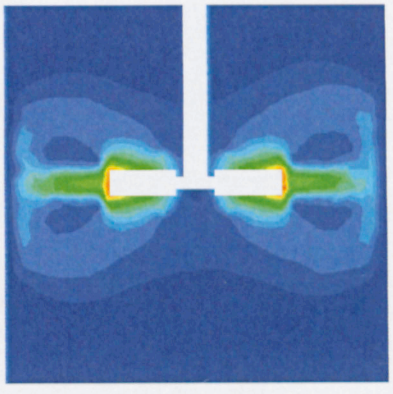

150 rpm (Re≈77.99)

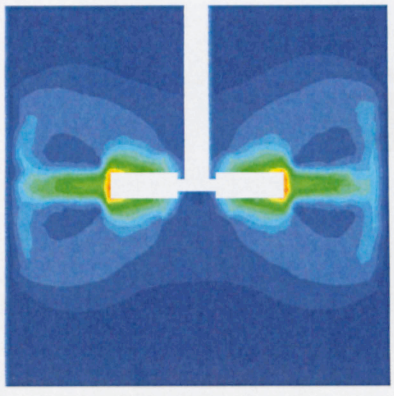

160 rpm (Re≈88.13)

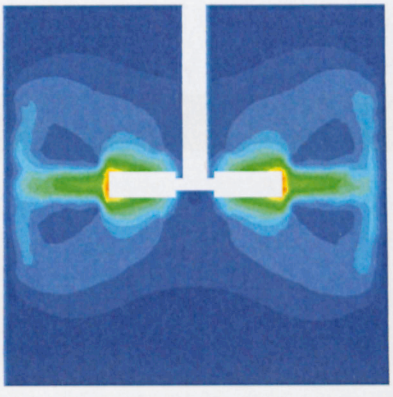

170 rpm (Re≈98.86)

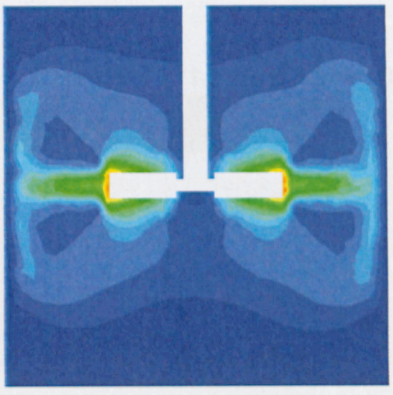

180 rpm (Re≈110.17)

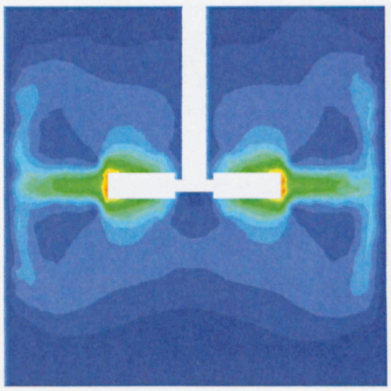

190 rpm (Re≈122.05)

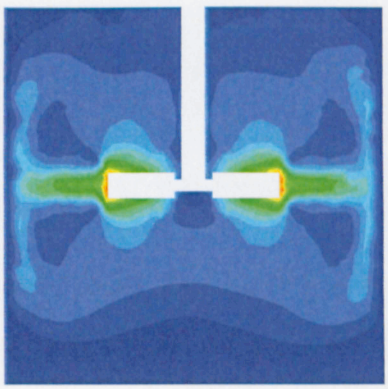

200 rpm (Re≈134.50)

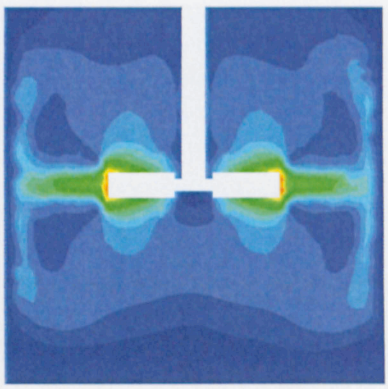

210 rpm (Re≈147.52)

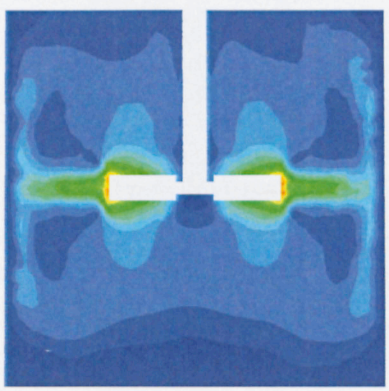

220 rpm (Re≈161.11)